Doctoral Dissertation
Doctoral Program in Energetics (32.nd cycle)

Diesel After-Treatment Systems Modeling Optimization Techniques

Francesco Sapio

* * * * * *

Supervisor
Prof. Federico Millo

Doctoral Examination Committee:
Prof. Ivan Arsie, Referee, Università Degli Studi di Napoli Parthenope
Prof. Angelo Onorati, Referee, Politecnico di Milano
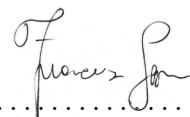Dr. Luigi Arnone, Kohler Engines
Dr. Panayotis Dimopoulos Eggenschwiler, EMPA

Politecnico di Torino
2020

I hereby declare that, the contents and organisation of this dissertation constitute my own original work and does not compromise in any way the rights of third parties, including those relating to the security of personal data.

. . . .

Francesco Sapio

Turin, 2020

Summary

The growing concern about the transportation industry pollution effects on the environment and on the human health has pushed the governments worldwide to adopt more stringent emissions standards and severe type approval procedures, representative of the real vehicle usage. With the newly introduced test procedures, which includes more energy-demanding driving cycles such as the Worldwide harmonized Light vehicles Test Cycles (WLTC) and the Real Driving Emissions (RDE) test cycle, engine emissions have to be controlled under a broader range of operating conditions, including low temperature and highly transient driving manoeuvres. In this scenario, the adoption of the after-treatment systems has become essential, in both spark and compression ignition engines, to comply with the emissions targets.

In particular, compression ignition engines require the combination of different after-treatment devices to perform the selective abatement of different pollutants species, such as CO, unburned HydroCarbons (HC), Nitrogen Oxides (NO_x) and Particulate Matter (PM), in a wide range of operating conditions, including at low temperature. Moreover, the emissions abatement must be guaranteed for the useful life of the vehicle, thus introducing additional constraints in the design of the after-treatment system.

In this context, the automotive industry demands for robust modeling methodologies and flexible simulation tools to support the vehicle engineering process, reducing the number of costly and time-consuming experimental campaigns and thus the time-to-market of the engine.

In this research work, different modeling approaches were explored ranging from detailed multi-dimensional models, suitable for component-level analysis and optimization, to mono-dimensional models suitable to perform system-level performance assessment, optimization and controls development. The aim of this research work was to develop robust methodologies to predict the conversion efficiency of complex after-treatment systems for the future generation of diesel powertrains, with a comprehensive approach and compassing both component- and system-level optimization to assess the after-treatment performance over the broad range of operating conditions which have to be explored for the real driving emissions compliance.

In the first chapter, a brief overview of the phenomena involved in automotive reactors is presented and the fundamental equations used to reproduce such phenomena in the simulations are described.

In the second chapter a 1D-CFD numerical model developed for an innovative Lean NO_x Trap catalyst is presented. The component, optimized for low temperature NO_x storage, was extensively characterized at the Synthetic Gas Bench (SGB) in terms of oxidative behaviour, NO_x storage under fuel-lean conditions, Oxygen Storage Capacity (OSC) and NO_x reduction under alternating fuel-rich and -lean conditions. The experimental results were used to calibrate the LNT model reaction parameters by means of optimization tools based on evolutionary algorithms. The calibrated model was finally validated over different WLTC and RDE driving cycle data to assess its predictive capabilities over transient operating conditions.

In the last chapter, a comprehensive methodology to extensively characterize complex after-treatment systems is presented. The methodology was used to analyze two Euro6-compliant after-treatment architectures for diesel passenger cars, which included a Diesel Oxidation Catalyst (DOC) mounted in closed-coupled configuration with an ammonia Selective Catalytic Reduction (SCR) catalyst coated on a Diesel Particulate Filter (DPF), also known as SCR on Filter (SCRoF or SCRF). First, an experimental campaign was carried out to characterize the analyzed systems in terms of physical and chemical properties of the monoliths, the Urea Water Solution UWS spray characteristics and the NO_x conversion efficiency under type-approval representative operating points. The experiments highlighted a performance gap between the two architectures, especially in the low temperature operating conditions. To further investigate the different systems behaviour and to clarify the source of the performance gap observed in the experimental campaign, a 3D-CFD numerical model was developed for the two systems and used to analyze the internal fluid and thermal dynamics, the UWS spray break-up and evolution, the liquid film development and the flow uniformity at the entrance of the SCRoF catalysts. The numerical analysis demonstrated that the different conversion efficiency achieved by the systems was mainly due to the different architecture of the UWS mixer, providing useful insights for the compact and efficient design of similar after-treatment components.

Acknowledgements

To my loving family

Contents

List of Tables

List of Figures

XIX

Publications

Parte del lavoro descritto in questa tesi è stato precedentemente pubblicato in:

Part of the work described in this thesis was previously published in:

- Sapio, F., Millo, F., Fino, D., Monteverde, A. et al., *"Experimental and Numerical Analysis of Latest Generation Diesel Aftertreatment Systems",* SAE Technical Paper 2019-24-0142, 2019, doi: 10.4271/2019-24-0142.

- Millo, F., Rafigh, M., Sapio, F., Wahiduzzaman, S., Dudgeon, R., Ferreri, P., and Barrientos, E., *"Modeling NO_x Storage and Reduction for a Diesel Automotive Catalyst Based on Synthetic Gas Bench Experiments",* Industrial & Engineering Chemistry Research 2018 57 (37), 12335-12351, doi: 10.1021/acs.iecr.8b01813

Chapter 1

Introduction

1.1   Scenario

In the last years, the transport sector was called to a dramatic reduction of vehicles emissions in the atmosphere due to the increasing concerns about global warming and the local pollution, especially in highly-populated urban areas. The latest emissions standards were progressively tightened worldwide and more severe test procedures introduced in order to bridge the gap between type-approval and real-world vehicle operations. In this framework, to comply with the regulations OEMs are developing solutions to reduce engine out emissions at the source, by improving the combustion system design, optimizing the control strategies and the integration the engine subsystems. On the other side, the adoption of the exhaust After-Treatment (AT) system has become mandatory.

As far as Compression Ignition (CI) engines are concerned, a number of different components is used to selectively abate pollutants in the exhaust gas. The oxidation of unburned HydroCarbons (HC), CO, H_2 and in general of incomplete combustion products is typically performed by the Diesel Oxidation Catalyst (DOC) which contains Platinum Group Metals (PGM) to catalyze the oxidation reactions. The DOC catalysts washcoat might also contain hydrocarbon absorbing materials, which are used to store unburned hydrocarbons during the cold start phases and release it afterwards, once the light-off temperature is reached. To perform the simultaneous oxidation of combustion byproducts, the low-temperature storage and the reduction of NO_x emissions, a NO_x Storage Catalyst (NSC) could be used instead. In the Lean NO_x Trap (LNT), for instance, Barium oxides are included in the washcoat to trap NO_x molecules during the fuel-lean operations, while in fuel-rich conditions the stored NO_x are reduced and the storage capacity restored. To comply with the tight NO_x emissions limits, often the NSC alone is not sufficient therefore an addition catalyst should be installed in the exhaust line, such as the Selective Catalytic Reduction (SCR) catalyst, coated with Zeolites, which could reach up to 90% or higher NO_x conversion thanks to the ammonia contained in an aqueous

solution, injected upstream of the catalyst. Diesel Particulate Filters (DPF) are widely adopted to trap up to more than 90% of the Particulate Matter (PM) emitted from the engine and often these catalyst are coated with a SCR washcoat to combine the PM abatement with the NO_x catalytic reduction properties, known in this case as SCR coated on Filter or SCRoF. Finally, an additional oxidation catalyst known as Ammonia Oxidation Catalyst (AOC), which consist of a SCR brick with a small PGM percentage in the washcoat, could be present in the exhaust line to oxidize the excess ammonia slipped through the upstream SCRs.

Furthermore, complex control strategies are required to accurately manage the AT operational requirements, such as defining the timing and quantity of Diesel Exhaust Fluid (DEF) injections or performing the DPF and the LNT regeneration, in order to periodically restore the storage/trapping capacity while minimizing the fuel consumption.

Finally, the multitude of different catalyst components should be properly arranged in an effective layout, in order to accelerate the warm-up and to provide each catalyst with the optimum temperature window which allows to maximize the conversion efficiency, while complying with the severe packaging constraint required by the vehicle architecture.

To address all the concurrent aspects a large number of design options has to be evaluated and tested under a wide range of operating conditions, especially in the earlier design phases. To reduce the costs of a time consuming experimental campaign and reduce the time to market, the AT architecture engineering could be supported by advanced simulation tools, capable of operating as virtual test-rig. Numerical models of AT systems and components are essential in industrial applications, since could serve to multiple purposes such as the evaluation of different exhaust line architectures under real driving operating conditions, to evaluate the sensitivity of catalysts components to different design parameters (e.g. geometry, dimensions, insulation materials, loading of precious metals etc), to support the development and optimization of control strategies (e.g. DEF injection, storage capacity regeneration, warm-up strategies etc.), to optimize the design of functional components (e.g. pipe routing, DEF mixers, exhaust valves and flaps etc) and many others.

In this chapter, an overview of the governing phenomena and of the modeling methodologies applied to develop AT numerical models is provided.

1.2 Governing Phenomena

Different catalyst technologies are used by the automotive industry and catalyst characteristics such as the monolith structure or the washcoat formulations are tailored to a specific application and might vary depending on the suppliers. In general, two different macro-categories of catalyst bricks could be identified:

- Flow Through (FT) monoliths

- Wall Flow (WF) monoliths

1.2.1 Flow Through Monoliths

In this first category of monoliths, the exhaust mixture is forced to flow within the reactor, through the matrix of channels, and undergoes a series of physical and chemical processes, as summarized in Figure 1.1.
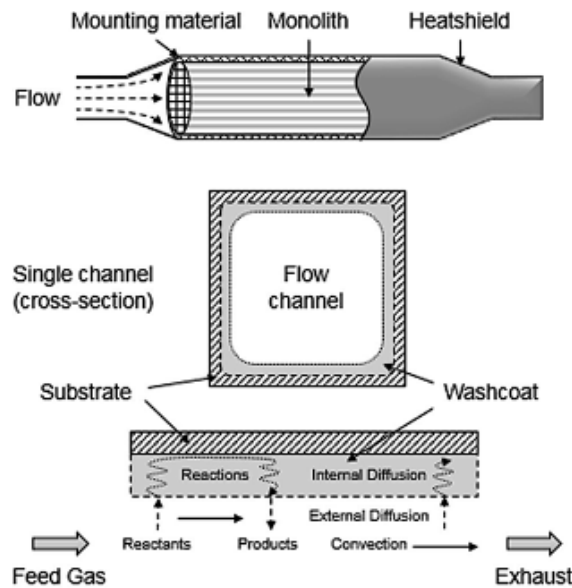
Figure 1.1: Overview of the main physical and chemical processes occurring in a washcoated monolith channel [1]

First, inside of each channel, the reactants molecules diffuse towards the channel surface, where the porous washcoat is deposited (external diffusion phase). Once on the surface, reactants diffuse further through the washcoat pores (internal diffusion phase). Here, the reactants are adsorbed by the active site, where the reaction occur, and afterwards the reaction products are released. The process is then replied backwards until the products diffuse back into the exhaust gas, before leaving the channel.

1.2.2 Wall Flow Monoliths

Differently, WF monoliths consist of FT monoliths with the channels alternatively plugged at the ends, in order to force the gas flow through the porous walls, as depicted in Figure 1.2. Depending on the size of the pores, which usually are in the order of few microns, the monoliths on this category could be operated as

mechanical filters for different size of solid particles, which makes such technology popular in automotive AT applications to filter the PM emitted from the engine.
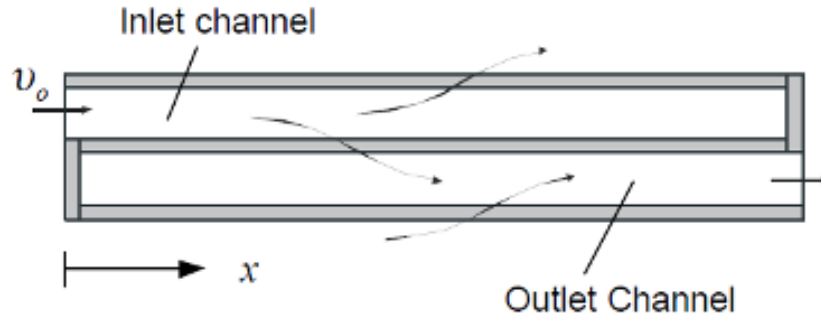
Figure 1.2: Flow pattern in a wall flow monolith [2]

Ceramic materials are generally used to manufacture WF monolith substrates in order to guarantee resistance at high temperatures and, at the same time, to ensure a low thermal expansion, which avoids mechanical damages when the monolith undergoes high thermal stresses. The particles filtration occurred by means of two different mechanisms, as depicted in Figure 1.3:

- Deep bed filtration

- Cake filtration
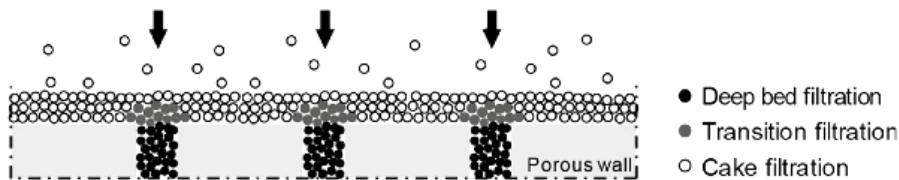
Figure 1.3: Filtration mechanisms in a wall flow monolith [3]

PM is generally made of a large number of small particles which can penetrate within the substrate pores. Here, the particles are collected on the pores surfaces by means of Brownian inertia. In this phase, known as the deep bed filtration, a rapid increase in the pressure drop is produced due to occlusion of the pores by the accumulated particles. Once the pores are saturated, the incoming particles start accumulating on the channel internal surface forming a soot layer, in the so called soot cake filtration regime. In this phase the pressure drop increases linearly as the particle continue accumulating, until the filter is regenerated.

1.3 Numerical Simulation of After-Treatment Systems

1.3.1 Simplifying Assumptions

Since the full numerical solution of the entire monolith could result prohibitively expensive in terms of computational resources, some simplified assumptions are applied in the models:

- The radial distribution of the gas flow at the entrance section of the monolith is assumed uniform, ignoring channel to channel variations

- Due to the relatively high space velocity encounter in automotive reactors, which implies a short residence time of the gas within the channels, the heat conduction and mass diffusion in the bulk gas could be neglected in the flow direction

- The flow field is assumed to be laminar within the channel due to the relatively low Reynolds number (< 1000) encountered in the reactors

- The cross sectional area is considered uniform along the channel

- Within the solid phase the transverse temperature gradients are negligible compared to the axial gradients

- Heat and mass transfer coefficients are used to account for radial gradients between fluid and solid phases

- Gas phase reactions are considered neglected, thus considering only surface reactions

1.3.2 Governing Equations

By applying the aforementioned simplifying assumptions the numerical model is reduced to a single channel representative of the mean behaviour of the reactor. The phenomena reported in Section 1.1 are described by means of a series of mathematical equations, which accounts for:

- Energy and species conservation in the gas phase

- Species conservation in the washcoat

- Energy conservation in the solid phase

The mentioned equation are solved along the channel axis (gas and solid phase conservation equations) and the washcoat thickness (washcoat conservation equation), thus the model is defined as 1+1 Dimensional (1+1D).

Often, the washcoat diffusion is neglected in the numerical models to further speed up the computation, thus reducing the model to a single dimension (1D).

The gas phase species conservation equation can be written as:

$$f_{vd}\rho_g \frac{\partial \omega_{g,i}}{\partial t} = -f_{vd}\rho_g u \frac{\partial \omega_{g,i}}{\partial x} - \rho_g k_i S(\omega_{g,i} - \omega_{s,i}) \tag{1.1}$$

The gas phase energy conservation equation can be written as:

$$f_{vd}\rho_g C_{pg} \frac{\partial T_g}{\partial t} = -f_{vd}\rho_g C_{pg} u \frac{\partial T_g}{\partial x} - hS(T_s - T_g) \tag{1.2}$$

The solid phase energy conservation equation can be written as:

$$\psi_s \frac{\partial T_s}{\partial t} = \frac{\partial}{\partial x} - hS(T_s - T_g) - h_x S_x(T_s - T_x) + \sum_{l=1}^{2} \sum_{n=1}^{n_{rxns}} \Delta H_n^{(l)} a_n^{(l)} \overline{r_n}^{(l)} \tag{1.3}$$

The effective thermal conductivity of the solid phase Λ_s is given by:

$$\Lambda_s = f_{sb}\lambda_{sb} + \sum_{l=1}^{2} f^{(l)}\lambda^{(l)} \tag{1.4}$$

The effective heat capacity of the solid phase ψ_s is defined as:

$$\psi_s = f_{sb}\rho_{sb}C_{p,sb} + \sum_{l=1}^{2} f^{(l)}\rho^{(l)}C_p^{(l)} \tag{1.5}$$

The average reaction rate $\overline{r_n}^{(l)}$ across the washcoat thickness is expressed as:

$$\overline{r_n}^{(l)} = \frac{1}{\delta^{(l)}} \int_0^{\delta^{(l)}} r_n^{(l)} dx, \ l = 1,2 \tag{1.6}$$

The effective washcoat thickness $\delta^{(l)}$ is defined as in equation 1.7 to account for the additional washcoat mass which accumulates in the channel corners.

$$\delta^{(l)} = \frac{f^{(l)}}{S}, \ l = 1,2 \tag{1.7}$$

The washcoat species conservation equation can be written as:

$$f^{(l)}\epsilon^{(l)}\rho_s \frac{\partial \omega_i}{\partial t} = f^{(l)}\rho_s D_{i,eff}^l \frac{\partial^2 \omega_i}{\partial y^2} + R_i^{(l)} \tag{1.8}$$

The ith species rate in the layer l, indicated as $R_i^{(l)}$, can be computed as:

8

$$R_i^{(l)} = MW_i \sum_{n=1}^{n_{rxns}} s_{i,n} a_n^{(l)} r_n^{(l)} \tag{1.9}$$

Finally, the site balance equation can be written as:

$$A_k^{(l)} \frac{\partial \theta_k^{(l)}}{\partial t} = \sum_{n=1}^{n_{rxns}} \sigma_{k,n} a_n^{(l)} r_n^{(l)}, \ l = 1,2 \tag{1.10}$$

The surface reaction rates are expressed based on the turnover number. According to this notation, individual reaction rates are scaled by the active site density, which indicates the moles of active site per catalyst volume, and expressed as moles reacted per moles of active site per second. The total volume rate of each reaction can be obtained as the product between the turnover rate and the active site density for a given reaction.

Turnover rates allow to easily carry over the kinetics between reactors with the same formulation but different catalysts loading, with the active site density acting as a scaling factor.
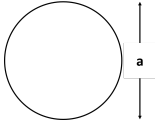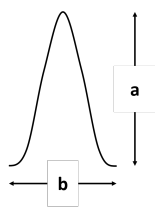
On the modeling site, using turnover reaction rates adds additional flexibility to the model. Furthermore, the active site density could be used to scale the kinetics to take into account, for instance, the activity loss due to the catalyst aging (active sites being partially deactivated).

1.3.3 Heat and Mass Transfer Coefficients

The rate of heat and mass transfer from the fluid to the solid walls depends on the channel geometry and on the flow conditions within the channel. The effect of heat and mass transfer on the exit conversion of automotive catalytic reactors was investigated by Gundlapally and Balakotaiah [4], who compared a multitude of different correlations used in the literature to express heat and mass transfer. It was demonstrated that in low Peclet number conditions, such as the ones encountered in automotive AT systems, the dimensionless Nusselt and Sherwood numbers can be used to effectively describe heat and mass transfer phenomena.

Therefore, for simulation purposes heat and mass transfer are determined by means of numerical coefficients obtained from the analogy with heat transfer problems and reported in Table 1.1. In fact, when the flow conditions within the channel are fully developed, Nusselt and Sherwood numbers approach asymptotic values which depend on the channel geometry and wall boundary conditions.

Table 1.1: Asymptotic values of Nusselt/Sherwood numbers and friction factors for commonly used channel geometries [4]

Channel Shape	$D_h(4R_\Omega)$	$(fRe)_\infty$	$Nu_{H2\infty}(Sh_{H2\infty})$	$Nu_T(Sh_T)$
	2a	16	4.364	3.656
	2a	14.23	3.089	2.977
	1.5419a	14.574	0.95	2.496
	1.418a	14.023	1.38	2.536
	1.2103a	13.023	1.55	2.476
	1.0466a	12.234	1.34	2.353
	0.8118a	11.207	0.90	2.110
	0.4673	10.123	0.33	1.719

1.4 Experimental Measurements and Model Calibration Protocol

In the simulation of after-treatment systems several concurrent phenomena are encountered, pertinent to the fluid and thermal dynamics and to each catalyst chemical kinetics.

To model the chemical activity of a single or even of multiple catalysts, the CFD modeling is paired with the chemical kinetics modeling, in which reaction rates parameters would require calibration to properly model the catalyst conversion. To this aim, a wide range of measurements is required to properly identify the reactions pathways involved in the pollutant conversion and to individually characterize the catalyst operations.

Different approaches were explored in the literature to simulate the catalysts kinetics involving different degrees of complexity.

In the so called micro kinetics models, each elementary sub-step behind every reaction pathway is considered and the kinetic scheme often consist of a large number of reactions [5]. This modeling approach requires a deep understanding of the kinetics involved in the catalyst operations to accurately identify and include all the required reactions sub-steps, furthermore a significant calibration effort and a large experimental dataset are required in order to develop the model. This approach produces accurate models and is used in the academia, while may be not suitable for industrial purposes.

On the other side, with global kinetic models each reaction pathway is described as a single step and the effect of each elementary sub-step is embedded in the kinetic constants of the corresponding global reaction [6, 7, 8]. By this means, the

resulting kinetic mechanism is greatly simplified and the calibration effort required is reduced. For these reasons this approach is widely used for industrial applications and applied to a wide range of different catalyst technologies.

In general, to obtain predictive models whose results are accurate on a large range of different operating conditions the definition of a comprehensive experimental campaign and of a proper calibration protocol is crucial.

The experiments used to characterize automotive catalyst are often carried out on small samples extracted from the full-size brick, on a specifically designed laboratory test-bench, known as the Synthetic Gas Bench (SGB). The samples are properly encapsulated in order to minimize the external heat transfer and tested under different operating conditions. Synthetic gases are used to reproduce the exhaust gas composition and to recreate specific test condition. The gas flow rate is set in order to operate the reactor at the same space velocity, and thus the same residence time of the gas within the channels, encountered on the full-size system during the typical engine operations.

The test protocol should be designed in order to characterize the largest number of catalyst operations, under a wide range of operating conditions. To this aim, tests with elementary species are used to individually characterize the reactor selectivity to a small subset of reactions, while more complex gas mixtures are used to evaluate the mutual interaction between different species and their effect on the catalyst conversion.

The model calibration protocol used in this work consist of a series of elementary steps:

1. The reactor-scale model is built and the kinetic scheme identified, based on the experimental observations

2. The model kinetic constants are calibrated based on the SGB experiments

3. The reactor-scale model is scaled up to represent the full-size component and validated over driving cycle data

This last step is fundamental to realize robust models for industrial applications, since allows to assess the model predictive capabilities under highly transient operating conditions, representative of the real catalyst usage. It should be noted that ideally, the chemical kinetics identified at the SGB should correspond to the chemical activity of the full-scale system used on the vehicle, thus the kinetic constants obtained for the reactor-scale model could be carried over to the full-size model without modifications. Unfortunately, often the full-size model validation over driving cycle data reveals some differences which are related to the different conditions encountered on the engine. The errors observed during the scale-up of reactor-scale models could be related to [9]:

1. The large number of HC species contained in the real exhaust gas may differ from the few ones (usually 1 or 2) used to characterize the catalyst samples at the SGB

2. The hypothesis of uniform mass flow distribution on the catalyst cross section could not apply to the full size component, in which entrance effects and flow distribution could became significant

3. The ageing conditions of the full-size catalyst operated on the engine might differ from the laboratory-scale samples tested at the SGB

For these reasons, fine tuning of the engine-scale model parameters could be required to improve its predictive capabilities.

Chapter 2

Modeling NO$_x$ Storage and Reduction for a Diesel Automotive Catalyst Based on Synthetic Gas Bench Experiments

Parte del lavoro descritto in questo capitolo è stato precedentemente pubblicato in:

Part of the work described in this chapter was previously published in:

2.1   Introduction

The growing concern about transport-related pollution effects on human health, increased further after the latest diesel scandal, is pushing worldwide towards increasingly more stringent emission regulations on one side, on the other the institutions are tightening CO_2 emissions limits to counteract global warming. Particularly in Europe, the Euro 6 regulation introduced type approval procedures more representative of the real vehicle usage, such as the Worldwide harmonized Lighduty vehicles Test Cycle (WLTC) and the Real Driving Emissions (RDE) driving cycles. In this scenario, compression ignition powertrains still have an important role in achieving the CO_2 reduction aimed by the regulations.

Considering the continuously increasing degree of vehicle electrifications and the newly introduced test procedures, the cold-start emissions abatement is crucial to comply with the regulations. Despite ammonia SCR systems represent one of the most promising solutions to drastically reduce NO_x emissions, such technology achieves the maximum efficiency in a narrow temperature window and is not suitable for low temperature NO_x abatement due to the high temperatures (higher than 180 degC) required to transform the urea-solution into the ammonia required for the SCR reactions. In Lean NOx Traps (LNTs) instead, during lean operating conditions NO_x are chemically stored by the Barium sites on the catalyst surface in the form of nitrates, even at temperatures below 150 degC [10, 11, 12]. However, LNTs introduce a higher level of complexity and appropriate control strategies need to be designed. The storage capacity in fact should be periodically regenerated by operating the engine in fuel-rich conditions for a brief period of time (in the order of seconds), inducing the reduction of the stored NO_x with the unburned hydrocarbons, the CO and the H_2 in the exhaust gas or the NO_x release due to the high temperatures [13, 14, 15]. The LNT NO_x conversion rapidly decreases at high temperature, thus an additional SCR should be required to maximize NO_x abatement during high load operating conditions. In addition, during the regeneration phase the LNT catalyst produces NH_3, which can be further used by a downstream SCR to abate NO_x, reducing the need of additional urea-solution. Finally, during the LNT regeneration phase some N_2O could be produced, which is an undesired byproduct. The additional complexity introduced and the required control design could be addressed by developing robust and reliable simulation tools, reducing the calibration effort especially in the early after-treatment development phase.

Different modelling approaches applied to LNT kinetics are available in the literature. Kota et al [5] used a micro-kinetics approach to model the main LNT reaction pathways through each elementary step, obtaining a high model fidelity. However, due to the complexity introduced in the model, this approach requires

a deep understanding of the kinetics behind the analysed phenomena, a large set of dedicated experiments and a significant calibration effort. A global kinetic approach instead could be more indicated for industrial applications, where time and budget are usually limited, since it represents each reaction pathway by means of a single global reaction, thus reducing the model complexity. This approach was used by Koltsakis et al to develop a single-channel LNT model starting from a Three Way Catalyst (TWC) model [8]. The kinetic scheme was extended to account for LNT operations and calibrated over experimental data obtained at the Synthetic Gas Bench (SGB) on small reactor samples. However, most of the LNT models available in the literature refer to laboratory-scale samples while there is a lack of full-size models validated over driving cycle data, which are crucial for industrial applications.

In this work, a comprehensive methodology to develop, calibrate and validate a 1D-CFD model of a latest-generation LNT catalyst is presented. First, a large set of SGB experiments was carried out on small catalyst samples to fully characterize the LNT in different operating conditions, representative of the engine operations. Catalyst samples were tested on a wide range of gas temperature, flow rate and compositions to fully characterize the LNT's oxidation performance, the NO$_x$ adsorption and desorption in lean conditions, the Oxygen Storage Capacity (OSC) and the NO$_x$ reduction performance under alternating lean and rich conditions. The model, developed to support the OEM in the early research and development phase of a novel after-treatment architecture, was built in GT-SUITE, a commercially available simulation platform. A global kinetic scheme was defined, extending the author's previous work presented in reference [16], and calibrated over the SGB experimental data. Finally, the reactor-scale model was up-scaled to represent the full-size component, inheriting the chemical kinetics parameters from the lab-scale model without relevant modifications, and validated over driving cycle data, including 2 different Worldwide harmonized Light vehicles Test Cycles (WLTC) and a Real Driving Emissions (RDE) cycle. The model correctly captured the LNT features even in critical operating conditions, such as catalyst's controlled regeneration events, high flow rates and gas temperature conditions, confirming the robustness of the applied methodology.

2.2 Experimental Analysis

2.2.1 Experimental Set-up

An extensive experimental campaign was carried-out, through a Synthetic Gas Bench (SGB), at General Motors R&D facilities to fully characterize the LNT kinetic under different gas mixtures, temperature and flow conditions.

The experimental campaign was conducted on cylindrical monolith samples, whose dimension are reported in Table 2.1, obtained from the full-scale component and placed into an isotherm reactor. Synthetic gases were fed to the reactor by means of mass flow controllers to reproduce each catalyst operation in terms of flow rate and composition, while the gas temperature was controlled by means of a heater. Particularly, the inlet gas mixture and composition were specifically designed for each test in order to separate and individually characterize small subsets of reactions, while the inlet Gas Hourly Space Velocity (GHSV or SV) and temperature were chosen in order to represent the full-scale monolith typical operating conditions. Prior to the experimental campaign, the catalyst samples were placed in a furnace and aged for 20 hours at a temperature of 800 degC, flowing a mixture of air and water (10% in volume).

K-type thermocouples were used to measure the gas temperature upstream and downstream the reactor. A wide band Universal Exhaust Gas Oxygen (UEGO) sensor was used to detect the lambda in the inlet batch, while the gases concentration at the reactor outlet was measured by means of a Fourier Transform Infra-Red (FTIR) with a sampling frequency of 1 Hz. The measured species included CO, CO_2, H_2O, NO, NO_x, NH_3, N_2O, and hydrocarbons (i.e. propylene and dodecane). Unfortunately, the measurement of H_2 was not available. A simple representation of the experimental apparatus is depicted in Figure 2.1.

2.2.2 Test Protocols

The test protocol has been categorized into several steps in order to individually characterize different phenomena. Primary single species tests were used to identify the rate of each reaction, while more complex gas mixtures were used to investigate the interaction between different species, over a wide range of temperatures. Different temperature control protocols were used to characterize both steady-state or transient phenomena.

Table 2.1: LNT catalyst geometry

Full Size Dimensions	
Diameter [mm]	125
Length [mm]	96
Laboratory Samples Dimensions	
Diameter [mm]	19
Length [mm]	43
Catalyst Properties	
Substrate	Cordierite
Washcoat	Alumina
PGM Loading [kg/m^3]	4.24
PGM Ratio (Pt:Pd:Rh)	103:12:5
Cell Density [cpsi]	400
Wall Thickness[mm]	0.114
Aging Protocol	Oven-aged (20h/800 degC, 10% H$_2$O + Air)
Sulphur Loading [g/m^3]	0

The test-protocol, summarized in Table 2.2, was designed to individually characterize the following LNT catalyst operations:

- CO and hydrocarbons oxidation Light-Off (LO)

- NO$_x$ storage and desorption

- NO$_x$ Storage and Reduction (NSR) under lean/rich cycling

- Oxygen Storage Capacity (OSC)
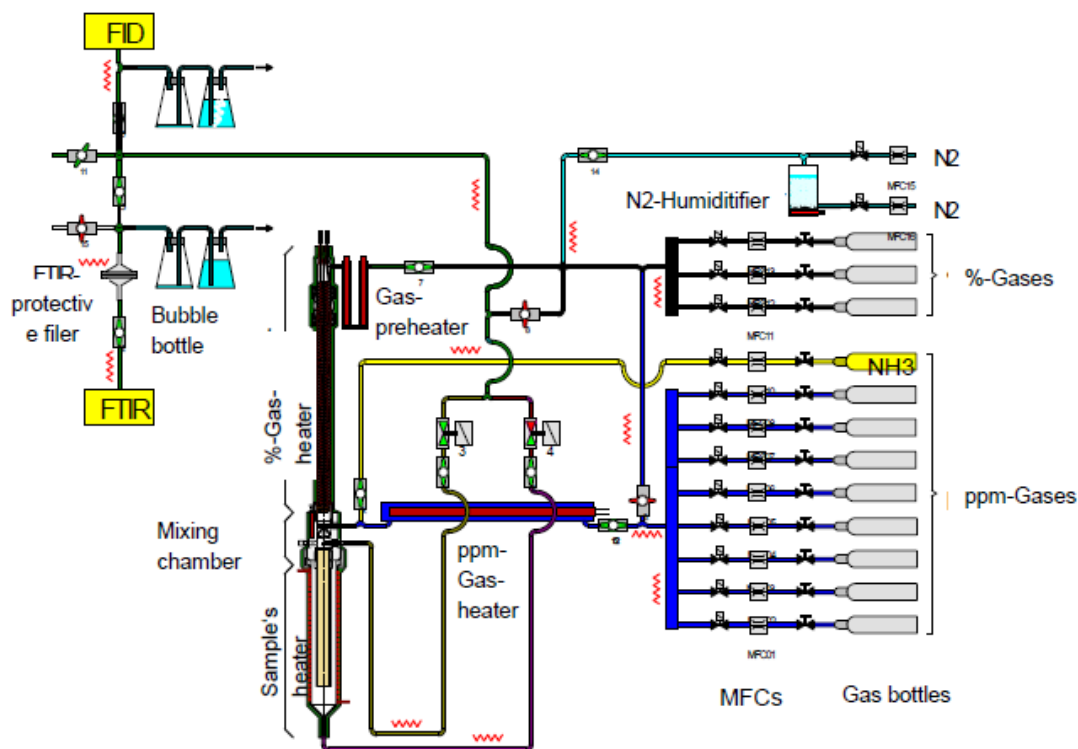
Figure 2.1: Schematic representation of a synthetic gas bench

The relatively low inlet gas flow rate and space velocity was selected in order to fully characterize the catalyst chemical kinetics, reducing the influence of mass transfer effects on the species conversion. Some of the tests were also repeated with higher flow rate, in order to investigate the effect of increased space velocity on the catalyst conversion.

2.2.3   Light-Off (LO)

A Temperature Programmed Reaction (TPR) test protocol was used to characterize the oxidative behavior of the catalyst in terms of light-off temperature, which is usually defined as the temperature where the 50% of conversion efficiency is reached for the species of interest. The reactor was fed with a constant concentration of a reducing agent, such as H_2, CO and hydrocarbons, in addition to a background composition of 12% O_2, 5% H_2O, 5% CO_2, and nitrogen. Different concentrations of the reducing agents were tested as well as the combination of different reducing species. Nitrogen oxides were also included in some of the tests to evaluate their inhibition effect on the oxidation reactions. As representative of unburned hydrocarbons, dodecane ($C_{12}H_{26}$) was chosen as slow oxidizing HC, while

Table 2.2: Test protocol for the LNT characterization

Characteristic	Temperature Control	Reducing Agent
Light-Off	Linear Ramp (100 - 500) degC rate 5 degC/min	H$_2$ CO HCs (Propylene, Dodecane)
NO$_x$ Storage	TPD (100 - 500) degC rate 5 degC/min	-
OSC	Steady-State (200 - 450) degC	H$_2$ CO HC (Propylene)
NSR	Steady-State (150 - 400) degC	H$_2$ CO HC (Propylene)

propylene (C$_3$H$_6$) was selected as fast oxidizing HC, in the proportion of 80% and 20% respectively. Once the concentration at the reactor inlet was stable, the gas temperature was linearly increased at a fixed rate of 5 degC/min until the maximum temperature of 500 degC was reached. The gas flow rate was set to approximately 0.18 m^3/h for all the tests, which resulted in a space velocity of 15000 h^{-1}. Some of the tests were also repeated setting the flow rate at 0.48 m^3/h, which roughly corresponds to a space velocity of 40000 h^{-1}.

As a result, the test matrix reported in Table 2.3 was produced.

Table 2.3: Test matrix for the LNT light-off characterization

Temperature Range	(100 - 500) degC
Temperature Rate	5 degC/min
HC Species	C_3H_6 (20%) - $C_{12}H_{26}$ (80%) on a ppmC1 basis
Background Gas Composition	12% O_2 5% CO_2 5% H_2O

Test	H_2	HC	CO	NO_x	$\frac{NO_2}{NO_x}$	SV
-	ppm	ppmC1	ppm	ppm	-	k/h
1	0	250	500	0	0	15, 40
2	0	500	1000	0	0	15
3	0	1000	2000	0	0	15, 40
4	50	1000	2000	0	0	15, 40
5	500	1000	2000	0	0	15
6	0	250	500	200	0	15
7	0	250	500	200	0.5	15
8	0	500	1000	100	0	15
9	0	1000	2000	100	0	15

In Figure 2.2 results of the SGB light-off tests number 1, 2 and 3 are depicted. All the three tests were performed introducing both CO and HCs in the inlet batch, with higher concentrations moving from test 1 to test 3. As expected, the CO light-off was reached first, than the fast- and the slow-oxidizing hydrocarbons respectively. As the concentration of the reducing agent increased, the light-off point was shifted towards higher temperatures due to the higher species self- and mutual-inhibition effects produced by the richer gas mixture.
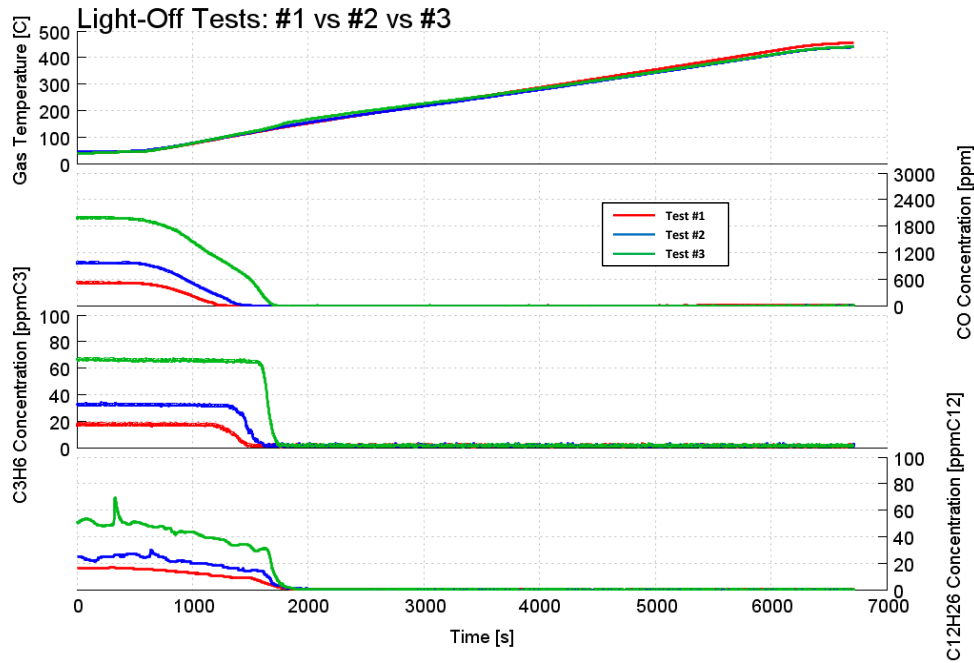
Figure 2.2: SGB results of the LNT light-off tests number 1 (red), 2 (blue) and 3 (green). GHSV of 15000 h^{-1}.

In tests number 4 and 5 all the reducing agents where introduced in the inlet batch. The addition of a small quantity of H$_2$ did not significantly affected the light-off performance of the catalyst, as can be observed in Figure 2.3 where test results are compared with the ones from test number 3. Increasing the inlet concentration of H$_2$ to 500 ppm instead, which is more representative of engine-like operating conditions, produced an initial increase in the gas temperature, due to the faster light-off of the H$_2$ oxidation, which consequently promoted the faster oxidation of the remaining reducing agents.

The effect of space velocity was investigated for tests number 1, 3 and 4. As the space velocity increases, the residence time of the gas within the reactor reduces, thus limiting the species conversion from the catalyst. In Figures 2.4, 2.5 and 2.6 the comparison between SV of 15000 h^{-1} and 40000 h^{-1} is shown for tests 1, 3 and 4 respectively. In general, a delayed light-off of the oxidation reactions was observed in the tests with higher SV, as expected.
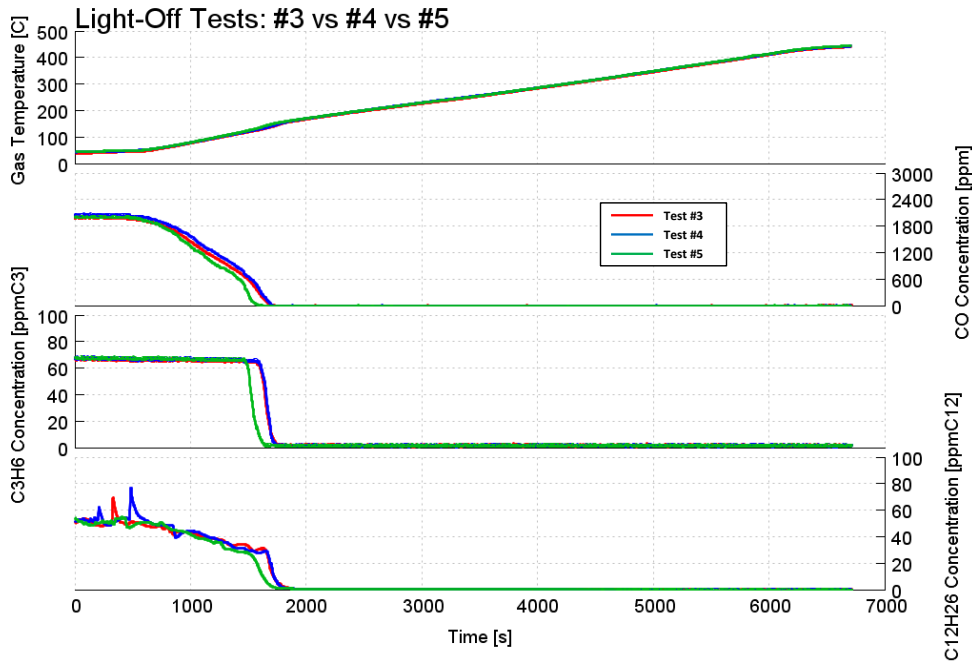
Figure 2.3: SGB results of the LNT light-off tests number 3 (red), 4 (blue) and 5 (green). GHSV of 15000 h^{-1}.
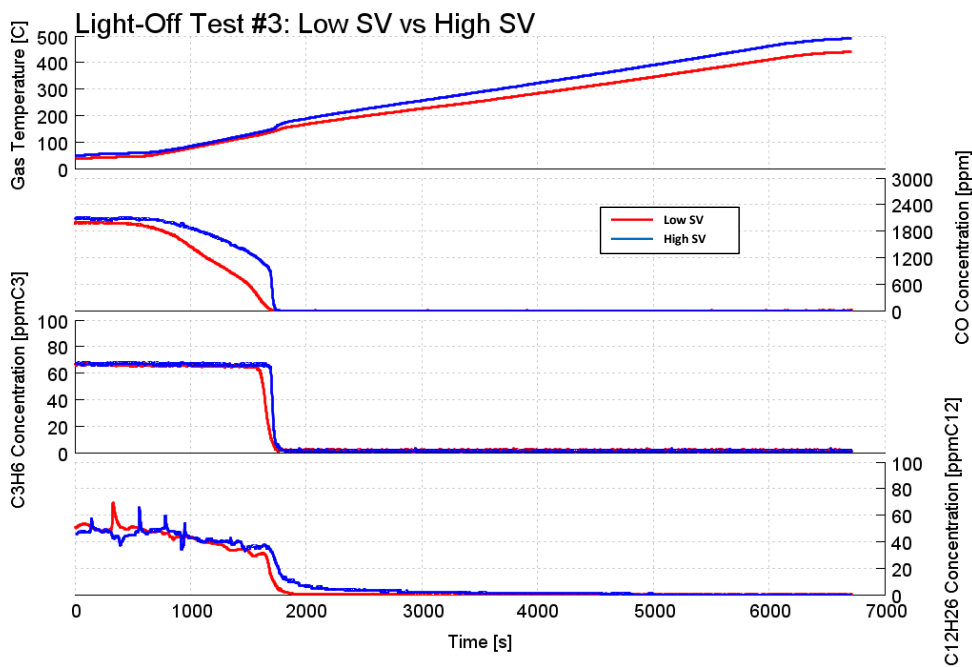
Figure 2.4: SGB results of the LNT light-off tests number 1, GHSV of 15000 h^{-1} (red) and 40000 h^{-1} (blue).
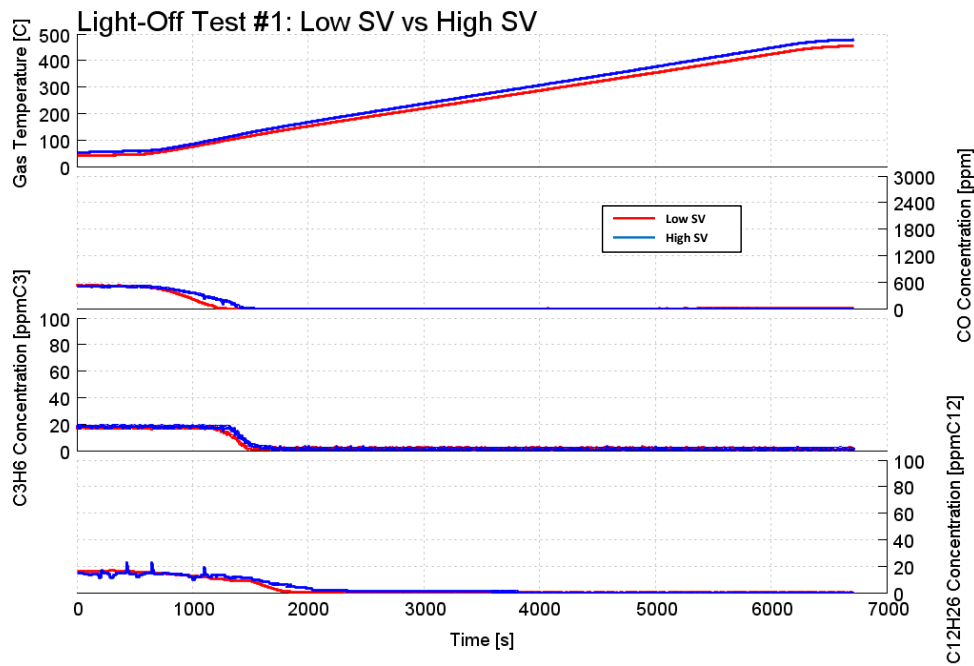
Figure 2.5: SGB results of the LNT light-off tests number 3, GHSV of 15000 h^{-1} (red) and 40000 h^{-1} (blue).
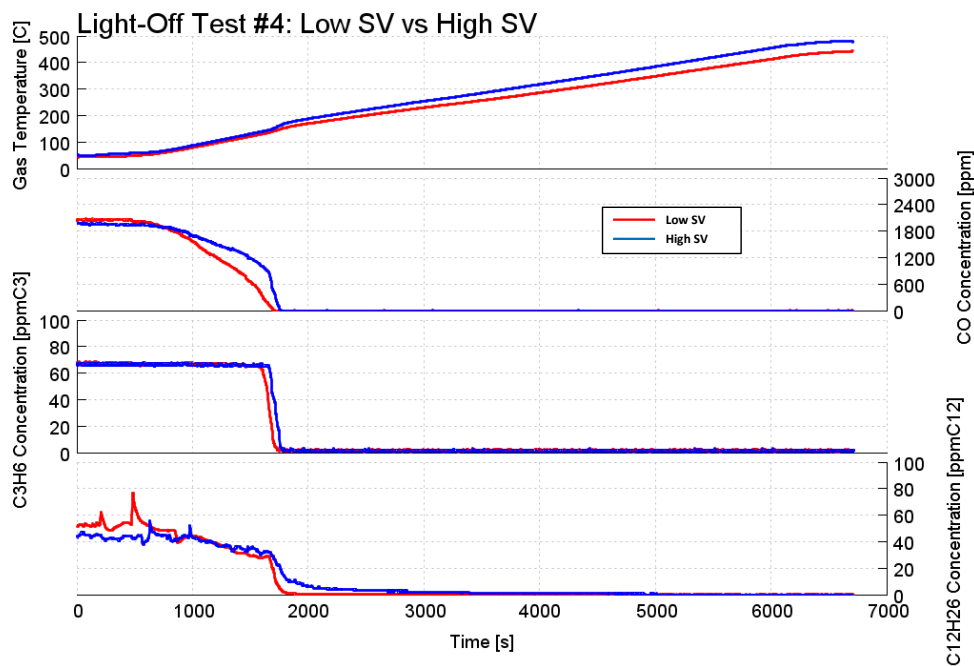
Figure 2.6: SGB results of the LNT light-off tests number 4, GHSV of 15000 h^{-1} (red) and 40000 h^{-1} (blue).

From tests number 6 through number 9, a small amount of NO_x was added to the inlet batch to investigate its effect on the oxidation of CO and HCs. NO was chosen as the inlet species, except for test number 7 in which an equimolar amount of NO and NO_2 was introduced. The competition for the available PGM sites produced an increase in the light-off temperature in all the tests, as shown in Figures 2.7 and 2.8 where reactor outlet traces are compared between tests number 1 and 6, 2 and 8 respectively.
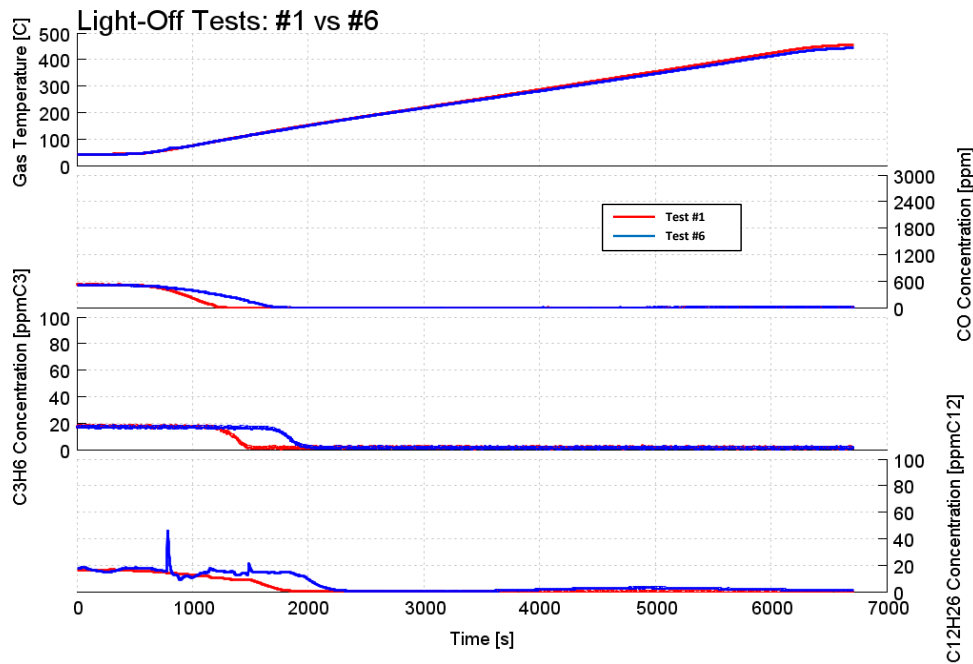
Figure 2.7: SGB results of the LNT light-off tests number 1 (red) and 6 (blue). GHSV of 15000 h^{-1}.

In Figure 2.9 the results of tests number 1, 6 and 7 are compared. As already mentioned, the introduction of NO_x in the inlet batch has the effect of retarding the reactions light-off (e.g. tests 6 and 7 against test 1). However, the introduction of a percentage of NO_2 produced faster light-off of the dodecane oxidation reaction, which could be related to the increased rate of the reduction reaction of NO_2 by means of dodecane.

25
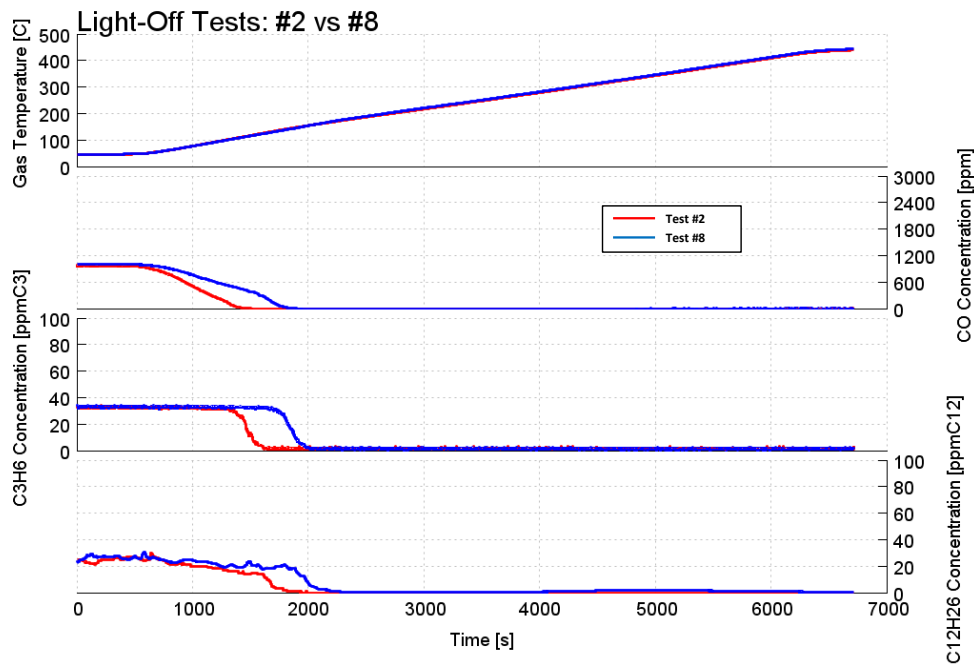
Figure 2.8: SGB results of the LNT light-off tests number 2 (red) and 8 (blue). GHSV of 15000 h^{-1}.
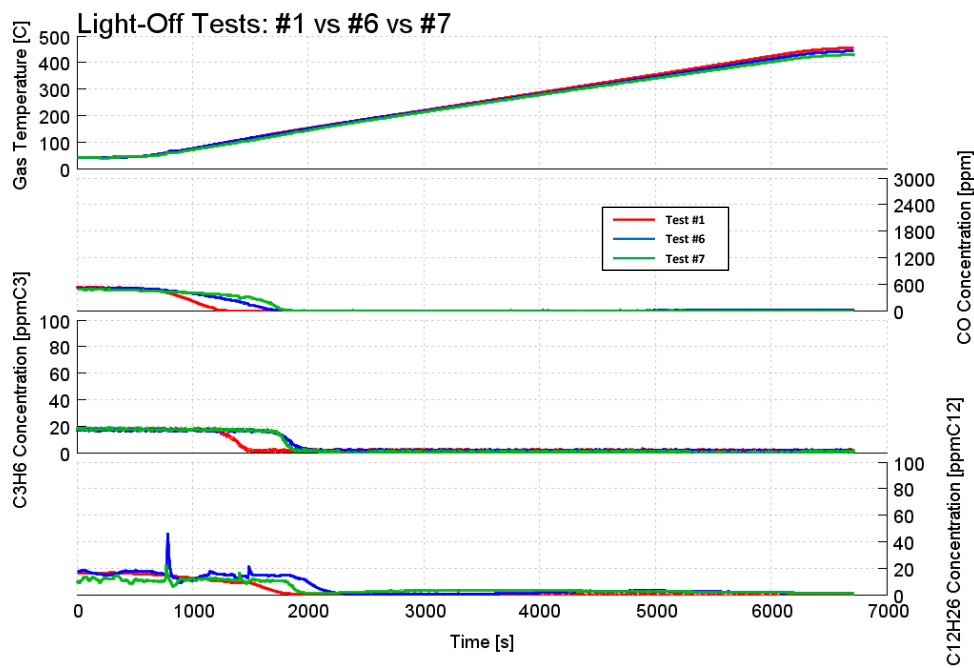
Figure 2.9: SGB results of the LNT light-off tests number 1 (red), 6 (blue) and 7 (green). GHSV of 15000 h^{-1}.

2.2.4 NO$_x$ Temperature Programmed Desorption (TPD)

To characterize NO$_x$ adsorption on Barium sites during lean operating conditions and its desorption as the temperature is increased, a TPD protocol was used. Each test was characterized by a loading phase, during which a constant amount of NO$_x$ was fed to the reactor at a fixed gas temperature until the storage sites were saturated and the outlet concentration matched the inlet one. At this point the NO$_x$ feed was stopped and the gas temperature increased linearly up to 500 degC, at a rate of 5 degC/min, to induce the NO$_x$ release and to clear Barium sites, as represented in Figure 2.10.
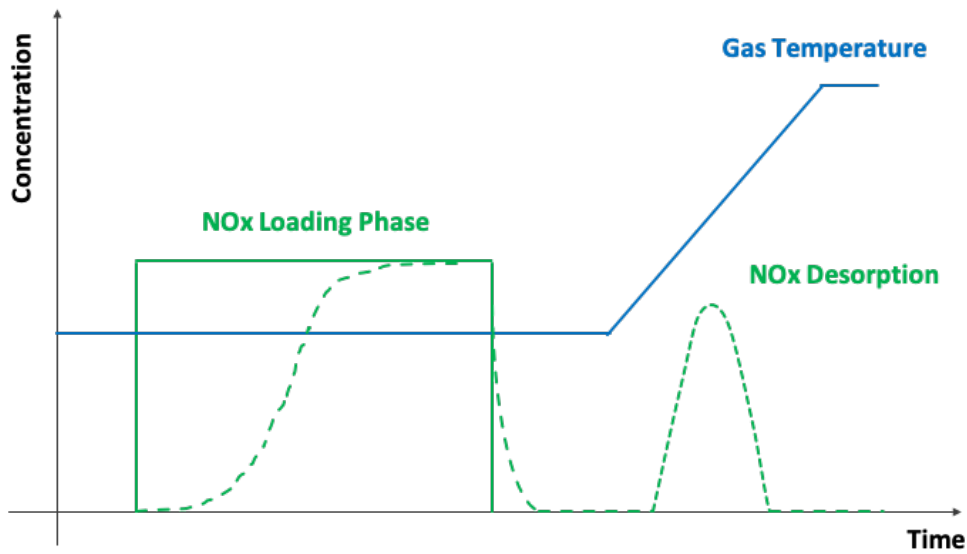
Figure 2.10: Example of NO$_x$ TPD protocol

A large number of different operating conditions was investigated, including different levels of inlet NO$_x$ concentration, different NO$_2$ to NO$_x$ ratios and different levels of gas temperature during the loading phase. The NO$_x$ TPD test protocol is summarized in Table 2.4.

An equimolar amount of NO and NO$_2$ was included in the inlet batch in tests 5, 10 and 20 which are depicted in Figures 2.11, 2.12 and 2.13 respectively. By looking at the NO$_x$ traces measured at the catalyst outlet, during the loading phase the NO breakthrough anticipated the NO$_2$ one in all the tests, indicating a larger NO$_2$ storage capacity. In test 5, where the inlet temperature was set to 125 degC, after the breakthrough the outlet NO$_2$/NO$_x$ ratio stabilized to a value of approximately 0.35, while the inlet one was kept to 0.5, as shown in Figure 2.11. This difference decreased at higher temperature, as observed in tests 10 and 20 (Figures 2.12 and 2.13). During the temperature ramp the stored NO$_x$ were released, especially in

Table 2.4: Test matrix for the LNT NO$_x$ storage and release characterization

Temperature Range	(T load - 500) degC
Temperature Rate	5 degC/min
Space Velocity	15000 h^{-1}

	Loading			Background		
Test	**T load**	**NO$_x$**	$\frac{NO_2}{NO_x}$	**O$_2$**	**CO$_2$**	**H$_2$O**
-	**degC**	**ppm**	**-**	**%**	**%**	**%**
5	125	200	0.5	12	5	5
7	150	200	0	12	5	5
10	200	200	0.5	12	5	5
16	250	200	0	5	10	10
17	250	200	0	16	3	3
20	250	200	0.5	12	5	5
28	300	200	0	5	10	10
29	300	200	0	16	3	3
32	450	200	0	12	5	5

the form of NO$_2$. Two distinct NO peaks were observed, respectively below and above 350 degC, suggesting the presence of two different storage sites. The same behavior was observed for the stored NO$_2$, however in this case the NO$_2$ release was observed at lower temperatures.

Only NO was included in the inlet batch in tests 7, 17, 29 and 32, depicted in Figures 2.14, 2.15, 2.16 and 2.17. The observed NO breakthrough during the NO$_x$ loading phase was deferred as the temperature increased above 200 degC (i.e. Figures 2.15, 2.16 and 2.17), suggesting an increase in the storage capacity at higher temperature. The two peaks in the released NO were observed at 150 degC (i.e. Figure 2.14) while the low-temperature storage site disappeared above 250 degC
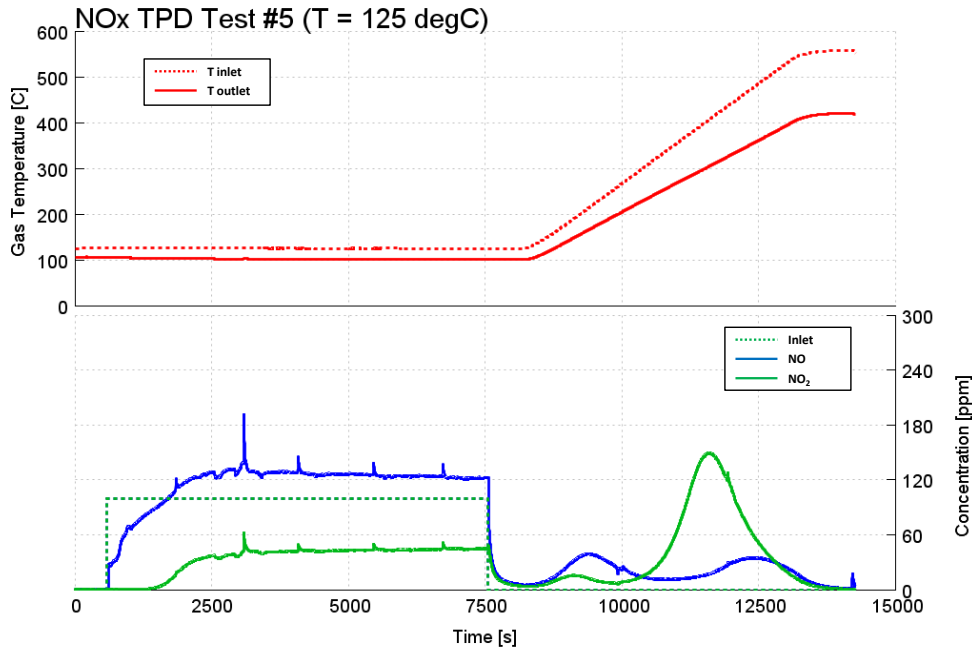
Figure 2.11: SGB results of the LNT TPD tests number 5. Gas temperature (red), NO (blue) and NO_2 (green) emissions. GHSV of 15000 h^{-1}.
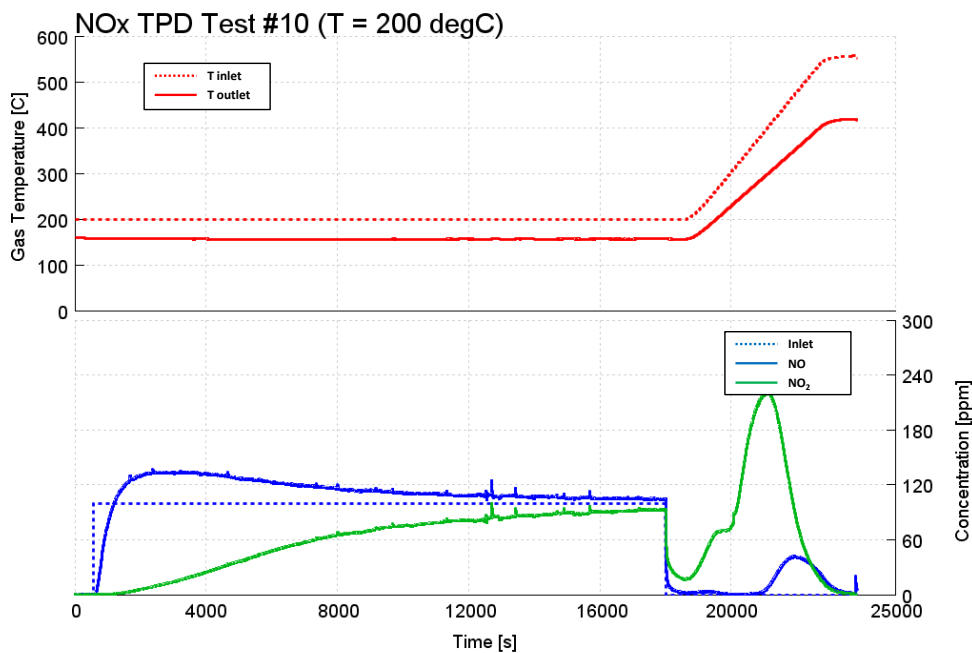
Figure 2.12: SGB results of the LNT TPD tests number 10. Gas temperature (red), NO (blue) and NO_2 (green) emissions. GHSV of 15000 h^{-1}.
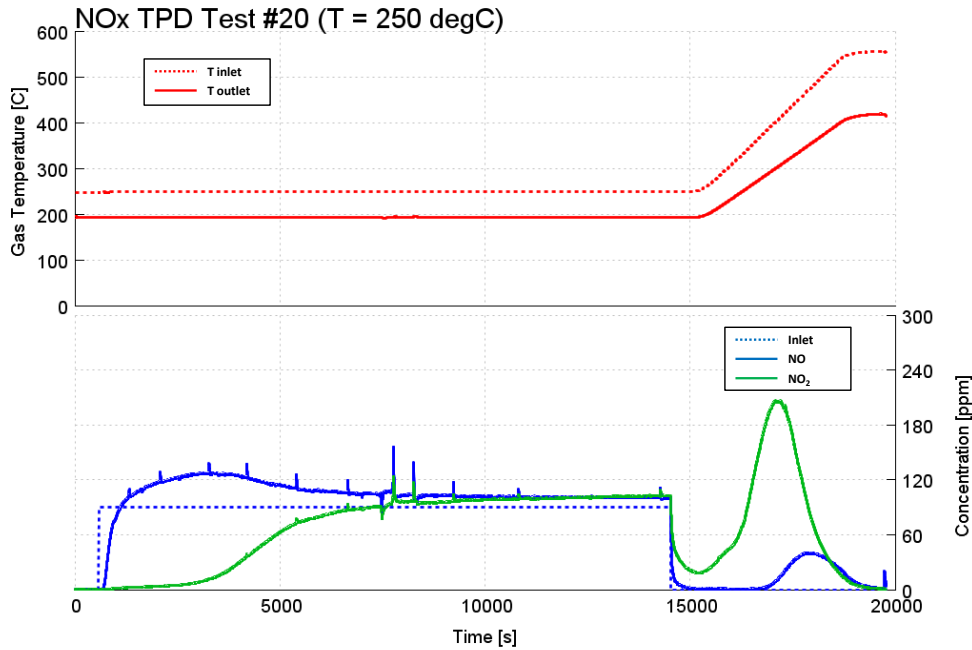
Figure 2.13: SGB results of the LNT TPD tests number 20. Gas temperature (red), NO (blue) and NO$_2$ (green) emissions. GHSV of 15000 h^{-1}.

(i.e. Figures 2.15, 2.16 and 2.17). A share of the inlet NO was oxidized to NO$_2$ in tests 17, 29 and 32, where the temperature was above 200 degC (i.e. Figures 2.15, 2.16 and 2.17). This activated the high temperature NO$_2$ storage site, as indicated by the large NO$_2$ peak during the temperature ramp.

To evaluate the effect of oxygen on NO$_x$ storage, tests 16 and 28 were performed using the same protocol of tests 17 and 29 (depicted in Figure 2.15 and 2.16) but with a different background concentration. In particular, a lower concentration of oxygen (i.e. 5% against 16%) and an increased concentration of CO$_2$ and H$_2$O (i.e. 10% against 3%) were used. The only appreciable difference observed in the results, depicted in 2.18 and 2.19, was a slight lower storage and release of NO$_2$, which could be related to the lower oxidation rate of the inlet NO due to the lower oxygen concentration.
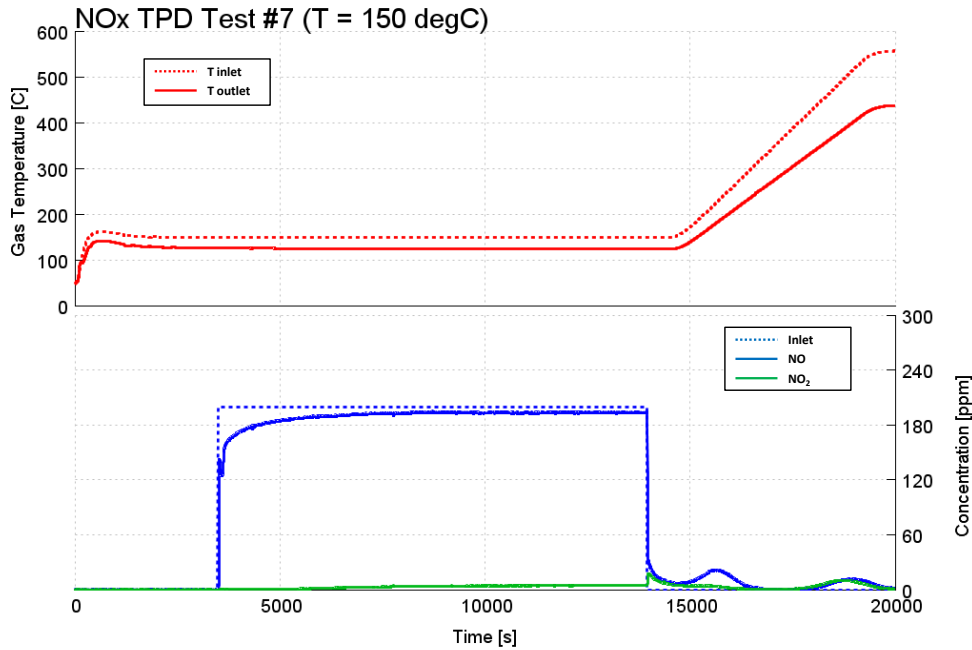
Figure 2.14: SGB results of the LNT TPD tests number 7. Gas temperature (red), NO (blue) and NO_2 (green) emissions. GHSV of 15000 h^{-1}.
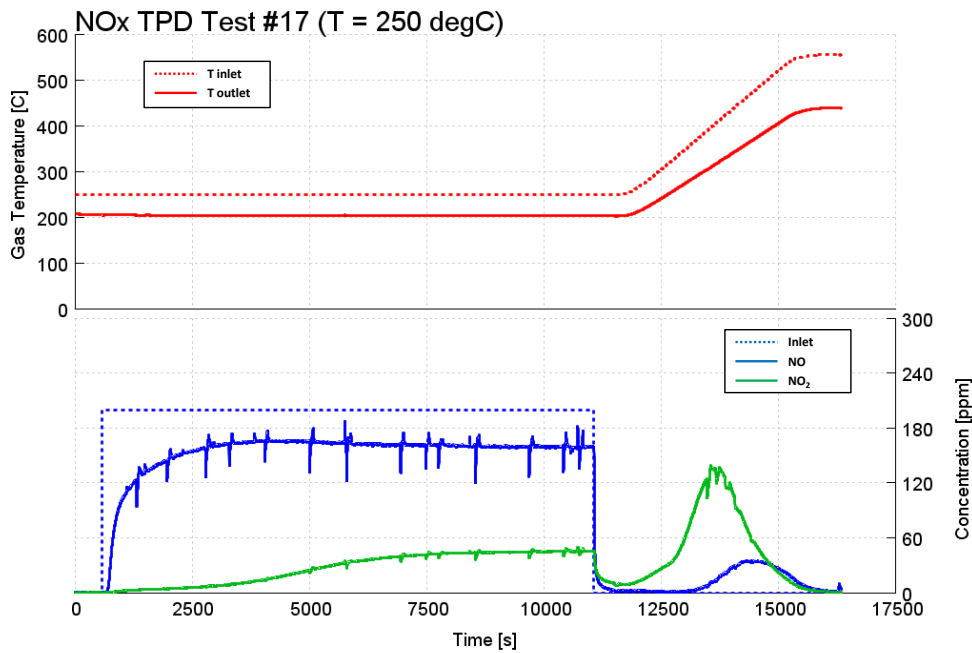
Figure 2.15: SGB results of the LNT TPD tests number 17. Gas temperature (red), NO (blue) and NO_2 (green) emissions. GHSV of 15000 h^{-1}.

31
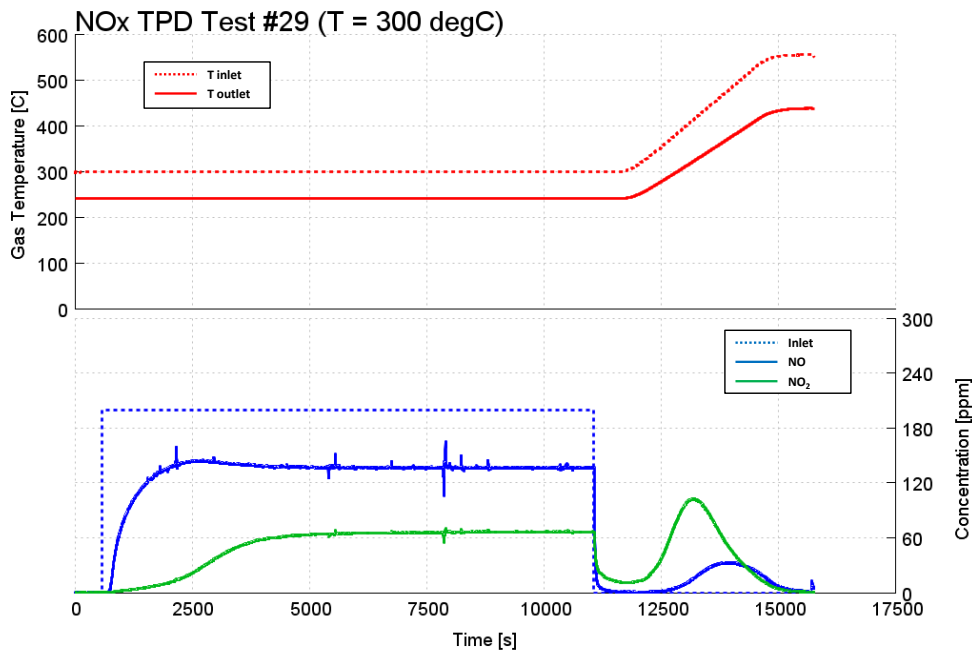
Figure 2.16: SGB results of the LNT TPD tests number 29. Gas temperature (red), NO (blue) and NO$_2$ (green) emissions. GHSV of 15000 h^{-1}.
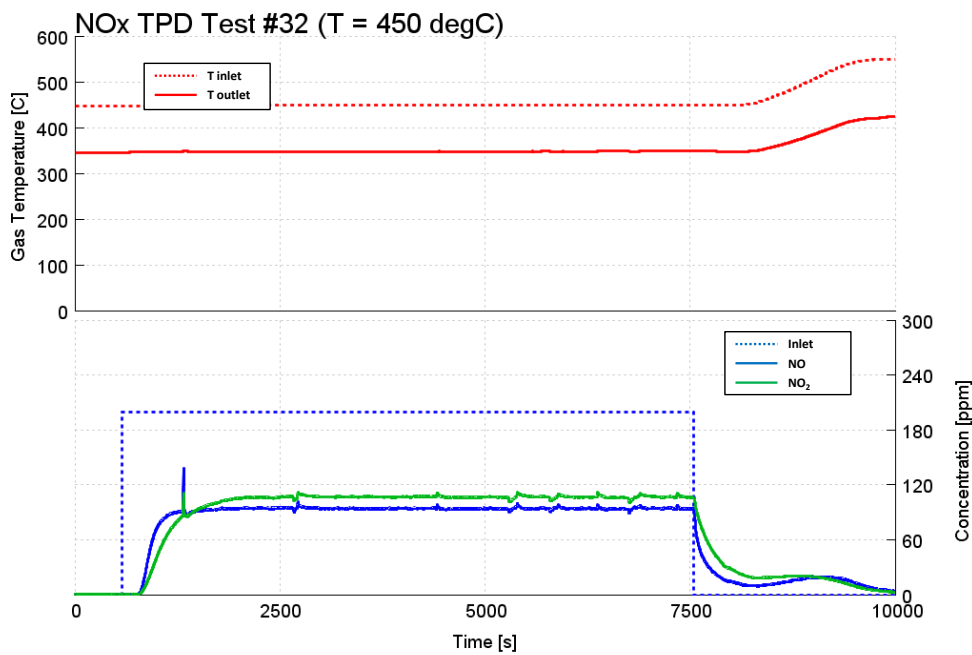
Figure 2.17: SGB results of the LNT TPD tests number 32. Gas temperature (red), NO (blue) and NO$_2$ (green) emissions. GHSV of 15000 h^{-1}.
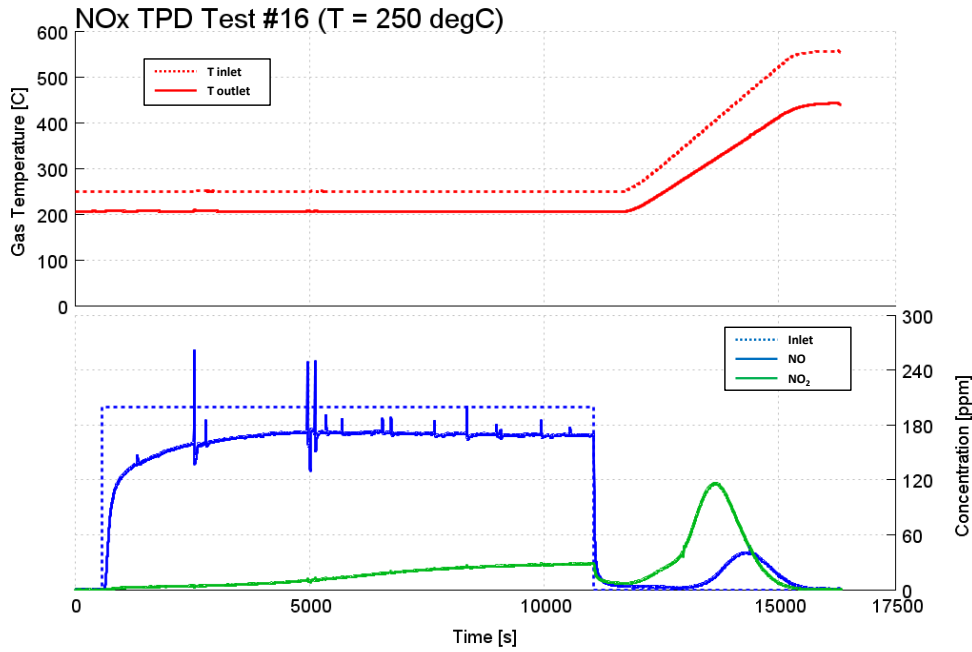
Figure 2.18: SGB results of the LNT TPD tests number 16. Gas temperature (red), NO (blue) and NO_2 (green) emissions. GHSV of 15000 h^{-1}.
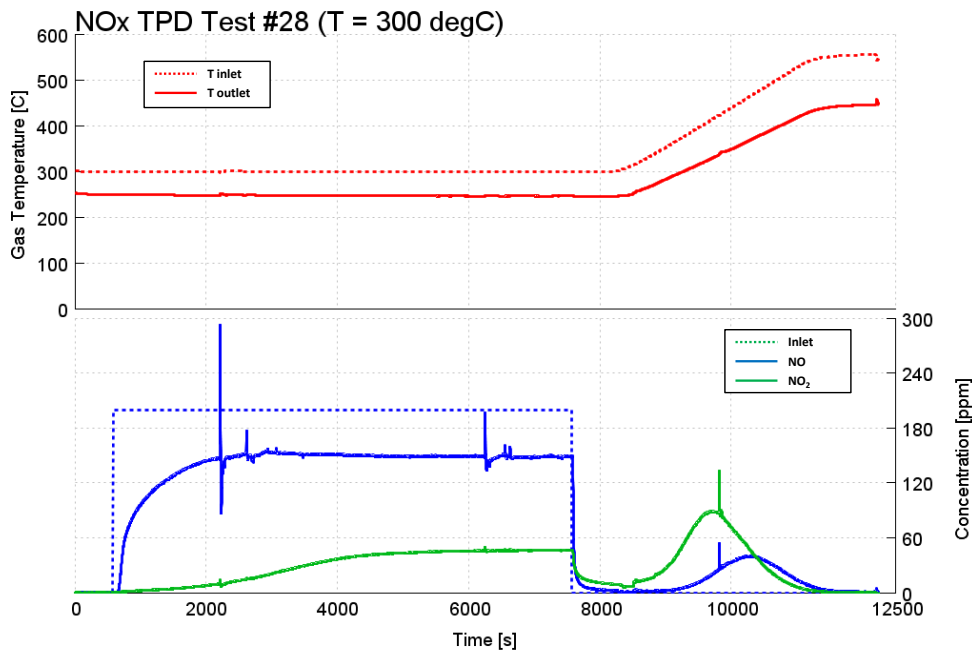
Figure 2.19: SGB results of the LNT TPD tests number 28. Gas temperature (red), NO (blue) and NO_2 (green) emissions. GHSV of 15000 h^{-1}.

2.2.5   Oxygen Storage Capacity (OSC)

The OSC experiments were performed to characterize the oxygen storage on ceria during lean air-to-fuel ratio operating condition and the oxygen release when a reducing agent is introduced in the system.

The reactor was exposed alternatively to lean and rich air-to-fuel conditions to induce oxygen storage and the subsequent purge of the ceria sites, using CO or propylene as reducing agents, at different inlet gas temperature levels and at a constant space velocity of 15000 h^{-1}. The inlet gas temperature was kept constant during each test and 5 different temperature levels were investigated, in the range from 150 degC to 400 degC. Oxygen was included in the inlet batch in a concentration of 12% during lean phases and switched off during rich pulses, while a background composition of 0.5% H$_2$O, 0.5% CO$_2$, and nitrogen was used in all the tests. The OSC test-matrix is summarized in Table 2.5.

In Figures 2.20, 2.21, 2.22, 2.23 and 2.24 are depicted the results of OSC tests number 2, 5, 8, 13 and 16 respectively, in which 10000 ppm of CO were fed to the reactor. At the beginning of each rich pulse a sudden drop in the lambda voltage was produced by the introduction of the reducing agent. However, a significant time delay was observed between the starting time of the rich phase and the CO breakthrough at the reactor outlet, due to oxidation reactions with the stored oxygen. As a result, a sudden increase in the measured gas temperature and a spike in CO$_2$ concentration were produced at the beginning of each rich phase. During the lean phase instead, at the beginning of the oxygen feeding a temperature increase was observed due to the heat released from the ceria due to the oxygen storage reactions, in conjunction with a short spike in the CO$_2$ and H$_2$O concentrations related probably to the temporary superposition of CO and O$_2$ gases, which induced oxidation reactions. As the temperature was increased, a larger delay in CO breakthrough was observed, indicating bigger OSC at higher temperatures. At higher temperatures, as shown for instance in 2.24 where test 16 is depicted (inlet gas temperature of 400 degC), the concentration of CO after breakthrough did not reach its nominal value due to the CO consumption by means of the Water Gas Shift (WGS) reaction. Such phenomenon was also indicated by CO$_2$ and H$_2$O traces in which an increase of the first and a decreased of the latter was observed, during the rich phase, compared to the inlet value.

The effect of oxygen on the WGS reaction was investigated in test number 9, depicted in 2.25, where a higher concentration of CO was fed during rich pulses along with a small percentage of oxygen. In this test the inlet gas temperature was kept to 250 degC, as in test 8, depicted in 2.22, during which almost 10% of the introduced CO reacted through WGS. In test 9 although the CO reached the

Table 2.5: Test matrix for the LNT OSC characterization

Background Composition			0.5% CO_2 0.5 % H_2O		
Space Velocity			15000 h^{-1}		
Hydrocarbons			C_3H_6		
		Lean		**Rich**	
Test	**Temp**	**O$_2$**	**O$_2$**	**CO**	**HC**
-	**degC**	**%**	**%**	**ppm**	**ppmC1**
2	150	12	0	10000	0
3	150	12	0	0	2500
5	200	12	0	10000	0
6	200	12	0	0	0
8	250	12	0	10000	0
9	250	12	1	25000	0
10	250	12	0	0	2500
13	300	12	0	10000	0
14	300	12	0	0	2500
16	400	12	0	10000	0

inlet value after the breakthrough indicating that WGS was inhibited by the leaner environment.

In tests 6, 10 and 14 a fast-oxidizing hydrocarbon, propylene (C_3H_6), was fed to the reactor during the rich phases, at different temperature levels, to purge the ceria sites occupied by the stored oxygen, as depicted in Figures 2.26, 2.27 and 2.28 respectively. Similarly to what observed with CO, the breakthrough of HC occurred after a slight delay, after the start of the rich pulse. The oxidation of propylene produced peaks in H_2O and CO_2 concentration at each lean-rich phase
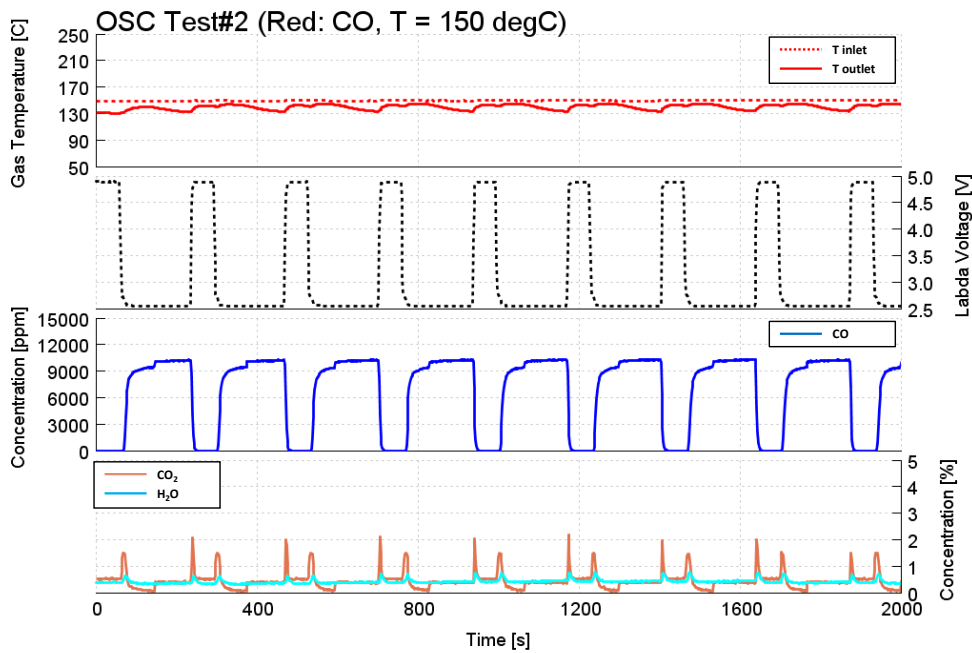
Figure 2.20: SGB results of the LNT OSC test number 2. Gas temperature (red), CO (blue), CO$_2$ (orange) and H$_2$O (light-blue) emissions. GHSV of 15000 h^{-1}.
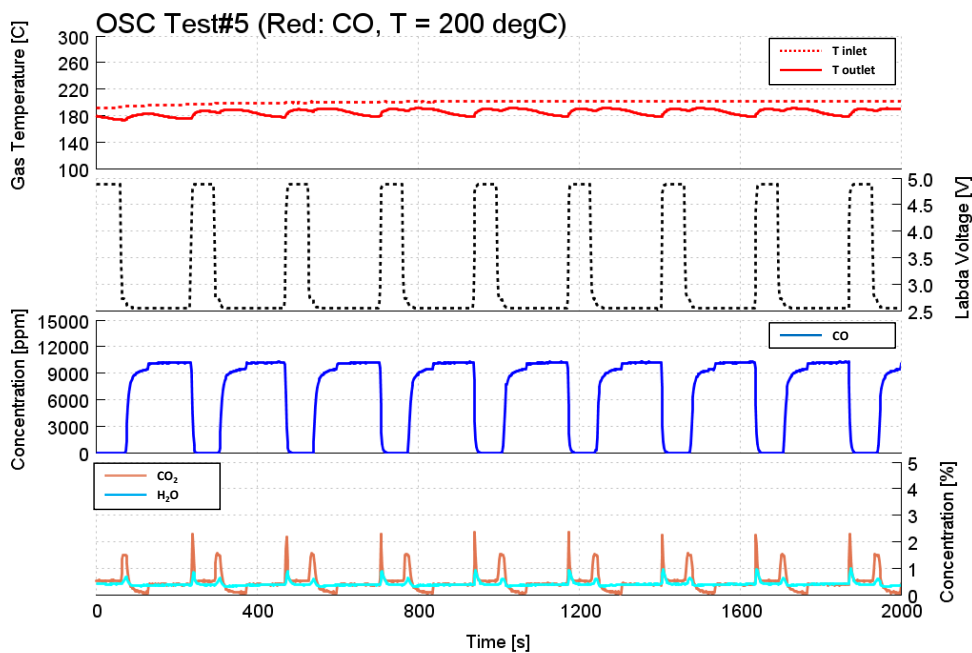
Figure 2.21: SGB results of the LNT OSC test number 5. Gas temperature (red), CO (blue), CO$_2$ (orange) and H$_2$O (light-blue) emissions. GHSV of 15000 h^{-1}.
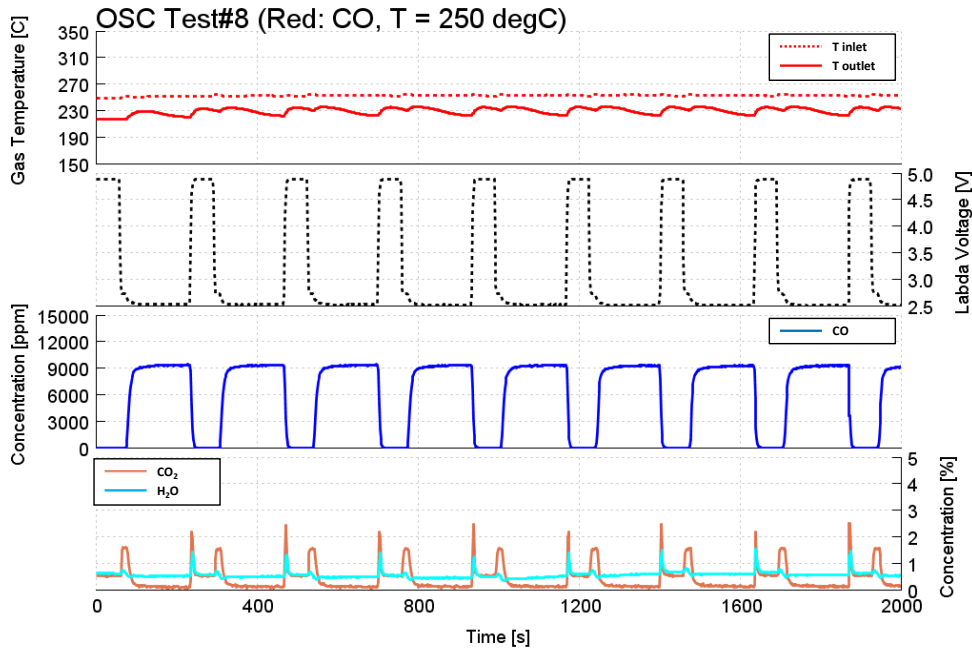
Figure 2.22: SGB results of the LNT OSC test number 8. Gas temperature (red), CO (blue), CO_2 (orange) and H_2O (light-blue) emissions. GHSV of 15000 h^{-1}.
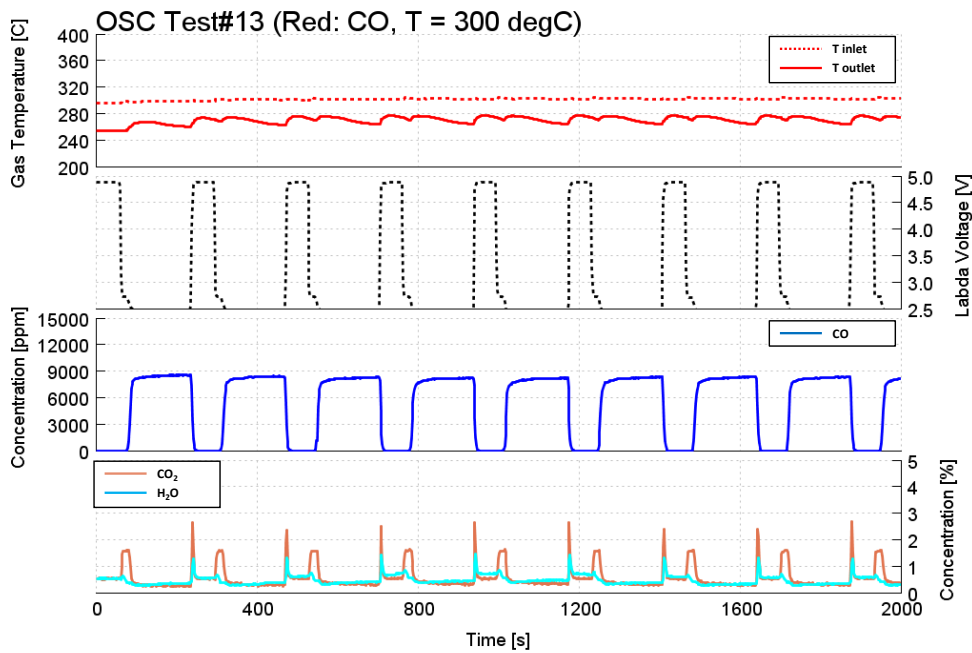
Figure 2.23: SGB results of the LNT OSC test number 13. Gas temperature (red), CO (blue), CO_2 (orange) and H_2O (light-blue) emissions. GHSV of 15000 h^{-1}.

37
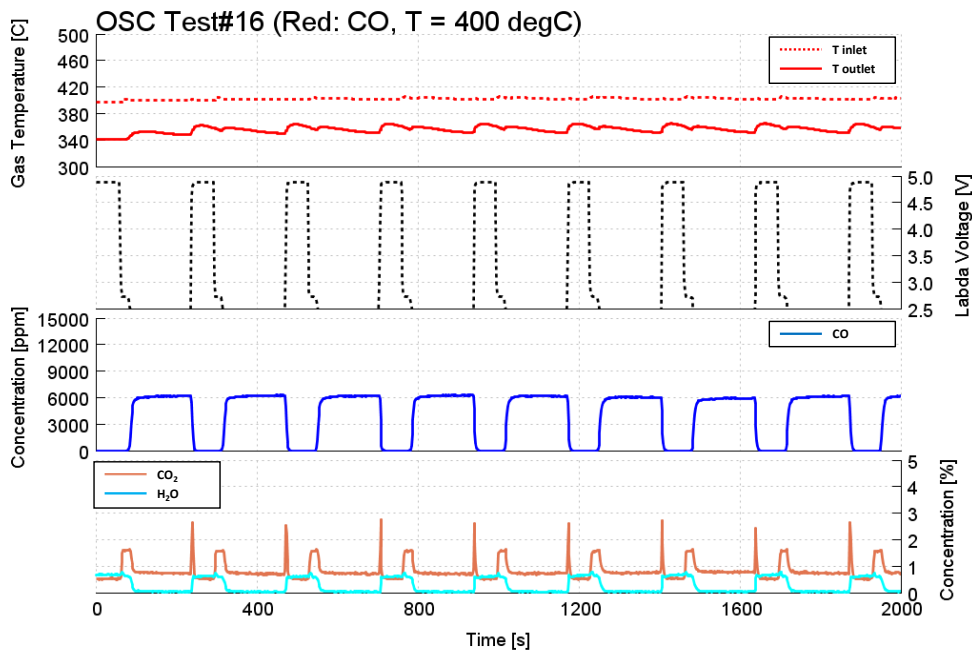
Figure 2.24: SGB results of the LNT OSC test number 16. Gas temperature (red), CO (blue), CO$_2$ (orange) and H$_2$O (light-blue) emissions. GHSV of 15000 h^{-1}.
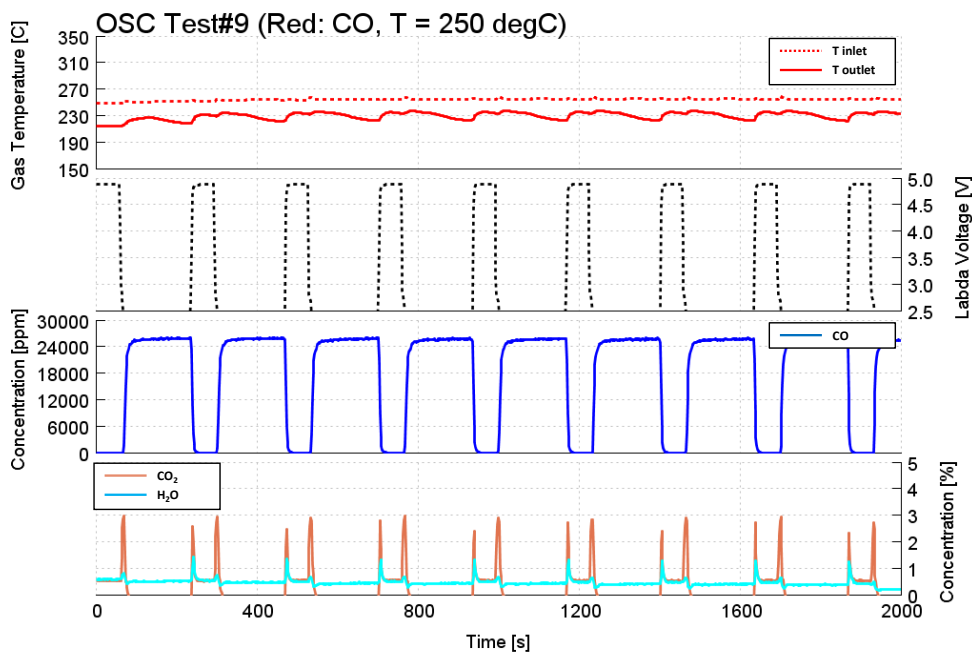
Figure 2.25: SGB results of the LNT OSC test number 9. Gas temperature (red), CO (blue), CO$_2$ (orange) and H$_2$O (light-blue) emissions. GHSV of 15000 h^{-1}.

switch as well as in the measured gas temperature. During each test, the HC outlet concentration matched the inlet one after the breakthrough, indicating that the Steam Reforming (SR) reaction was still inactive.
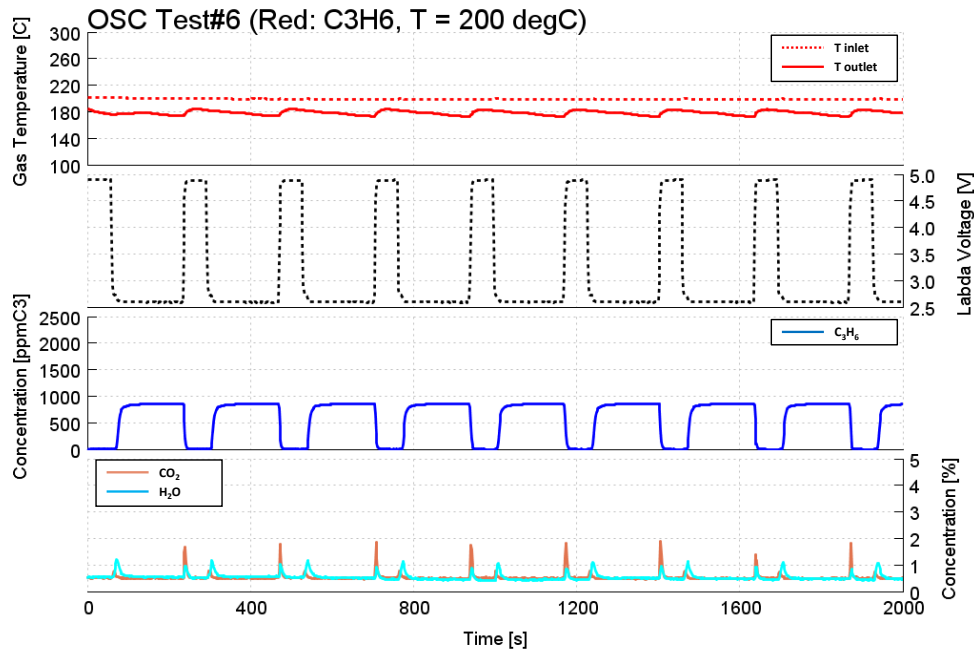
Figure 2.26: SGB results of the LNT OSC test number 6. Gas temperature (red), C_3H_6 (blue), CO_2 (orange) and H_2O (light-blue) emissions. GHSV of 15000 h^{-1}.
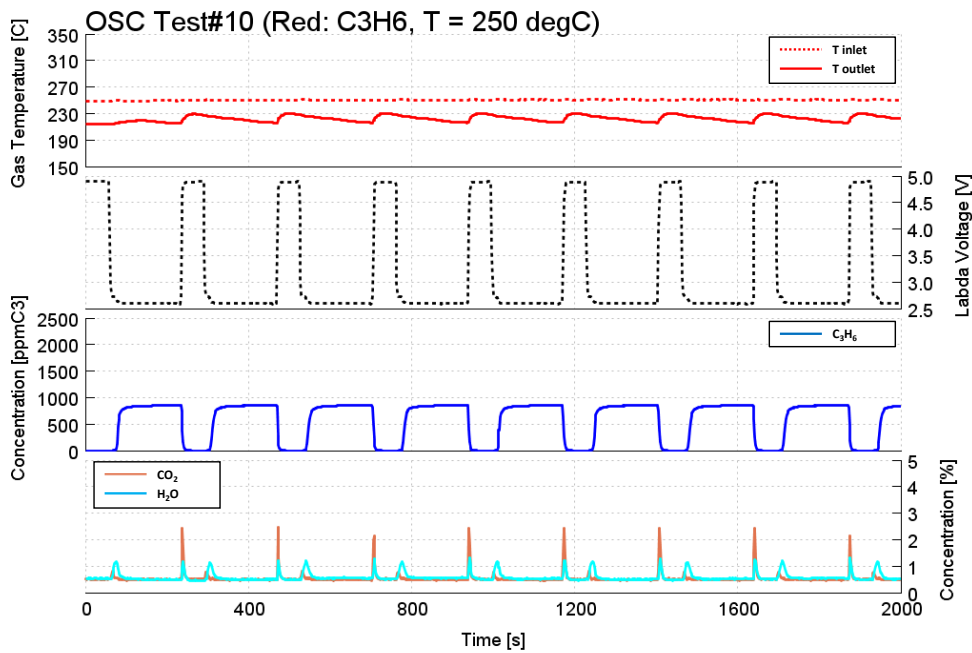
Figure 2.27: SGB results of the LNT OSC test number 10. Gas temperature (red), C$_3$H$_6$ (blue), CO$_2$ (orange) and H$_2$O (light-blue) emissions. GHSV of 15000 h^{-1}.
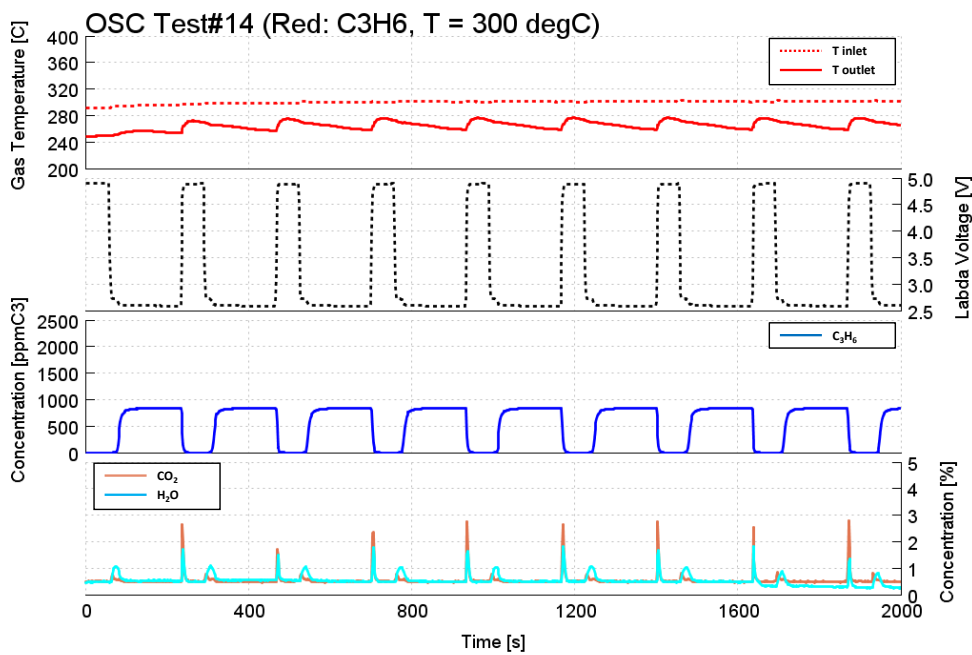
Figure 2.28: SGB results of the LNT OSC test number 14. Gas temperature (red), C$_3$H$_6$ (blue), CO$_2$ (orange) and H$_2$O (light-blue) emissions. GHSV of 15000 h^{-1}.

2.2.6 NO_x Storage and Reduction (NSR)

NO_x Storage and Reduction (NSR) tests were carried out to characterize the LNT operation under alternating lean and rich conditions. Each test was performed at a space velocity of 15000 h^{-1}, after a preliminary reduction phase during which H_2 was fed to the reactor. After that, the reactor was exposed repeatedly to a lean phase, during which NO_x were fed to the reactor to allow storage, and a rich phase, during which a reducing agent was fed to reduce the adsorbed NO_x and clear the storage sites, respectively. The duration of the rich phase was set to allow the complete regeneration of the catalyst NO_x storage capacity. The test protocol included feeding of NO, during lean phases, as representative of the entire engine-out NO_x composition. Three different inlet gas temperatures were investigated, 200 degC, 250 degC and 350 degC respectively, and three different reducing agent were used during the NO_x reduction phases, namely H_2, CO and propylene. Unfortunately, the concentration of H_2 at the reactor outlet was not available. The produced NSR test matrix is reported in Table 2.6.

In tests 1, 9 and 20 hydrogen was used as reducing agent, at three different temperature levels, 200 degC, 250 degC and 350 degC respectively. Test results are depicted in Figures 2.29, 2.30 and 2.31 respectively. The transition between rich and lean phases was controlled by means of a valve, whose position is reported in each figure and whose value indicates lean conditions if equal to 1, rich otherwise. Since the measurement of H_2 was not available, the concentration of CO is reported instead in each figure, to monitor the WGS reaction. The limited duration of the lean phases, where NO_x were fed to the reactor, leaded to an almost null slip of NO_x at the reactor outlet. At the beginning of the rich phases instead, due to the reduction reactions on Barium sites, NO_x spikes were observed both in form of NO and NO_2. Simultaneously, N_2O was released at the reactor outlet, especially at temperature below 300 degC, as depicted in Figures 2.29 and 2.30, while this phenomena was not observed at 350 degC (Figure 2.31). After the N_2O release, a lower amount of ammonia was also observed at the reactor outlet in the tests below 300 degC. An appreciable amount of WGS was observed only at 350 degC, as depicted in Figure 2.31, where a concentration of approximately 100 ppm of CO was produced during the rich pulses.

CO was the reducing agent used in tests 3, 11 and 22, depicted in Figures 2.32, 2.33 and 2.34 respectively. During rich phases, the CO concentration measured at the reactor outlet was lower than the inlet one in each tests, due to the WGS reaction, whose effect increased with temperature. In test number 22 for instance, depicted in Figure 2.34, the consumption of H_2O and the production of CO_2 through WGS could be observed looking at the related measured outlet traces. Large peaks of NO_x, mostly in the form of NO, and N_2O were observed at the beginning of each

Table 2.6: Test matrix for the LNT NSR characterization

Background Composition			5% CO$_2$, 5% H$_2$O			
Space Velocity			15000 h^{-1}			
Hydrocarbons			C$_3$H$_6$			

		Lean		Rich			
Test	**Temp**	**O$_2$**	**NO**	**O$_2$**	**H$_2$**	**CO**	**HC**
-	**degC**	**%**	**ppm**	**%**	**ppm**	**ppm**	**ppmC1**
1	200	12	200	0	2500	0	0
2	200	12	200	0	0	10000	0
3	200	12	200	0	0	0	2500
9	250	12	200	0	2500	0	0
10	250	12	200	0	0	10000	0
11	250	12	200	0	0	0	2500
20	350	12	200	0	2500	0	0
21	350	12	200	0	0	10000	0
22	350	12	200	0	0	0	2500

lean phase, due to the reduction reactions on Barium sites through CO. A small amount of released ammonia was detected during the rich phase, after the N$_2$O peak, especially at low temperature (e.g. Figure 2.32).

(a)
(b)
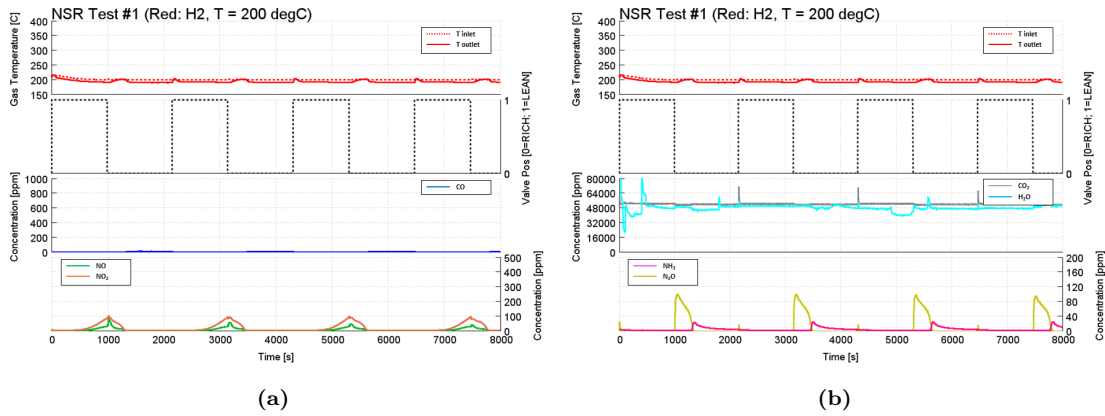
Figure 2.29: SGB results of the LNT NSR test number 1. Gas temperature (red), CO (blue), NO (green), NO_2 (orange), CO_2 (grey), H_2O (light-blue), N_2O (yellow) and NH_3 (purple) emissions. GHSV of 15000 h^{-1}.

(a)
(b)
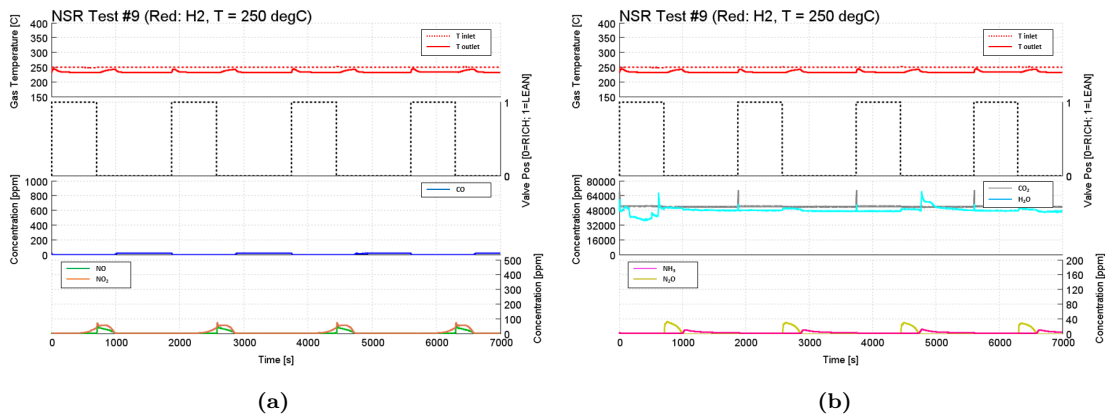
Figure 2.30: SGB results of the LNT NSR test number 9. Gas temperature (red), CO (blue), NO (green), NO_2 (orange), CO_2 (grey), H_2O (light-blue), N_2O (yellow) and NH_3 (purple) emissions. GHSV of 15000 h^{-1}.
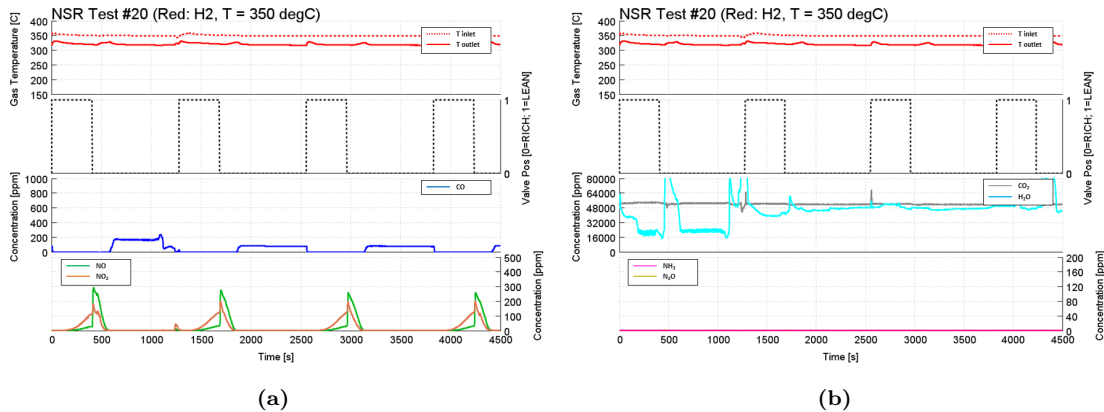
Figure 2.31: SGB results of the LNT NSR test number 20. Gas temperature (red), CO (blue), NO (green), NO$_2$ (orange), CO$_2$ (grey), H$_2$O (light-blue), N$_2$O (yellow) and NH$_3$ (purple) emissions. GHSV of 15000 h^{-1}.
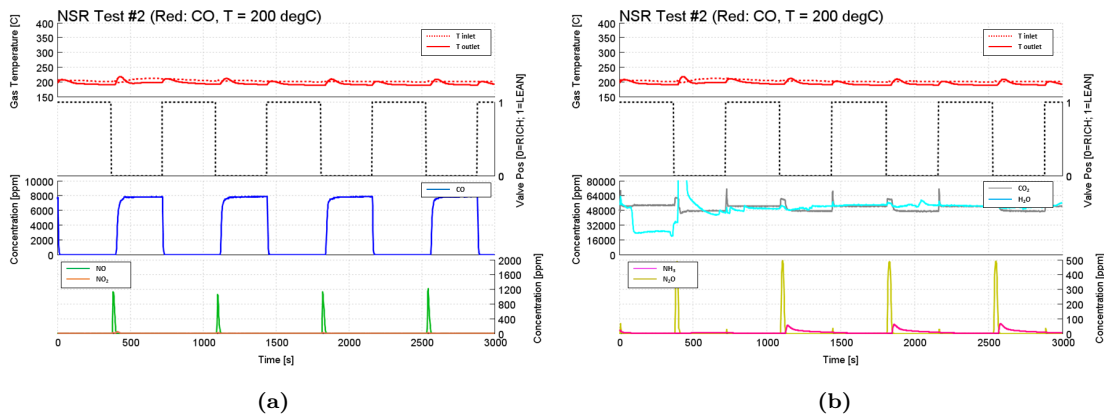
Figure 2.32: SGB results of the LNT NSR test number 2. Gas temperature (red), CO (blue), NO (green), NO$_2$ (orange), CO$_2$ (grey), H$_2$O (light-blue), N$_2$O (yellow) and NH$_3$ (purple) emissions. GHSV of 15000 h^{-1}.

(a)   (b)
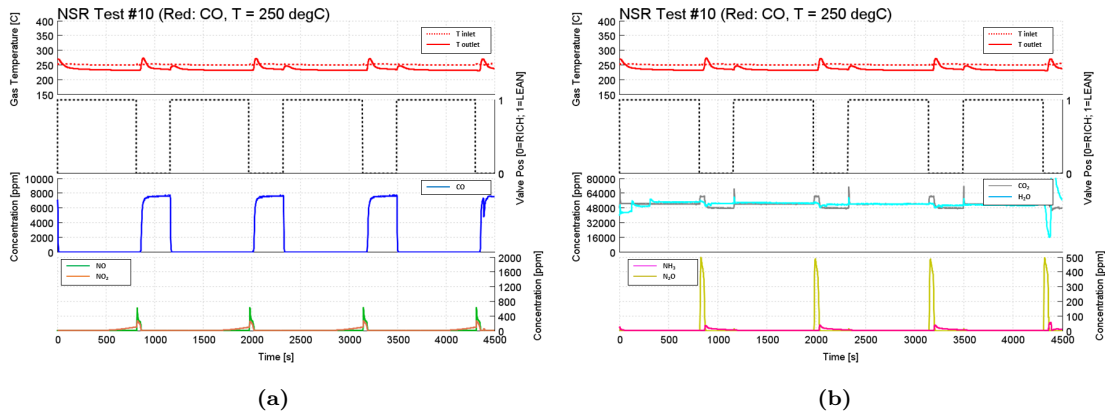
Figure 2.33: SGB results of the LNT NSR test number 10. Gas temperature (red), CO (blue), NO (green), NO_2 (orange), CO_2 (grey), H_2O (light-blue), N_2O (yellow) and NH_3 (purple) emissions. GHSV of 15000 h^{-1}.

(a)   (b)
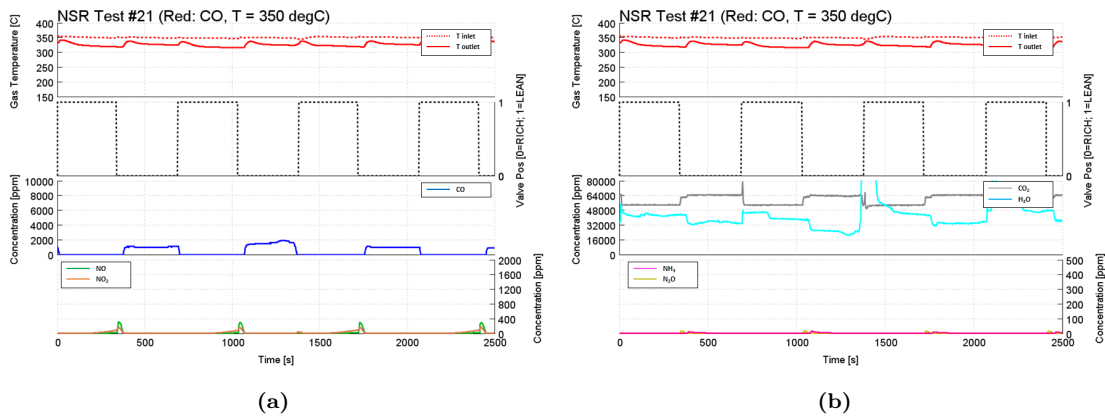
Figure 2.34: SGB results of the LNT NSR test number 21. Gas temperature (red), CO (blue), NO (green), NO_2 (orange), CO_2 (grey), H_2O (light-blue), N_2O (yellow) and NH_3 (purple) emissions. GHSV of 15000 h^{-1}.

Propylene was used as the reducing agent in tests 3, 11 and 22, depicted in 2.35, 2.36 and 2.37. Similarly to the other tests, NO and a lower amount of NO$_2$ were released as the feed of reducing agent started. Two different peaks in the N$_2$O concentration were observed at the beginning and at the end of each rich pulse, which could be related to the oxidation of propylene with NO. The production of ammonia was practically null during each test. At 350 degC, as depicted in Figure 2.37, the outlet concentration of propylene was lower than the inlet one, due to the activation of the steam reforming reaction.
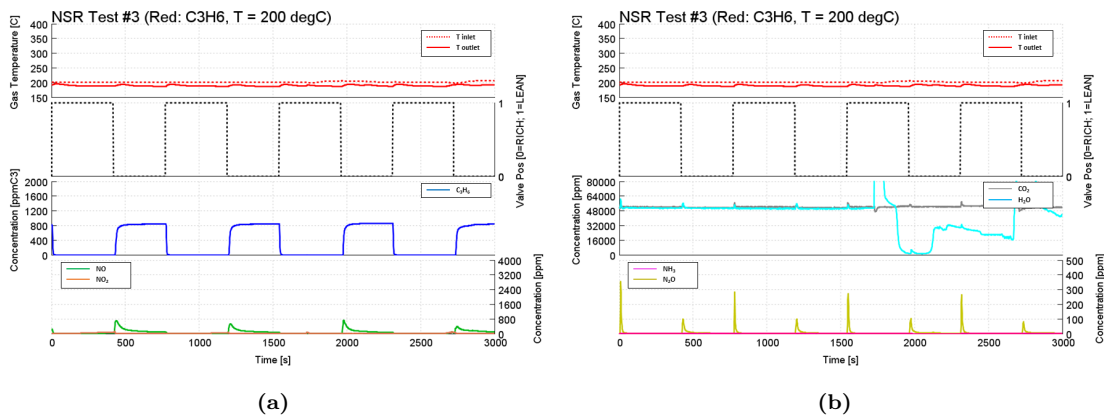
Figure 2.35: SGB results of the LNT NSR test number 3. Gas temperature (red), C$_3$H$_6$ (blue), NO (green), NO$_2$ (orange), CO$_2$ (grey), H$_2$O (light-blue), N$_2$O (yellow) and NH$_3$ (purple) emissions. GHSV of 15000 h^{-1}.
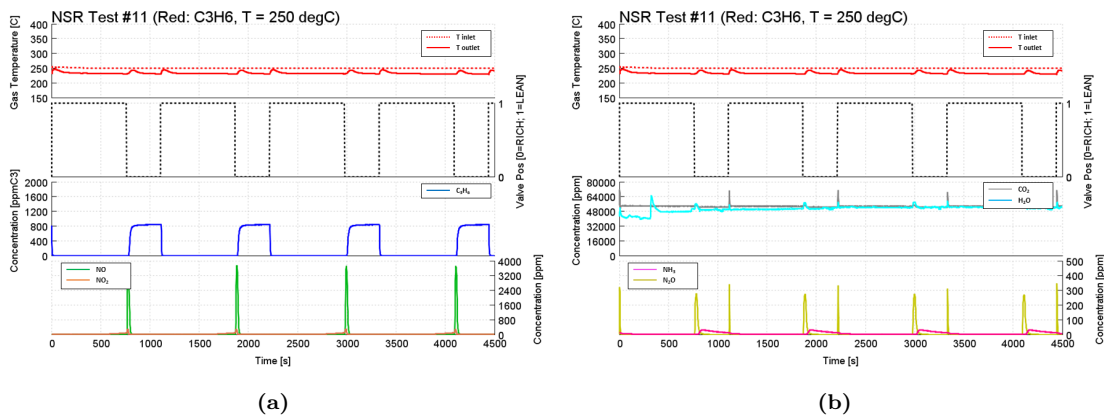
Figure 2.36: SGB results of the LNT NSR test number 11. Gas temperature (red), C$_3$H$_6$ (blue), NO (green), NO$_2$ (orange), CO$_2$ (grey), H$_2$O (light-blue), N$_2$O (yellow) and NH$_3$ (purple) emissions. GHSV of 15000 h^{-1}.

(a)

(b)
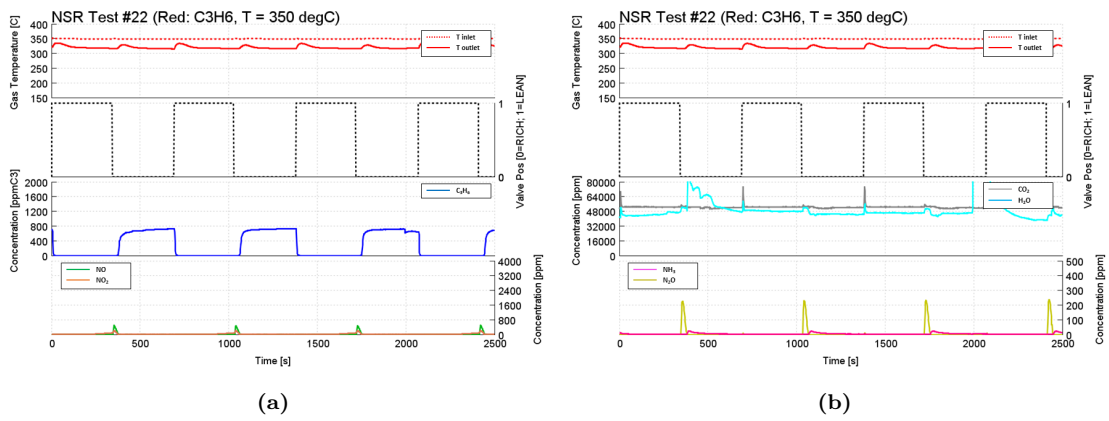
Figure 2.37: SGB results of the LNT NSR test number 22. Gas temperature (red), C_3H_6 (blue), NO (green), NO_2 (orange), CO_2 (grey), H_2O (light-blue), N_2O (yellow) and NH_3 (purple) emissions. GHSV of 15000 h^{-1}.

2.3 Simulation Model

In this work, a 1D-CFD simulation model of the tested LNT catalyst was built in GT-SUITE. LNT operations were described by means of a global kinetic scheme, which was defined and calibrated based on the SGB experimental data by means of a sequential approach to reduce the number of unknowns and to correctly calibrate the model sensitivity to the different reaction pathways. To this aim, a simulation model of the reactor-scale sample was built and the SGB experiments were recreated in the virtual environment to perform the model calibration. Furthermore, the calibrated model was re-scaled to the full-size component and validated over driving cycle data, inheriting the chemical kinetics parameters from the lab-scale model without relevant modifications. The validation was performed using the exhaust gas conditions obtained from different driving cycles, such as the WLTC and the RDE test procedures, which included controlled and uncontrolled catalyst regeneration events, thus considering the performance of the after-treatment under real driving conditions.

2.3.1 Modeling Methodology

The 1D mathematical model used to describe the physical and chemical processes of the LNT under investigation was built in GT-SUITE under the following assumptions:

- gas flow in the channels is considered laminar due to the Reynolds number typical of these applications (Re < 1000)

- diffusion and conduction in the bulk phase are negligible in the flow direction, due to the high space velocity typical of these applications

- the channel cross section is considered uniform along the whole length

- only surface reactions are considered (i.e. in the washcoat) while gas-phase reactions are neglected

- global reactions are used to represent the catalyst chemical kinetics

- the inlet radial gas flow distribution is considered uniform, channel to channel variations are thus neglected

- temperature gradients in the solid phase are considered only along the channel axial direction

- radial gradients between fluid and solid are accounted for using heat and mass transfer coefficients

As a result, a 1D LNT model with a single-channel representative of the whole reactor behavior was developed.

The LNT kinetic scheme was built by means of global-type surface reactions and reaction rates were expressed according to the Turnover Number format. Particularly, volume reaction rates were expressed by means of Arrhenius terms and calculated as reported in Equation 2.1:

$$R_i = A_i * e^{\frac{-E_i}{R*T}} * C_j * G(i) * \theta(i) * C_s \qquad (2.1)$$

In which R_i indicates the total volume rate of reaction i, A_i is the pre-exponential factor and E_i the reaction activation Energy of the Arrhenius term, R is the universal gas constant, T is the surface temperature, C_j is the concentration-dependent term for species j, $G(i)$ accounts for general functions such as the Langmuir–Hinshelwood inhibition terms, $\theta(i)$ is the site coverage (used in case of reactions involving storage sites) and C_s indicates the associated site density.

The site density, required when reactions are formulated as turnover number rates, indicates the ratio between the moles of active sites and the catalyst volume. This formulation allows to scale the chemical kinetics as a function of the number of active sites in the washcoat, therefore could be applied without relevant modifications on catalysts with different loading of active sites. To evaluate the PGM active site density, the nominal PGM loading was used as starting value and multiplied by a "dispersion factor", which takes into account the deviation between the ideal case (all the sites are active) and the real case (only some of the sites are active). This value was used as a calibration parameter to adjust the PGM site density in order to represent the behavior of the component under investigation. The site density of the LNT storage sites, namely Barium for NO_x storage and Ceria for Oxygen storage, physically represents the maximum storage capacity and therefore was calculated based on the SGB storage experiments.

The calibration of the model was carried out using the NSGA-III Genetic Algorithm (GA) embedded in GT-SUITE [17]. As most evolutionary algorithms, a series of optimization step are carried out in order to minimize a target objective function. During the first optimization steps, the GA randomly generates a user-defined number of individuals, each one of which consist of a different combination of the independent variables, to form what is called a population. Then simulations are carried out to evaluate the fitting function of each individual based on

49

the target function. At the end of this step, the best fitting individuals are then selected and used to evolve the population using evolutionary operators, such as crossover, selection and mutation, creating a new one. Each population of individuals is defined as a generation. The algorithm progresses as the desired number of iteration is explored and, as a result, returns the evolved individual that minimizes the target function. Site densities, pre-exponent multipliers and activation energies were used as independent variables to calibrate each reaction rate and its inhibition functions.

2.3.2   Reactor Scale Model

To calibrate the LNT model, the experimental testing protocol was reproduced in GT-SUITE. In order to reduce the number of independent variables in each calibration step and to individually characterize the reactions involved, a sequential calibration approach was carried-out. The SGB tests were used for the model calibration in the following order:

1. Catalyst Light-Off

2. NO$_x$ Storage TPD

3. Oxygen Storage Capacity

4. NO$_x$ Storage and Reduction

In the following sections, results of the lab-scale model calibration will be presented.

2.3.3 Light-Off Model

The reaction kinetics used to describe light-off tests is reported in Table 2.7, which includes the oxidation reactions, occurring on PGM sites, of CO, fast- and slow-oxidizing HCs (namely propylene and dodecane, respectively), H_2 and NO. A Voltz-type inhibition function [18], reported in Table 5, was used to account for mutual competition of CO, C_3H_6 and NO on PGM sites. The oxidation reaction of NO on PGM, which is limited by chemical equilibrium at high temperature, was modelled as reported in Table 1, using an temperature-dependent inhibition function to reproduce the chemical equilibrium curve. The inlet conditions defined during the experimental test protocol, described in Table 2.3, were used as the input for the simulation, including different space velocities, different concentration of the reducing agents and the presence of NO_x with different NO_2/NO_x ratios.

Table 2.7: LNT Model Light-Off Kinetic Scheme

Number	Site Element	Reaction
1	PGM	$CO + 0.5\,O_2 \longrightarrow CO_2$
2	PGM	$C_3H_6 + 4.5\,O_2 \longrightarrow 3\,CO_2 + 3\,H_2O$
3	PGM	$C_{12}H_{26} + 18.5\,O_2 \longrightarrow 12\,CO_2 + 13\,H_2O$
4	PGM	$H_2 + 0.5\,O_2 \longrightarrow H_2O$
5	PGM	$H_2O + CO \longrightarrow CO_2 + H_2$
6	PGM	$C_3H_6 + 3\,H_2O \longrightarrow 3\,CO + 6\,H_2$
7	PGM	$NO + 0.5\,O_2 \longrightarrow NO_2$

To reduce the number of independent variables in each optimization step, the following calibration protocol was used:

1. The catalyst sample heat transfer coefficient was calibrated in order to match the measured outlet gas temperature, at each space velocity.

2. Pre-exponent and exponential Arrhenius factors were calibrated for each oxidation reaction and for the species mutual inhibition function on PGM. In this step, the experimental tests where NO_x was not present in the inlet batch were considered.

3. The oxidation reaction inhibition due to NO was calibrated using tests 6 and 8, in which a fixed concentration of NO was included in the inlet batch.

In Figure 2.38 simulation results of tests 1, 2 and 3 are depicted, in which different concentrations of CO, Propylene and Dodecane were included in the inlet batch. The model was able to accurately reproduce the oxidation of all the species on PGM sites as well as the gas temperature measured at the reactor outlet.
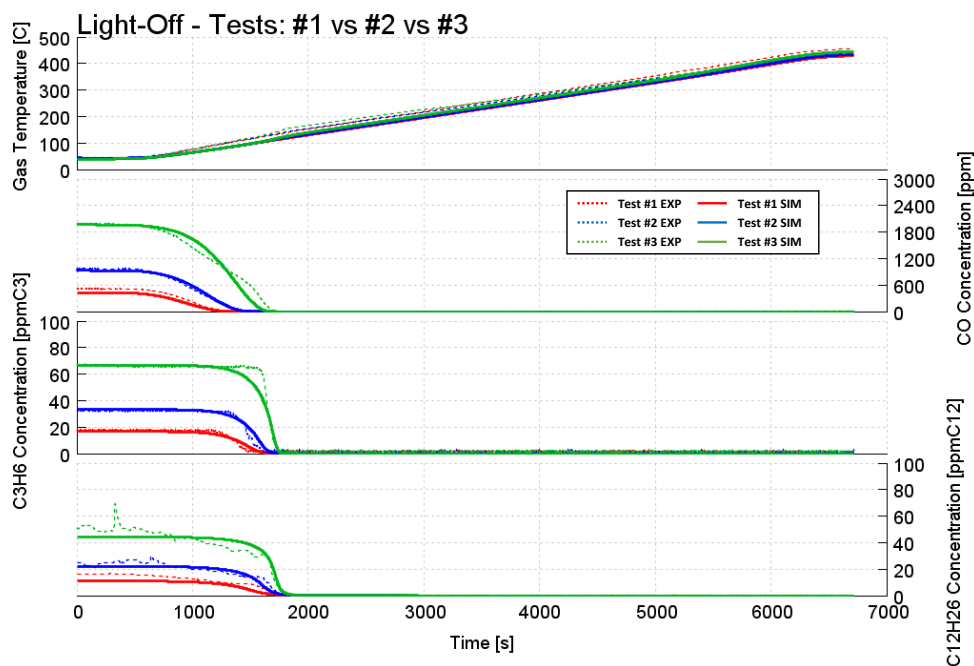
Figure 2.38: Simulation results (solid line) versus experiments (dashed line) on the LO tests number 1 (red), 2 (blue) and 3 (green). GHSV of 15000 h^{-1}.

Figures 2.39, 2.40 and 2.41 reports simulation results of LO tests number 2, 3 and 4 respectively performed at different GHSV, namely 15000 h^{-1} and 40000 h^{-1}. In the simulation, a delayed LO of the oxidation reactions was observed in all the tests after increasing the GHSV, in agreement with the experiments. This phenomenon was more clear in the tests with a larger concentration of reducing agents in the inlet batch, as shown in Figures 2.40 and 2.41.
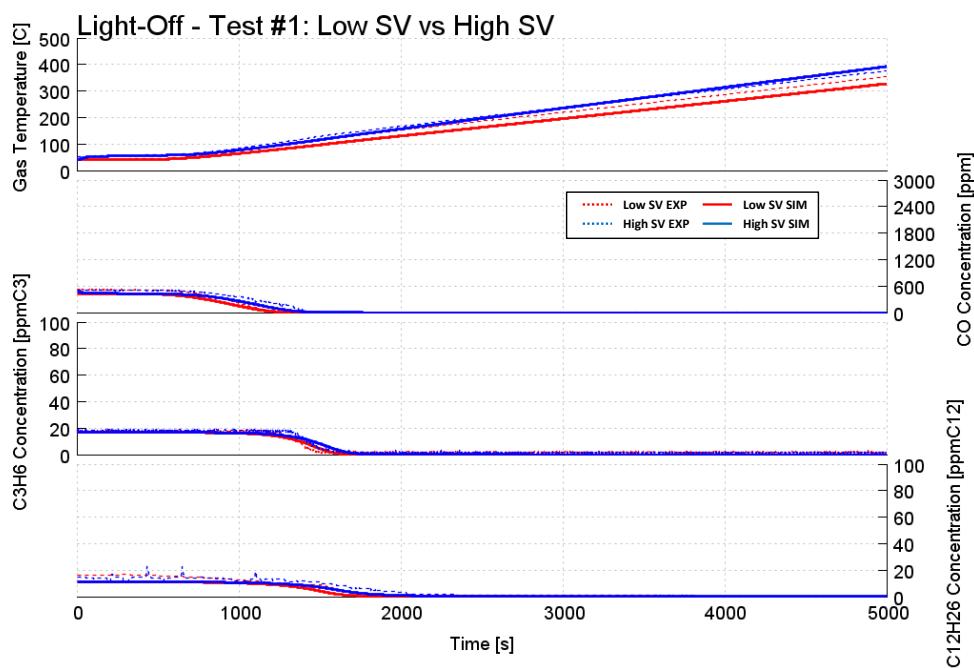
Figure 2.39: Simulation results (solid line) versus experiments (dashed line) on the LNT light-off test number 1, GHSV of 15000 h^{-1} (red) and 40000 h^{-1} (blue).
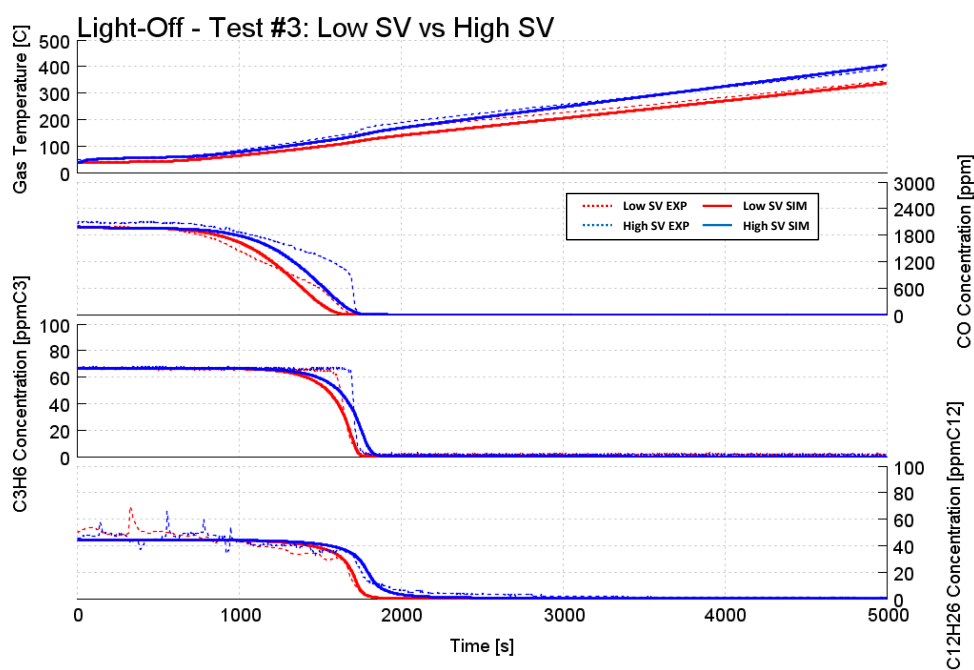
Figure 2.40: Simulation results (solid line) versus experiments (dashed line) on the LNT light-off test number 3, GHSV of 15000 h^{-1} (red) and 40000 h^{-1} (blue).
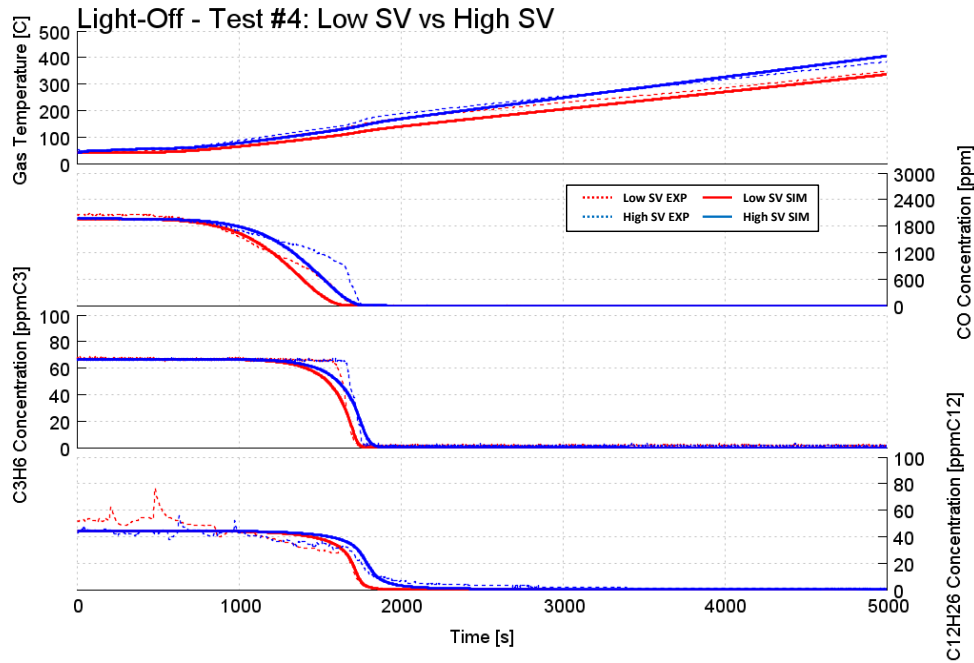
Figure 2.41: Simulation results (solid line) versus experiments (dashed line) on the LNT light-off test number 4, GHSV of 15000 h^{-1} (red) and 40000 h^{-1} (blue).

As mentioned at the beginning of this section, the NO$_x$ inhibition effect on oxidation reactions was simulated introducing a dedicated inhibition function in the kinetic scheme. The inhibition rate was calibrated tuning the corresponding pre-exponent and exponential Arrhenius factors over the experimental tests number 6 and 8. These tests were performed with the same inlet conditions of tests 1 and 2 respectively, plus a fixed concentration of NO. In Figure 2.42 simulation results of tests 1 and 6 are compared, while simulation results of tests 2 and 8 are compared in Figure 2.43. After the calibration, the inhibition effect of NO was captured and a delayed LO of the oxidation reactions was simulated, as observed in the experiments.
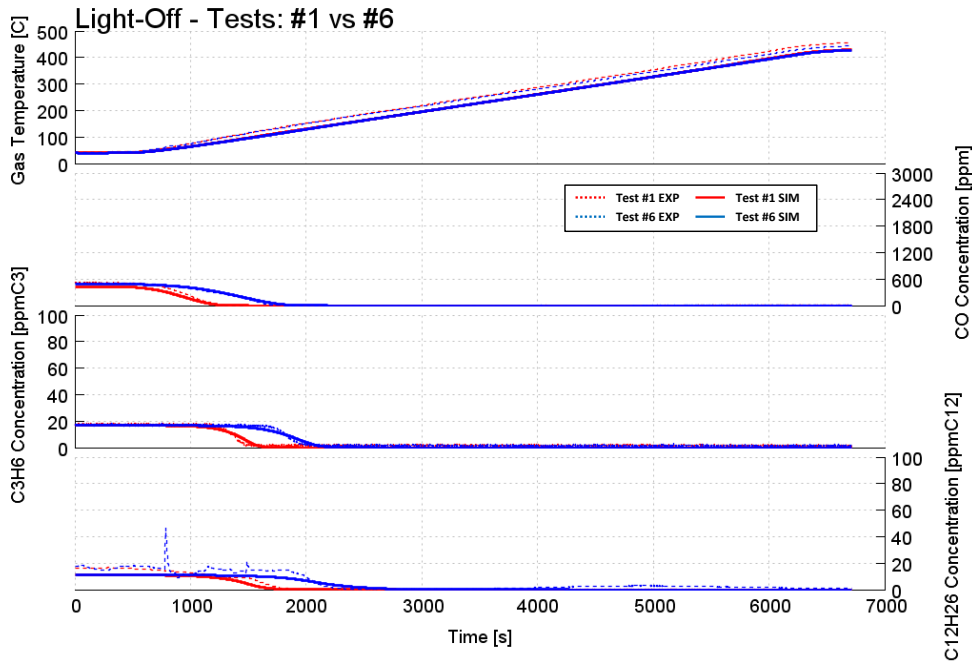
Figure 2.42: Simulation results (solid line) versus experiments (dashed line) on the LO tests number 1 (red) and 6 (blue). GHSV of 15000 h^{-1}.
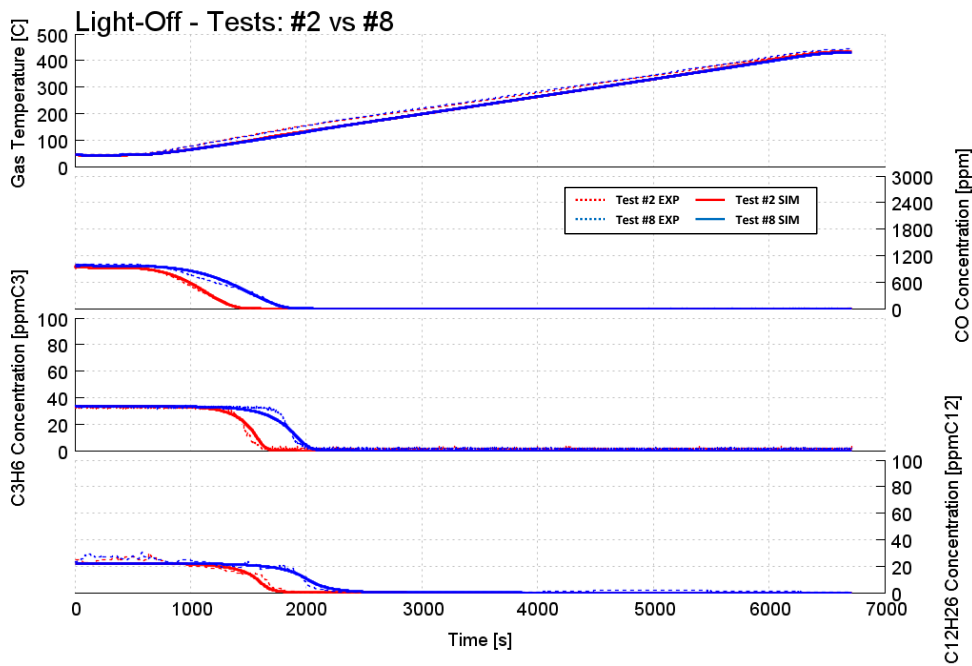
Figure 2.43: Simulation results (solid line) versus experiments (dashed line) on the LO tests number 2 (red) and 8 (blue). GHSV of 15000 h^{-1}.
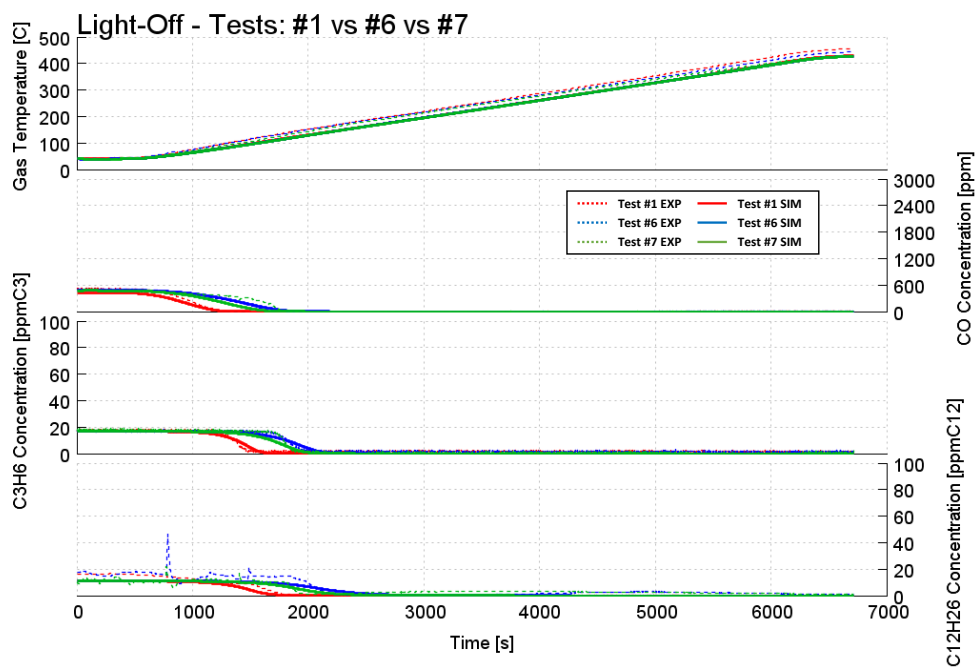
Figure 2.44: Simulation results (solid line) versus experiments (dashed line) on the LO tests number 1 (red), 6 (blue) and 7 (green). GHSV of 15000 h^{-1}.

2.3.4   NO$_x$ Storage and Release Model

To simulate the LNT NO$_x$ storage and release the reactions listed in Table 2.8 were used, while reaction rates were expressed as a function of temperature and concentration, as reported in Table 2 in the Appendix 4. As observed in the SGB NO$_x$ TPD tests described in Chapter 2.2.4, more than one Barium site is responsible for NO$_x$ storage and desorption, which is activated depending on the temperature. In this work, 3 different storage sites were used to account for:

- NO and NO$_2$ storage and low-temperature release

- NO and NO$_2$ storage and high-temperature release

- NO$_2$ only storage and release

Reaction parameters were calibrated using the measurement of the NO$_x$ TPD experiments, whose test-matrix is reported in Table 2.4. TPD experiments were carried out at a space velocity of 15000 h^{-1}, considering different temperatures for the NO$_x$ loading phase and different NO$_2$/NO$_x$ ratios. Adsorption reactions were considered independent from the temperature, therefore activation temperature was not considered. Low temperature NO$_2$ adsorption was inhibited for the site BaIII by means of an inhibition function (reported in the Appendix 4, Table 5). Activation temperature was calibrated instead to simulate NO$_x$ desorption at different temperatures for the different sites. In particular, low temperature desorption was inhibited for the site BaII by means of an inhibition function, reported in 5.

Since the simultaneous calibration of NO$_x$ storage and desorption reaction on three different Barium sites could be critical, even with advanced optimization tools such as the GA, and to prevent error sources from overlapping, a sequential calibration methodology was defined as follows:

1. First, NO oxidation was calibrated over the experimental trace after the breakthrough occurred and a steady-state behavior was reached. In this step, only the tests without NO$_2$ in the inlet batch were used.

2. NO$_x$ storage, low- and high-temperature release reaction parameters were calibrated considering the tests with only NO in the inlet batch and where the formation of NO$_2$ due to NO oxidation was limited, such as test 7, to avoid the interference of the NO$_2$ storage site.

3. Inhibition functions parameters were calibrated considering tests at different temperatures to achieve the required amount of storage.

Table 2.8: LNT Model NO$_x$ Storage Kinetic Scheme

Number	Site Element	Reaction
8	Barium-I	$BaIO + 3\,NO_2 \longrightarrow BaI(NO_3)_2 + NO$
9	Barium-I	$BaIO + 2\,NO + 1.5\,O_2 \longrightarrow BaI(NO_3)_2$
10	Barium-I	$BaI(NO_3)_2 \longrightarrow BaIO + 2\,NO_2 + 0.5\,O_2$
11	Barium-II	$BaIIO + 3\,NO_2 \longrightarrow BaII(NO_3)_2 + NO$
12	Barium-II	$BaIIO + 2\,NO + 0.5\,O_2 \longrightarrow BaII(NO_2)_2$
13	Barium-II	$BaII(NO_2)_2 \longrightarrow BaIIO + 2\,NO + 0.5\,O_2$
14	Barium-II	$BaII(NO_3)_2 \longrightarrow BaIIO + 2\,NO_2 + 0.5\,O_2$
15	Barium-III	$BaIIIO + 2\,NO_2 + 0.5\,O_2 \longrightarrow BaIII(NO_3)_2$
16	Barium-I	$BaI(NO_3)_2 \longrightarrow BaIO + 2\,NO + 1.5\,O_2$
17	Barium-III	$BaIII(NO_3)_2 \longrightarrow BaIIIO + 2\,NO_2 + 0.5\,O_2$

4. Finally NO$_2$ storage and release on the dedicated Barium site was calibrated using tests with an equimolar amount of NO and NO$_2$ in the inlet batch, such as tests 5, 10 and 20.

Figures from 2.45 to 2.48 report simulation results for tests 7, 17, 29 and 32 respectively, in which NO was used as the only NO$_x$ representative species at the reactor inlet. In test 7, depicted in Figure 2.45, the reactor was fed with 200 ppm of NO at a constant temperature of 150 degC. At this temperature, the oxidation of NO into NO$_2$ was limited and the catalyst storage behaviour in presence of NO could be characterized. During the temperature increase ramp applied to induce the desorption of the stored NO$_x$, the experiments showed two distinct peaks for NO, at low and high temperature respectively, and one for NO$_2$ at high temperature which were correctly reproduced by the model. At this temperature however, the catalyst storage capacity was slightly overestimated by the model, which could be probably due to the lack of a low-temperature storage inhibition for the high-temperature NO$_2$ storage and release site, which could be introduced in a future model update. In tests 17 and 29 (Figures 2.46 and 2.47), where the inlet temperature was increased to 250 degC and 300 degC respectively, the formation of

NO$_2$ due to oxidation reactions activated the NO$_2$ storage site, as demonstrated by the large NO$_2$ release spike observed during the temperature ramp. Moreover, at these temperature conditions the activity of low-temperature storage site was drastically reduced. The model captured these trends predicting with satisfactory accuracy the temperature-dependent release timing and magnitude. Finally, simulation results of test 32, which was performed at a temperature of 450 degC, are depicted in Figure 2.48. At this temperature, the catalyst storage capacity was strongly reduced and the model well correlated with experimental measurements. However, some differences were observed in the NO and NO$_2$ concentrations reached after the NO$_x$ breakthrough during the constant-temperature storage phase, which could be reduced improving the calibration of the NO oxidation reaction and of the NO/NO$_2$ equilibrium curve. Unfortunately, additional dedicated light-off experiments to cover more temperature operating conditions would be required, which were not available after the experimental campaign.

Figure 2.45: Simulation results (solid line) versus experiments (dashed line) on the LNT TPD tests number 7. Gas temperature (red), NO (blue) and NO$_2$ (green) emissions. GHSV of 15000 h^{-1}.

Simulation results for the NO$_x$ TPD tests 5, 10 and 20, in which the reactor was fed with an equimolar amount of NO and NO$_2$ at different temperature levels (i.e. 125 degC, 200 degC and 250 degC respectively), are depicted in Figures from 2.49 to 2.51. As shown by the experiments, the simultaneous presence of NO and NO$_2$ activated the NO$_2$ storage site from the lowest temperature, as in test 5 of Figure 2.49, producing a noticeable NO$_2$ desorption spike during the temperature
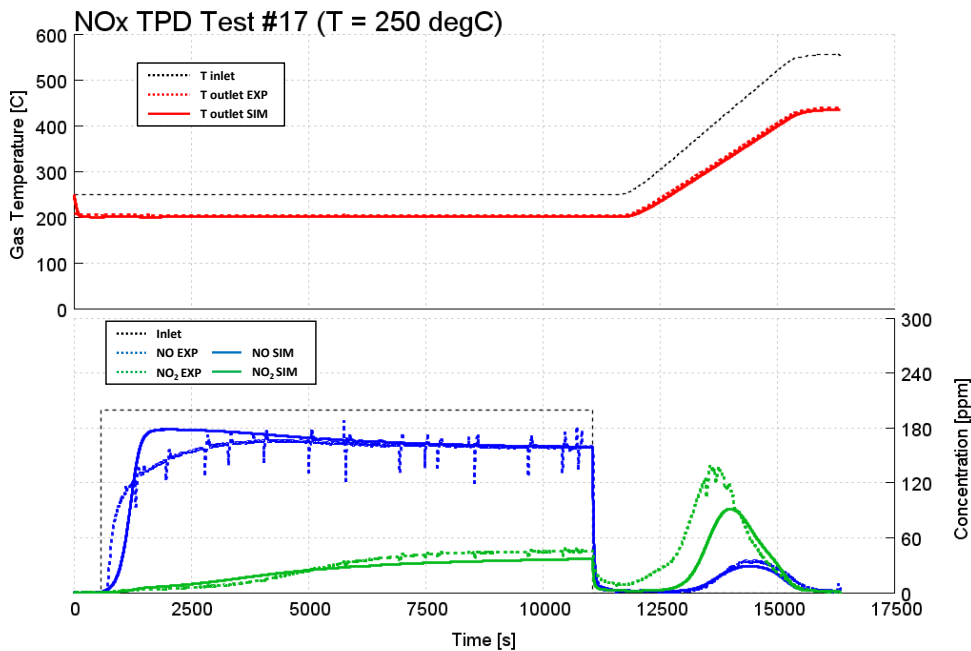
Figure 2.46: Simulation results (solid line) versus experiments (dashed line) on the LNT TPD tests number 17. Gas temperature (red), NO (blue) and NO$_2$ (green) emissions. GHSV of 15000 h^{-1}.

ramp. Such trend was further enhanced at the higher temperature levels of tests 10 and 20, depicted in Figures 2.50 and 2.51 respectively, and captured by the model which correctly estimated the NO$_x$ storage between the different adsorption sites and predicted the timing and magnitude of the released NO$_x$ during the subsequent temperature ramp.
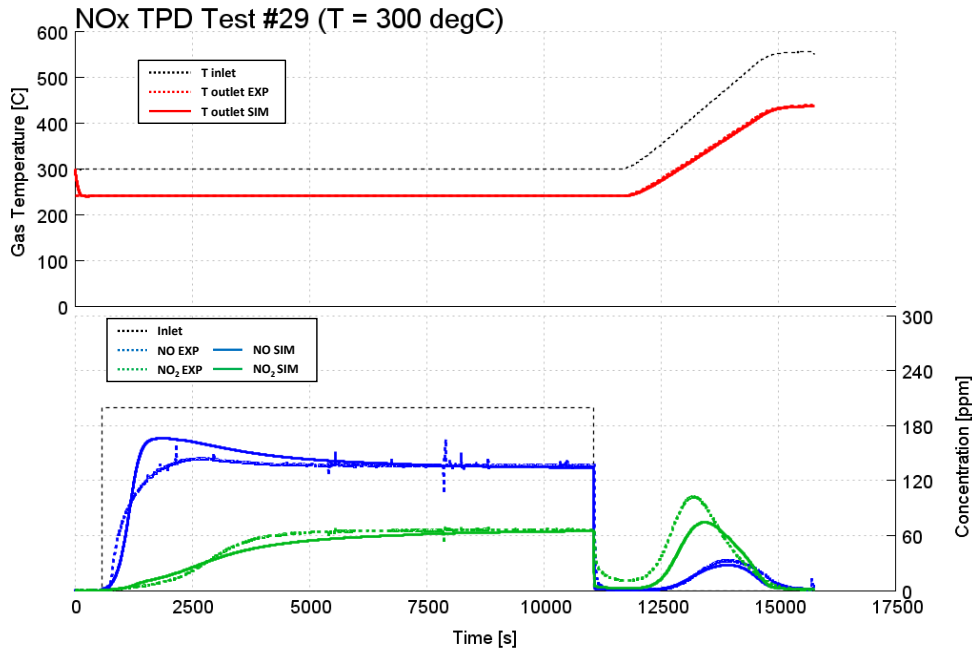
Figure 2.47: Simulation results (solid line) versus experiments (dashed line) on the LNT TPD tests number 29. Gas temperature (red), NO (blue) and NO_2 (green) emissions. GHSV of 15000 h^{-1}.
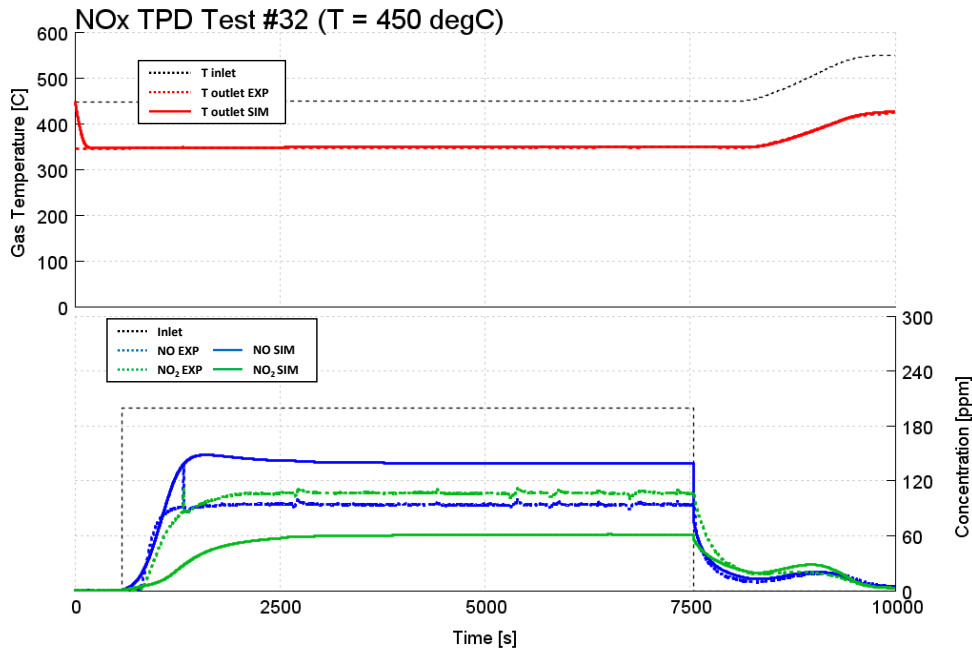
Figure 2.48: Simulation results (solid line) versus experiments (dashed line) on the LNT TPD tests number 32. Gas temperature (red), NO (blue) and NO_2 (green) emissions. GHSV of 15000 h^{-1}.

61

Figure 2.49: Simulation results (solid line) versus experiments (dashed line) on the LNT TPD tests number 5. Gas temperature (red), NO (blue) and NO$_2$ (green) emissions. GHSV of 15000 h^{-1}.

Figure 2.50: Simulation results (solid line) versus experiments (dashed line) on the LNT TPD tests number 10. Gas temperature (red), NO (blue) and NO$_2$ (green) emissions. GHSV of 15000 h^{-1}.

Figure 2.51: Simulation results (solid line) versus experiments (dashed line) on the LNT TPD tests number 20. Gas temperature (red), NO (blue) and NO_2 (green) emissions. GHSV of 15000 h^{-1}.

2.3.5 OSC Model

The reactions used to simulate the storage of oxygen on ceria sites during lean operations and the subsequent reduction of the stored oxygen by means of a reducing agent are reported in Table 2.9. In addition, water-gas-shift and steam-reforming reactions on PGM were included in the kinetic scheme due to the presence of H$_2$O in the inlet feed. The storage of oxygen storage on ceria was modelled using a temperature-dependent equilibrium function, reported in Table 5, which takes the difference between the instantaneous CeO$_2$ coverage and the temperature-dependent equilibrium coverage to impose the limit. By this means the maximum storage capacity, which increases with temperature, is limited by a maximum storage equilibrium curve [7]. In addition, a dedicated inhibition function was introduced to limit the OSC at high temperature. Coverage-dependent activation terms were used for the reduction reactions on Ceria sites.

The model calibration was carried out by taking into account the OSC experimental tests reported in Table 2.5. The experimental tests consisted of alternating lean and rich phases, during which Ceria sites store oxygen and then are purged by means of a reducing agent. The test-protocol inlet composition included three different reducing agents, H$_2$, CO and C$_3$H$_6$, tested in different temperature conditions at a space velocity of 15000 h^{-1}.

Table 2.9: LNT Model OSC Kinetic Scheme

Number	Site Element	Reaction
18	cerium	$Ce_2O_3 + 0.5\,O_2 \longrightarrow 2\,CeO_2$
19	cerium	$2\,CeO_2 + CO \longrightarrow Ce_2O_3 + CO_2$
20	cerium	$2\,CeO_2 + H_2 \longrightarrow Ce_2O_3 + H_2O$
21	cerium	$2\,CeO_2 + 0.11\,C_3H_6 \longrightarrow Ce_2O_3 + 0.33\,CO_2 + 0.33\,H_2O$

Ceria site density, reactions pre-exponential factors and activation temperatures were considered as the independent variables in the optimization process. In particular, Ceria site density was calibrated to reproduce the experimental storage capacity at different temperatures, by looking at the breakthrough point of the reducing agents in each test. Pre-exponential factors and activation temperatures of the reactions on Ceria sites were calibrated, for each reducing agent included in the experiments, based on the measured outlet concentrations of each species.

WGS and SR reactions parameters were calibrated considering the concentration of CO and C_3H_6 in the last portion of the rich phase, after a steady-state behavior was reached. At the beginning of the rich phase in fact, the oxygen stored on Ceria consumes the CO and C_3H_6 present in the gas thus complicating the distinction between the share of conversion due to WGS or SR and the one due to the oxidation. Considering that H2 was not measured at the reactor outlet and that CO_2 was not included in the inlet batch, the CO_2 measured at the reactor outlet, after steady state conditions have been reached, could be used instead to quantify the H_2 consumed through WGS, due to the stoichiometry of the reaction. Also in this case, the aforementioned Voltz-type inhibition term was used to account for mutual competition on PGM sites.

The calibration protocol adopted for the OSC kinetics calibration consists of:

1. WGS and SR reaction parameters calibration considering reducing agents outlet concentration during rich pulses, after a steady-state trend was achieved.

2. Ceria site density calibration to match the reductants breakthrough observed experimentally and to achieve the observed OSC, at each temperature.

3. Fine tuning of pre-exponent and exponential Arrhenius parameters of reduction reactions on Ceria, in order to match the reductants measured outlet traces.

Simulation results for all the tests in which CO was used as the reducing agent are depicted in Figures from 2.52 to 2.58. The reactor external convection coefficient was calibrated to correctly represent the heat losses observed duing the eperiments. Since the formation of Cerium oxides due to oxygen storage is an exothermic process, the heat of formation related to CeO_2 sites was set to -200 kJ/mol [19] (the - sign indicates that heat is released) within the model to match the temperature increase observed in the experiments during the lean phase. As a result, the simulated gas temperature obtained at the reactor outlet showed the temperature increase during the storage of oxygen, in agreement with the experiments. During the rich phase, where the temperature increase is due to the heat released by species oxidation reactions, minor differences were observed between the simulated and the experimental gas temperature. Particularly, the simulated gas temperature was generally underestimated during rich operations when CO was used as the reducing agent, especially at temperatures below 300 degC, even if the CO_2 emissions and thus the rate of CO oxidation were accurately predicted. The CO breakthrough was accurately matched as well as the steady-state concentration reached during the rich phase. A peak was observed in the CO_2 simulated emissions at the beginning of the rich phase, due to the reaction of CO with the oxygen

65

stored on ceria, in agreement with the experimental data. The other CO_2 peak observed in the experiments, which was probably due to the overlapping of CO and oxygen in the inlet batch during the rich-to-lean transition, was underestimated by the model due to a shorter simulated phase transition.

Figure 2.52: Simulation results (solid line) versus experiments (dashed line) on the LNT OSC test number 2. Gas temperature (red), CO (blue), CO_2 (orange) and H_2O (light-blue) emissions. GHSV of 15000 h^{-1}.

66

Figure 2.53: Simulation results (solid line) versus experiments (dashed line) on the LNT OSC test number 5. Gas temperature (red), CO (blue), CO_2 (orange) and H_2O (light-blue) emissions. GHSV of 15000 h^{-1}.

Figure 2.54: Simulation results (solid line) versus experiments (dashed line) on the LNT OSC test number 8. Gas temperature (red), CO (blue), CO_2 (orange) and H_2O (light-blue) emissions. GHSV of 15000 h^{-1}.

67

Figure 2.55: Simulation results (solid line) versus experiments (dashed line) on the LNT OSC test number 13. Gas temperature (red), CO (blue), CO$_2$ (orange) and H$_2$O (light-blue) emissions. GHSV of 15000 h^{-1}.

Figure 2.56: Simulation results (solid line) versus experiments (dashed line) on the LNT OSC test number 16. Gas temperature (red), CO (blue), CO$_2$ (orange) and H$_2$O (light-blue) emissions. GHSV of 15000 h^{-1}.

Figures from 2.57 to 2.59 report simulation results of tests 6, 10 and 14 respectively, in which propylene was used as the reducing agent. The model predictions were in agreement with the experiments in terms of both gas temperature and propylene breakthrough, in all the analysed test conditions. The impact of steam reforming was limited in the tests, since the outlet propylene concentration always matched the inlet value once the stored oxygen was consumed. In the simulations, the CO_2 and H_2O spikes produced during the transition between rich and lean phases were not reproduced. Also in this case this difference could be explained by a quasi-instantaneous phase-switch in the virtual test against a longer one in the real test, which allowed the oxidation of the propylene with the oxygen introduced at the beginning of the lean phase.
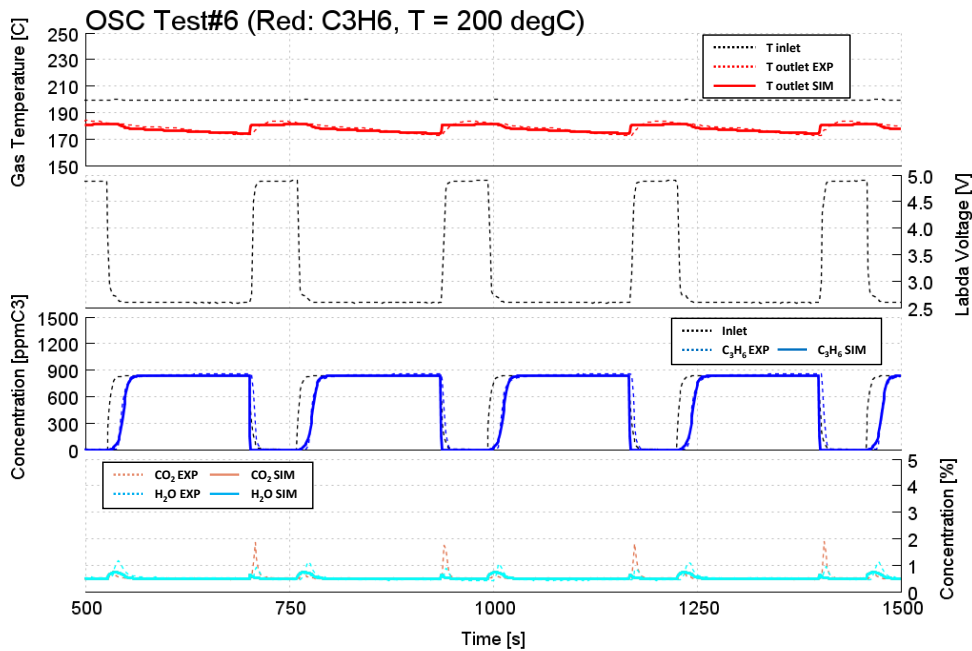
Figure 2.57: Simulation results (solid line) versus experiments (dashed line) on the LNT OSC test number 6. Gas temperature (red), C_3H_6 (blue), CO_2 (orange) and H_2O (light-blue) emissions. GHSV of 15000 h^{-1}.
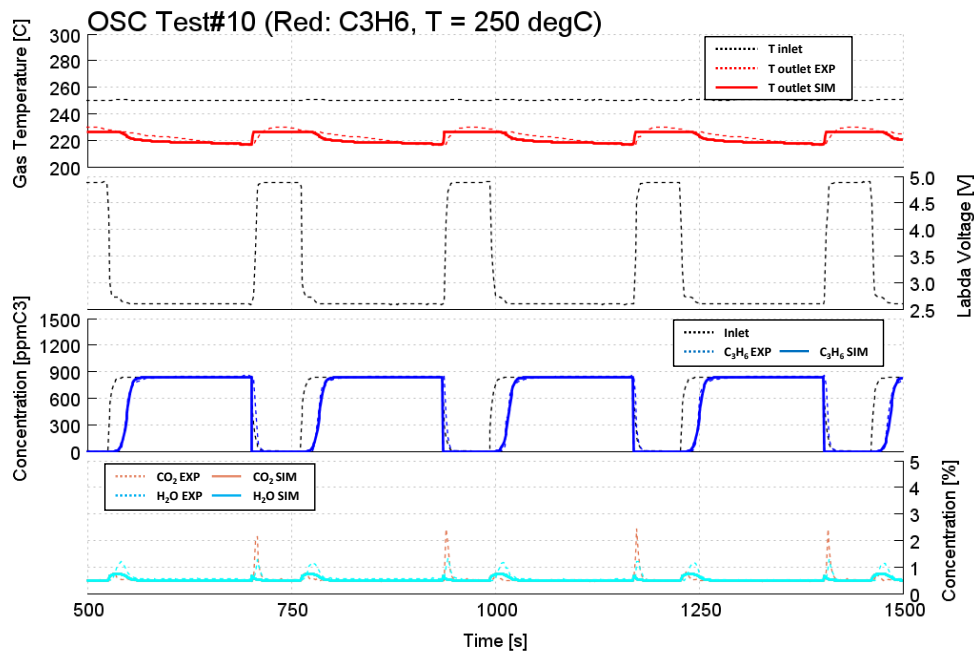
Figure 2.58: Simulation results (solid line) versus experiments (dashed line) on the LNT OSC test number 10. Gas temperature (red), C$_3$H$_6$ (blue), CO$_2$ (orange) and H$_2$O (light-blue) emissions. GHSV of 15000 h^{-1}.
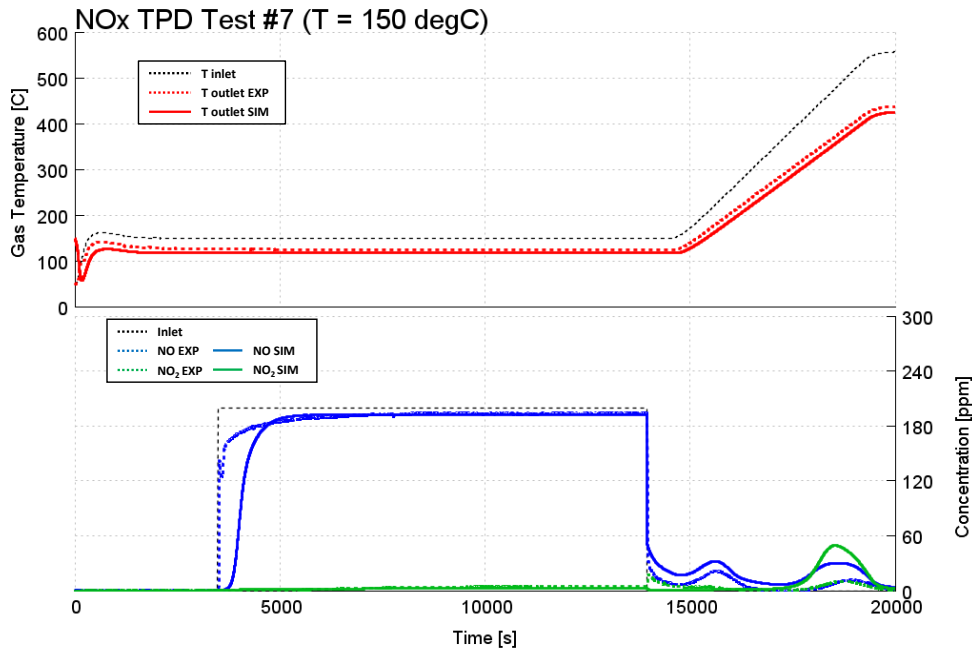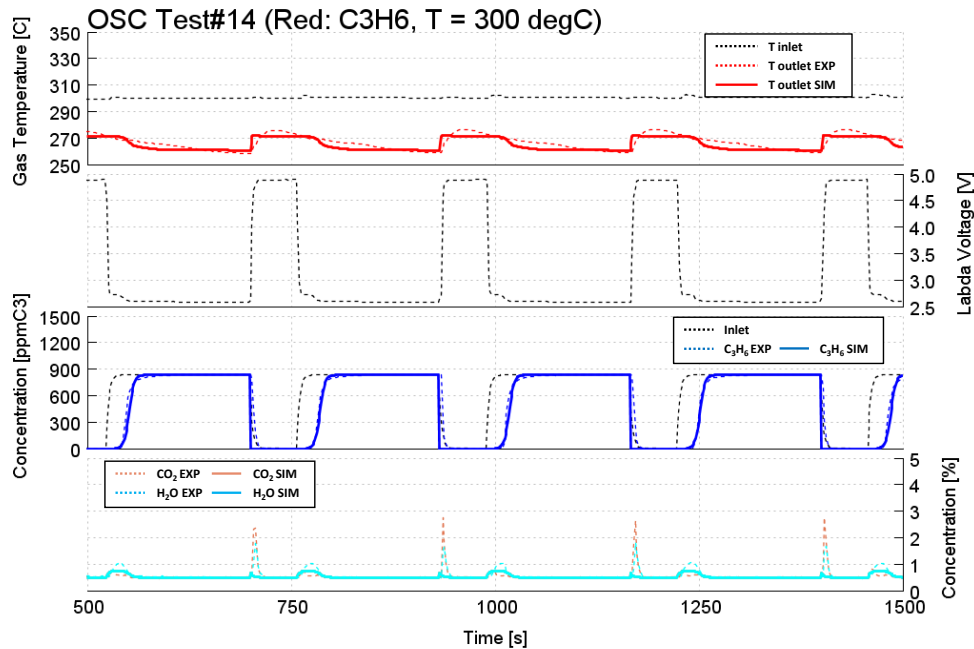

Figure 2.59: Simulation results (solid line) versus experiments (dashed line) on the LNT OSC test number 14. Gas temperature (red), C$_3$H$_6$ (blue), CO$_2$ (orange) and H$_2$O (light-blue) emissions. GHSV of 15000 h^{-1}.

2.3.6 NSR Model

The NO_x storage was modelled using three different Barium sites as described in Chapter 2.3.4. To simulate the stored NO_x reduction, the reactions listed in 2.10 were used. By this means, NO_x on each site could react with different reducing agents, namely CO, H_2, NH_3 and propylene. Different reaction pathways were considered in the mechanism, including the complete NO_x reduction to N_2 and partial reduction to NO, N_2O or NH_3. An oxygen-dependent inhibition function of the type $(1 + kC(O_2))$ was applied to the reduction reactions, in which k is represented with an Arrhenius function (reported in the appendix 4, Table 5), to account for the lower rate of the reduction reactions during lean conditions, as also reported in the literature [20, 21].

The model was calibrated and validated over the experimental tests described in Section 2.2.6, modifying reaction parameters in order to match the experiments. Alternating lean and rich phases were simulated to reproduce NO_x storage on Barium sites and the subsequent reduction by means of a reducing agent. Different inlet gas temperature and mixtures were simulated at a constant GHSV of 15000 h^{-1}. The calibration process was carried out individually for each group of reactions involving a specific reducing agent, over the related set of experiments.

Table 2.10: LNT Model NSR Kinetic Scheme

Number	Site	Reaction
22	Barium-II	$BaII(NO_2)_2 + 6\,H_2 \longrightarrow BaIIO + 2\,NH_3 + 3\,H_2O$
23	Barium-II	$BaII(NO_2)_2 + 2\,NH_3 \longrightarrow BaIIO + 2\,N_2 + 3\,H_2O$
24	Barium-II	$BaII(NO_2)_2 + 0.4\,NH_3 \longrightarrow BaIIO + 2.4\,NO + 0.6\,H_2O$
25	Barium-II	$BaII(NO_3)_2 + 3.33\,NH_3 \longrightarrow BaIIO + 2.67\,N_2 + 5\,H_2O$
26	Barium-II	$BaII(NO_3)_2 + 2\,NH_3 \longrightarrow BaIIO + 2\,N_2O + 3\,H_2O$
27	Barium-I	$BaI(NO_3)_2 + 8\,H_2 \longrightarrow BaIO + 2\,NH_3 + 5\,H_2O$

Number	Site	Reaction
28	Barium-I	$BaI(NO_3)_2 + 3.33\,NH_3 \longrightarrow BaIO + 2.67\,N_2 + 5\,H_2O$
29	Barium-III	$BaIII(NO_3)_2 + 3\,H_2 \longrightarrow BaIIIO + 2\,NO + 3\,H_2O$
30	Barium-III	$BaIII(NO_3)_2 + 8\,H_2 \longrightarrow BaIIIO + 2\,NH_3 + 5\,H_2O$
31	Barium-III	$BaIII(NO_3)_2 + 3.33\,NH_3 \longrightarrow BaIIIO + 2.67\,N_2 + 5\,H_2O$
32	PGM	$NO + 2.5\,H_2 \longrightarrow NH_3 + H_2O$
33	Barium-II	$BaII(NO_2)_2 + 3\,CO \longrightarrow BaIIO + N_2 + 3\,CO_2$
34	Barium-II	$BaII(NO_2)_2 + CO \longrightarrow BaIIO + 2\,NO + CO_2$
35	Barium-II	$BaII(NO_3)_2 + 4\,CO \longrightarrow BaIIO + 4\,CO_2 + N_2O$
36	Barium-I	$BaI(NO_3)_2 + 5\,CO \longrightarrow BaIO + 5\,CO_2 + N_2$
37	Barium-III	$BaIII(NO_3)_2 + 5\,CO \longrightarrow BaIIIO + 5\,CO_2 + N_2$
38	Barium-II	$BaII(NO_3)_2 + 3\,CO \longrightarrow BaIIO + 3\,CO_2 + 2\,NO$
39	Barium-II	$BaII(NO_2)_2 + 0.11\,C_3H_6 \longrightarrow BaIIO + 0.33\,H_2O + 0.33\,CO_2 + 2\,NO$
40	Barium-II	$BaII(NO_3)_2 + 0.56\,C_3H_6 \longrightarrow BaIIO + 1.67\,H_2O + 1.67\,CO_2 + N_2$
41	Barium-I	$BaI(NO_3)_2 + 0.56\,C_3H_6 \longrightarrow BaIO + 1.67\,H_2O + 1.67\,CO_2 + N_2$
42	Barium-I	$BaI(NO_3)_2 + 0.33\,C_3H_6 \longrightarrow BaIO + H_2O + CO_2 + 2\,NO$
43	Barium-III	$BaIII(NO_3)_2 + 0.56\,C_3H_6 \longrightarrow BaIIIO + 1.67\,H_2O + 1.67\,CO_2 + N_2$

Number	Site	Reaction
44	Barium-III	$BaIII(NO_3)_2 + 0.33\,C_3H_6 \longrightarrow BaIIIO + H_2O + CO_2 + 2\,NO$
45	PGM	$C_3H_6 + 18\,NO \longrightarrow 9\,N_2O + 3\,CO_2 + 3\,H_2O$
46	PGM	$C_3H_6 + 9\,NO \longrightarrow 3\,H_2O + 3\,CO_2 + 4.5\,N_2$

Simulation results of tests 1, 9 and 20, in which H_2 was used as the reducing agent, are depicted in Figures 2.60, 2.61 and 2.62. An accurate correlation with the experiments was achieved in terms of NO_x, N_2O and NH_3, while the H_2 experimental measurement was not available. In agreement with the experiments, in the simulation a large quantity of NO_x was released at the beginning of each rich pulse as a consequence of the reaction of H_2 on Barium sites, producing mainly NO. Part of the stored NO_x was also converted into N_2O and NH_3. Particularly, in the simulation the NH_3 breakthrough delay, compared with N_2O, was correctly captured since part of the produced ammonia was initially consumed reacting on Barium sites.
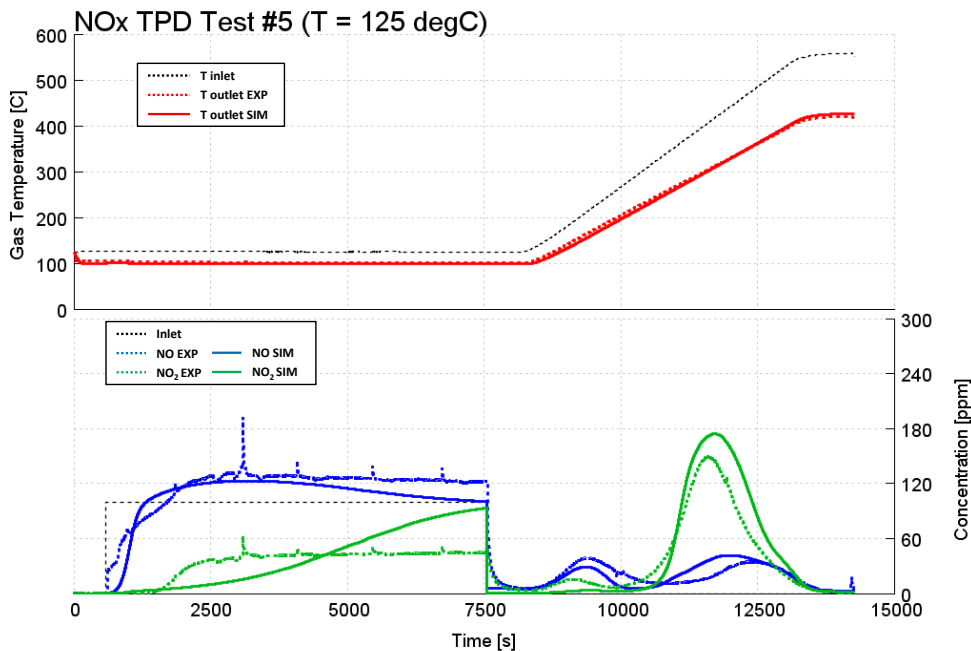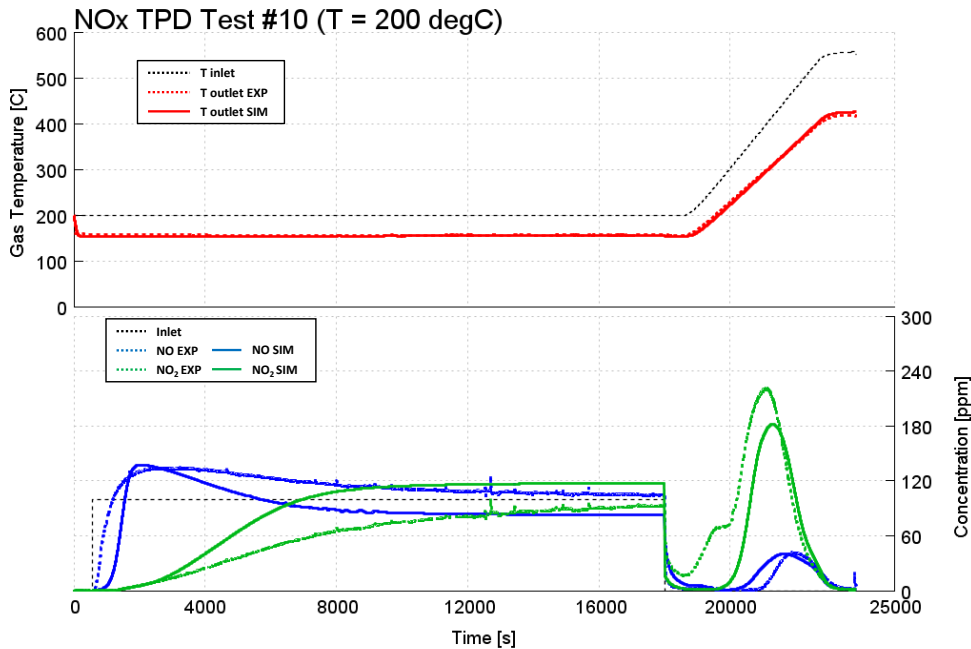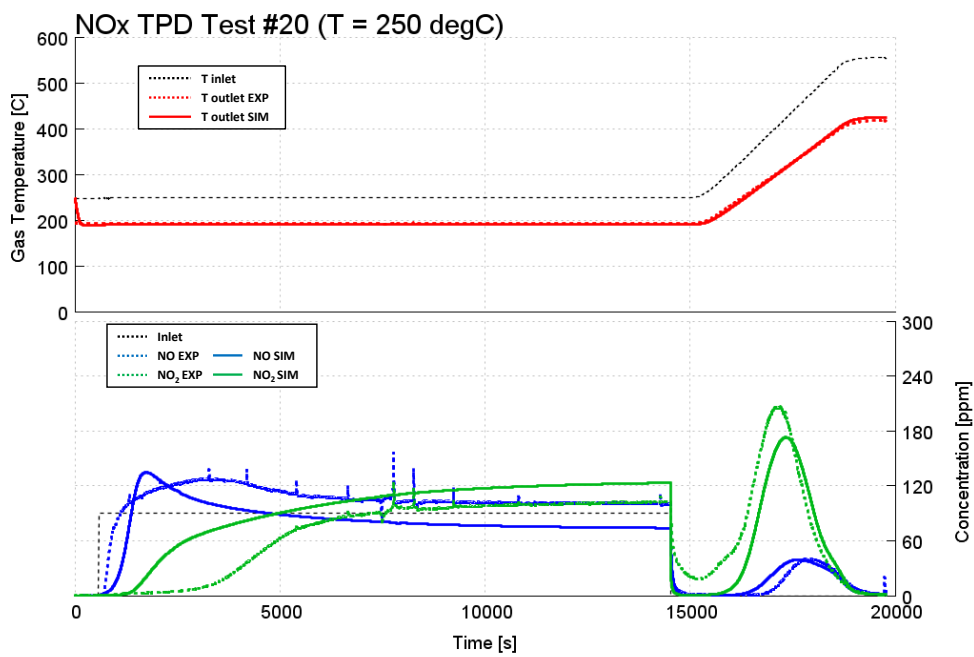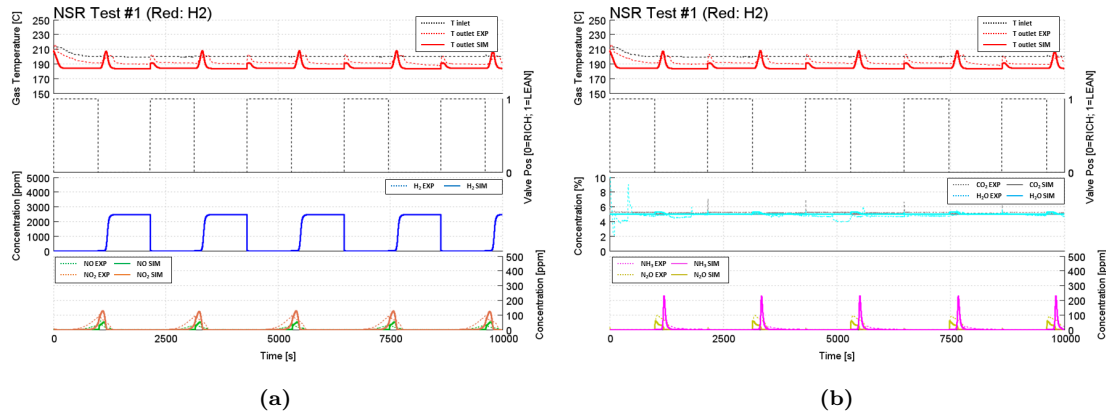

Figure 2.60: Simulation results (solid line) versus experiments (dashed line) on the LNT NSR test number 1. Gas temperature (red), H_2 (blue), NO (green), NO_2 (orange), CO_2 (grey), H_2O (light-blue), N_2O (yellow) and NH_3 (purple) emissions. GHSV of 15000 h^{-1}.
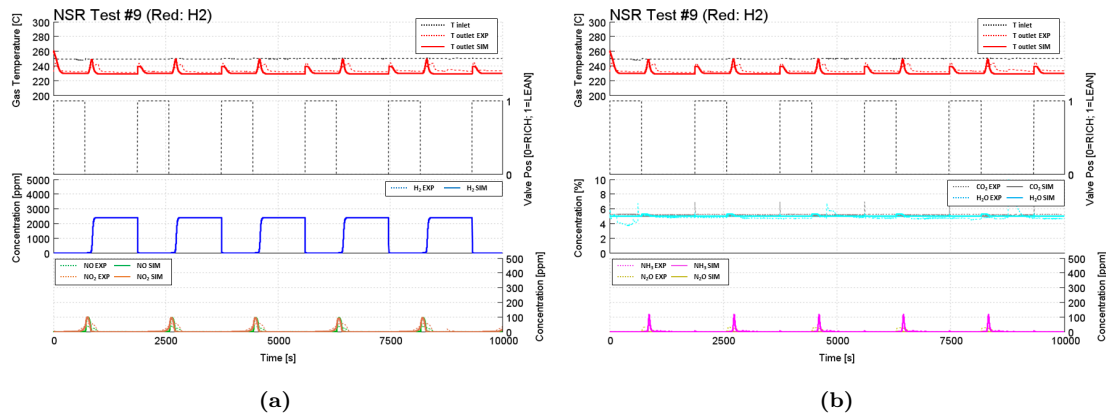
Figure 2.61: Simulation results (solid line) versus experiments (dashed line) on the LNT NSR test number 9. Gas temperature (red), H$_2$ (blue), NO (green), NO$_2$ (orange), CO$_2$ (grey), H$_2$O (light-blue), N$_2$O (yellow) and NH$_3$ (purple) emissions. GHSV of 15000 h^{-1}.
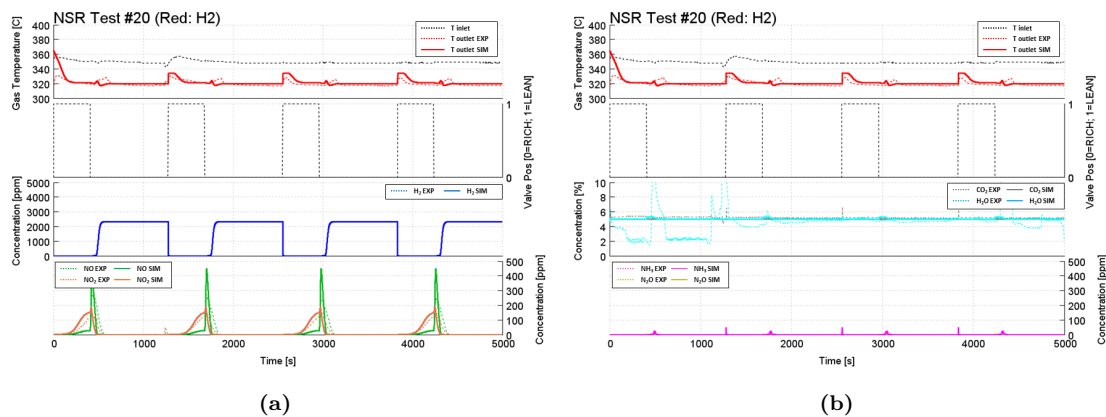
Figure 2.62: Simulation results (solid line) versus experiments (dashed line) on the LNT NSR test number 20. Gas temperature (red), H$_2$ (blue), NO (green), NO$_2$ (orange), CO$_2$ (grey), H$_2$O (light-blue), N$_2$O (yellow) and NH$_3$ (purple) emissions. GHSV of 15000 h^{-1}.

In Figures 2.63, 2.64 and 2.65 are depicted simulation results of tests 2, 10 and 21 respectively, in which CO was used as the reducing agent. The model captured the release of NO$_x$, N$_2$O and NH$_3$ at the beginning of each rich phase, especially below 300 degC. The production of NH$_3$ was limited due to the lower concentration of H$_2$, which was produced by means of WGS. The simulated outlet concentration of CO was reduced as the temperature increased, due to the higher rate of WGS reaction, as in the experiments.

Propylene was used as the reducing agent in tests 3, 11 and 22 whose simulation results are depicted in Figures 2.66, 2.67 and 2.68 respectively. After the calibration, the model captured the NO$_x$ release under rich conditions as a consequence of the reaction of propylene on Barium sites, producing mostly NO. The influence of

(a) **(b)**
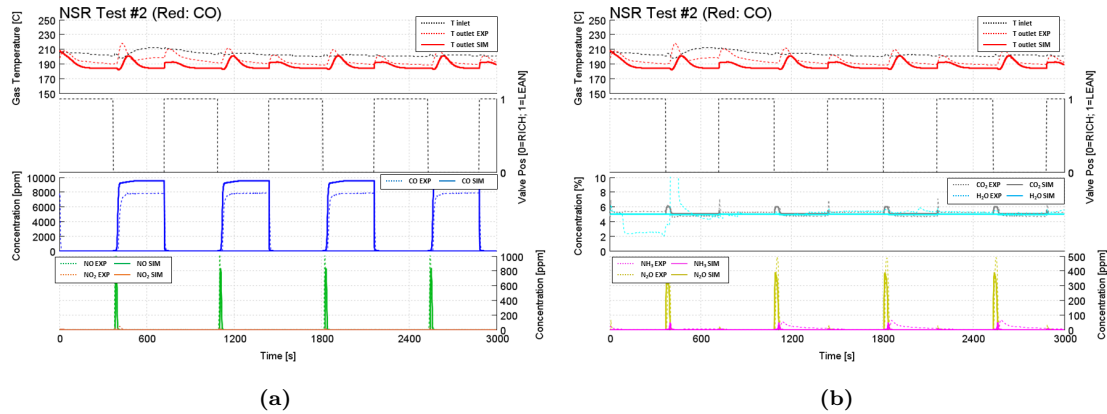
Figure 2.63: Simulation results (solid line) versus experiments (dashed line) on the LNT NSR test number 2. Gas temperature (red), CO (blue), NO (green), NO_2 (orange), CO_2 (grey), H_2O (light-blue), N_2O (yellow) and NH_3 (purple) emissions. GHSV of 15000 h^{-1}.

(a) **(b)**
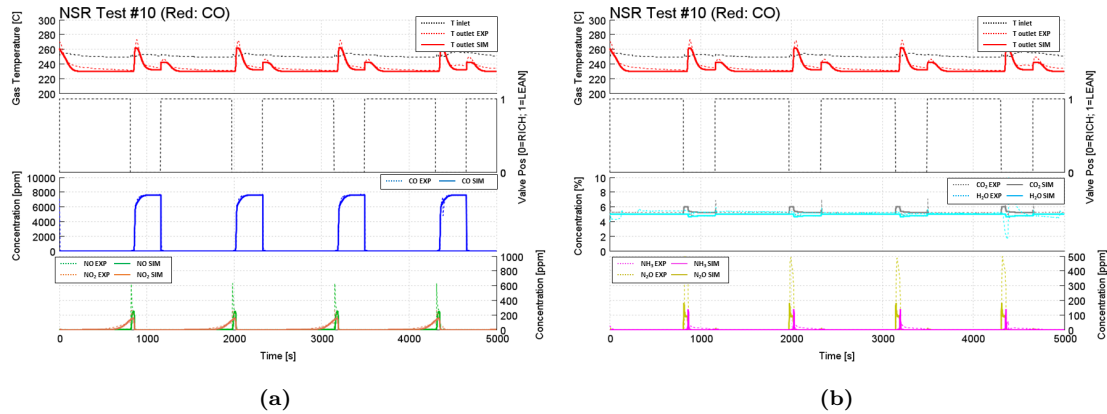
Figure 2.64: Simulation results (solid line) versus experiments (dashed line) on the LNT NSR test number 10. Gas temperature (red), CO (blue), NO (green), NO_2 (orange), CO_2 (grey), H_2O (light-blue), N_2O (yellow) and NH_3 (purple) emissions. GHSV of 15000 h^{-1}.

steam reforming on the C_3H_6 concentration was shown only above 300 degC, as in Figure 2.68. The N_2O production at the beginning of the rich phase was simulated through the reduction of NO with C_3H_6 on PGM. The second peak observed at the beginning of each lean phase, which could be related to the simultaneous presence of NO and propylene during the phase change, was not reproduced by the model due to a faster rich-to-lean transition, compared to the experiments.
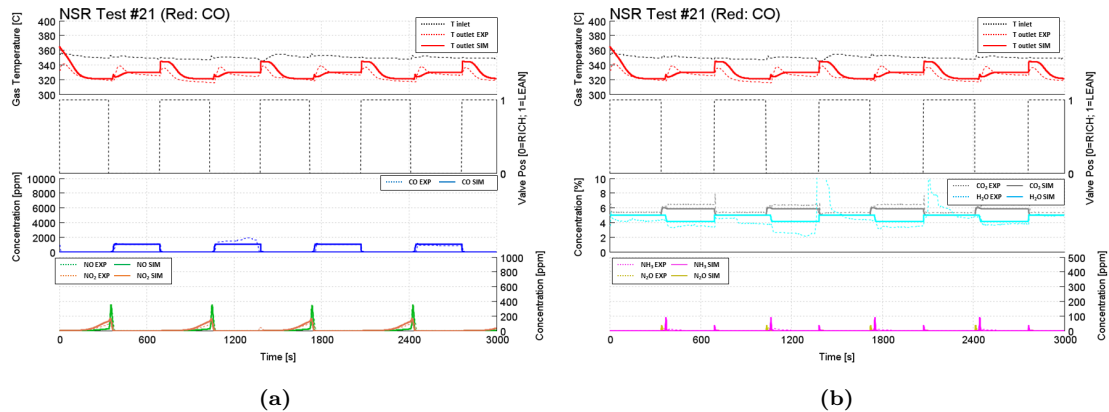
Figure 2.65: Simulation results (solid line) versus experiments (dashed line) on the LNT NSR test number 21. Gas temperature (red), CO (blue), NO (green), NO$_2$ (orange), CO$_2$ (grey), H$_2$O (light-blue), N$_2$O (yellow) and NH$_3$ (purple) emissions. GHSV of 15000 h^{-1}.
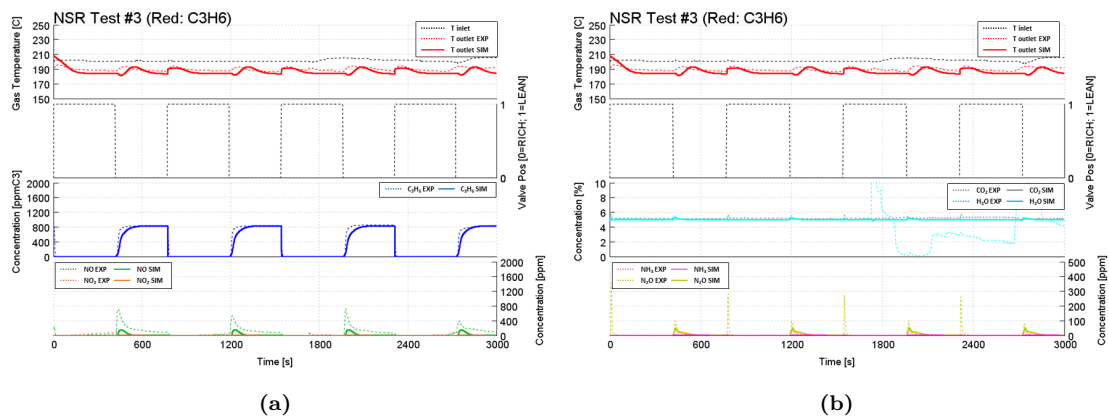
Figure 2.66: Simulation results (solid line) versus experiments (dashed line) on the LNT NSR test number 3. Gas temperature (red), C$_3$H$_6$ (blue), NO (green), NO$_2$ (orange), CO$_2$ (grey), H$_2$O (light-blue), N$_2$O (yellow) and NH$_3$ (purple) emissions. GHSV of 15000 h^{-1}.

(a)   (b)
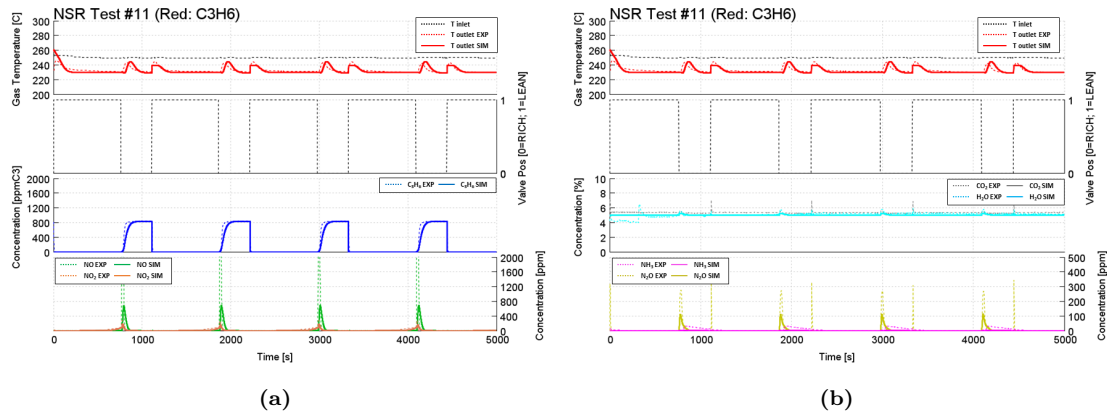
Figure 2.67: Simulation results (solid line) versus experiments (dashed line) on the LNT NSR test number 11. Gas temperature (red), C_3H_6 (blue), NO (green), NO_2 (orange), CO_2 (grey), H_2O (light-blue), N_2O (yellow) and NH_3 (purple) emissions. GHSV of 15000 h^{-1}.
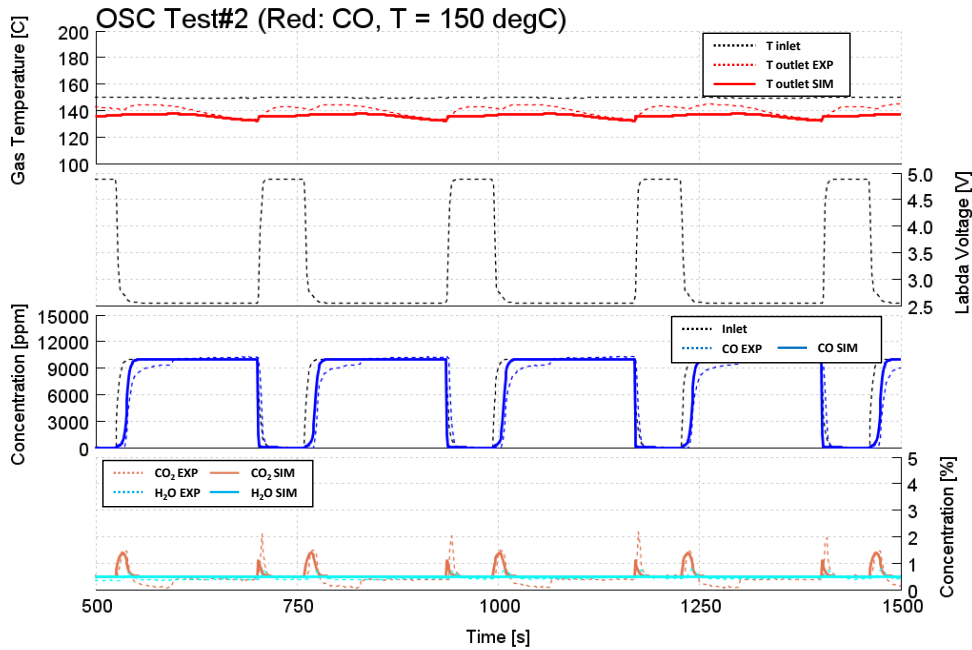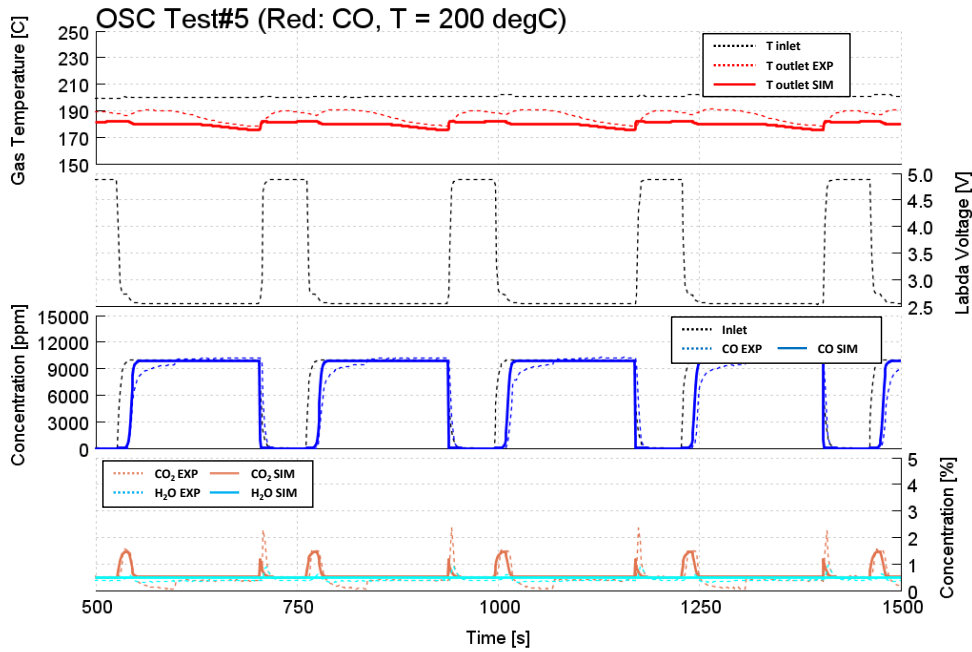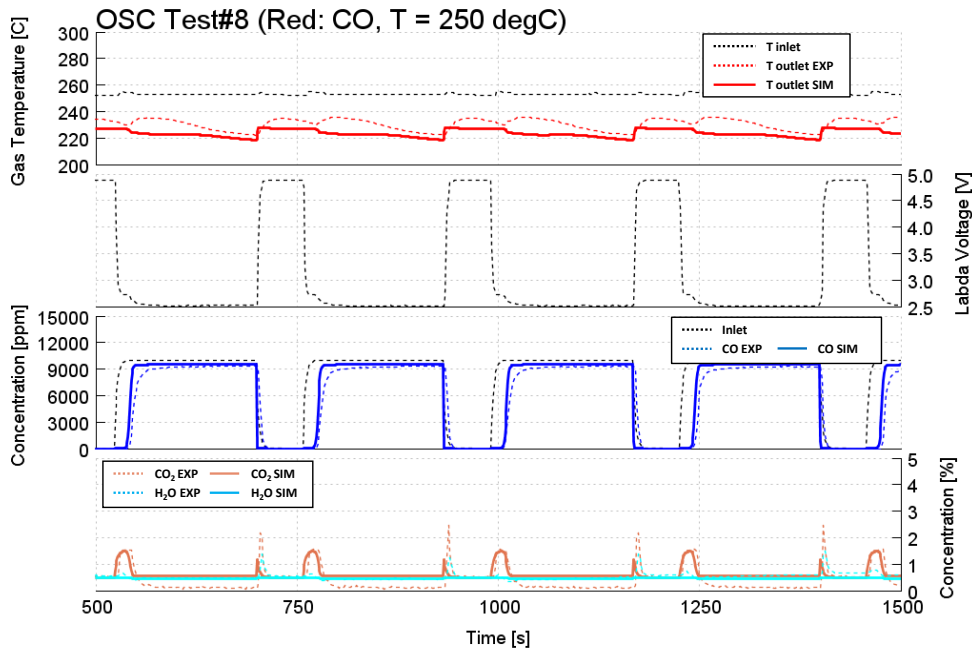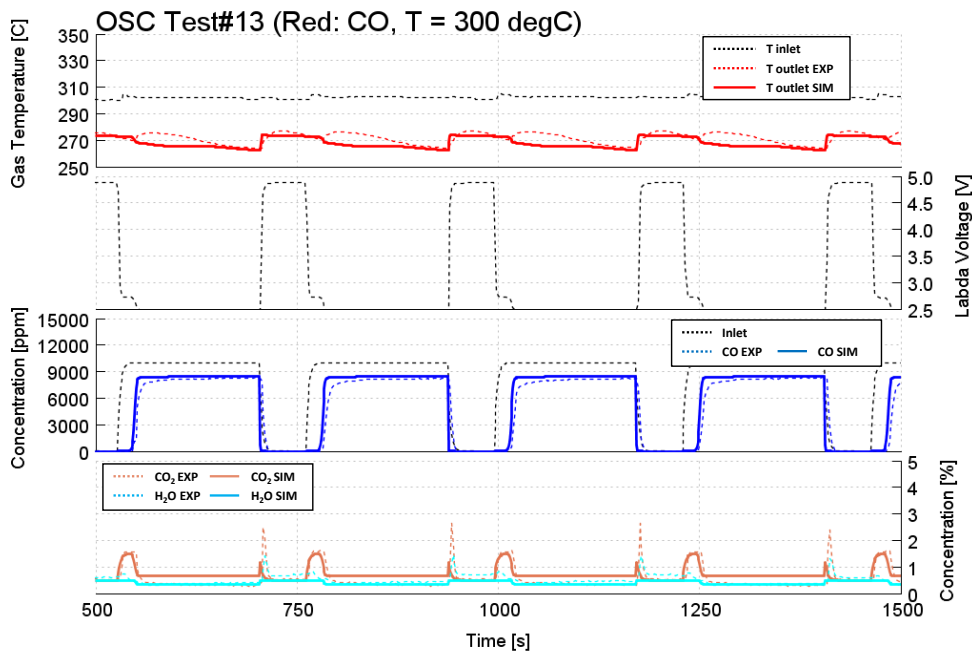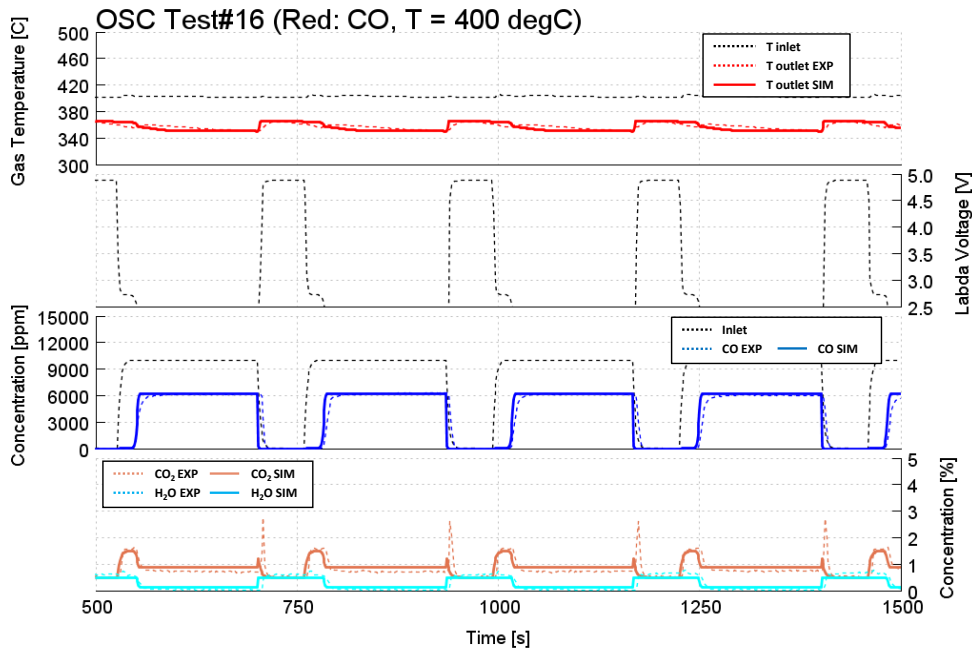

(a)   (b)
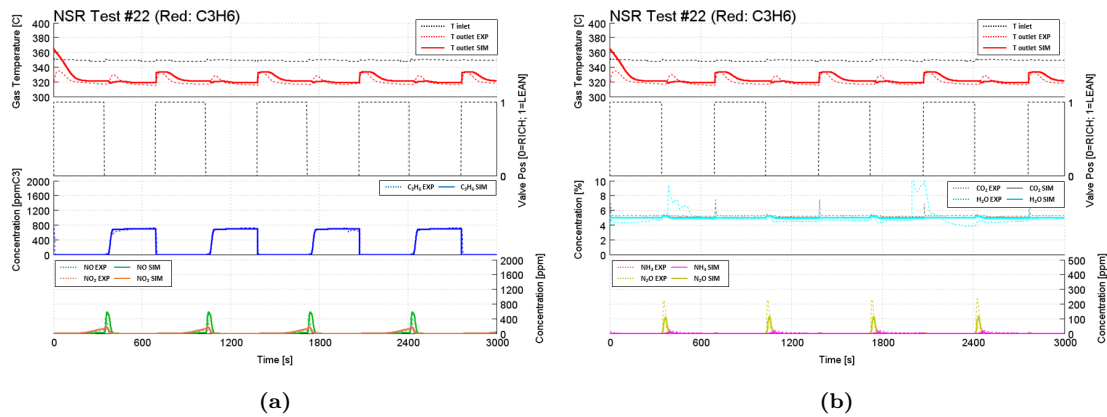
Figure 2.68: Simulation results (solid line) versus experiments (dashed line) on the LNT NSR test number 22. Gas temperature (red), C_3H_6 (blue), NO (green), NO_2 (orange), CO_2 (grey), H_2O (light-blue), N_2O (yellow) and NH_3 (purple) emissions. GHSV of 15000 h^{-1}.

2.4 Model Up-Scaling

Ideally, the kinetics developed for the reactor-scale model based on the SGB experiments should be directly used in the full-scale system model without relevant modifications of the reaction rate parameters. However, it is often found that the model predictions do not agree with full-scale experiments due to various reasons [22]. One of the primary source of error between laboratory-scale and engine-scale kinetics lies in the limited number of HC species available for the SGB tests whereas the real engine-out exhaust gas is characterized by a wide spectrum of HCs which can lead to differences in the overall simulated HCs conversion [9]. Another source of error which might compromise similarity between the engine- and laboratory-scale systems lies in the entrance effects, since heat and mass dispersion could became significant in the engine-scale component, where the hypothesis of uniform mass flow distribution on the catalyst cross section could not be applied [22]. Finally, the ageing conditions and the catalyst activity could differ between laboratory-scale samples and the full size component tested on the engine-dyno [23]. For these reasons minor adjustments to the kinetics could be required to adapt the model to an engine-scale system.

After completion of the reactor-scale model calibration and validation, the model of the full-size component was built by:

- updating the geometry of the monolith to the full-size, as reported in table 2.1.

- updating the information to properly account for the external heat transfer, such as thickness and materials details of the insulating external layers and of the external metallic canning, as reported in Table 2.11. The ideal catalyst insulation was assumed, imposing the external convection coefficient of 0 W/(m²K) as the external boundary condition. Preliminary simulation results in terms of LNT outlet gas temperature confirmed the initial assumption of ideal catalyst insulation.

- inheriting the reactor-scale model kinetic parameters.

- fine tuning of CO and HCs oxidation reactions parameters based on the experimental data to account for the promoting effect of H$_2$ [24] and its enhancing effect on the actual oxidation state of the catalyst.

The engine-scale model was validated over a comprehensive experimental dataset

Table 2.11: LNT Catalyst Insulation Setup

External Convection		0 W/(m^{2}K)
Layer	**Material**	**Thickness [mm]**
Insulating Layer	Fiberglass	4
External Canning	Stainless Steel	1.5

of driving cycle data. The experimental campaign was carried out at the engine-dyno test facilities of GM Global Propulsions Systems, in Turin, on a latest generation 1.6 L compression ignition engine for passenger cars, whose main design parameters are reported in Table 2.12.

Table 2.12: Tested engine main features

Engine Type	**Compression Ignition**
Number of Cylinders	4 Inline
Displacement	1598 cm^3
Bore x Stroke	(79.7 x 80.1) mm
Compression ratio	16:1
Turbocharger	Single-stage with VGT
Fuel Injection System	Common Rail with Solenoid Injectors
EGR Circuit	High Pressure
Maximum Power	100 kW @ 4000 rpm
Maximum Torque	320 Nm @ 2000 rpm

The analyzed LNT was installed in the exhaust line after the turbine and tested over different WLTC and a RDE driving cycles including different engine calibrations, with and without controlled DeNOx events to regenerate the NO$_x$ trap efficiency by means of post-injections. The engine-dyno test protocol is summarized in Table 2.13.

Table 2.13: Engine-dyno experimental test protocol

Preconditioning	Regeneration + 5 DeNO$_x$	
Test ID	**Test Cycle**	**DeNO$_x$ Events**
WLTC-A	WLTC (cold)	None
WLTC-B	WLTC (cold)	at 1711 s
RDE	RDE (cold)	at 1331 s and 2241 s

Engine out emissions were measured by means of an emission bench, able to detect THC, CO, NO, NO$_x$ and O$_2$ concentration during along the cycle, while emissions at the LNT outlet were measured by means of a FTIR analyzer, including NH$_3$ and N$_2$O species concentrations. K-type thermocouple sensors were used to monitor the gas temperature before and after the catalyst. Prior to each test a preconditioning protocol was applied in order to guarantee homogeneous initial conditions for each tests, consisting of a DPF regeneration followed by 5 controlled DeNO$_x$ events to clean the LNT storage sites.

The engine-out HCs were speciated within the model as 20% of propylene (fast-oxidizing, C$_3$H$_6$) and 80% of dodecane (slow-oxidizing, C$_{12}$H$_{26}$) in agreement with the speciation used during the SGB test-campaign. H$_2$ and H$_2$O, which are requested inputs for the model, were not included in the species measured at the engine-out emissions bench, thus their concentration at the LNT inlet was estimated according to Katare et al [24], based on the CO and CO$_2$ measured concentrations.

In the following section, simulation results of the engine-scale LNT model will be compared with experimental observation. The y axes scales will be hidden to preserve proprietary information.

2.4.1 WLTC-A Results

The up-scaled model results using as input the gas temperature, mass flow and composition measured on the WLTC-A test cycle are here reported.

The WLTC-A test did not include controlled DeNO$_x$ events. The simulated gas temperature, shown in Figure 2.69, matched the experimental trace with an average error of 10 degC, confirming the initial assumption of negligible heat losses through the external environment. The LNT NO$_x$ conversion, depicted in Figure 2.70 was limited since only 20% of the inlet NO$_x$ were converted by the catalyst. Model predictions were in agreement with the experimental data, with an error of 5% on the cumulated NO$_x$ mass at the catalyst outlet. As far as HCs and CO are concerned, the model underestimated the overall conversion efficiency which resulted in 87% instead of the experimental 95% for HCs and in 90% instead of 97% for CO, as shown in Figures 2.71 and 2.72 respectively. Particularly, as can be noticed from Figure 2.71 the model underestimated the HCs conversion during the first 50 s of the cycle, when the catalyst temperature was still below the light-off point. This difference could be related to the different behaviour of the real gas temperature and the signal measured by the thermocouple sensor in the exhaust stream, which is used as input for the model. A different trend was observed with CO, since the model correctly captured the conversion during the first stage of the cycle while the overall CO abatement during the cycle was slightly underestimated, especially in presence of quick and fuel-rich transient conditions. It is worth noting that, during this short and uncontrolled rich events, the catalyst NO$_x$ capacity was spontaneously regenerated as demonstrated by the slope change in the catalyst outlet NO$_x$ cumulated curve and by the spikes in NH$_3$ and N$_2$O curves, depicted in Figures 2.73 and 2.74 respectively. The simulation captured the cumulated mass and the position of the spikes of NH$_3$ and N$_2$O with satisfactory accuracy, achieving an absolute error lower than 0.1 g. The large spikes of NH$_3$ measured by the FTIR and not captured by the model should be neglected, since were detected during engine shut-off conditions, as also shown by the cumulated mass which does not increase in presence of the spikes since the exhaust mass flow is null.

81
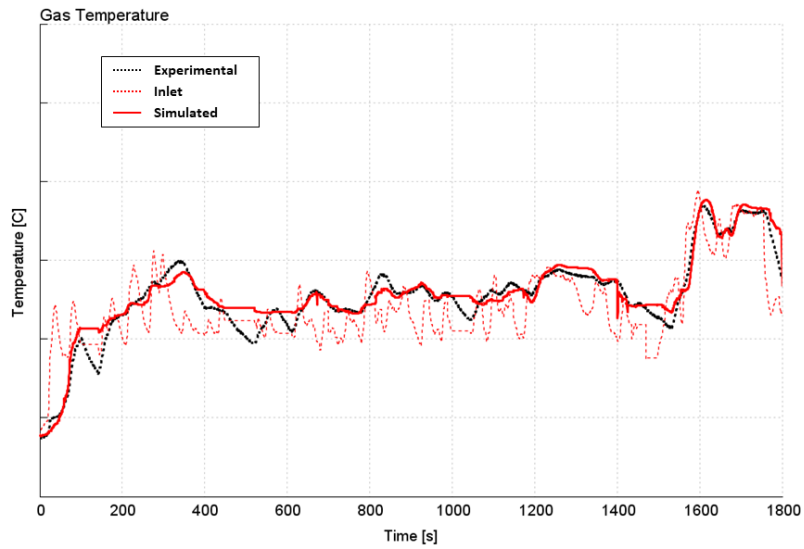
Figure 2.69: Engine-scale simulation results on the WLTC-A. Gas temperature. Simulation results (red solid line) compared with experimental data (black dashed line).
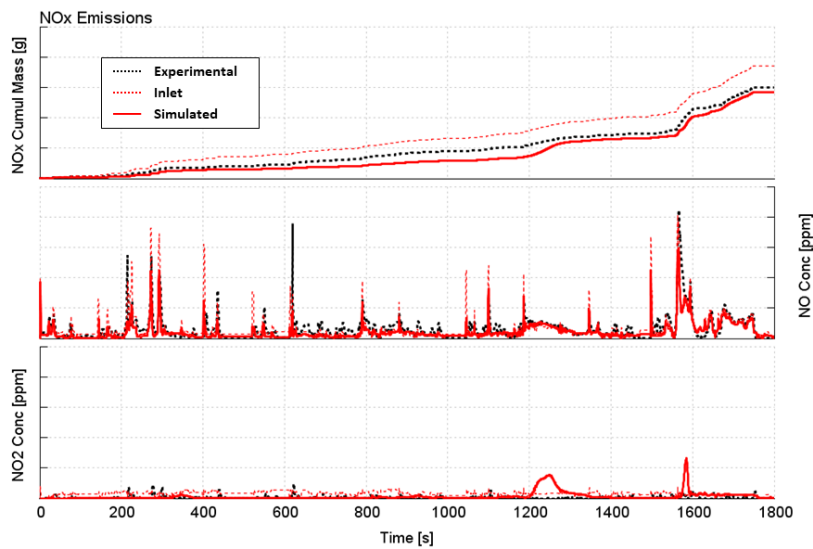
Figure 2.70: Engine-scale simulation results on the WLTC-A. NO$_x$ emissions. Simulation results (red solid line) compared with experimental data (black dashed line).
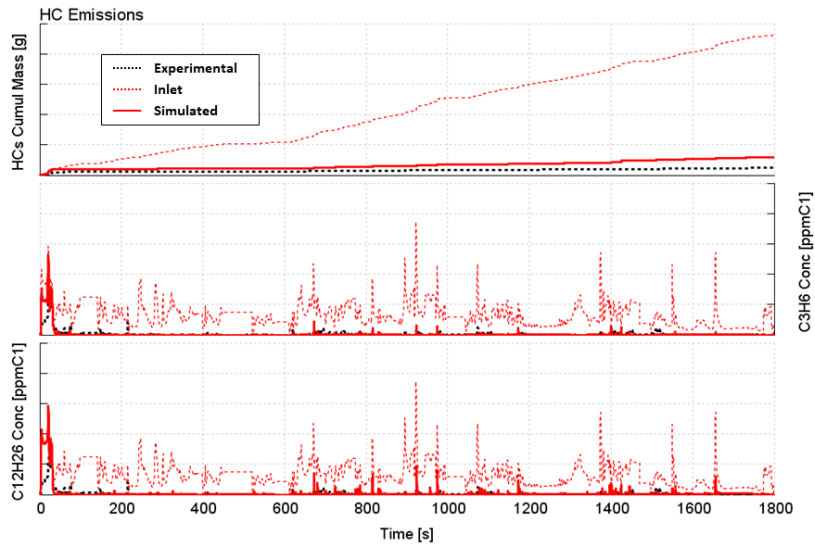
Figure 2.71: Engine-scale simulation results on the WLTC-A. HCs emissions. Simulation results (red solid line) compared with experimental data (black dashed line).
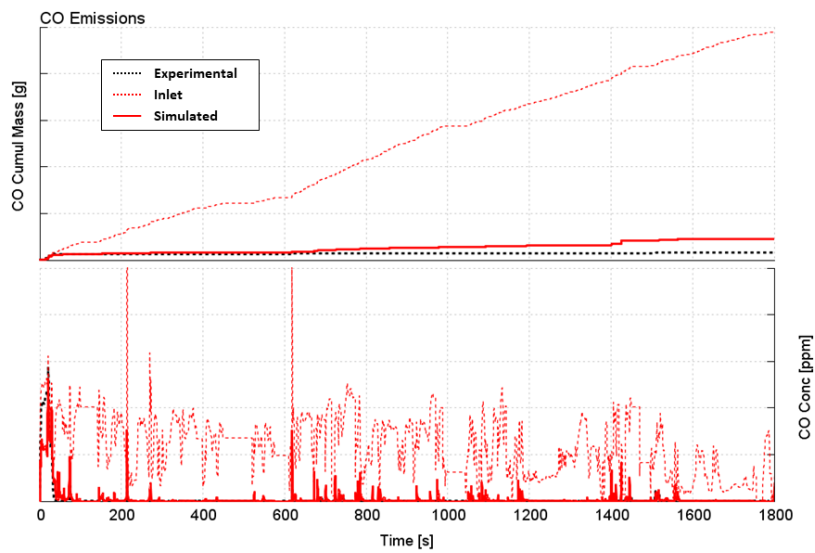
Figure 2.72: Engine-scale simulation results on the WLTC-A. CO emissions. Simulation results (red solid line) compared with experimental data (black dashed line).

83
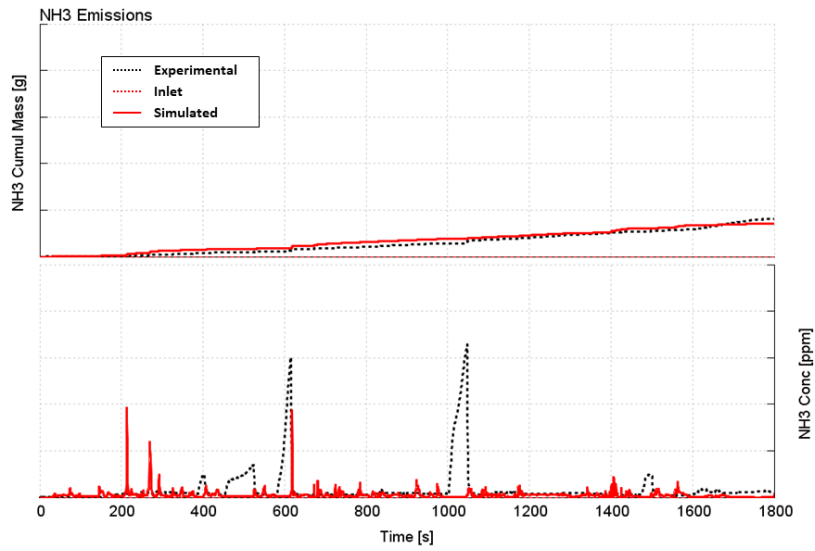
Figure 2.73: Engine-scale simulation results on the WLTC-A. NH$_3$ emissions. Simulation results (red solid line) compared with experimental data (black dashed line).
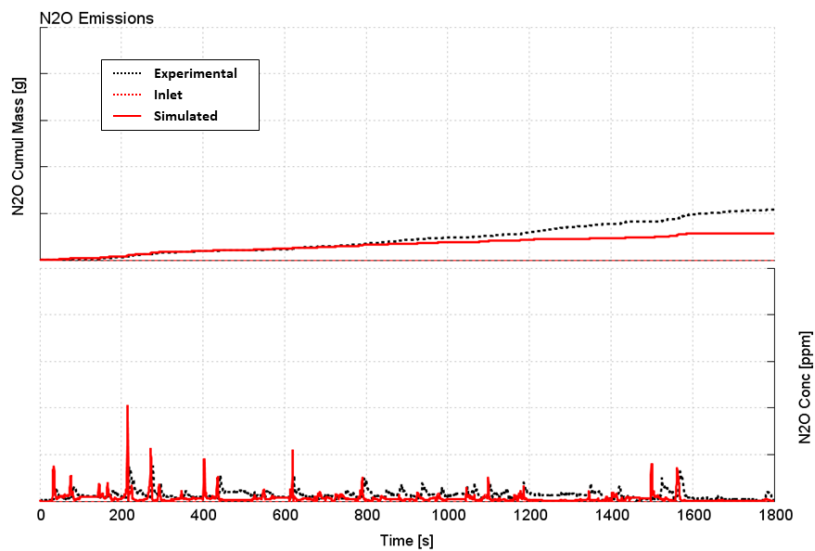
Figure 2.74: Engine-scale simulation results on the WLTC-A. N$_2$O emissions. Simulation results (red solid line) compared with experimental data (black dashed line).

2.4.2 WLTC-B Results

In this sections simulation results of the up-scaled model on the WLTC-B test cycle of Table 2.13 are reported and compared with experimental measurements.

A controlled DeNO$_x$ event was performed, by means of post-injections, during WLTC-B after 1711 s, as can be noticed by the high exhaust temperature rise, shown in Figure 2.75. The average error on temperature was contained within 15 degC in the simulation. Low NO$_x$ conversion was observed also in this case, as depicted in Figure 2.76, which remained below 20% despite the controlled DeNO$_x$ event which occurred in the last and highly-dynamic section of the cycle. The model predictions were in substantial agreement with the experimental results, with an overall error of 10% on the cumulated NO$_x$ mass. Also in this case the HCs conversion was underestimated in the first stage of the cycle, while the catalyst outlet HC spike consequent to the DeNO$_x$ event was not captured during the simulation, as shown in Figure 2.77. The overall HCs conversion achieved in the simulation was of 91% instead of the 87% measured at the test-bench. The conversion excess is also shown by the temperature increase in the last section of the cycle, as depicted in 2.75, which is higher in the simulation compared to the experiments. A similar trend was observed for CO, as shown in Figure 2.78, whose conversion was of 92.5% in the simulation against the 93.5% observed at the test-bench. Simulated NH$_3$ and N$_2$O emissions, depicted in Figures 2.79 and 2.80 respectively, were in good agreement with the experiments and a maximum error lower than 0.1 g was achieved. However, the model did not captured the short NH$_3$ and N$_2$O spikes observed after the controlled DeNO$_x$ event. This differences could be related to multiple concurring factors. For instance, as observed during the experimental campaign described in section 2.2.6, H$_2$ is mainly responsible for the production of ammonia from the reduction of the stored NO$_x$. Since the H$_2$ engine-out concentration was not available from the measurements, it was estimated as a function of CO and CO$_2$ measurements through correlations found in the literature [25], therefore the estimated concentration might be inaccurate especially in rich-transient operating conditions. Moreover, during the controlled DeNO$_x$ events the catalyst was exposed to high temperatures, exceeding the range under which the catalyst was characterized during the SGB test campaign and thus outside of the kinetic scheme calibration range. Finally, also in this case the large NH$_3$ spike measured in the experiments after 1000 s should be neglected since occurred in zero-mass-flow operating conditions which induced a false-positive reading of the measuring instrument.
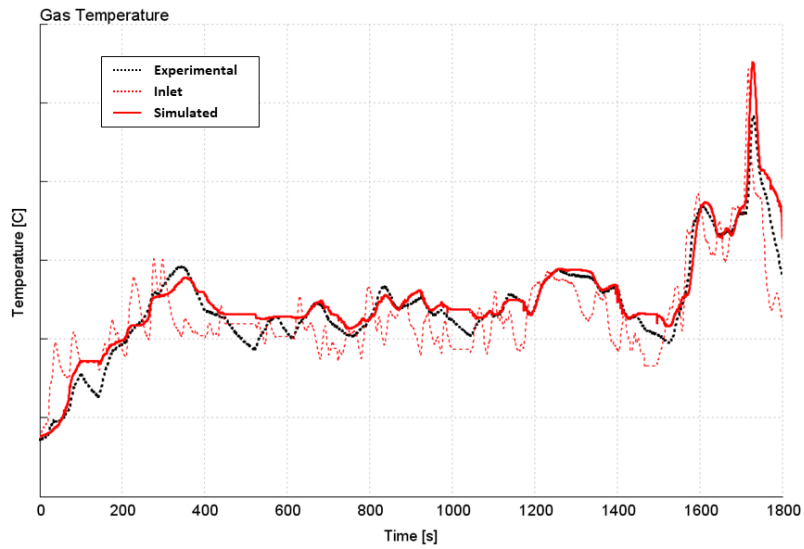
Figure 2.75: Engine-scale simulation results on the WLTC-B. Gas temperature. Simulation results (red solid line) compared with experimental data (black dashed line).
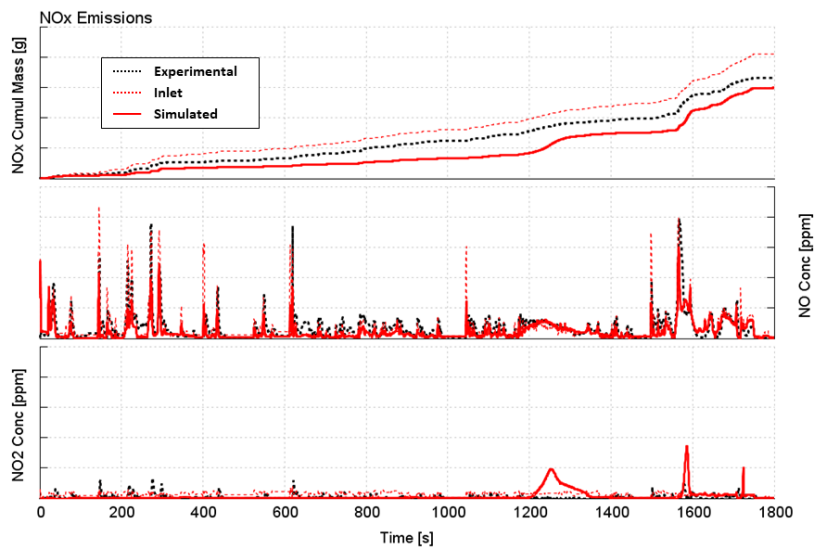
Figure 2.76: Engine-scale simulation results on the WLTC-B. NO$_x$ emissions. Simulation results (red solid line) compared with experimental data (black dashed line).
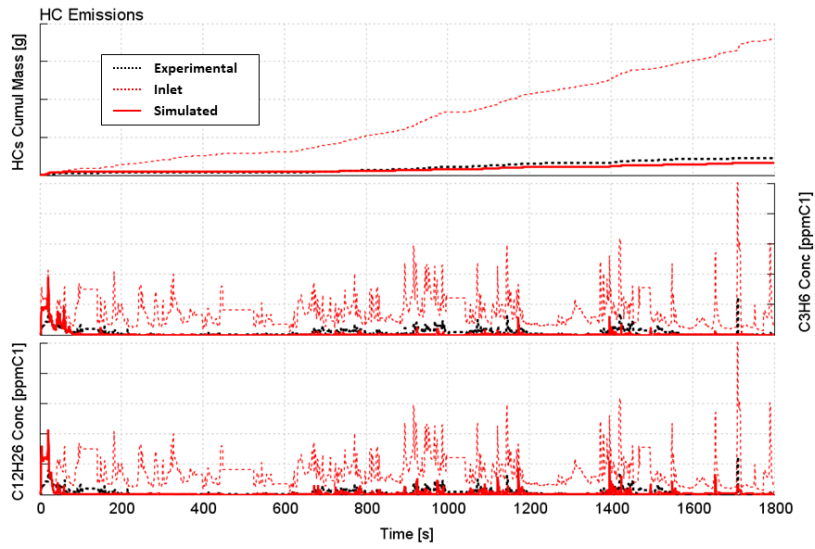
Figure 2.77: Engine-scale simulation results on the WLTC-B. HCs emissions. Simulation results (red solid line) compared with experimental data (black dashed line).
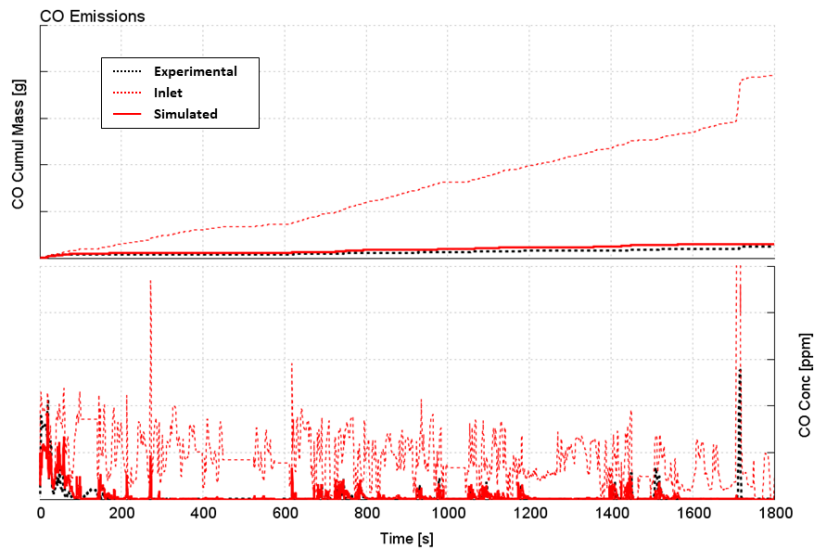
Figure 2.78: Engine-scale simulation results on the WLTC-B. CO emissions. Simulation results (red solid line) compared with experimental data (black dashed line).
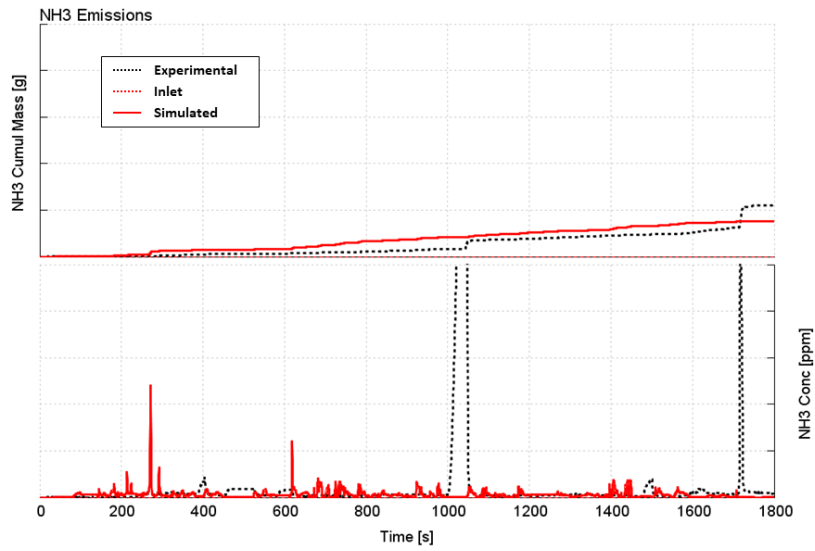
Figure 2.79: Engine-scale simulation results on the WLTC-B. NH$_3$ emissions. Simulation results (red solid line) compared with experimental data (black dashed line).
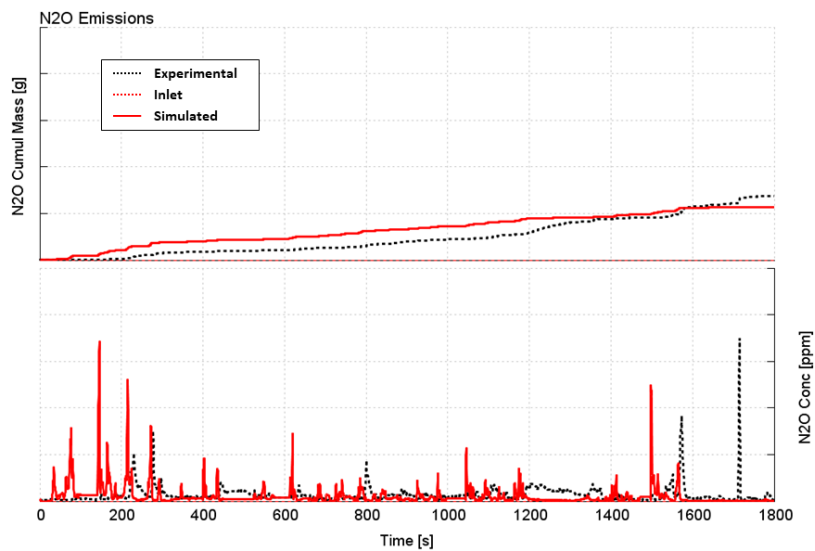
Figure 2.80: Engine-scale simulation results on the WLTC-B. N$_2$O emissions. Simulation results (red solid line) compared with experimental data (black dashed line).

2.4.3 RDE Results

In this sections simulation results of the LNT model over the RDE driving cycle of Table 2.13 are reported. This driving cycle, compared to the WLTC analyzed in the previous sections, is characterized by a more pronounced vehicle dynamics in terms of vehicle speed and acceleration. Moreover, two controlled $DeNO_x$ events were performed, at 1331 s and 2241 s respectively, to restore the LNT storage capacity. This produced higher exhaust flow rates as well as higher temperatures at the catalyst inlet thus determining critical conditions for its operations. In Figure 2.81 the experimental temperature trace is compared with simulation results. The model captured the system thermal dynamics with sufficient accuracy, achieving an average error on the gas temperature of approximately 12 degC. The high temperature and flow dynamics resulted in a poor NO_x conversion, which stopped at just 4%, as shown in Figure 2.82. The model overestimated such conversion of 10%, which still was considered as a satisfactory result. The conversion gap between the simulation and the experiments was observed in the last portion of the cycle, were the gas flow entering the reactor is characterized by high temperature and flow rate, outside of the range analyzed at the SGB. This issue could be addressed in the future by extending the component analysis range during the SGB experimental test campaign, to better identify the high temperature NO_x storage and conversion behaviour. In Figures 2.83 and 2.84 are depicted HCs and CO emissions, respectively. In both cases model predictions were in agreement with experimental results. The predicted HCs conversion was of 92.3% against the experimental value of 92.4% while the CO simulated conversion was of 96.7% instead of the experimental 96.3%. In particular is it possible to notice from Figure 2.83, where the cumulated and instantaneous HCs emissions are depicted, that two HCs spikes are detected, at the inlet, when the controlled $DeNO_x$ events are performed, namely at 1331 s and 2241 s. In this case, due to the high temperatures, only a small fraction of the injected HCs is measured downstream of the LNT and this result is also confirmed by the simulation. As far as CO is concerned, a large spike was detected at the LNT outlet only after the second $DeNO_x$ event, while in the simulation almost all the inlet CO was converted. The $DeNO_x$ could be observed also in the LNT outlet NH_3 traces, depicted in Figure 2.85, which show spikes in the location of the regeneration events. A number of different spikes were also detected in the first part of the cycle, mainly in correspondence of high load transients, while some of the larger spikes were again fake readings by the FTIR in engine-off conditions. The model captured some of the events and the error on the cumulated NH_3 emissions was lower than 0.1 g, while the large spike after the second $DeNO_x$ was not observed in the simulation. Similarly, N_2O emissions were captured accurately in the simulation, apart from the spikes located before the first $DeNO_x$ event, resulting in an error on the total mass lower than 0.1 g.
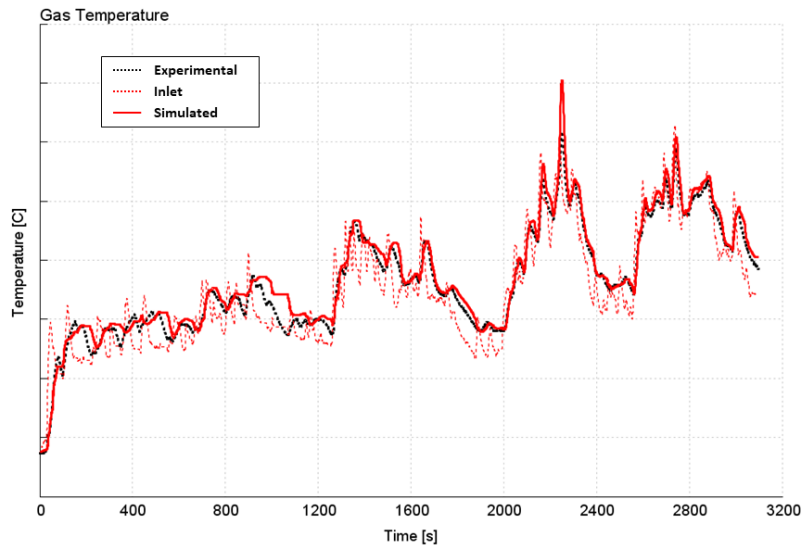
Figure 2.81: Engine-scale simulation results on the RDE. Gas temperature. Simulation results (red solid line) compared with experimental data (black dashed line).
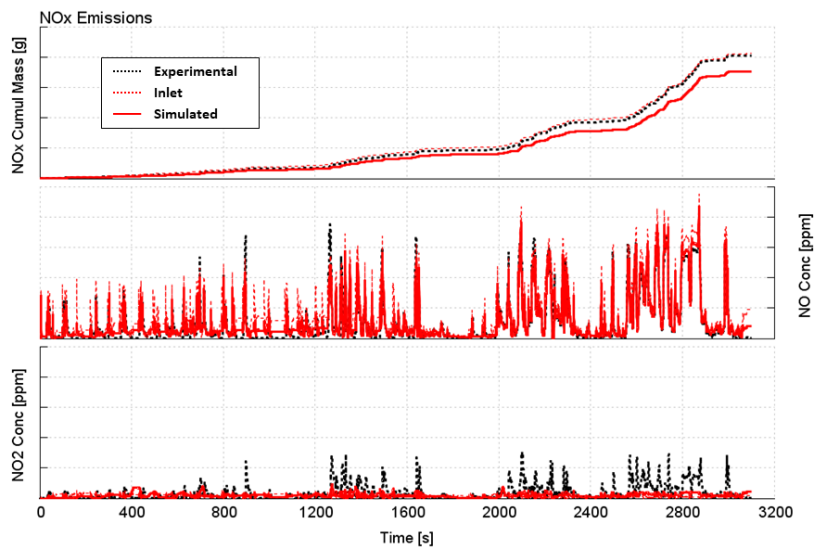
Figure 2.82: Engine-scale simulation results on the RDE. NO$_x$ emissions. Simulation results (red solid line) compared with experimental data (black dashed line).
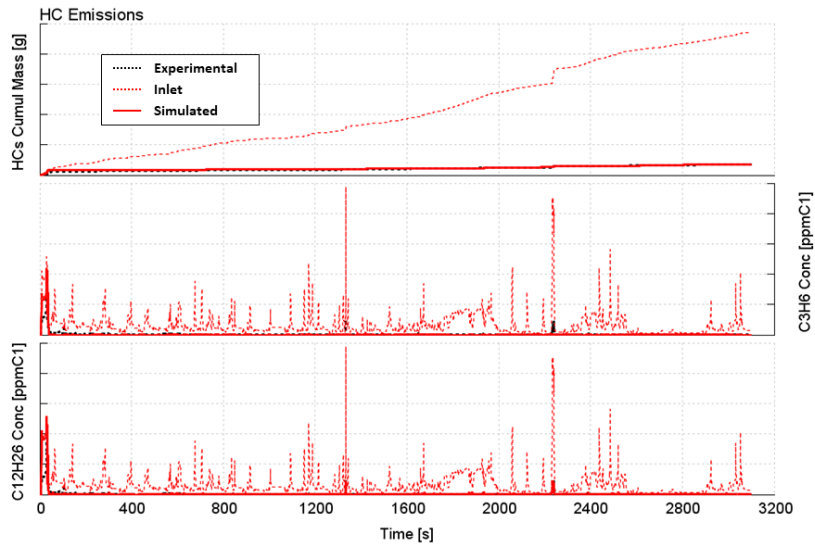
Figure 2.83: Engine-scale simulation results on the RDE. HCs emissions. Simulation results (red solid line) compared with experimental data (black dashed line).
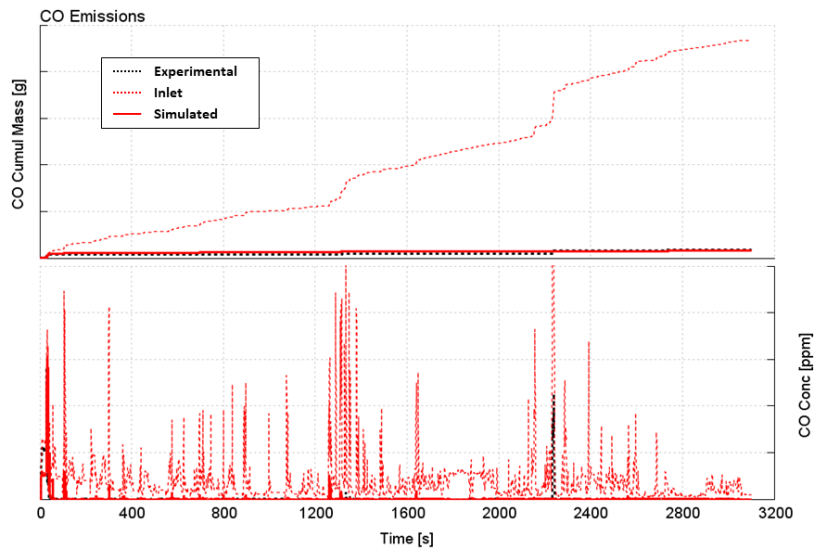
Figure 2.84: Engine-scale simulation results on the RDE. CO emissions. Simulation results (red solid line) compared with experimental data (black dashed line).

91
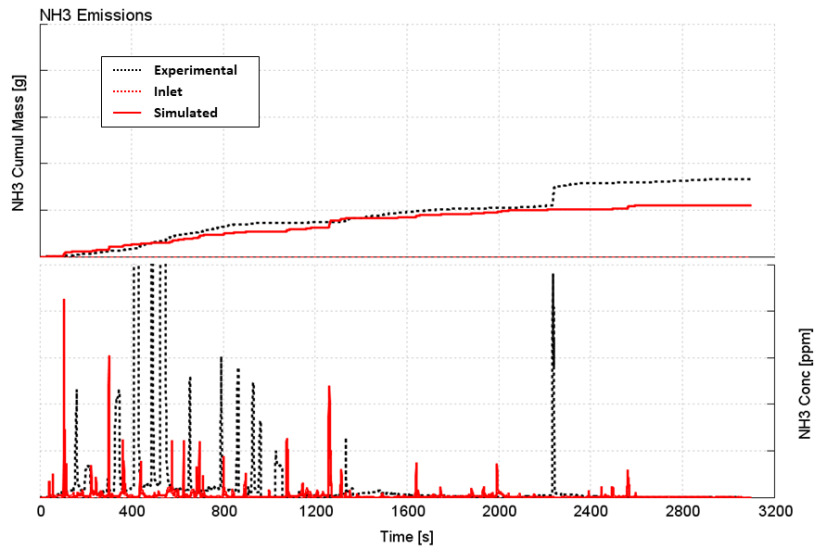
Figure 2.85: Engine-scale simulation results on the RDE. NH$_3$ emissions. Simulation results (red solid line) compared with experimental data (black dashed line).
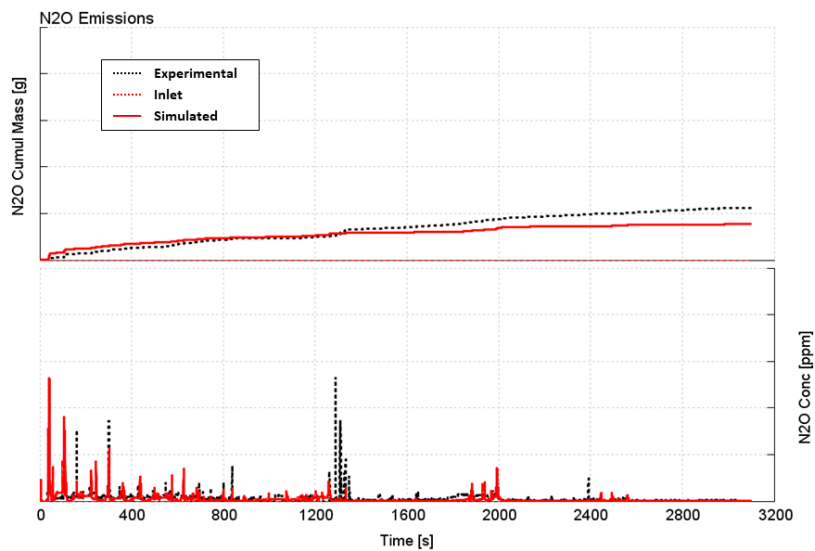
Figure 2.86: Engine-scale simulation results on the RDE. N$_2$O emissions. Simulation results (red solid line) compared with experimental data (black dashed line).

2.4.4 Engine-Scale Model Results Summary

Simulation results are summarized in Table 2.14.

Table 2.14: Summary of engine-scale model simulation results

	WLTC-A	WLTC-B	RDE
Average NO$_x$ Conversion			
Exp	19%	19.5%	4%
Sim	23%	27%	14%
Average HCs Conversion			
Exp	95%	87%	92%
Sim	87%	91%	92%
Average CO Conversion			
Exp	97%	93.5%	96%
Sim	91%	92.5%	97%
Max error on cumulated NH$_3$ < 0.1 g			
Max error on cumulated N$_2$O < 0.1 g			

2.5 Conclusions

In the present work, a 1D-CFD simulation model of a Lean NOx Trap (LNT) for a light-duty compression ignition engine was developed in a commercially available code, GT-SUITE. A comprehensive Synthetic Gas Bench (SGB) test campaign was conducted to fully characterize catalyst's operations such as Light-off of the oxidation reactions, the Oxygen Storage Capacity (OSC), NO$_x$ Storage and Reduction (NSR). The experiments were performed on small lab scale samples extracted from the engine-scale monolith and the test protocol was specifically designed to characterize a large number of operating conditions in terms of Gas Hourly Space

Velocity (GHSV), gas temperature and gas mixture composition, including two different unburned hydrocarbons species, namely propylene and dodecane, and different reducing agents, such as H$_2$, CO and propylene. The model of the laboratory-scale LNT sample was developed by carrying-over a previously developed kinetic scheme, which included 3 different Barium sites for NO$_x$ storage and reduction, and re-calibrated based on the SGB test results. The set of optimum calibration parameters, which included the site density of PGM, Ceria and Barium, pre-exponent multipliers and activation temperatures of each reaction was found in order to minimize the error between simulated and experimental concentrations of the reaction products downstream of the catalyst. Finally, the engine-scale model was built by updating the geometry and the heat-transfer boundary conditions to reproduce the full-size component behaviour, while the kinetic scheme was inherited from the laboratory-scale model. To validate the model, driving cycle data obtain at the test bench were used, including two different WLTC and one RDE cycles. Measured engine-out emissions, exhaust mass flow rate and temperature were used as boundary conditions for the model and simulation results in terms of LNT outlet NO$_x$, HCs, CO, N$_2$O and NH$_3$ emissions were compared with experimental measurements. Despite the theoretical limitations that can affect the direct application of a reactor-scale based kinetics to a full-size component, a satisfactory agreement between experimental data and simulation results was achieved. The model successfully reproduced the principal LNT operations, even in highly transient and load-severe operating conditions, confirming the robustness of the methodology.

Chapter 3

Experimental and Numerical Characterization of State-of-the-art Diesel After-Treatment Systems

Parte del lavoro descritto in questo capitolo è stato precedentemente pubblicato in:

Part of the work described in this chapter was previously published in:

- Sapio, F., Millo, F., Fino, D., Monteverde, A. et al., *"Experimental and Numerical Analysis of Latest Generation Diesel Aftertreatment Systems",* SAE Technical Paper 2019-24-0142, 2019, doi: 10.4271/2019-24-0142.

3.1 Introduction

The engine after-treatment system has been continuously evolved to comply with increasingly tight emissions standards. Moreover, the rapid growth of environmental concerns, increased further by the recent emissions scandals, has forced the institutions to introduce more severe type approval procedures for passenger cars, representative of the real-world vehicle usage. Particularly, in Europe the Commission introduced in 2014 the Euro 6 emissions standards, which establish more stringent limits on pollutant emissions and newly developed test procedures, such as the Worldwide harmonized Light vehicles Test Procedure (WLTP) and the Real Driving Emissions (RDE) test cycle. In this framework, the after-treatment system has to meet several requirements, such as:

- Cold-start emissions abatement

- High load emissions abatement

- Rapid catalysts light-off

- Compact packaging layout

Cold start HC and NOx emissions abatement could be achieved with low temperature storage catalysts, such as zeolite-based DOCs [26] or barium-containing LNTs [16]. To eliminate particulate matter from the exhaust gases, DPFs are widely used, placed just downstream the oxidation catalyst to facilitate the filter's regeneration. Ammonia-SCR systems are used to abate NO_x emissions by means of the ammonia contained in an aqueous solution of water and urea, injected upstream the catalyst. Due to the limited space available in automotive exhaust systems, low-pressure dosing systems without air-assisted atomizer are used. In such systems, water evaporates due to the high exhaust gas temperatures, leaving a molten-solid urea solution, which finally produces ammonia by urea thermolysis and hydrolysis of the formed isocyanic acid [27]. To accelerate the aforementioned process and to ensure the required ammonia flow and uniformity at the SCR catalyst inlet, a dedicated mixing devices is often used to break-up the liquid spray into tiny droplets. However, with such architecture the formation of a considerable amount of liquid film could be produced due to the liquid spray impingement on the exhaust pipes, especially during low temperature operating conditions [28]. Afterwards, the urea film deposited on the exhaust pipes might undergo several undesirable secondary reactions, leading to obstructing solid deposits thus introducing serious reliability issues [29].

Finally, placing the catalysts in closed-coupled configuration near the engine could drastically reduce the whole system warm-up time, while ensuring a compact packaging in the vehicle. In this framework, different after-treatment solutions were proposed by the automotive industry to achieve the emissions standard. Focusing on lean-burn compression ignition engines, a common Euro 6 compliant after-treatment architecture consists of a DOC followed by an SCRF and an additional downstream SCR catalysts, as in Volkswagen and Daimler 2.0 L Diesel engines [30, 31]. The effectiveness of this layout was further investigated by Bosch, whose system was capable to deliver less than 80 mg/km of NO_x under real-world representative driving conditions and severe low temperature [32]. In Landsberg et al [33], NO_x emissions below 50 mg/km were achieved on a test-vehicle, equipped with an LNT, SCR on filter and an ammonia slip catalyst after-treatment, under demanding operating conditions representative of urban driving.

To address the increasing complexity in engineering after-treatment systems and to fully exploit their emissions abatement potential, comprehensive methodologies which involve both experimental and numerical analyses are required [28, 34, 35].

In this chapter, two state-of-the-art after-treatment systems for compression ignition passenger cars are extensively analyzed. These systems integrate, in closed-coupled configuration, a Diesel Oxidation Catalyst (DOC) followed by a Selective Catalytic Reduction (SCR) catalyst coated on a Diesel Particulate Filter (DPF), known as SCR on Filter (SCRoF or SCRF). The Urea Water Solution (UWS) dosing and mixing section is placed in between the two catalysts. First, both the ATS were experimentally characterized to determine the physical-chemical properties of the catalysts, the UWS spray characteristics (i.e. liquid penetration, droplets size) and to evaluate the NO_x conversion efficiency under steady state flow conditions, representative of type-approval operating conditions. The experiments highlighted significant differences in terms of NO_x conversion efficiency between the two ATS, especially at low temperature operation. In order to highlight the root causes of these differences, numerical analyses were then conducted by means of a commercial 3D CFD code. A systematic methodology was developed to build a robust and reliable simulation setup, for both the ATS, and validated over the experimental data. The resulting simulation model was then used as a virtual test bench to understand the UWS spray evolution, breakup and mixing, the amount and location of liquid film and to evaluate the SCRoF inlet conditions in terms of species composition and flow uniformity indexes. The numerical analysis demonstrates that the different conversion of NO_x at low temperature is mainly due to the different mixing systems design, which could enhance the production of ammonia from the UWS when the temperature conditions are far from the optimum, providing useful insights for future design and optimization of similar ATS.

3.2 Test Case

The two after-treatment systems analyzed in this chapter, which will be referenced to as System-A and System-B, were designed to fulfill the Euro 6 emissions standards mounted on two different 2.0 L compression ignition engines for light-duty applications. The same dosing module was used for dosing the urea-water mixture.

In Table 3.1 are summarized the main geometric features of the analyzed after-treatment systems. It can be noted that in System-B catalysts diameters are larger than in System-A, thus a lower pressure drop along the whole operating range is expected for System-B.

Table 3.1: Catalysts dimensions as Diameter [mm] x Length [mm]

	DOC/LNT	**SCRF**	**SCR/ASC**
System-A	116 x 120	167 x 136	-
System-B	156 x 100	177 x 112	177 x 150

3.2.1 Urea Water Solution Dosing Module

The injector, represented in Figure 3.1a, is used to provide the required amount of urea solution to the after-treatment and is placed in a dedicated seat, on the exhaust external canning. To avoid overheating, due to the high exhaust temperatures reached during the system operations and to the engine proximity, the injector is water-cooled by means of a dedicated coolant jacket, coupled with the engine cooling circuit. A two-holes orifice disc, depicted in Figure 3.1b is used to split the urea-solution in two spray plumes.

(a)   (b)
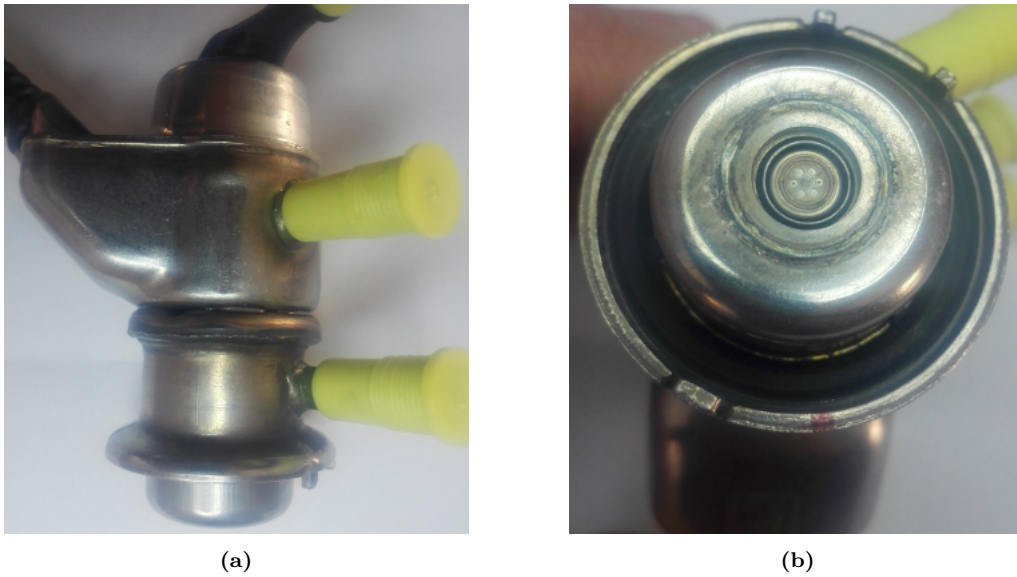
Figure 3.1: Urea-water solution dosing module (a) and orifice disc (b)

3.2.2 System-A

As represented in Figure 3.2, System-A consist of a closed-coupled oxidation catalyst and a SCR-coated particulate filter, packed in a typical "telephone handset" shape, while the UWS dosing and mixing system is located in between the two catalysts. To prevent the slip of the excess ammonia, an additional SCR catalyst is located under the vehicle body, although this analysis will be focused on the closed-coupled section. System-A features a dual-stage baffles mixer, shown in Figure 3.3, located in the u-bend section after the oxidation catalyst. The first row of fins is used to break-up the spray into smaller droplets, while the second row is used to generate turbulence which enhances mixing and mixture preparation before the SCRoF.

Figure 3.2: System-A numerical representation

(a)	**(b)**

Figure 3.3: System-A flow mixing system (a) and numerical representation (b)

3.2.3 System-B

Similarly to System-A, System-B consists of a closed-coupled oxidation catalyst, a SCR-coated particulate filter and a SCR brick, as depicted in Figure 3.4. The urea solution metering and mixing section is located after the oxidation catalyst. In this case, the spray break-up is induced by a mixer consisting of a series of evaporator plates, depicted in Figure 3.5, arranged in the flow direction, whose holes facilitates the droplets penetration and flow circulation. The droplet mixing with air takes

place in the following tube, which conveys the flow towards the SCRoF.
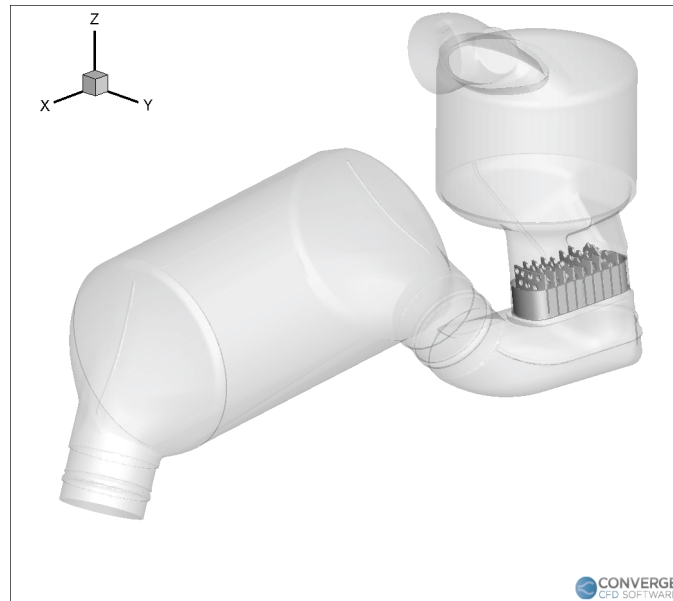
Figure 3.4: System-B numerical representation.
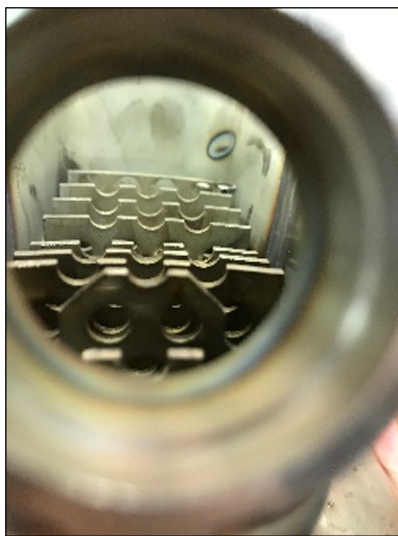
| (a) | (b) |

Figure 3.5: System-B flow mixing system (a) and numerical representation (b)

3.3 Experimental Analysis

An extensive experimental campaign was conducted to fully characterize the two after-treatment architectures. The physical-chemical analysis was conducted at the Applied Science and Technology Department (DISAT) of Politecnico di Torino to investigate the composition and the morphology of each catalyst substrate. The spray characteristics, such as droplets sizing, distribution and penetration, as well as the whole systems performance in engine-like operating conditions were evaluated at STSe laboratory in Perugia. The experimental setup, the experimental procedures and the results of the experimental campaign are described in the following paragraphs.

3.3.1 Physical-Chemical Characterization

The substrate geometry and composition has an influence on a quantity of aspects which determine the catalyst performance, such as conversion efficiency, light-off, pressure losses and durability [36]. For these reasons an extensive experimental campaign was carried out on small catalyst samples, which were fully characterized in terms of morphology and chemical composition. The morphology of substrate samples was obtained by means of a Field-Emission Scanning Electron Microscopy (FESEM) JEOL-JSM-6700F. The Energy Dispersive X-ray Spectrometry Detector EDX OXFORD INCA was used to characterize the elemental composition of each catalyst substrate.

The cross sectional views of the two oxidation catalysts is depicted in Figure 3.6. The oxidation catalyst used in System-A (Figure 3.6a) presents a metallic substrate, specifically a Fe-Cr alloy, with sinusoidal channels, which ensures faster light-off, thermal durability and a reduced pressure drop [37]. The oxidation catalyst used in System-B (Figure 3.6b) presents a ceramic cordierite substrate with symmetrical honeycomb channels. The EDX elemental analysis on the DOC samples of System-A and System-B, whose spectra are depicted in Figure 3.7a and 3.7b respectively, revealed, aside with the presence of Platinum and Palladium, a relevant percentage of Barium in the washcoat, estimated around 4% in weight for both catalysts, which suggests the capability of low-temperature NO_x storage. In System-A a higher Platinum Group Metal (PGM) content was found while System-B showed a higher Pt/Pd ratio, as reported in Table 3.2, which should enhance NO_2 selectivity [38, 39].

SCRoF samples FESEM results revealed an asymmetrical honeycomb structure in both System-A and -B, as shown in Figure 3.8a and 3.8b respectively. This

Table 3.2: Elemental composition (% wt) of the DOC for System-A and System-B

Element:	Pt	Pd	Ba	Pt/Pd
Unit:		[% wt]		
System-A	1.8	2.9	4	0.62
System-B	2.85	0.78	3.47	3.65

(a)   (b)
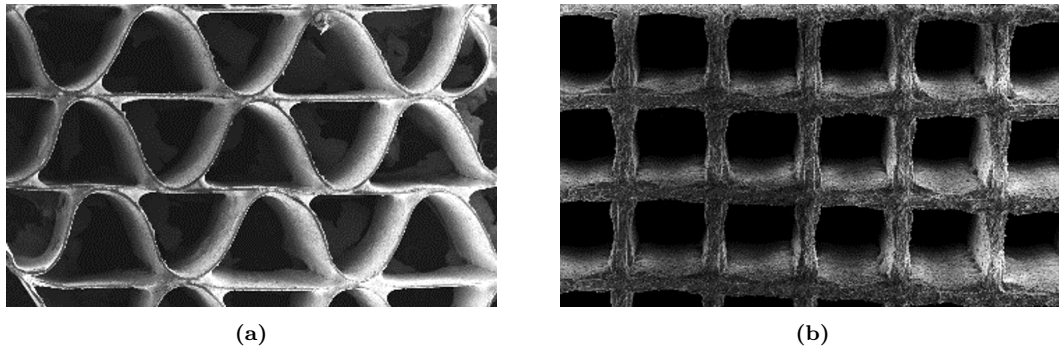
Figure 3.6: DOC cross sectional FESEM images of System-A (a) and System-B (b) samples

structure is used to reduce the pressure drop, especially in loaded conditions, and to increase the ash storage capacity of the monolith [40]. The elemental analysis, whose results are summarized in Table 3.3, revealed a Silicon Carbide (SiC) support for both the SCRoFs, with a combination of Cu and Fe Zeolites on the surface. This architecture allows to increase the catalyst activity temperature window, increasing the NOx conversion efficiency [41]. It was not possible to determine the zeolites Si/Al ratio due to the interference of Si enclosed in the SiC substrate, as can be observed in 3.9 where the EDX spectra for the two SCRoF are depicted.

The main morphological properties of the analyzed catalysts are summarized in Table 3.4 and Table 3.5, for System-A and -B respectively.
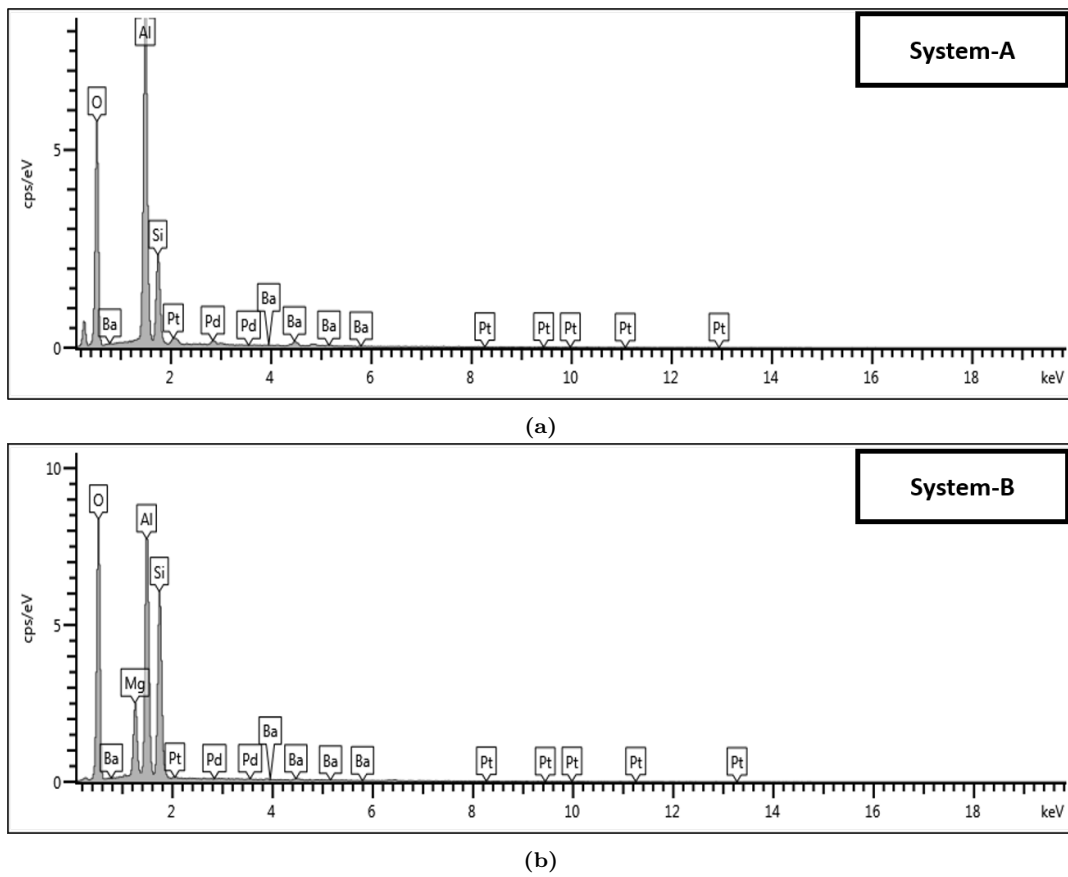
Figure 3.7: Results of the EDX elemental analysis on System-A (a) and System-B (b) DOC samples
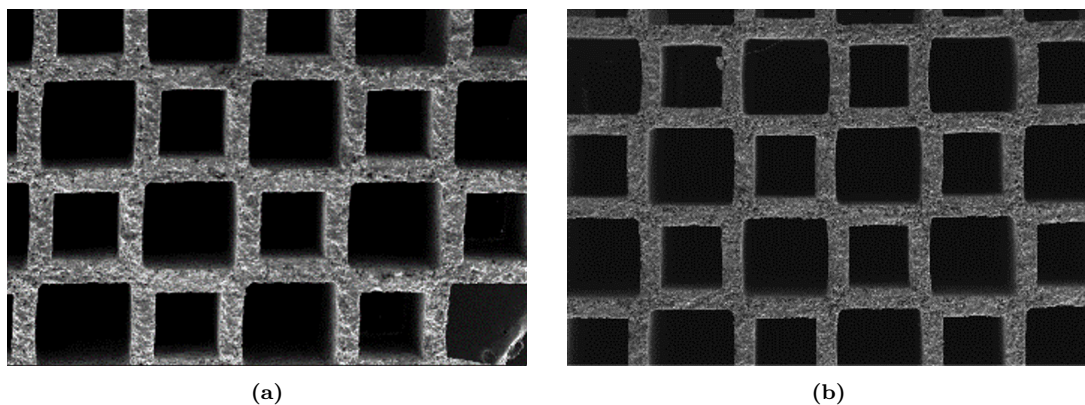
Figure 3.8: SCRF cross sectional FESEM images of System-A (a) and System-B (b) samples

Table 3.3: Elemental composition (% wt) of the SCRoF for System-A and System-B

	System-A SCRoF	System-B SCRoF
O	49.6	49.8
Al	4.4	3.2
Si	43.6	46.1
Cu	1.3	1.2
Fe	0.3	0.9
Zr	0.7	-
Cu/Fe	4.6	1.3

Table 3.4: DOC and SCRF morphological properties for System-A

System-A	*DOC*	*SCRoF*
Material	Metallic (Fe-Cr-Al)	SiC
Configuration	Sinusoidal	Honeycomb-Symmetric
Cell density [cpsi]	200	300
Wall Thickness [μm]	40	350
Channel size [μm]	1500 x 1390	1300 (inlet) / 940 (outlet)

(a)

(b)
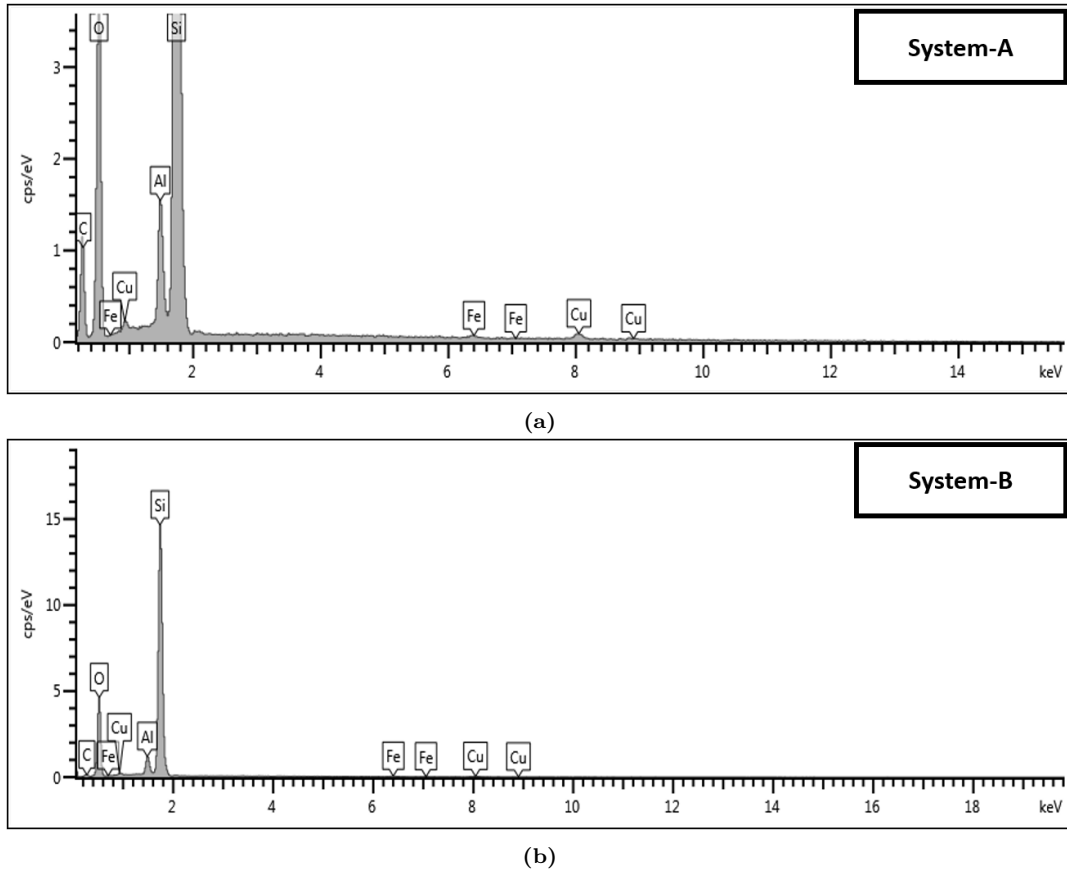
Figure 3.9: Results of the EDX elemental analysis on System-A (a) and System-B (b) SCRF samples

Table 3.5: DOC and SCRF morphological properties for System-B

System-B	DOC	SCRoF
Material	Cordierite	SiC
Configuration	Honeycomb-Symmetric	Honeycomb-Asymmetric
Cell density [cpsi]	200	300
Wall Thickness [μm]	100	330
Channel size [μm]	870	1300 (inlet) / 970 (outlet)

107

3.3.2 Spray Analysis

Since the two analyzed after-treatment systems were equipped with the same urea-solution injector, an extensive spray analysis was carried out to fully characterize the spray evolution in terms of spray angle, cone angle, liquid penetration and droplets sizing, in a wide range of temperatures.

Experimental Setup

To this aim, an experimental setup based on the pulsed laser back-light principle was used, depicted in Figure 3.10, were the injector was located between the CCD camera and the back-light illuminator.
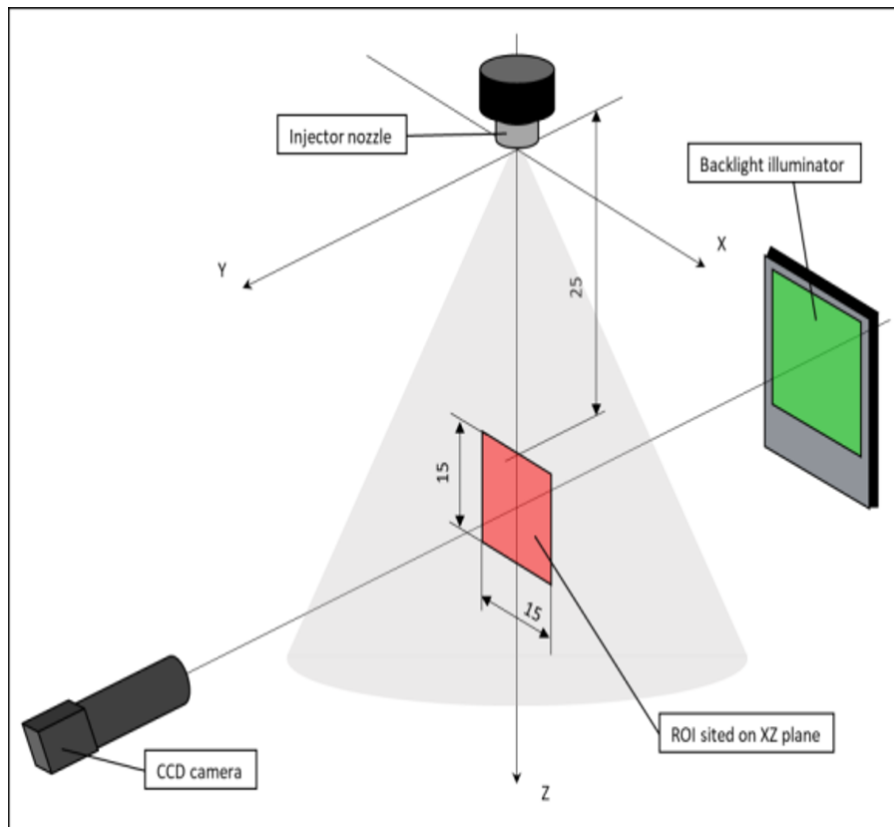
Figure 3.10: Schematic representation of laser back-light imaging setup, used in the drop sizing test campaign (dimensions in mm)

The experimental apparatus, depicted in Figure 3.11, consisted of an injector installed on a vertical frame fitted on the test vessel, which can operate up to 400 degC in ambient pressure conditions. The air flow, heated by means of a 6

kW cartridge heater, entered from the bottom of the systems at approximately 10 nl/min and was used to compensate the vessel thermal dissipation and to purge the system from the residual liquid. A pulsed Nd-YAG Laser was used as the light source, characterized by a wavelength of 532 nm and an energy of 50 mJ/pulse. The laser beam was conveyed to a flat back-light illuminator, through an optic fiber cable, in order to obtain a uniform lighting from the background, and operated with a pulse duration of 10 ns to avoid blurred spray images. The images were acquired by means of a JAI RM-4200 CCD camera (resolution of 2048x2048, 12 bit, exposure time of 10 μs) which was synchronized with the light source and with the injector actuation.

A 90x45 mm Region Of Interest (ROI) over the XZ plane was used to analyze the global spray evolution in terms of liquid penetration, spray angle etc. The ROI was then restricted to a 15x15 mm square placed 30 mm downstream the nozzle exit to perform the spray sizing analysis, in order to obtain a 7.3 μm/pixel image resolution (as schematized in Figure 3.10).
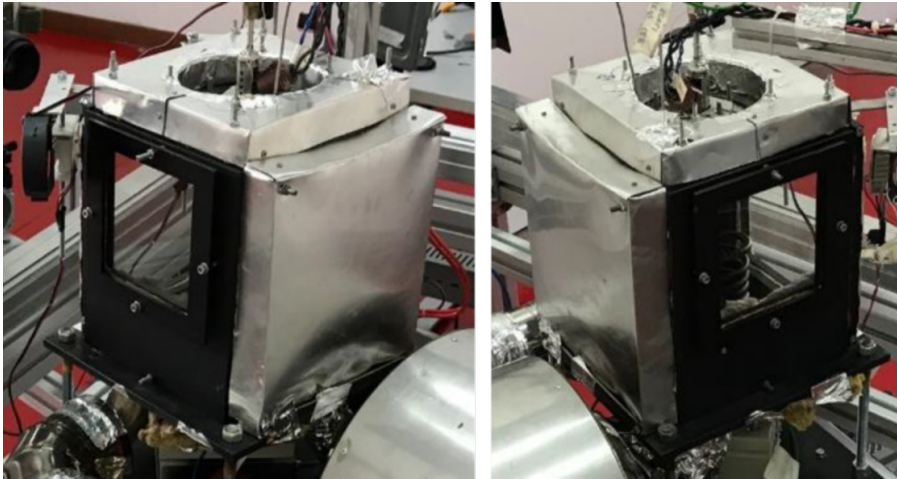
Figure 3.11: Test vessel used for the spray experimental campaign

Due to the limited maximum operating frequency (10 Hz) of both the Nd-Yag Laser and the CCD camera, the spray evolution analysis and the drop sizing investigation were carried out according to an ensemble average approach. A single frame was acquired, at a given time after the Energizing Time (ET) start, during each injection event. During the global spray analysis, in order to properly capture the shot-to-shot spray shape dispersion, 30 images were acquired in each experiment, while 400 images were acquired in each test during the drop sizing investigation to obtain a statistically robust distribution of diameters.

The signals acquired during the spray evolution and drop sizing analyses were

processed by means of a specifically developed algorithm, in the LabVIEW environment. For the spray evolution image analysis a modified version of the Triangle's Method [42] was used for the spray boundary recognition. Since low-pressure sprays are characterized by non-spherical droplets, the imaging-based spray sizing procedure was specifically tuned, as described in [43].

Spray Evolution and Sizing

The spray evolution was analyzed, by means of the aforementioned setup, in a wide range of vessel temperatures, as reported in Table 3.6.

Table 3.6: Spray analysis test conditions

Injector	Bosch 0 444 025 048-01
Nozzle	2 holes x 0.136 mm
Injection Pressure	5 bar,g
Energizing Time (ET)	103 ms
Test Vessel Pressure	100 kPa
Test Vessel Temperature	100 °C, 200 °C, 300 °C, 400°C

In Figures 3.12 and 3.13 are depicted snapshots of the spray acquired by the CCD camera in two different tests, at a vessel Temperature of 400 degC and 100 degC respectively, 5000 ms after the start of the ET, when the spray could be considered completely developed. In both cases the spray shown very thin flow structures characterized by large droplets, stripped from an almost continuous liquid stream. The spray structure, characterized by large droplets uniform in size, suggests an atomization process in the so-called Rayleigh regime, in which the liquid breakup is produced due to the effects of liquid inertia and surface tension. Due to this peculiar structure, the spray jet showed a similar behaviour even in largely different vessel temperature conditions, as observed form Figures 3.12 and 3.13.

In Figure 3.14, test result of the global spray evolution are depicted. A linear trend in the liquid penetration was observed for the entire spray development, with a limited influence of the vessel temperature. The jet was characterized by an initial development phase up to 3000 μs, after which a stable structure was

(a)

(b)
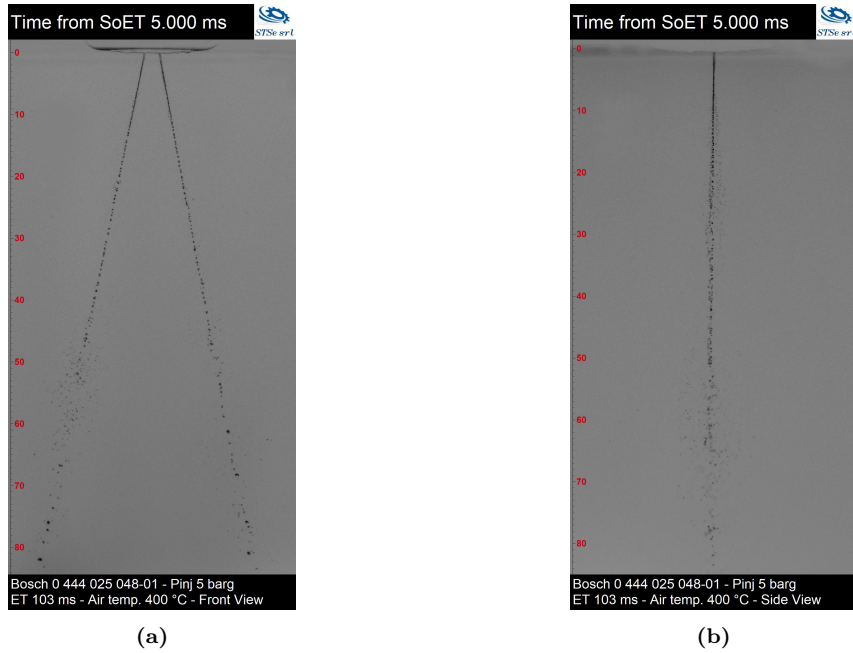
Figure 3.12: UWS spray at 5000 ms from the start of ET, Pinj 5bar,g, Pvessel 100 kPa, Tvessel of 400 degC. Front view (a) and side view (b)

(a)

(b)
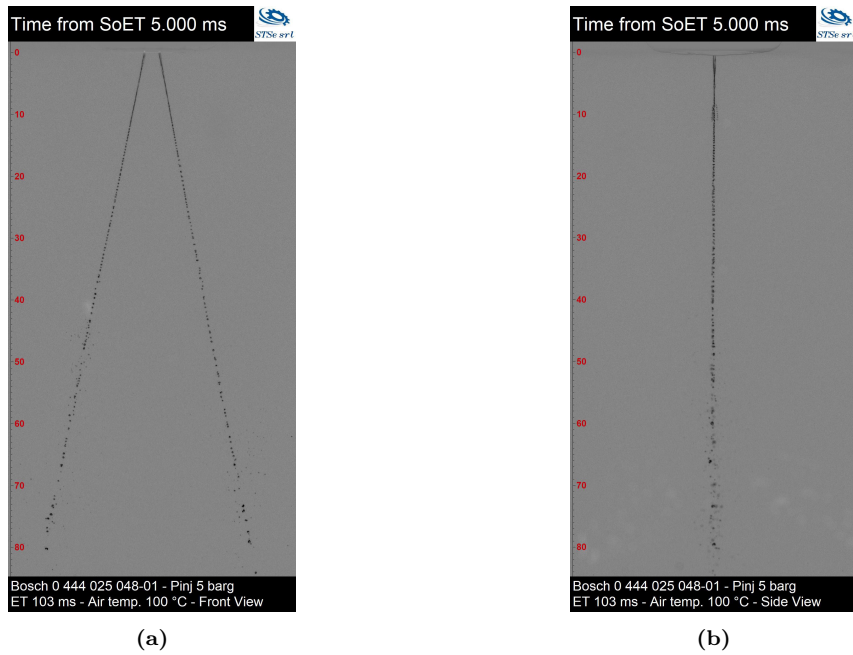
Figure 3.13: UWS spray at 5000 ms from the start of ET, Pinj 5bar,g, Pvessel 100 kPa, Tvessel of 100 degC. Front view (a) and side view (b)

obtained characterized by an almost uniform velocity until the end of the test. The

111

penetration curve reached its maximum at 80 mm after 4500 μs from the ET start, when the liquid approached the border of the field visible from the camera.
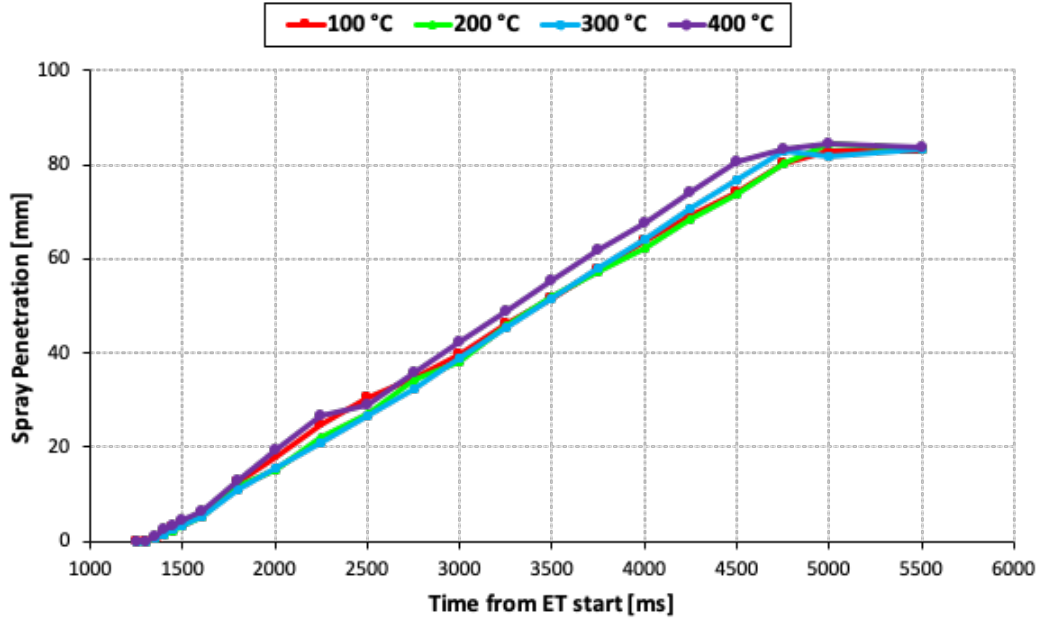
Figure 3.14: UWS spray tip penetration at different Tvessel. Pinj 5bar,g, Pvessel 100 kPa

A similar trend was observed in terms of global spray angle, which is defined as the angle between the two jets, depicted in Figure 3.15. Also in this test, after the initial spray development phase in which the temperature effect could be observed, a uniform trend was reached and a global angle of about 22 deg was measured between the jets.

To perform the droplet sizing analysis, a squared ROI of 15 mm was defined, placed at 30 mm from the nozzle tip and centred on one of the two jets, as depicted in Figure 3.16a. The analysis was carried out according to the procedure described in [43]. To obtain a minimum droplets count of 10000 for each acquired timing, 400 images per timing were digitally acquired and processed.

The results of the droplet sizing analysis, in terms of Probability Density Function (PDF) and volume fraction distribution at the vessel temperature of 400 degC, the highest in the tested range, is depicted in Figure 3.16b. An almost constant distribution was observed in each time-frame analyzed, thus confirming the regular development of the spray. The obtained PDF was characterized by two distinct peaks, the first one due to small droplets with diameters around 50 μm while the other was produced by larger droplets, in the range of diameters between 150 μm and 200 μm. The volume fraction distribution showed a single, large peak in the
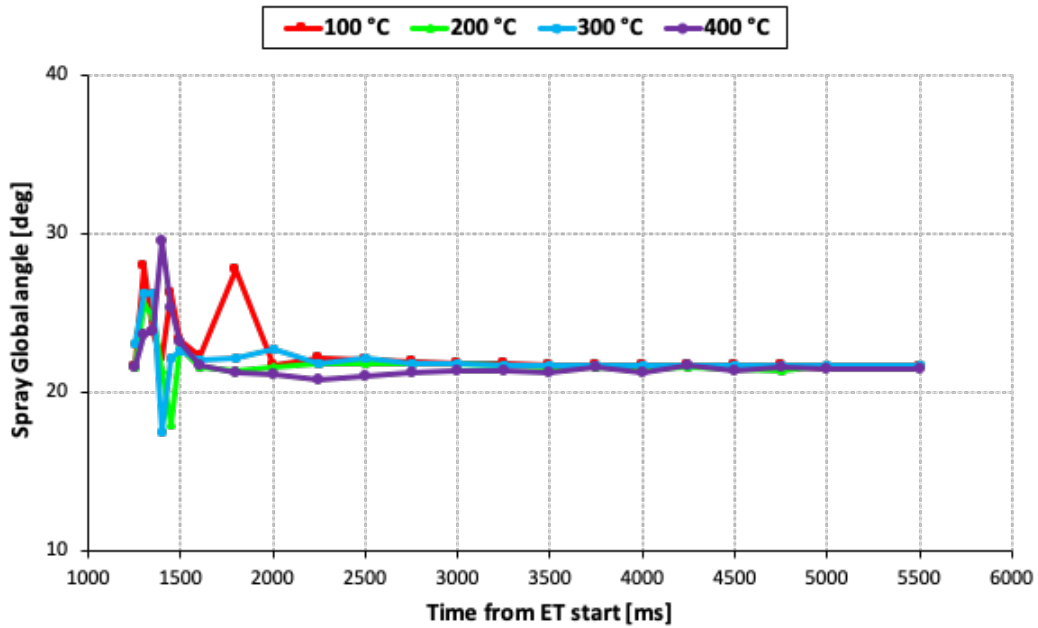
Figure 3.15: UWS spray cone angle at different Tvessel. Pinj 5bar,g, Pvessel 100 kPa

larger droplets region, indicating that the spray structure mainly consist of these droplets, with diameters between 100 μm and 300 μm, while smaller droplets have a negligible contribution on the total spray volume.

(a)

(b)
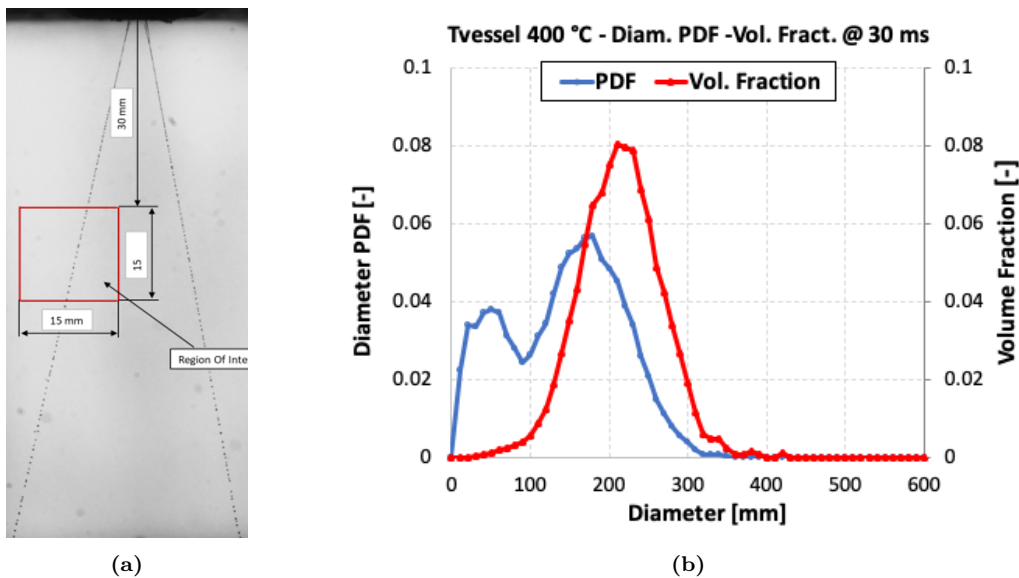
Figure 3.16: UWS spray PDF and Volume fraction at 400 degC

In Figure 3.17 and 3.18 the droplets mean diameters and Sauter Mean Diameter

113

(SMD) are reported. The observed droplets mean diameter (Figure 3.17) was of approximately 180 μm at vessel temperatures between 100 degC and 300 degC, while the temperature effect on the diameter was visible only at 400 degC producing a drop in the mean diameter size to 150 degC. A slightly different situation was observed in terms of SMD. In this case, the SMD increased as the vessel temperature increased above 100 degC, while decreased again at 400 degC. The initial increase could be explained by the selective evaporation of smaller particles while the SMD drop at 400 degC could be related to the evaporation of the large particles.
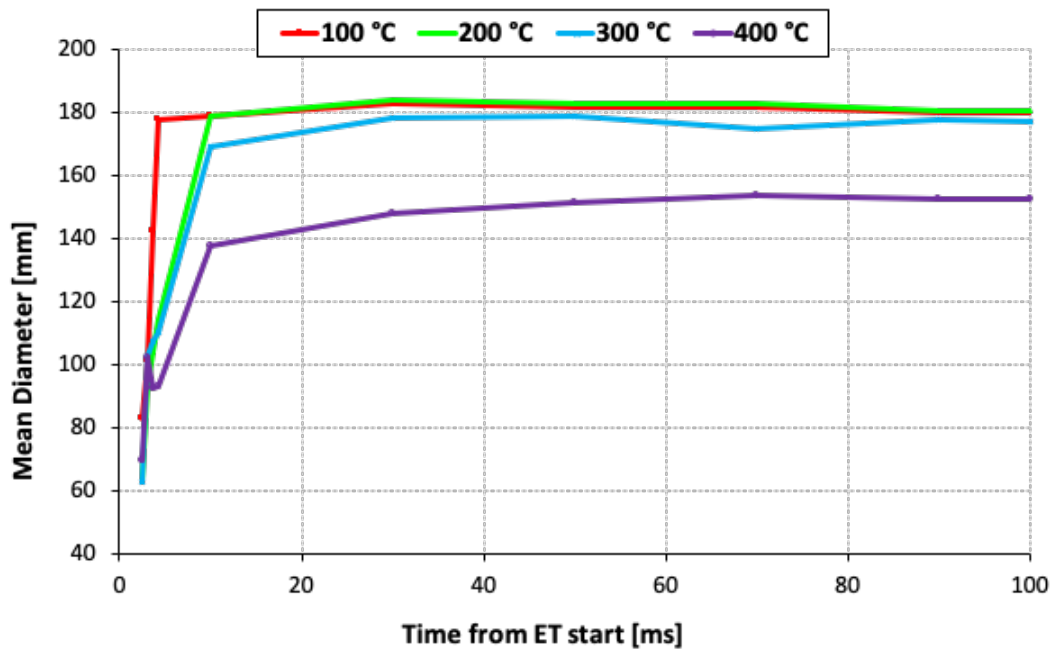
Figure 3.17: UWS spray mean diameter at different Tvessel. Pinj 5bar,g, Pvessel 100 kPa

3.3.3   SCR Efficiency Analysis

The two systems were tested on the Hot Flow Bench (HFB) at the STSe facilities, depicted in Figure 3.19a, which is specifically designed for the characterization of automotive exhaust systems in terms of NO_x abatement performance, UWS conversion and mixing operations in different exhaust flow rate and temperature operating conditions and different pollutants (i.e. NO_x) concentrations. The HFB layout, as depicted in Figure 3.19b, consist of a side-channel blower (1) which is used to deliver the required flow rate, measured by the laminar flow-meter (Meriam Instruments 50-MC2-4) (2). The exhaust gas is sent through a regenerative tube-and-shell heat exchanger (3) and through the electric heater (4) before reaching the exhaust system that has to be characterized (5). Finally, the hot gas flow is
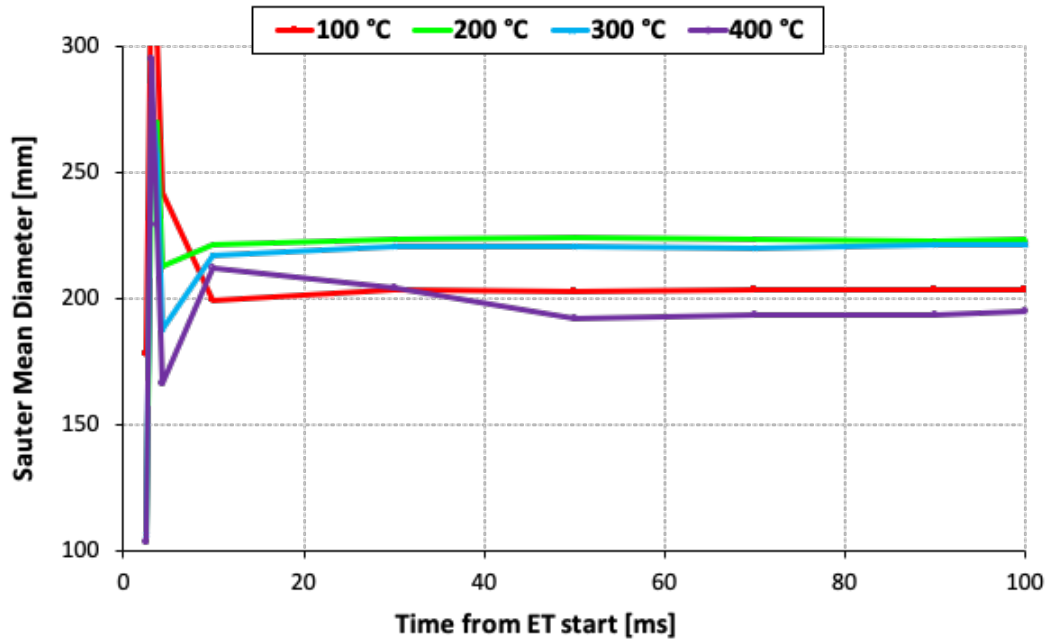
Figure 3.18: UWS spray SMD at different Tvessel. Pinj 5bar,g, Pvessel 100 kPa

cooled down in the air-water heat exchanger (6) before leaving the system. The test bench layout makes it flexible and could be adapted to different exhaust systems architectures, which can be operated on an air mass flow rate up to 600 kg/h and at a temperature of maximum 600 degC, with a maximum pressure of 1.4 bar absolute at the inlet of the test section. The HFB is managed by a proprietary control system developed in the LabVIEW environment.

(a)   (b)
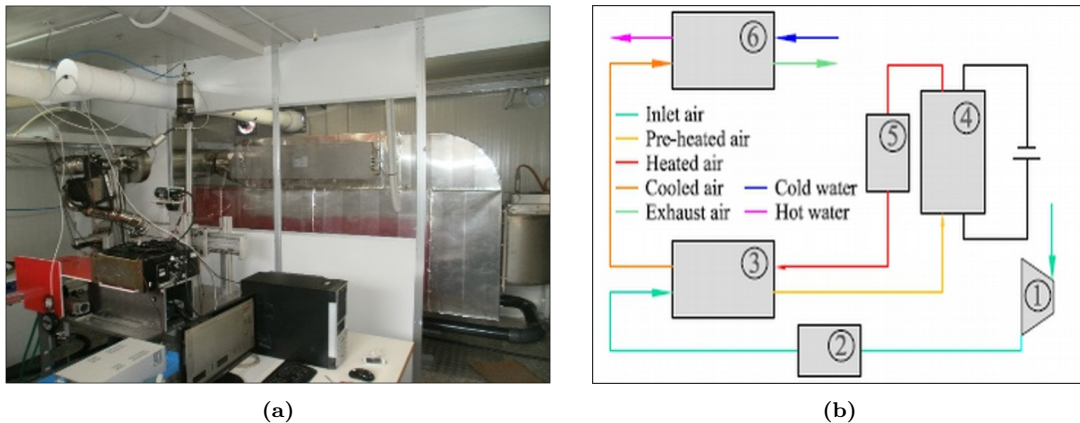
Figure 3.19: STSe Hot Flow Bench

The systems analyzed in this work were assembled on the HFB as depicted in the scheme of Figure 3.20. In the proposed layout gaseous pollutants, namely NO

and NO_2, were stored separately in pressurized tanks and introduced in the exhaust gas stream during the tests. To deliver the desired amount (with 1% of accuracy) of NO_x for each analyzed operating condition, separate hot-wire flow Bronkhorst Mini Flow controllers were used. The UWS injector, placed between the oxidation catalyst and the SCRoF, was operated in controlled operating conditions in terms injection pressure, actuation time and frequency. A Siemens Sitrans MassFlow 3000 Coriolis mass flow meter was used to monitor the injected UWS mass flow rate and ensure the desired UWS/NO_x ratio. The emissions at the system outlet were monitored by means of a QCL Horiba Mexa 1400 QL NX laser spectroscopic exhaust gas analyzer. The instrument allowed to perform the simultaneous measurement of NO_x (both NO and NO_2), N_2O and NH_3 with a sampling frequency of 1 Hz and up to a maximum volume concentration of 1000 ppm. To ensure a reliable measurement and avoid flow disturbances the gas probe was placed downstream of the SCRoF catalyst, counter flow and in the center of the exhaust pipe, whose section was designed to ensure a L/D ratio greater than 5. The sampling tube was thermally conditioned at a controlled temperature of 180 degC to avoid the ammonia condensation. Prior to each test campaign, the analyzed SCRoF catalyst were oven-aged at 500 degC for 2 hours and at a flow rate of 150 kg/h, to stabilize the catalysts.
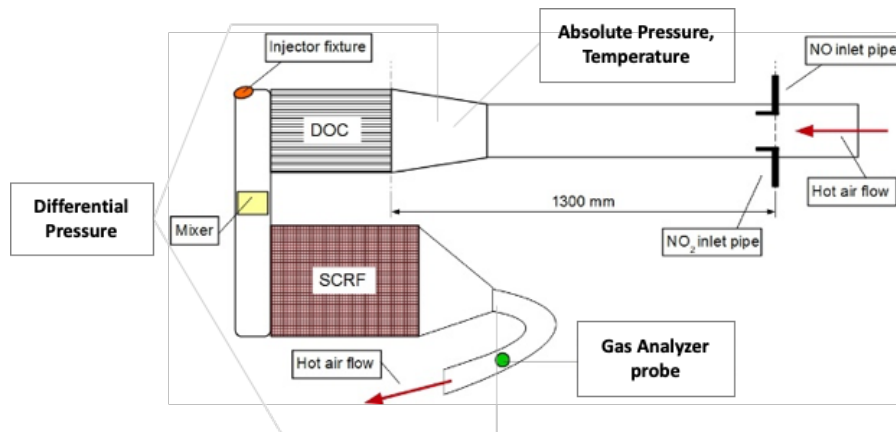
Figure 3.20: SCR converter instrumentation and NOx insertion

The typical output of the HFB during a SCR system efficiency analysis is depicted in Figure 3.21, in which NO, NH_2, NH_3, N_2O concentrations measured at the sampling point and the NO_x conversion are plotted versus the experiment time. The test protocol consisted of three distinct phases:

1. System stabilization phase (interval A in Figure 3.21): the system was fed with air until the desired operating conditions in terms of flow rate and temperature were achieved. At this point the required concentration of pollutants

was fed into the mixture, without injection of UWS, and monitored by the gas analyzer until a stable concentration was measured. The flow conditions registered in the last minute of this phase were considered as the reference conditions for the test.

2. NO_x conversion phase (interval B in Figure 3.21): after the HFB stabilization, the UWS injection was activated with the pre-defined operating conditions in terms injection pressure, actuation time and frequency. Once the stabilization of the NO_x conversion efficiency and of the NH_3 slip was reached, the NO_x conversion phase was terminated by deactivating the UWS injection.

3. Ammonia storage evaluation phase (interval C in Figure 3.21): in this phase the inlet NO_x feed was kept active to evaluate the amount of ammonia stored on the catalyst surface during the test, until the NO_x conversion reached 0 and the inlet amount of NO_x was measured at the outlet of the system.
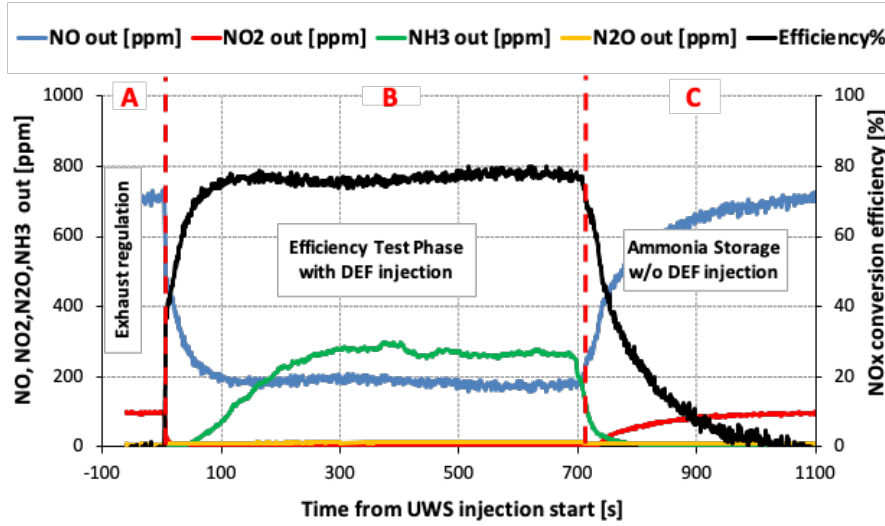
Figure 3.21: Example of NO_x conversion test output

The total amount of ammonia ideally injected in the system could be calculated as in Equation 3.1:

$$m_{NH_3,ing} = \int_{t_0}^{t_{inj}} \dot{m}_{UWS} * 0.325 * 2 * \frac{Mw_{NH_3}}{Mw_{Urea}} * dt \qquad (3.1)$$

in which $m_{NH_3,ing}$ is the ammonia injected mass, $\dot{m}_{UWS}$ the UWS mass flow rate, 0.325 represent the fraction of urea in the UWS, 2 refers to the number of NH_3 moles ideally produced from the total conversion of one mole of Urea, Mw_{NH_3} and Mw_{Urea} indicate the molar mass of NH_3 and Urea, respectively.

117

The theoretical storage of ammonia was calculated according to Equation 3.2, as the balance between the injected ammonia, calculated assuming the ideal case of complete UWS to NH_3 conversion (equation 3.1), the ammonia consumed to convert NO_x and the ammonia slipped at the outlet of the system.

$$m_{NH_3,th} = \int_{t_0}^{t_{end}} \dot{m}_{NH_3,inj} - (\dot{m}_{NO_x,in} - \dot{m}_{NO_x,out}) * \frac{Mw_{NH_3}}{Mw_{NO_x}} - \dot{m}_{NH_3,slip} * dt \quad (3.2)$$

In equation 3.2, $m_{NH_3,th}$ is the total ammonia stored, $\dot{m}_{NH_3,inj}$ the theoretical mass flow of injected ammonia (refer to equation 3.1), $\dot{m}_{NO_x,in}$ and $\dot{m}_{NO_x,out}$ the inlet and outlet NO_x mass flow respectively, Mw_{NH_3} and Mw_{NO_x} indicate the molar mass of ammonia and NO_x respectively, $\dot{m}_{NH_3,slip}$ refer to the mass flow rate of NH_3 at the system outlet.

The actual ammonia storage might be lower than the theoretical one due to the inefficiencies in the UWS to NH_3 conversion process, which could lead to a lower concentration of ammonia at the catalyst inlet, compared to the theoretically expected value, as depicted in the scheme of Figure 3.22. The incomplete conversion of UWS into NH_3 is especially common at relatively low temperature and in presence of complex and compact exhaust systems layout, as in the two architectures analyzed in this work, which reduce the residence time of the urea mixture in the exhaust gas.

To obtain a more realistic indication of the ammonia stored on the catalyst surface, the actual NH_3 inlet concentration should be considered instead of the theoretical one, as in equation 3.3:

$$m_{NH_3,act} = \int_{t_0}^{t_{end}} \dot{m}_{NH_3,in} - (\dot{m}_{NO_x,in} - \dot{m}_{NO_x,out}) * \frac{Mw_{NH_3}}{Mw_{NO_x}} - \dot{m}_{NH_3,slip} * dt \quad (3.3)$$

in which $\dot{m}_{NH_3,in}$ is the ammonia measured at the catalyst inlet.

Since the ammonia inlet concentration was not available during the test campaign, the actual NH_3 storage was calculated during the ammonia storage evaluation phase, by integrating over the phase duration the moles of NO_x consumed. During this phase, the only contribution to the NO_x consumption was related to the stored ammonia, since the UWS injection was inactive. By evaluating the amount of ammonia stored at the end of the NO_x conversion phase (interval B in Figure 3.21), the average NH_3 flow introduced at the catalyst inlet, $\dot{m}_{NH_3,in}$, was estimated and used to compute the actual storage during the test.

The ratio between $m_{NH_3,act}$ and $m_{NH_3,th}$ was used as an indicator of the efficiency of the ammonia preparation process and of the urea to ammonia conversion.
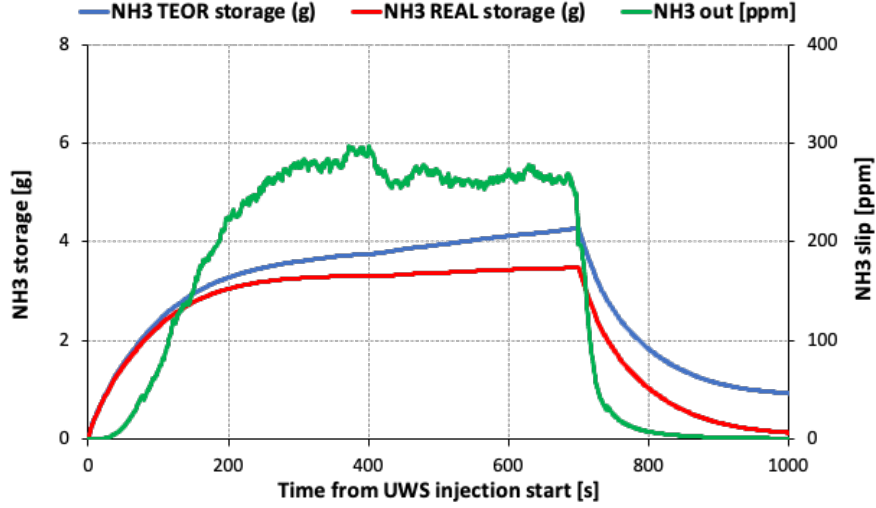
Figure 3.22: Example of NH_3 storage test output

To fully characterize the two systems, the four k-points reported in Table 3.7 were identified, representative of engine operating conditions critical for the after-treatment system in terms of mass flow rate, temperature and concentration of pollutants. The selected k-points named OP1, OP2 and OP3 are representative of high, medium and low load and temperature conditions, respectively, while OP3.1 differs from OP3 in terms of inlet NO_2/NO_x ratio. In Figure 3.23, the selected k-points are plotted versus typical WLTC operating conditions, representative of a passenger car powered by a 2.0 L compression ignition engine.

Table 3.7: K-points selected for the SCR efficiency analysis. System inlet conditions

Point ID	Exhaust Flow Rate	Temperature	NO	NO$_2$	NH$_3$
[-]	[kg/h]	[degC]		[ppm]	
OP1	350	350	800	0	800
OP2	250	250	800	0	800
OP3	100	180	160	0	160
OP3.1	100	180	140	20	160

119
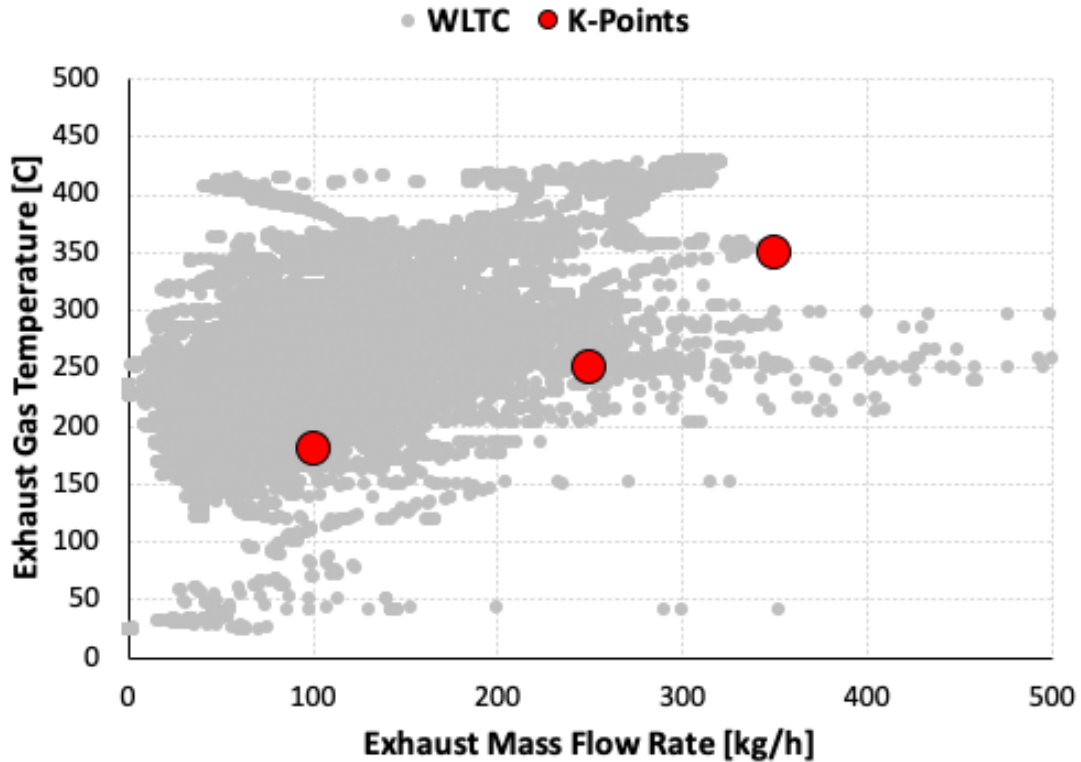
Figure 3.23: K-points chosen for the efficiency analysis on the WLTC operating range of a diesel passenger car

The first 600 seconds of the time profiles obtained for System-A during the NO_x conversion phase (interval B in Figure 3.21) in all the analyzed operating conditions are depicted in Figure 3.24. Each test was carried out until a stable condition was reached in terms of NO_x conversion efficiency. In the tests with higher exhaust mass flow rates the steady-state trend was achieved faster compared to low mass flow rate tests while the gas temperature greatly influenced the urea mixture preparation and the SCR operations.

The summary of the test results for System-A in terms of NO_x conversion efficiency (Figure 3.25a), UWS to NH_3 conversion (Figure 3.25b), NH_3 storage (Figure 3.25c, calculated according to the procedure previously described) and overall pressure drop (Figure 3.25d) is depicted in Figure 3.25.

In terms of System-A NO_x conversion (Figure 3.25a), the maximum efficiency of 77.6% was achieved in OP1, in which the inlet gas temperature was set to 350 degC. The conversion efficiency decreased of about 20% in OP2, where the inlet gas temperature was set to 250 degC, while a NO_x conversion below 30% was obtained
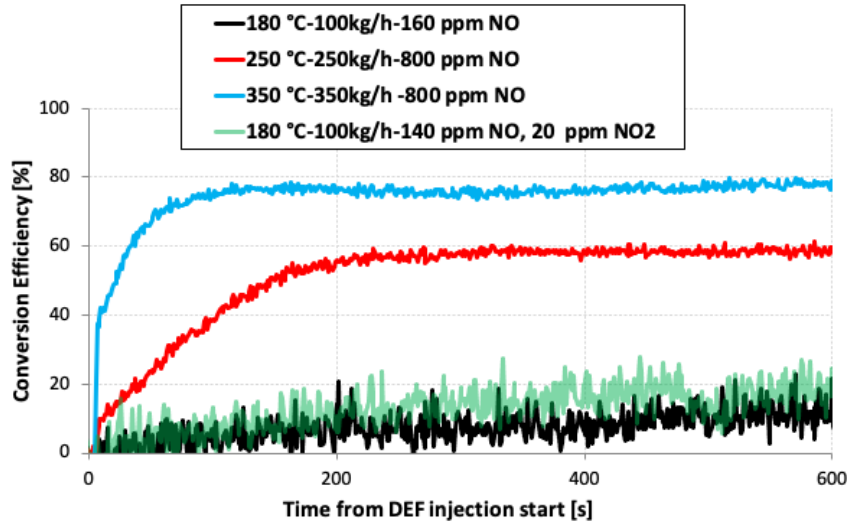
Figure 3.24: NO_x conversion efficiency test results, System-A

in OP3, in which the inlet gas temperature was set to 180 degC. In OP3.1, in which NO_2 was introduced in the inlet batch to achieve a NO_2/NO_x ratio of about 15%, representative of typical engine out conditions [44], the NO_x conversion was increased of 4.5%, probably due to a higher NO_2/NO_x ratio at the DOC outlet which promoted the efficient fast SCR reaction pathway.

The estimated UWS to NH_3 conversion (Figure 3.25b) confirmed that the efficiency drop observed in OP3 could be mainly due to the urea-mixture preparation process which is strongly affected by the gas temperature. As a result, in OP3 and OP3.1 less than 30% and 40% of the injected urea was converted into the ammonia required for the SCR operation, respectively.

Similar results were achieved in terms of the ammonia stored at the end of each NO_x conversion phase (Figure 3.25c), while the measured pressure drop across the system (Figure 3.25d) showed a proportional relationship with the exhaust mass flow rate, as expected.

In Figure 3.26 are depicted the first 800 seconds of the NO_x efficiency time profiles for System-B, in all the tested operating conditions. Also in this case, a stable trend was achieved faster for the higher mass flow rate operating conditions (OP1 and OP2). Although, System-B showed a higher reactivity and efficiency compared to System-A, in all the tested operating conditions.

Figure 3.27 shows the summary of the results obtained for System-B at the end of each test, in terms of NO_x conversion efficiency (Figure 3.27a), UWS to NH_3 conversion (Figure 3.27b), NH_3 storage (Figure 3.27c) and overall pressure drop

(a) NO$_x$ conversion efficiency

(b) NH$_3$ conversion efficiency

(c) NH$_3$ storage

(d) Pressure drop
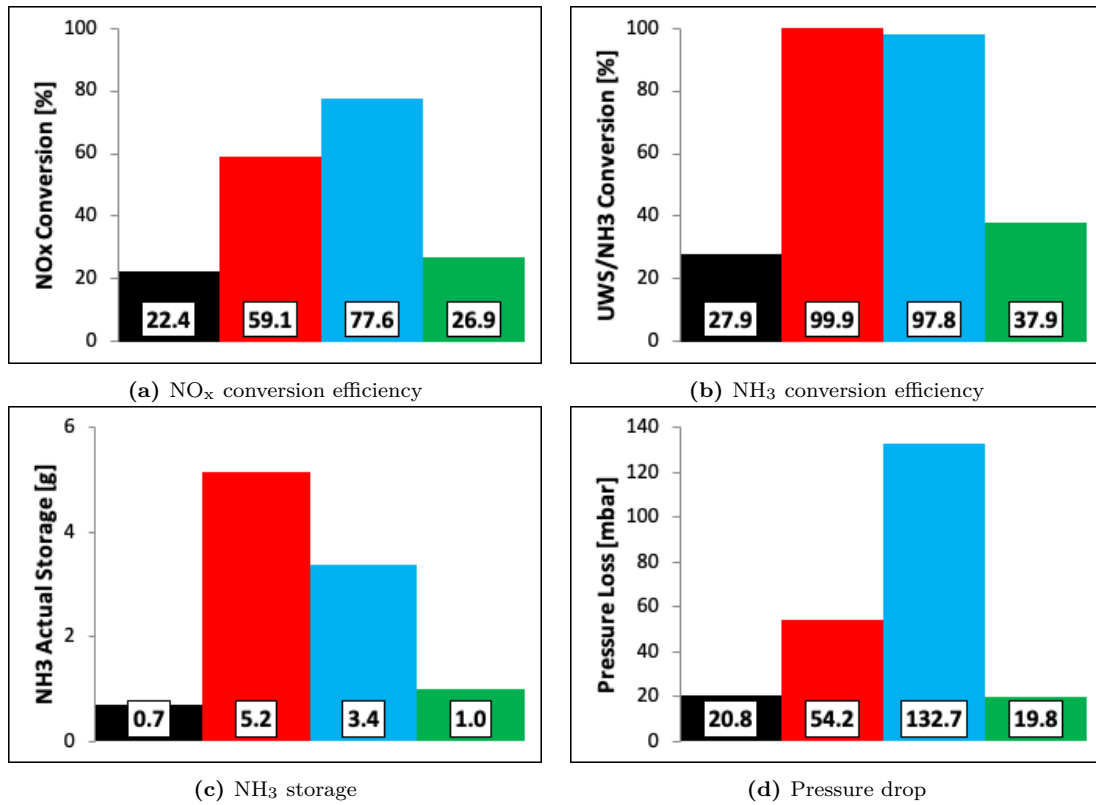
Figure 3.25: SCR efficiency results of System-A
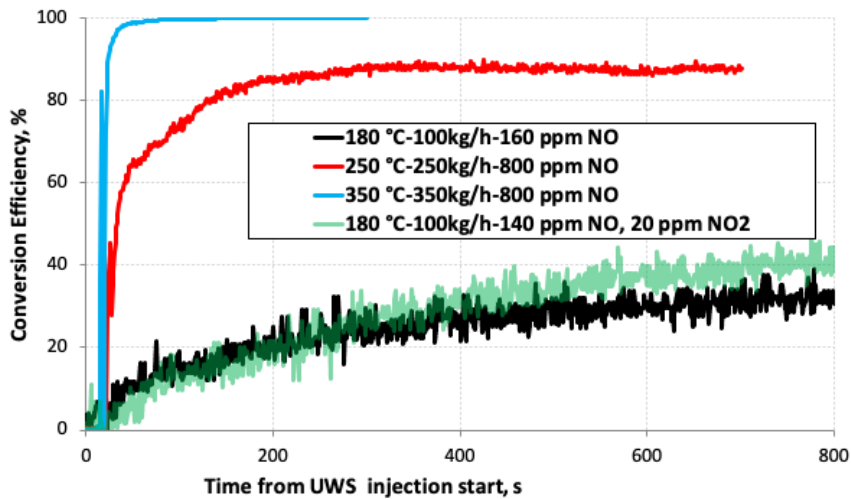
Figure 3.26: NO$_x$ conversion efficiency test results, System-B

(Figure 3.27d).

In System-B a generally higher efficiency was observed, compared to System-A. Almost all the inlet NO_x were converted in OP3, while almost 90% of efficiency was achieved in OP2. In addition a higher low temperature NO_x abatement was found in System-B, which achieved a maximum conversion of 47.9% in OP3, while System-A in the same conditions stopped at 22.4%. Although, in System-B the NO_x conversion obtained in the OP3.1 was lower than in OP3 and the difference could be related to a different DOC activity. Unfortunately, the emission measurement at the DOC outlet was not performed during the test campaign.

Results showed a better estimated UWS to NH_3 conversion, achieving values higher than 60% even in critical temperature operating conditions, such as in OP3 (Figure 3.27b). This result confirms the efficiency of the system design and the large performance gap observed at low temperature, in terms of NO_x conversion, with respect to System-A.

The calculated amount of ammonia stored at the end of the NO_x conversion phase (Figure 3.27c) was maximum in OP2, while higher values were obtained in low temperature conditions (i.e. OP3 and OP3.1) compared to System-A results.

Finally, to confirm the goodness of the System-B design, a lower pressure drop was measured along the exhaust line in all the analyzed test conditions, which could positively impact the engine fuel consumption.

(a) NO$_x$ conversion efficiency

(b) NH$_3$ conversion efficiency

(c) NH$_3$ storage

(d) Pressure drop
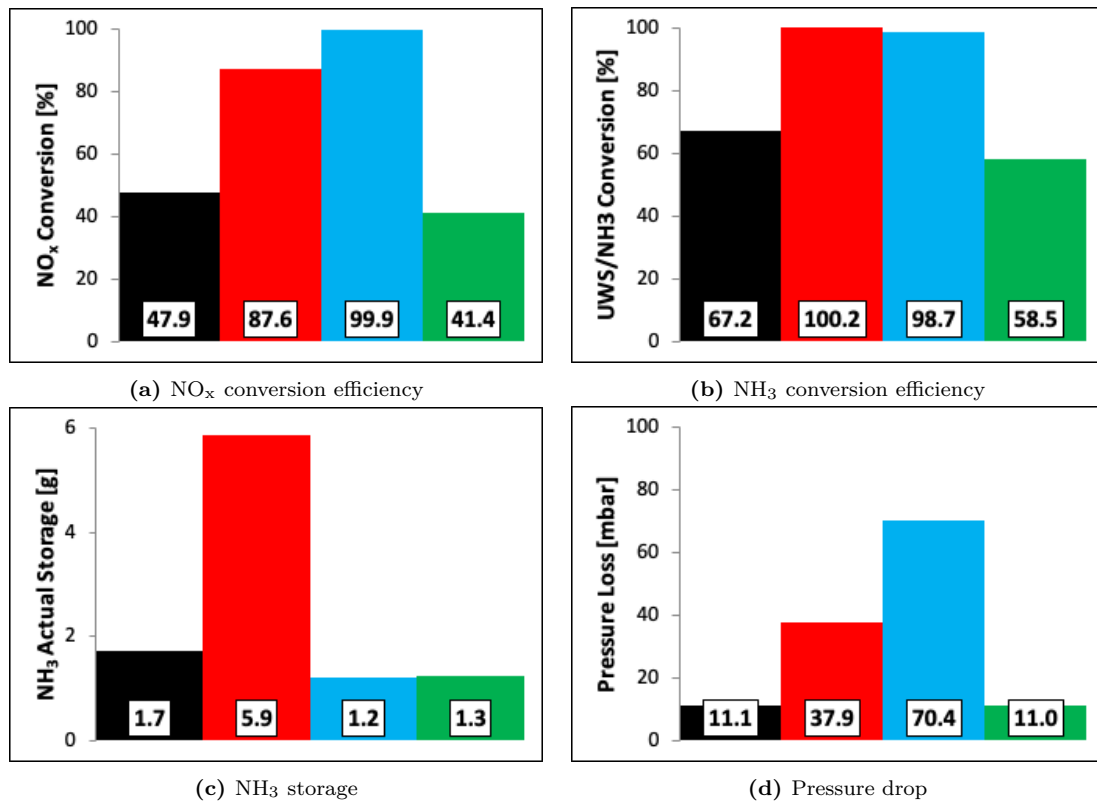
Figure 3.27: SCR efficiency results of System-B

3.4   Numerical Analysis

In the previous section, the experimental campaign carried out to investigate the performance of the two ATS systems, under type-approval representative operating conditions, was described. The experiments showed a large performance gap in favor of System-B, although the root causes behind such gap were not completely understood. The numerical analysis hereby described was carried out to further investigate and assess the different performance between the two after-treatment systems by means of a commercially available 3D-CFD code, CONVERGE. In this section, the simulation setup used for the numerical analysis is first presented and the specific modeling choices briefly described and motivated. Finally, simulation results on a selected operating point, representative of type-approval conditions and critical for the whole after-treatment systems, are presented.

A systematic modeling methodology was developed to properly model the huge complexity and variety of the involved phenomena, which include the liquid spray development and mixing with the exhaust gas, the UWS chemical conversion to form ammonia, the UWS liquid film formation, development and thermal interaction with the solid, the exhaust gas flow and thermal dynamics. Particularly, the simulation setup used for the numerical analysis was obtained after a series of preliminary steps:

1. Spray model calibration based on experimental measurements. The experimental tests described in Section 3.3.2 were reproduced in the numerical domain by means of a virtual test vessel and the spray model constants were calibrated in order to capture the experimental liquid penetration, injection velocity and spray droplets diameters in different vessel temperature operating conditions.

2. Internal geometry definition by means of 3D Computed Tomography (CT) of the two analyzed systems, which allowed the accurate definition of the complex internal geometry within the simulation environment. This step was particularly crucial to properly reproduce the internal features, which could significantly influence the local flow conditions, and to accurately model the geometry of the two unconventional urea-solution mixers and their influence on the ammonia mixture formation.

3. Simulation setup definition and parameters sensitivity (grid resolution, physics model constants etc.) with steady-state and transient simulations, in order to obtain robust and grid-independent results. The obtained setting were used in the described numerical analysis.

4. Numerical analysis on the selected k-points in order to investigate the flow and spray development within the two analyzed systems.

3.4.1 Base Grid and Embedding Definition

The CAD files obtained from the CT scan of the systems were used to define the internal geometry within the virtual environment.

In CONVERGE, differently from others conventional CFD tools, the mesh is automatically generated at run-time by dividing the continuous geometrical domain in discrete cells. To this aim the software integrates a modified cut-cell Cartesian grid generation method in which at first a base structured mesh is generated according to the user desired cell size, then the base grid could be locally refined based on the user fixed-embedding settings. Moreover, in this work the Adaptive Mesh Refinement (AMR) algorithm integrated in CONVERGE was used to dynamically add grid resolution during the simulation where the flow field is most under-resolved, as the solution changes. To determine where the grid should be refined, the AMR estimates the magnitude of sub-grid fields and automatically refines the mesh where and when needed.

In this work, after a preliminary grid-sensitivity analysis a base mesh size of 4 mm was used to generate the simulation domain, for both the analyzed systems. To increase the solution accuracy in critical regions, such as the the spray cone region, the mixer solid region and the surrounding fluid region, the grid was permanently refined locally, as reported in Table 3.8.

Table 3.8: Grid settings and local embedding

Base Cartesian Grid Size: 4 mm		
Region	**Embedding Type**	**Grid Size**
Spray Cone	Permanent	0.5 mm
Mixer: Solid Region	Permanent	0.25 mm
Mixer: Fluid Region	Permanent	1 mm
All Fluid Regions	Adaptive Refinement (Velocity, Temperature)	Up to 0.5 mm

In detail, a fixed embedding was applied to the grid within the solid region to

ensure an accurate solution of the temperature gradient, which allowed a minimum of 5 cells between two opposite faces of each mixer blade. The AMR was used within the fluid domain to dynamically refine the mesh based on velocity and temperature values, whose sub-grid threshold values were set to 0.5 m/s and 20 degK respectively. Finally, the AMR was used to ensure the adequate grid resolution to describe the kinetic and thermal boundary layer near the solid walls enclosing the simulating domain. Since in this study a wall function approach was used to simulate the boundary layer, as described in the dedicated section 3.4.4, the achieved y+ value, between 30 and 150 in all the tested conditions, was considered adequate.

3.4.2   Boundaries and Regions Definition

Within the simulation domain, different regions were defined and different properties were assigned to properly account for the physics involved.

The internal volume of the two systems was treated as a fluid region, while the volume enclosed by the mixer surface was treated as a solid region, therefore considering the mixer walls as interfaces between the fluid and the solid region. Instead of directly modeling the internal geometry of the DOC, the SCRoF and the SCR catalysts, which consist of a multitude of tiny channels, a dedicated region was defined for each one and treated as a porous media. With this approach, which represents a common practice in 3D-CFD modeling of catalysts, transverse and longitudinal inertial and viscous pressure loss coefficients were used to reproduce the flow-straightening effect induced by the catalysts porous channels of the real catalyst and the pressure loss introduced in the exhaust line. The longitudinal coefficients were obtained from experimental tests, carried out at different flow rates to characterize the pressure drop introduced by each catalyst. Extremely high values were used instead for transverse coefficients, in order to force the fluid flow along the axial direction. Porous regions dimensions were set equal to the corresponding catalyst ones, measured during the experimental activity previously described.

Two open boundaries were used for the system inlet and one outlet. At the inlet, a constant mass flow rate was applied and Dirichlet conditions were used to specify the inlet gas temperature and species concentration (only air was introduced in the system). The initial turbulence intensity was set to 10% and length scale was set to reproduce a fully developed flow on the inlet boundary. A constant static pressure of 105325 Pa was applied at the outlet boundary and Dirichlet boundary conditions were used for back-flow. With the mentioned setup the inlet pressure was left unconstrained and thus the obtained value during the simulation was dependent only on the system resistance.

Different boundary conditions were assigned to the walls enclosing the virtual domain, based on the results of the preliminary simulations. The walls not involved in spray impingement or liquid film formation phenomena were treated as fixed temperature walls, set equal to the inlet gas temperature (assumption of fully insulated walls), while the wall boundaries in which a significant formation of liquid film or spray impingement was observed were used to define interfaces between fluid and solid regions, to take into account the related heat transfer.

3.4.3 Conjugate Heat Transfer

To accurately modeling the spray impingement on the internal walls, the liquid film formation and development, the heat transfer between liquid and solid phases, also known as Conjugate Heat Transfer (CHT), must be taken into account in the simulation.

In this particular case the impingement of the UWS spray is expected to cause the gradual cooling of the mixer solid region, especially in the near-surface areas, which could lead to the formation of a liquid film on the surface. The liquid mass trapped within the wall film has a direct impact on the system NO_x conversion, since it retains part of the ammonia used for the SCR reactions.

One of the major issue in modeling CHT resides in the different time scales which characterize the fluid and the solid thermal dynamics. In particular, time scales associated with solid heat transfer are in the order of minutes, which makes the small time-steps used for the fluid simulation unacceptable, especially in large computational domains. In CONVERGE this issue has been overcome by means of a specific CHT modeling strategy named Super-Cycling (SC) [45]. With SC, the fluid phase simulation is periodically freezed and the solid phase heat transfer is handled separately with a steady-state solver to accelerate convergence.

More in detail, each SC stage can be summarized in 4 sub-steps, as depicted in Figure 3.28:

1. The heat transfer between fluid and solid regions is solved with the fluid-related time-step, Heat Transfer Coefficients (HTCs) and Near Wall Temperatures (NWTs) for each cell at the fluid/solid interface are stored during this phase.

2. After a user-defined time interval, the fluid region simulation is frozen and the time-averaged HTCs and NWTs are calculated.

3. The heat transfer within the solid region is solved using a steady-state solver and the time-averaged HTCs and NWTs stored during the first simulation step as boundary conditions.

4. The solid region temperature field is updated and the fluid solver unfreezed for another SC stage.

Thanks to the SC methodology, the thermal fluid and solid heat transfer simulation could be greatly accelerated.

In this work, a time-averaging interval (step 1 of the SC stage) of 0.25 s was considered, which corresponds to the time interval between two consecutive UWS injections.
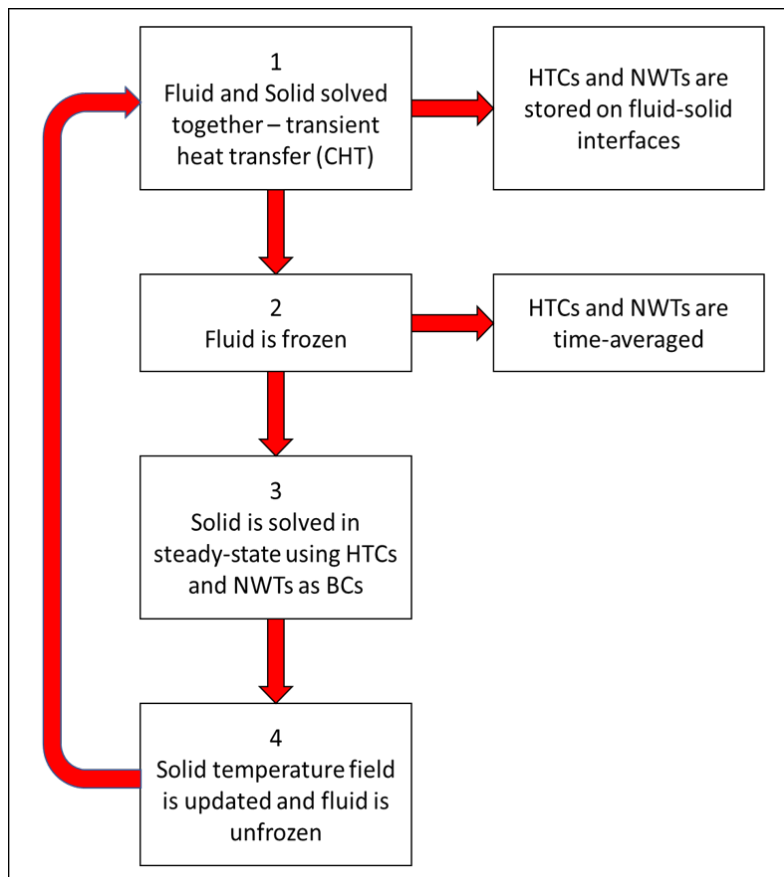
Figure 3.28: Super-cycling modelling strategy

3.4.4   Turbulence Modeling

In this work, the Reynolds-Averaged Navier-Stokes (RANS) equations were used, in conjunction with the RNG k-ϵ turbulence model [46], to simulate the turbulent flow inside the two systems, while the O'Rourke and Amsden model [45] was used to account for the turbulent heat transfer. The RNG model consist of a two-equations modified version of the conventional k-ϵ mode, in which the model constants are analytically derived applying the ReNormalization Group (RNG) theory to solve the Navier-Stokes equations. This model, despite a lower numerical stability compared to the standard k-ϵ, accounts for the effects of smaller scales of motion [47], which are crucial in highly rotating flows such as those expected in the analyzed systems, especially in proximity of the urea-solution mixer.

Finally, to reduce the computational effort required for the simulation, the law-of-wall approach was used to describe the flow boundary layer instead of a full numerical solution of the flow field near the walls, which would require a higher grid resolution, unfeasible in terms of simulation time. With this approach scalable wall functions were used to describe the boundary layer velocity and thermal effects, while a value of y+ between 30 and 150 in the near-wall cells was ensured using the AMR.

3.4.5   Spray and Liquid Film Simulation

The spray and liquid film simulation was carried out using a Lagrangian solver to model the injection of discrete parcels within the flow domain, while the gaseous phase simulation was handled by means of an Eulerian solver.

The injected UWS was considered as 0.325 parts of urea and the remaining of water. A comprehensive database of temperature-dependent physical properties was built for the urea, from data available in the literature, and used for the simulations.

The Kelvin-Helmholtz model was used to simulate the spray droplets break-up and the model constants were specifically calibrated with respect to the constant volume vessel experiments, in order to achieve a satisfactory agreement between the numerical spray properties and the experimental measurements in a wide range of vessel temperatures.

To obtain accurate results in the spray simulation the correct number of discrete parcels should be chosen to represent the whole spray and the proper grid sizing should be checked in the region surrounding the injector [48]. In this work, after a

preliminary sensitivity analysis a number of parcels which ensured a maximum ratio of 1.0e-10 kg/parcels was used for the spray simulation. The grid settings in the injection region were finally assessed based on the experimental results described in Section 3.3.2.

In terms of dynamic and turbulence effects on the droplets, the No-Time-Counter (NTC) model was used to account for droplet-droplet collisions and the Dynamic Drop-drag model was used to consider the drag and lift forces acting on the droplets. Furthermore, the droplet dispersion induced by turbulence was accounted for using the O'Rourke turbulent dispersion model.

Finally, the liquid vaporization induced in the droplets by the surrounding gas was modeled using the Frossling correlations, while flsah evaporation and water dynamics were accounted for using a boiling model.

The liquid film formation which results from droplet-wall interactions was simulated using the Kuhnke wall film model, which was specifically developed for simulation of urea-based impinging sprays in automotive exhaust systems [45]. A film strip model was used to account for the interactions between the high-speed injected droplets and the liquid film formed on the walls, which are expected to occur especially in compact layouts with impinging surfaces as in the analyzed systems. Finally, the heat transfer between the fluid, the solid walls and the liquid film was accounted for by means of the Wruck model, which considers also the Leidenfrost effect [49].

3.4.6 UWS decomposition

Different approaches are available to simulate the chemical processes involved in the conversion of the injected UWS into its byproducts. Detailed models include multi-components evaporation model for the spray droplets and the detailed reaction kinetics to simulate the urea thermal decomposition and the polymerization of byproducts to form solid deposits [50]. Although, with this approach additional complexity is added to the model, thus increasing the computational time, and dedicated experiments are required to evaluate urea properties and deposits formation under different operating conditions. Simplified models include a single-component evaporation model and a limited set of global reactions to simulate the urea decomposition, drastically reducing the required computational time. Despite such models present some limitations in the prediction of urea solid deposits, there are numerous examples of successful applications in the literature, proving the approach effectiveness in a wide range of different operating conditions [28, 51]. Since the detailed simulation of urea deposits was not the scope of this work, a simplified

simulation approach was used to simulate the urea-solution decomposition.

With this approach, named the Molten Solid Urea Decomposition, it is assumed that only water evaporates from the UWS droplet, since the urea vapour pressure is low at ambient pressure. Water evaporation from the droplet is modelled according to the Frossling correlation, until only urea is left within the droplet which is then treated as a solid particle. The urea decomposition and the production of ammonia is modeled by means of Arrhenius reaction rates as a 2-steps process:

- Urea thermolysis to form ammonia and isocyanic acid:

$$(NH_2)_2CO\,(s) \longrightarrow NH_3\,(g) + HNCO\,(g) \tag{3.4}$$
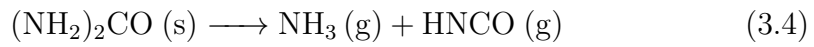
- Isocyanic acid hydrolysis to form ammonia and CO_2:

$$HNCO\,(g) + H_2O\,(g) \longrightarrow NH_3\,(g) + CO_2\,(g) \tag{3.5}$$
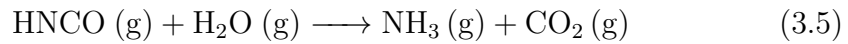
The Arrhenius coefficients used to describe the global reactions 3.4 and 3.5 were taken from [28] and [52] respectively.

3.4.7 Uniformity Index

To achieve the severe legislation emission limits it is fundamental to efficiently use the entire catalyst surface, by uniformly distributing the gas flow on the catalyst cross section. To measure the goodness of the distribution, for instance, of gas flow velocity and species at the catalyst entrance, a specific index called the Uniformity Index (UI) was defined. Maximizing the flow uniformity during the early design phase could result in increased NO_x abatement in SCR systems [53]. The UI could be defined according to different definitions:

- L1 norm: based on the average absolute deviation (commonly used)

- L2 norm: based on the standard deviation (less frequently used, more sensitive to extreme values)

In this work, the UI at each SCRoF entrance section was calculated according to the L1 definition, expressed as in equation 3.6, to evaluate the distribution of flow axial velocity and species of interest (namely NH_3 and HNCO), considering

time-averaged consistently with the common procedures used to experimentally evaluate the UI.

$$UI_{L1} = 1 - \frac{1}{2} * \sum_{k=1}^{N} \frac{A_k}{A_{tot}} * \frac{|\overline{\psi_k} - \overline{\psi_{avg}}|}{\overline{\psi_{avg}}} \tag{3.6}$$

3.5 Spray Bomb Simulation Results

In this section are reported the results of the constant volume vessel simulations, carried out to calibrate the spray models constants and validate the simulation setup over the experimental data presented in Section 3.3.2. In detail, the spray model calibration was carried out on the highest temperature test, which corresponds to a vessel temperature of 400 degC. The other tests, in which the vessel temperature was set to 300 degC, 200 degC and 100 degC, were used for the model validation. The operating conditions observed during the experiments were reproduced within the virtual vessel and the simulated spray was compared with the experimental measurements in terms of liquid penetration length and mean particles diameters.

In the following figures, simulation results, depicted in red solid line, are compared with the experimental measurements, represented by black solid lines. The liquid penetration is depicted in the upper row of each figure while the spray SMD is reported in the bottom row. Since the experimental liquid penetration was obtained as the mean over 30 consecutive injections, the average value is reported in each figure and the maximum experimental deviation is represented by the dashed black lines. To compare the simulated spray SMD with the experimental measurement, which was evaluated in a limited ROI defined downstream of the nozzle, as described in section 3.3.2, a customized ROI was defined in the virtual domain with the same features of the experimental one and used to evaluate the simulated SMD.

In Figure 3.29 are depicted simulation results for the calibration point, in which the vessel temperature was set to 400 degC. At this temperature, in the experiments the liquid spray almost reached the end of the evaluation window (80 mm from the nozzle) after 3 ms, showing a linear penetration curve which yielded after approximately 1 ms from the start of the injection. The simulated spray penetration was in satisfactory agreement with the experiments, although the penetration yield was more gradual compared to the experimental. The simulated SMD matched the experimental value of 200 μm, after the spray reached the ROI (about 0.9 ms from the start of injection) and a stable structure was achieved.

The spray model setup, obtained after the calibration on the test at 400 degC

133

Figure 3.29: Spray bomb simulation results. Penetration distance (top) and droplets SMD (bottom). Simulation (red) vs experiments (black). Validation point: vessel temperature = 400 degC, vessel pressure = 100 kPa

of vessel temperature, was used to validate the model on the remaining tests. In Figures 3.30, 3.31 and 3.32 are reported simulation results obtained for the tests in which the vessel temperature was set to 100 degC, 200 degC and 300 degC respectively.

Simulation results were found in good agreement with the experiments, both in terms of liquid penetration and in term of spray SMD. More in detail, the spray penetration simulated at a vessel temperature of 200 degC and 300 degC, Figures 3.31 and 3.32 respectively, was slightly overestimated but in an acceptable range (average error was contained below 5%) and aligned with the experimental dispersion. In both cases the spray SMD was underestimated of the same order by the model, which was acceptable considered the scope of the numerical analysis. Simulation results were accurately aligned with experimental results in the test at 100 degC, as shown in Figure 3.30, both in terms of liquid penetration and spray SMD.
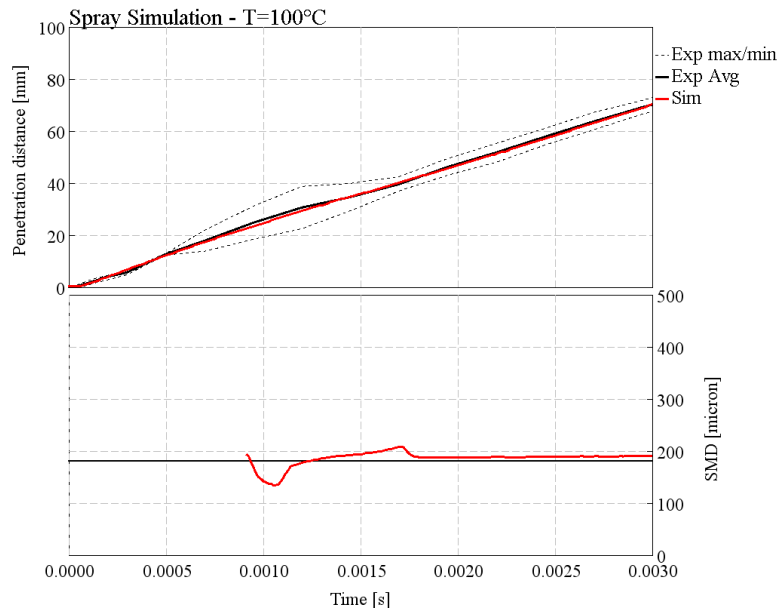
Figure 3.30: Spray bomb simulation results. Penetration distance (top) and droplets SMD (bottom). Simulation (red) vs experiments (black). Validation point: vessel temperature = 100 degC, vessel pressure = 100 kPa
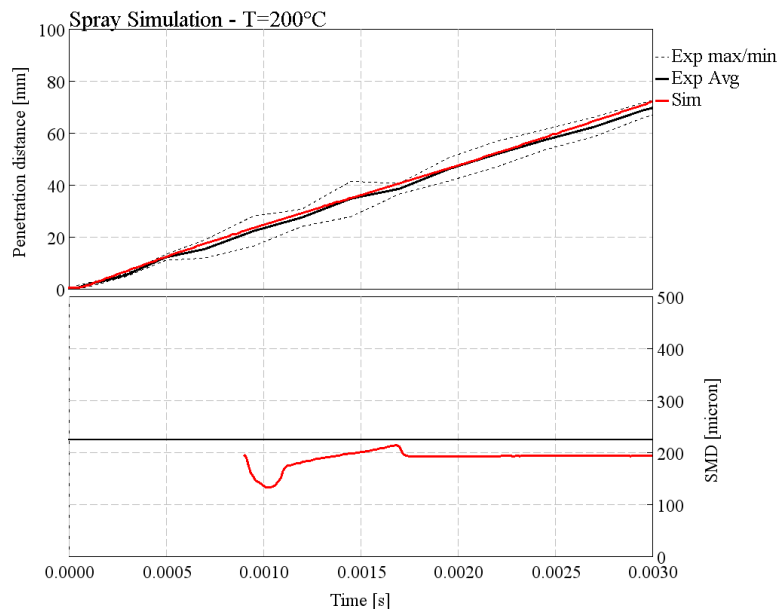
Figure 3.31: Spray bomb simulation results. Penetration distance (top) and droplets SMD (bottom). Simulation (red) vs experiments (black). Validation point: vessel temperature = 200 degC, vessel pressure = 100 kPa
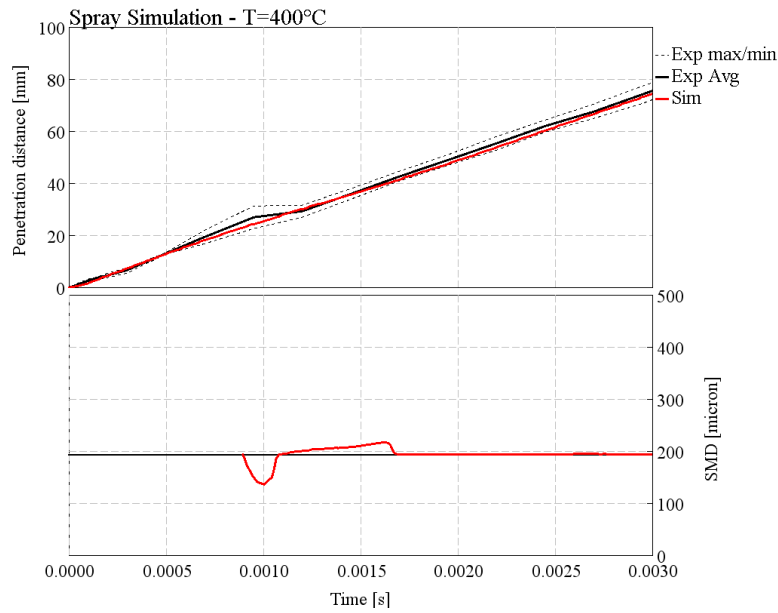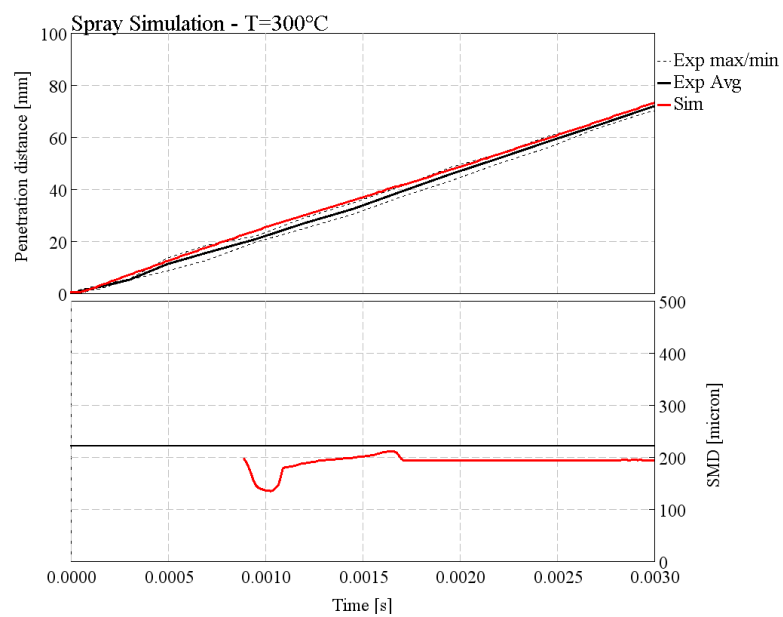
Figure 3.32: Spray bomb simulation results. Penetration distance (top) and droplets SMD (bottom). Simulation (red) vs experiments (black). Validation point: vessel temperature = 300 degC, vessel pressure = 100 kPa

3.6   System Modeling Results

In this section are presented and discussed the main outcomes of the numerical analysis conducted on the most critical operating condition highlighted during the SCR efficiency analysis described in Section 3.3.3. The operating conditions of the low load representative k-point, OP3 of Table 3.7, were reproduced in the virtual domain for the analyzed systems. The aforementioned operating conditions, which consist of a mass flow rate of 100 kg/h and a gas temperature of 180 degC, are in fact critical for the SCR operations, especially in terms of UWS to ammonia conversion. Moreover, in this conditions a large performance gap was observed, during the experimental campaign, in favor of System-B, thus the numerical analysis was aimed at investigating the source of such gap. The validated spray model setup described in the previous section 3.5 was carried over and used for this analysis.

Both the analyzed systems simulations were initialized, in terms of fluid and solid region temperatures, after a preliminary steady-state run in order to accelerate the dissipation of the initial transient. The virtual injector was operated at a frequency of 4 Hz consistently with the experimental setting for the operating point, and the start of the UWS injection was set after 0.05 s from the simulation start, in order to let the flow field stabilize. A total time of 2.05 s was simulated for each system, which included 8 UWS injection events, and steady state conditions were observed at the end of the simulations.

In Figure 3.33 the simulated average solid temperature trace of the mixer region is depicted, for both System-A (red solid line) and System-B (blue solid line). The sudden temperature steps periodically observed in the simulated traces correspond to the end of each Super-Cycle stage (described in detail in section 3.4.3), when the solid temperature is updated after the steady-state run on the solid region, with the fluid solver frozen. This modeling approach allowed to quickly approach a steady state trend at the end of the simulated time (of just 2 s), where the temperature variations within the solid were contained within 1 degK, capturing at the same time the cooling effect due to the repeated UWS injections.

In Figure 3.34 and 3.35 are depicted the velocity streamlines computed from the simulation of System-A, colored based on the velocity (velocity increases from blue to red), from the isometric and the back view respectively. The gas flow is straightened by the DOC porous media, as it enters within the simulation domain, and is then conveyed into the mixer section, where encounters a sharp bend. As can be observed from the simulation, a limited part of the gas flow bypass the mixer from the sides, where is accelerated by the narrow section. The first stage of mixer fins, which should serve the purpose of performing the liquid spray break-up, addresses

137
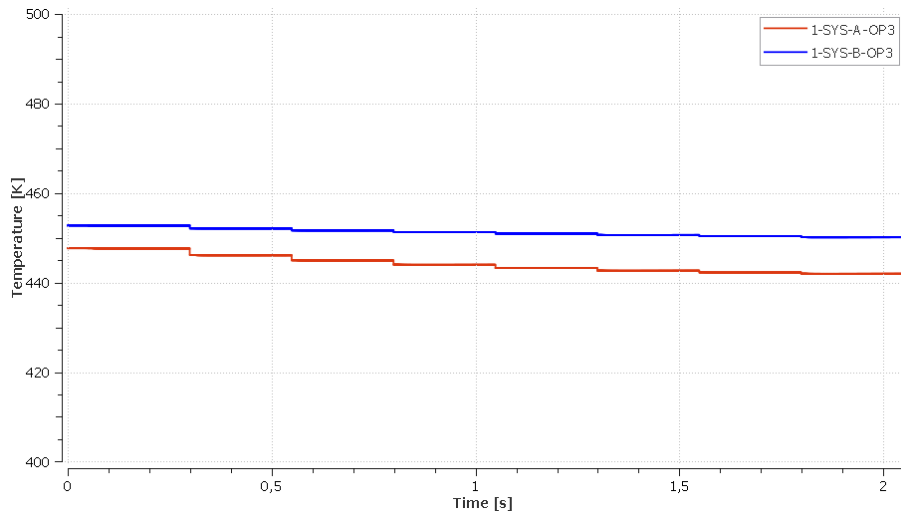
Figure 3.33: Solid region (UWS mixer) average simulated temperature. Comparison between System-A (red line) and System-B (blue line)

the flow towards the center of the section, while the second stage towards the opposite direction inducing the formation of two counter-rotating vortices downstream of the mixer. The rotating flow field in this section should accelerate the droplets evaporation and thus the ammonia production and , at the same time, should enhance the mixing between the exhaust flow and the produced ammonia, before the SCRoF region. The gas flow is finally forced to enter in the SCRoF region where is slowed-down by the porous media before leaving the domain.
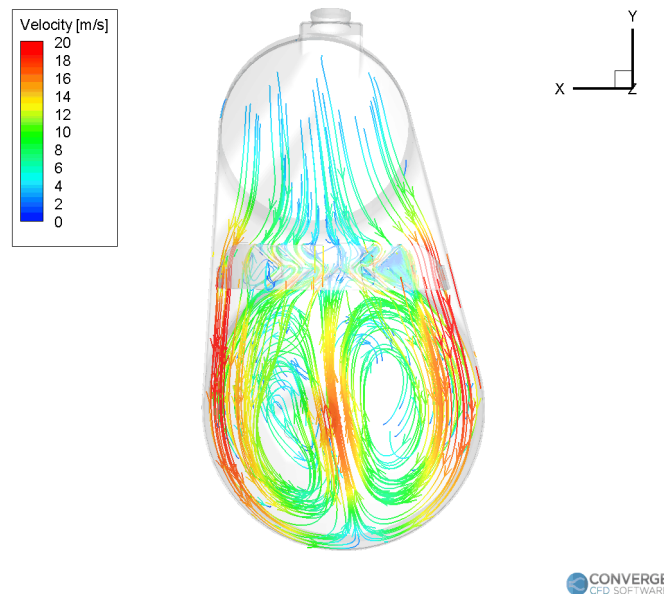
Figure 3.34: Computed flow streamlines for System-A. Isometric view

138
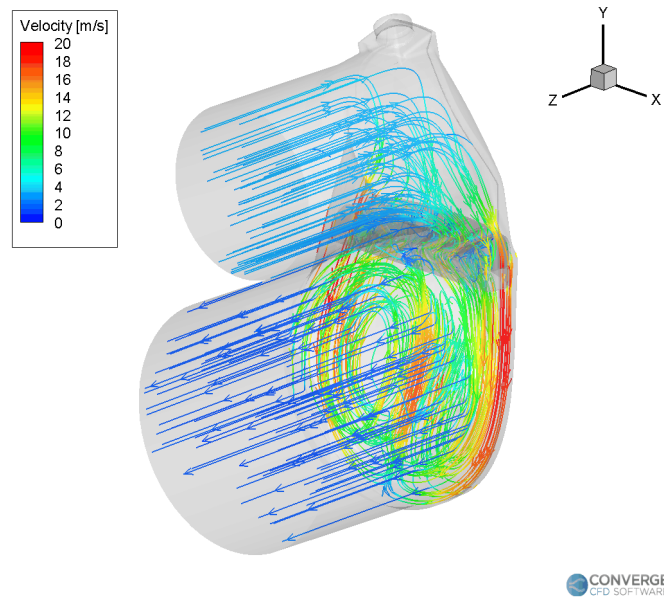
Figure 3.35: Computed flow streamlines for System-A. Rear view

Similarly, the simulated flow streamlines for System-B are depicted in Figures 3.36 and 3.37, respectively. In System-B, the flow is introduced within the domain from a narrow inlet section which locally accelerates the gas flow before the DOC entrance section. The sharp bend and the sudden expansion before the DOC inlet produce a non uniform flow field and the streamlines inside the DOC porous region are mainly concentrated through the center as a result. The downstream cone section accelerates the flow into the mixer region, where the streams easily breaks through the mixer plates. A sharp curve is then encountered downstream of the mixer, where the flow impacts on the bottom flat surface due to its high kinetic energy. At the same time, the flat surface splits the gas flow into two separate streams which deviates from the center towards the outside, forming two counter rotating vortices, similarly to what observed in System-A. The turbulence generated in this section contributes to the UWS conversion and the flow mixing with the ammonia, which continues along the next pipe until the entrance of the SCRoF region. Here the flow is forced through the two porous media (SCRoF and SCR) before leaving the domain.

For a deeper understanding of the different flow fields, the axial velocity at the SCRF entrance section is depicted in Figure 3.38 and 3.39 for System-A and -B respectively. A uniform axial velocity distribution was observed in System-B, in System-A instead the obtained distribution showed several peaks, especially at the bottom of the analyzed section. These results confirmed that the flow uniformity at the SCRF inlet was favored, in System-B, by the longer mixing section placed before
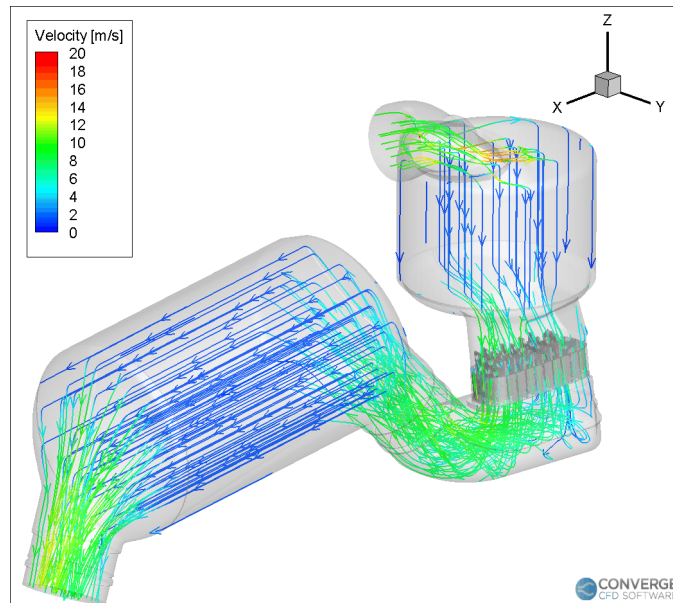
Figure 3.36: Computed flow streamlines for System-B. Isometric view
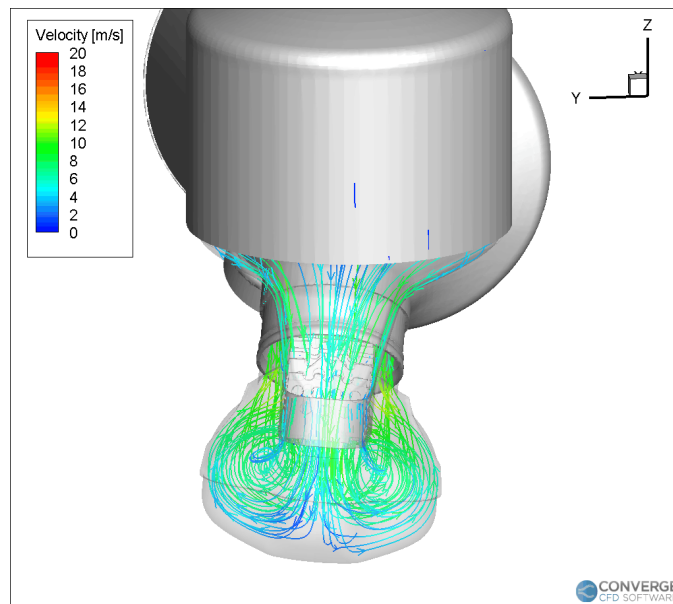
Figure 3.37: Computed flow streamlines for System-B. Rear view

the SCRF inlet, while in System-A the reduced space between the mixer and the catalyst inlet and the sharp direction changes induced in the gas flow deteriorated the distribution at the SCRF entrance.

In Figure 3.40 is depicted the flow velocity and species (NH_3 + HNCO) UI, calculated according to the L1 definition (as described in Section 3.4.7) at the
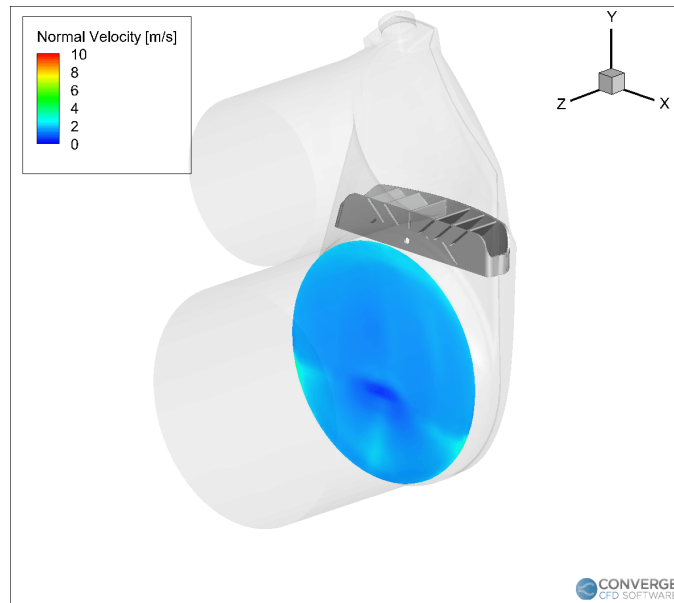
Figure 3.38: Computed normal velocity distribution at SCRF inlet. System-A
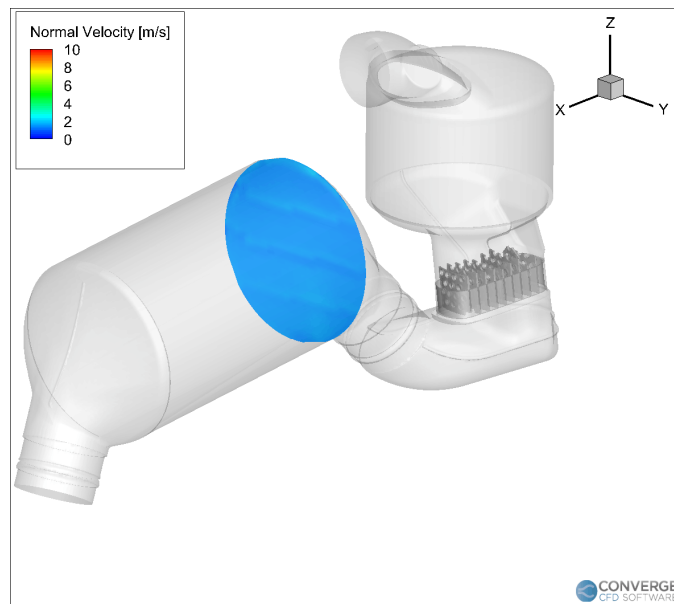
Figure 3.39: Computed normal velocity distribution at SCRF inlet. System-B

SCRF entrance section, for System-A (red bars) and -B (blue bars).

The results confirmed the trends described before, a significantly higher uniformity was observed for System-B at the SCRF inlet section. In System-A, a UI index of 0.94 and of 0.92 was obtained for the velocity and the species distribution

respectively, which could be related to the large vortices and thus to the flow instability observed in the section upstream of the SCRF. In System-B, the longer mixing section allowed a better mixing and a more uniform flow field before the SCRF, which resulted in higher UI, of 0.97 both for species and flow velocity. This first result in part explains the higher peak NO_x conversion efficiency obtained in System-B during the experimental campaign, especially in the high temperature conditions where the UWS was entirely converted into the NH_3 required for the SCR reactions.
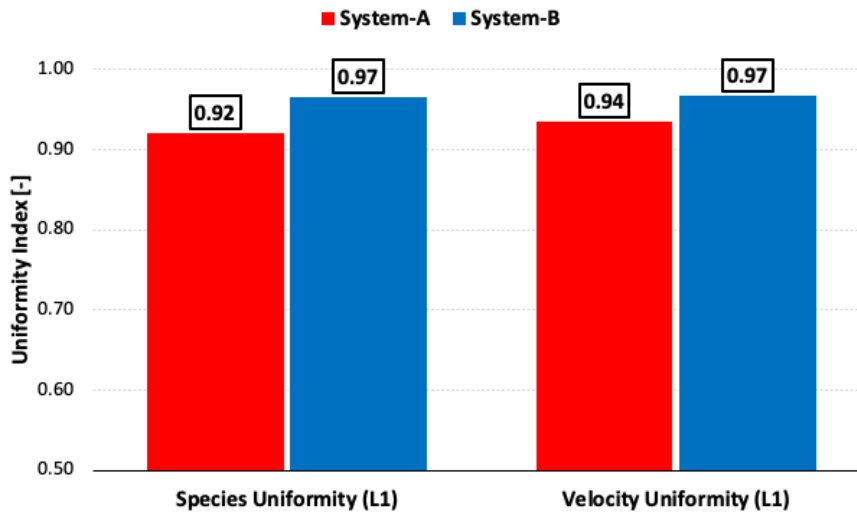
Figure 3.40: Calculated uniformity index (L1) at SCRF inlet for species (NH_3 + HNCO) and velocity. Comparison between System-A (red) and System-B (blue)

To further understand the differences observed at low temperature, where the UWS conversion into ammonia is limited by the reduced evaporation rate of the droplets and the low reactions kinetics, the NH_3 and HNCO molar flow rate at the SCRF entrance section should be considered, depicted in Figure 3.41 and normalized to its maximum value, for System-A (red bar) and -B (blue bar).

The NH_3 reaching the SCRF in System-B during the simulation was 60% higher compared to flow rate obtained in System-A. This large difference could be explained considering two features which differ between the analyzed systems:

- Different effectiveness of the UWS mixer design: in System-B, the plate mixer design was more effective in inducing the spray breakup into tiny droplets, thus enhancing the evaporation and the ammonia production.

- Different mixing volumes: in System-A, the volume available between the mixer and the SCRF entrance section, in which the droplets evaporates and

the ammonia mixes with the exhaust gas, was significantly lower compared to the System-B layout.

The simulation results were aligned with the large NO_x abatement gap observed during the experimental campaign in such critical operating conditions, which corresponded to a 55% efficiency gap.
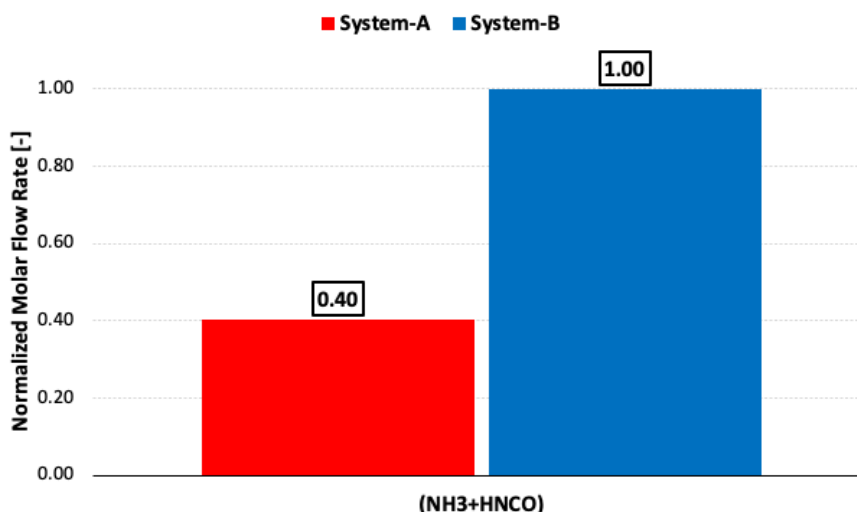
Figure 3.41: Calculated normalized molar flow rate of $NH_3 + HNCO$ at SCRF inlet. Comparison between System-A (red) and System-B (blue)

The different mixers design strongly influenced the spray break-up and the mixture preparation before the SCRF in both the analyzed systems.

The simulated spray parcels during a UWS injection event are depicted in Figures 3.42 and 3.43 for System-A and -B respectively, colored by the droplet water content. In both cases, before hitting on the mixer surfaces the droplets evaporation was limited, as suggested by the high water content (indicated by the red color). The poor spray atomization offered by the injector nozzle and the large particles injected contributed to this trend, leaving the break-up effort almost entirely to the mixer. After hitting on the mixer surfaces, a large number of dispersed particles was produced in both the systems, inducing the water evaporation and thus the urea conversion into ammonia.

More in detail, in System-A (Figure 3.42) the main spray break-up occurred on the first stage of mixer fins, while the second stage contributed in generating the turbulence required for the mixing.

Similarly, in System-B (Figure 3.42) a first spray break-up stage was induced by the mixer plates, after which a large number of smaller droplets was generated.

In addition, a secondary break-up stage occurred after the particles were dragged by the high speed gas flow onto the flat surface located downstream of the mixer. After this stage most of the water evaporated from the particles and the ammonia mixing with the exhaust gas was enhanced by the two vortices formed in the gas stream.
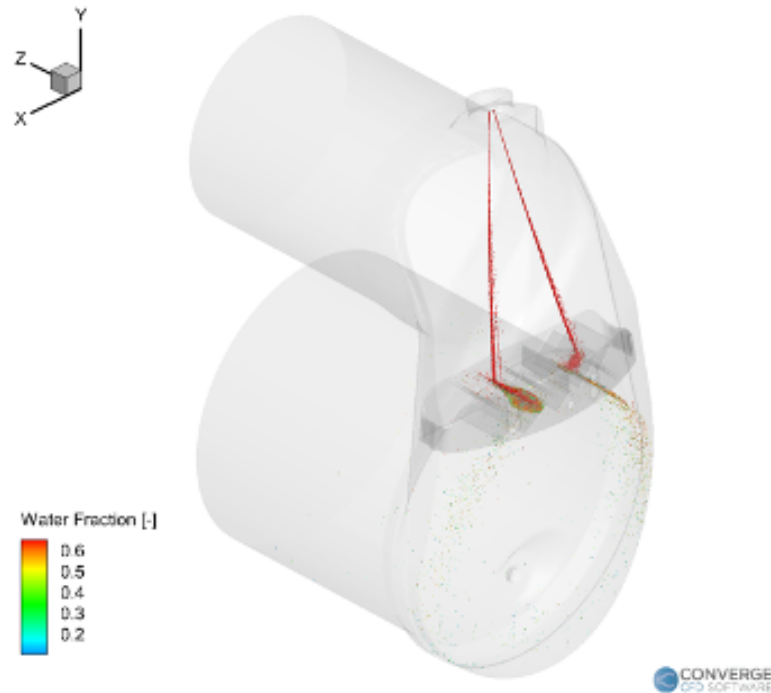
Figure 3.42: System-A UWS spray parcels during the injection colored by the droplet water fraction (water content decreases from red to blue)

Finally, a key factor in the design of ammonia SCR systems lies in the minimization of liquid film formation, especially in complex and compact layouts, thus reducing the risk of solid deposits which could introduce serious reliability issues. In fact, the UWS liquid droplets impact on the mixer during each injection event, locally cooling the contact surface which, especially at relatively low temperature, could lead to the formation of liquid film and consequently to the risk of solid deposits. In the analyzed operating conditions, the formation of liquid film is likely expected.

In Figures 3.44 and 3.45 the simulated liquid film mass in System-A is depicted, from the isometric and the back views respectively. A significant amount of liquid film was formed mainly on the mixer surface, around the spray impingement area and between the first and the second stage of fins, where the liquid droplets accumulated during the injections. The formation of solid deposits in these areas could
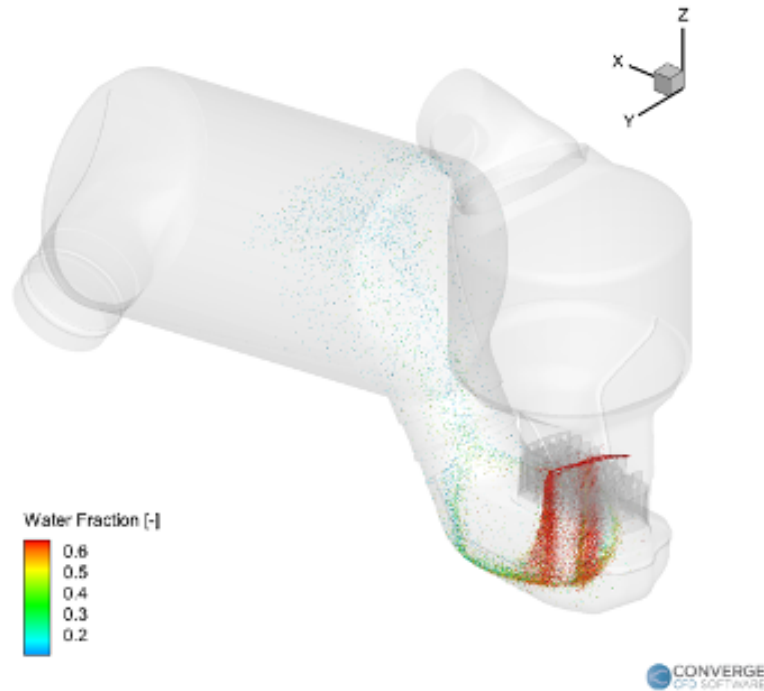
Figure 3.43: System-A UWS spray parcels during the injection colored by the droplet water fraction (water content decreases from red to blue)

be particularly dangerous, leading to the partial clogging of the narrow sections between the mixer blades thus increasing the pressure drop and further deteriorating the system efficiency.

The simulated liquid film mass in System-B is depicted in Figures 3.46 and 3.47, from the isometric and the back views respectively, which confirmed also in this case the formation of liquid film. In System-B, part of the liquid film was formed between the mixer plates, close to the spray impingement area, and was spread on a larger area due to the spray break-up and the higher droplets dispersion. A second film location was found on the bottom flat surface, where the liquid was dragged by the gas flow stream and by means of gravity, forming two large liquid stains. The overall liquid film mass obtained for System-A and -B was comparable, although slightly lower in System-B.

Despite the evaluation of solid deposits was not in the scope of this analysis, the liquid film locations obtained in the simulation were compared with the traces found on the components surfaces at the end of the experimental campaign. In Figures 3.48 and 3.49 the pictures of the surfaces downstream the mixers of System-A and -B, took at the end of the experimental campaign, are depicted. In both cases, the presence of white deposits was observed.
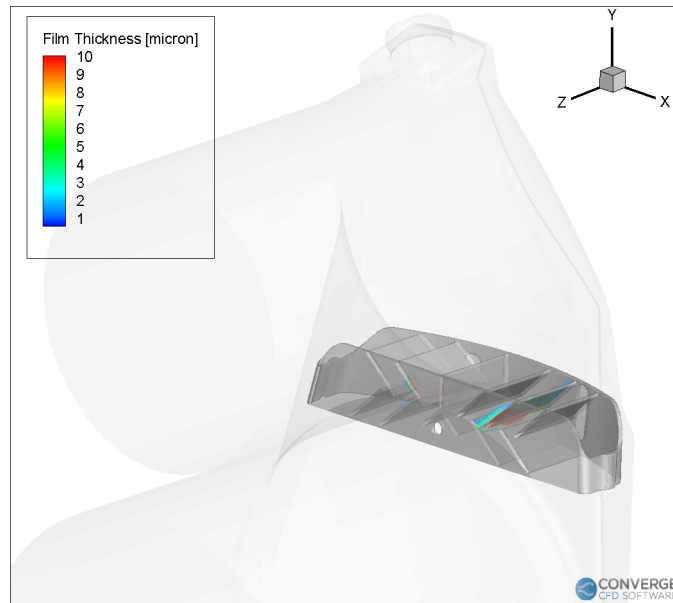
Figure 3.44: Computed wall film thickness and location for System-A. Isometric view
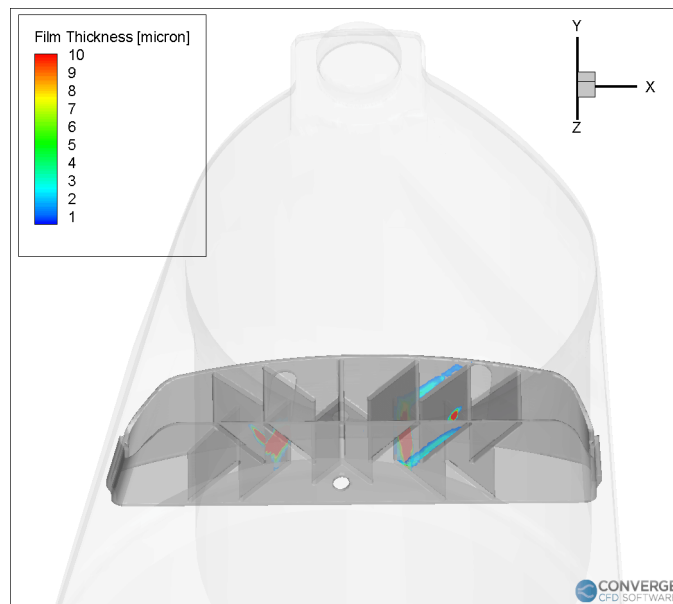
Figure 3.45: Computed wall film thickness and location for System-A. Rear view

In particular, in System-A (Figure 3.48) deposits traces were found between the mixer fins, near the spray impingement areas in agreement with model's predictions. Lighter traces were also observed on the canning surface enclosing the mixer region, in correspondence of the flow vortices observed during the simulation and produced by the second stage of mixer blades.
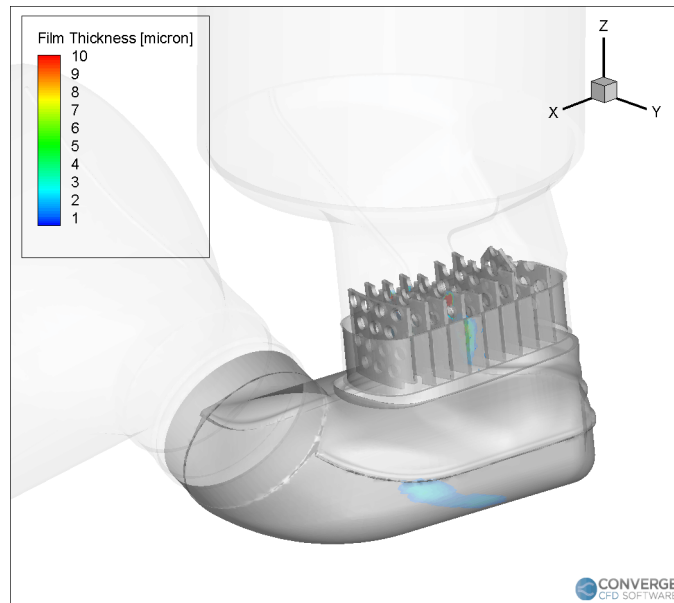
Figure 3.46: Computed wall film thickness and location for System-B. Isometric view
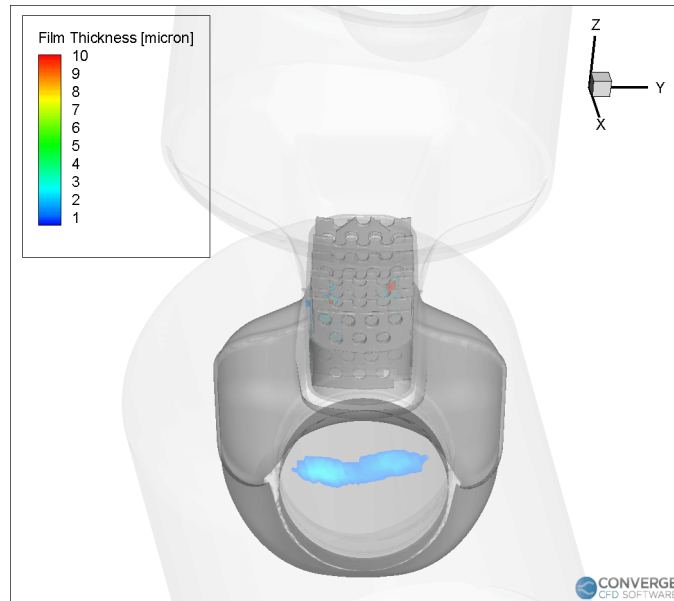
Figure 3.47: Computed wall film thickness and location for System-B. Rear view

The pictures of the flat surface downstream the mixer in System-B (Figure 3.49) confirmed the presence of solid deposits traces in the locations observed during the simulation. In addition, a large white stain was observed on one side of the mixing tube, located between the mixer and the SCRF entrance section, which although was not observed in the simulations.

Figure 3.48: Urea deposits on System-A after the experimental campaign. Upper Mixer view (top) and bottom mixer view (bottom)

Figure 3.49: Urea deposits on System-B after the experimental campaign

3.7 Conclusions

Two state-of-the-art exhaust after-treatment systems, referred to as System-A and System-B, were comprehensively characterized and analyzed.

An extensive experimental campaign was carried out in the laboratory to examine the systems chemical properties, such as the catalysts morphology and elemental composition, to characterize the UWS solution spray in terms of liquid penetration, cone angle and droplet sizing, and to investigate the systems $deNO_x$ performance under a wide range of operating conditions, representative of type-approval engine operations.

In the experiments similar chemical properties were found between the two systems catalyst components. Although, a significant performance gap between the systems was observed in the 4 different operating conditions analyzed, especially in terms of NO_x abatement. At low temperature, when the UWS conversion to ammonia is at a minimum, System-B outperformed System-A achieving a more than double NO_x conversion. System-B was confirmed more effective in terms of $deNO_x$ performance also in the other tested conditions.

To further investigate the differences between the systems and to find the root causes of the efficiency gap highlighted during the experimental campaign, a numerical analysis was carried out by means of a commercially available 3D CFD tool. The internal geometry of the analyzed systems was obtained via CT scan and used to define the virtual domain. The UWS spray experimental data were used to calibrate the break-up constants of the spray model, in order to predict liquid penetration and droplets mean diameters. The obtained simulation model was used as a virtual test rig by reproducing the operating conditions used for the experimental campaign focusing on the low load and temperature operating condition, which corresponds to a mass flow of 100 kg/h and a gas temperature of 180 degC, critical for the SCR system performance. As a result were computed the flow streamlines within the virtual domain, the distribution of velocity and species the SCRF entrance section, the liquid film mass and location within the domain and the UWS byproducts flow rate, namely ammonia and isocyanic acid, at the SCRF inlet.

The simulations allowed to understand the flow path and dynamics within the systems, highlighting the differences produced by the different mixers design and systems layout. The System-B architecture was found more effective in inducing the spray break-up into tiny droplets, boosting the evaporation and the UWS conversion into ammonia, and at the same time the system layout enhanced the mixing between UWS byproducts and the exhaust flow achieving a higher uniformity of

the flow field at the SCRF inlet, compared to System-A. The formation of liquid film was observed in the simulations for both systems, confirmed by the traces of deposits found in the real components after the experimental campaign.

The applied methodology proved to be effective in characterizing such complex and compact exhaust systems, highlighting how important is the employment of proper experimental and numerical techniques in engineering and optimizing such complex architectures, to achieve lower emissions and higher efficiency.

Chapter 4

Concluding Remarks

The future generation of diesel powertrains will have a relevant role in achieving the CO_2 fleet limits, due to its unmatched efficiency figures. Although, to comply with the latest emissions standards state-of-the-art after-treatment systems are required to simultaneously oxidize unburned hydrocarbons and CO, to reduce NO_x and to trap the particulate matter. Moreover, the increasing powertrain electrification and the more demanding test procedures introduced by the legislation require the after-treatment system to efficiently operate at both low-temperature and during high load and flow rate operating conditions.

To this aim, the after-treatment architecture combines a number of different catalyst technologies which require a comprehensive control system to optimize the after-treatment operations depending on the boundary conditions. In this complex scenario, the automotive industry demands for reliable and computationally efficient simulation tools to support the development of the after-treatment system, from the design of the individual component to the assessment and optimization of the whole exhaust line. This models are fundamental to preliminary identify the most promising technology mix to reach the emissions targets, thus reducing the number of costly experimental campaigns required and the vehicle time-to-market.

In the literature, numerous researchers investigated a multitude of modeling approaches to virtually analyze different automotive after-treatment technologies, ranging from highly-detailed kinetic models, which require a large set of experimental data, to simplified map-based models whose accuracy is granted only within a limited range. However, these methodologies are mostly designed for research purposes and often require large efforts in the model development and calibration processes, lacking of validation on real driving representative operating conditions and of well defined protocols, which are essential for industrial applications.

The objective of this research work was to contribute in clearing the gap between on-road and virtual testing by developing comprehensive modeling methodologies to obtain flexible simulation tools that can be used for virtual testing and optimization of complex after-treatment architectures, reducing the number of expensive proto-types and experimental campaigns required especially in the early design phase of a new powertrain concept.

To this aim, different modeling approaches were explored under this research programme and applied for the numerical analysis of complex and multi-dimensional problems as well as to characterize the after-treatment system chemical activity in real-driving conditions, identifying the minimum set of data required for the modeling activity and using advanced numerical techniques for the efficient models calibration. In addition, robust methodologies were defined to characterize the distinctive system operations, to develop and calibrate the simulation model based on the available experimental data by means of automated numerical tools, to finally validate the model predictive capabilities under a wide range of real driving representative operating conditions.

On the system level, a systematic modeling methodology was developed and used to build a 1D-CFD model, in the GT-SUITE environment, of an innovative low-temperature Lean NO_x Trap for a diesel passenger car. First, the catalyst chemical kinetics was extensively characterized by means of a specifically designed Synthetic Gas Bench test protocol, designed in order to identify the catalyst oxidation performance, the oxygen storage capacity, the NO_x storage during fuel-lean conditions and the NO_x reduction under fuel-rich conditions, in a wide range of different gas temperatures, space velocity and mixture composition conditions. A Genetic-Algorithm-based optimizer was used to calibrate the LNT global kinetic model constants by minimizing the error between the model predictions and the SGB experimental results. To reduce the number of reactions involved in each calibration step and thus the number of calibration parameters, a sequential calibration protocol was defined. First, the oxidation reactions parameters were calibrated based on the experimental oxidation light-off tests, then the NO_x Temperature Programmed Desorption (TPD) tests were used to calibrate the NO_x storage and release reactions under fuel-lean conditions. The OSC tests were used to calibrate the oxygen storage and reduction reactions and finally the NO_x Storage and Reduction (NSR) experiments were used to calibrate the NO_x reduction reactions under alternating fuel-lean and -rich conditions. The calibrated LNT model was finally scaled to represent the full-size component used on the engine and validated over driving cycle data, including of two different WLTC and a RDE test cycles with controlled DeNO$_x$ events. The model captured the LNT thermal behavior, the HC and CO conversion, the NO_x abatement, the ammonia and N_2O production even under remarkably transient conditions, confirming the robustness of the applied

152

methodology.

On the component level, a comprehensive methodology was developed to characterize two latest-generation after-treatment systems which consisted of an oxidation catalyst, capable of NO_x storage at low temperature, in closed coupled configuration with a Selective Catalytic Reduction catalyst coated on a Diesel Particulate Filter, or SCRoF. The systems were first experimentally analyzed to investigate the catalysts morphology and chemical composition, the Urea Water Solution spray characteristics and the systems $DeNO_x$ performance, in different type-approval representative operating conditions. The experimental analysis highlighted a large performance gap between the two architectures, especially at low temperature, despite the similar physical-chemical characteristics. A numerical analysis was carried out to further investigate the fluid dynamics within the systems and to understand the possible cause of the observed $DeNO_x$ performance gap. To this aim, a 3D-CFD simulation model was developed in CONVERGE, by recreating the internal geometry for both the systems and calibrating the spray model based on the experimental data. The obtained model was used as a virtual test bench to evaluate the systems flow development, the UWS spray break-up and interaction with the different mixers, the liquid film formation and the flow and species uniformity obtained at the SCRoF entrance section, in the low-temperature operating conditions. The numerical analysis revealed how the different mixing device design and architectures mainly influenced the spray break-up, atomization and mixing with the exhaust gas, leading to largely different flow uniformity and ammonia flow rate at the SCRoF entrance section, thus confirming the performance difference observed during the experimental campaign.

The robustness and the flexibility of the developed methodologies allowed to comprehensively analyze complex after-treatment systems providing numerical tools which could serve multiple purposes, ranging from the design optimization of individual components, to the development of control strategies and the performance assessment of an after-treatment architecture over type-approval operating conditions, supporting the OEM in the efficient design of future diesel powertrains.

LNT Model Kinetics

In the following tables rate expressions, general and inhibition functions are reported for the LNT model described in Chapter 2.

Light-Off Kinetics

Table 1: LNT Model Light-Off Concentrations Expression

Number	Site Element	Concentration Expression
1	PGM	$K_1 * CO * O_2/G(1)/G(2)$
2	PGM	$K_2 * C_3H_6 * O_2/G(1)/G(2)$
3	PGM	$K_3 * C_{12}H_{26} * O_2/(G(1) * G(2)) * \theta_2$
4	PGM	$K_4 * H_2 * O_2/G(1)/G(2) * \theta_3$
5	PGM	$K_5 * (CO * H_2O - (H_2 * CO_2/G(4)))/G(1)/G(2) * \theta_4$
6	PGM	$K_6 * C_3H_6 * H_2O/G(1)/G(2) * \theta_5$
7	PGM	$K_7 * (NO * O_2{}^{0.5} - NO_2 * G(3))/G(1)/G(2) * \theta_6$

NO$_x$ Storage and Release Kinetics

Table 2: LNT Model NOx TPD Concentrations Expression

Number	Site Element	Concentration Expression
8	Barium-I	$K_8 * NO_2 * \theta_{BaIO}$
9	Barium-I	$K_9 * NO * O_2{}^{0.1} * \theta_{BaIO}$
10	Barium-I	$K_{10} * 1 * \theta_{BaI(NO_3)_2}$
11	Barium-II	$K_{11} * NO_2/G(9) * \theta_{BaIIO}$
12	Barium-II	$K_{12} * NO * O_2{}^{0.1}/G(9) * \theta_{BaIIO}$
13	Barium-II	$K_{13} * G(5) * \theta_{BaII(NO_2)_2}$
14	Barium-II	$K_{14} * 1 * \theta_{BaII(NO_3)_2}$
15	Barium-III	$K_{15} * NO_2 * O_2{}^{0.1}/G(6) * \theta_{BaIIIO}$
16	Barium-I	$K_{16} * 1 * \theta_{BaI(NO_3)_2}$
17	Barium-III	$K_{17} * 1 * \theta_{BaIII(NO_3)_2}$

OSC Kinetics

Table 3: LNT Model OSC Concentrations Expression

Number	Site Element	Concentration Expression
18	cerium	$K_{18} * O_2 * G(7)/G(8) * \theta_{Ce_2O_3}$
19	cerium	$K_{19} * CO * G(10) * \theta_{CeO_2}$
20	cerium	$K_{20} * H_2 * G(11) * \theta_{CeO_2}$
21	cerium	$K_{21} * C_3H_6 * G(10) * \theta_{CeO_2}$

NO$_\text{x}$ Reduction Kinetics

Table 4: LNT Model NSR Concentration Expressions

Number	Site Element	Concentration Expression
22	Barium-II	$K_{22} * H_2/G(12) * \theta_{BaII(NO_2)_2}$
23	Barium-II	$K_{23} * NH_3/G(12) * \theta_{BaII(NO_2)_2}$
24	Barium-II	$K_{24} * NH_3/G(12) * \theta_{BaII(NO_2)_2}$
25	Barium-II	$K_{25} * NH_3/G(12) * \theta_{BaII(NO_3)_2}$
26	Barium-II	$K_{26} * NH_3 * G(13)/G(12) * \theta_{BaII(NO_3)_2}$
27	Barium-I	$K_{27} * H_2/G(12) * \theta_{BaI(NO_3)_2}$
28	Barium-I	$K_{28} * NH_3/G(12) * \theta_{BaI(NO_3)_2}$
29	Barium-III	$K_{29} * H_2/G(12) * \theta_{BaIII(NO_3)_2}$
30	Barium-III	$K_{30} * H_2/G(12) * \theta_{BaIII(NO_3)_2}$
31	Barium-III	$K_{31} * NH_3/G(12) * \theta_{BaIII(NO_3)_2}$
32	PGM	$K_{32} * NO * H_2/G(1)/G(2)/G(12)$
33	Barium-II	$K_{33} * CO/G(12) * \theta_{BaII(NO_2)_2}$
34	Barium-II	$K_{34} * CO/G(12) * \theta_{BaII(NO_2)_2}$
35	Barium-II	$K_{35} * CO/G(12) * \theta_{BaII(NO_3)_2}$
36	Barium-I	$K_{36} * CO/G(12) * \theta_{BaI(NO_3)_2}$
37	Barium-III	$K_{37} * CO/G(12) * \theta_{BaIII(NO_3)_2}$

Number	Site Element	Concentration Expression
38	Barium-II	$K_{38} * CO/G(12) * \theta_{BaII(NO_3)_2}$
39	Barium-II	$K_{39} * C_3H_6/G(12) * \theta_{BaII(NO_2)_2}$
40	Barium-II	$K_{40} * C_3H_6/G(12) * \theta_{BaII(NO_3)_2}$
41	Barium-I	$K_{41} * C_3H_6/G(12) * \theta_{BaI(NO_3)_2}$
42	Barium-I	$K_{42} * C_3H_6/G(12) * \theta_{BaI(NO_3)_2}$
43	Barium-III	$K_{43} * C_3H_6/G(12) * \theta_{BaIII(NO_3)_2}$
44	Barium-III	$K_{44} * C_3H_6/G(12) * \theta_{BaIII(NO_3)_2}$
45	PGM	$K_{45} * C_3H_6 * NO/G(1)/G(2)$
46	PGM	$K_{46} * C_3H_6 * NO/G(1)/G(2)/G(12)$

General and Inhibition Functions

Table 5: LNT Model General and Inhibition Functions

Function ID	Expression
G(1)	$(1 + Ai_{CO} * exp(Ta_{CO}/T) * CO+$ $+Ai_{C_3H_6} * exp(Ta_{C_3H_6}/T) * C_3H_6)^2 *$ $*(1 + Ai_{CO,C_3H_6} * exp(Ta_{CO,C_3H_6}/T) * CO^2 * C_3H_6{}^2)$
G(2)	$(1 + Ai_{NO} * exp(-Ta_{NO}/T) * NO)$
G(3)	$Ai_{NO_{x,eq}} * exp(-Ta_{NO_{x,eq}}/T)/\sqrt{(T)}$
G(4)	$exp((WGSi_1 + WGSi_2 * T - WGSi_3 * T^2)/WGSi_4/T)$
G(5)	$Ai_{BaI} * exp(-Ta_{BaI}/T * (1 - \alpha * \theta_{BaII(NO_2)_2}))$
G(6)	$1 + Ai_{BaIII} * exp(Ta_{BaI}/T) * NO$
G(7)	$max(0, 1 - 376/max(T, 385) - \theta_{CeO_2})$
G(8)	$1 + Ai_{OSC} * exp(-Ta_{OSC}/T) * NO$
G(9)	$1 + Ai_{BaII} * exp(Ta_{BaII}/T) * NO$
G(10)	$exp(-Ta_{OSC,CO}/T * (1 - 0.9 * \theta_{CeO_2}))$
G(11)	$exp(-Ta_{OSC,H_2}/T * (1 - 0.7 * \theta_{CeO_2}))$
G(12)	$1 + Ai_{NSR} * exp(Ta_{NSR}/T) * O_2$
G(13)	$Ai_{N_2O} * exp(Ta_{N_2O}/T)$

Bibliography

[1] S. R. Gundlapally, I. Papadimitriou, et al. "Development of ECU Capable Grey-Box Models from Detailed Models—Application to a SCR Reactor". In: *Emission Control Science and Technology* 2.3 (July 2016), pp. 124–136. ISSN: 2199-3629. DOI: 10.1007/s40825-016-0039-x. URL: http://dx.doi.org/10.1007/s40825-016-0039-x%20http://link.springer.com/10.1007/s40825-016-0039-x.

[2] Z. G. Liu and R. K. Miller. "Flow Distributions and Pressure Drops of Wall-Flow Diesel Particulate Filters". In: *SAE 2002 World Congress & Exhibition*. SAE International, Mar. 2002. DOI: 10.4271/2002-01-1311. URL: https://doi.org/10.4271/2002-01-1311%20https://www.sae.org/content/2002-01-1311/.

[3] F. Payri, F. J. Arnau, et al. "Lumped Approach for Flow-Through and Wall-Flow Monolithic Reactors Modelling for Real-Time Automotive Applications". In: *WCX World Congress Experience*. SAE International, Apr. 2018. DOI: https://doi.org/10.4271/2018-01-0954. URL: https://doi.org/10.4271/2018-01-0954.

[4] S. R. Gundlapally and V. Balakotaiah. "Heat and mass transfer correlations and bifurcation analysis of catalytic monoliths with developing flows". In: *Chemical Engineering Science* 66.9 (May 2011), pp. 1879–1892. ISSN: 00092509. DOI: 10.1016/j.ces.2011.01.045. URL: https://linkinghub.elsevier.com/retrieve/pii/S0009250911000650.

[5] A. S. Kota, D. Luss, and V. Balakotaiah. "Micro-kinetics of NO storage and reduction with H2/CO/C3H6 on Pt/BaO/Al2O3 monolith catalysts". In: *Chemical Engineering Journal* 262.x (Feb. 2015), pp. 541–551. ISSN: 13858947. DOI: 10.1016/j.cej.2014.09.060. URL: http://dx.doi.org/10.1016/j.cej.2014.09.060%20https://linkinghub.elsevier.com/retrieve/pii/S138589471401256X.

[6] D. Bhatia, R. W. McCabe, et al. "Experimental and kinetic study of NO oxidation on model Pt catalysts". In: *Journal of Catalysis* 266.1 (2009), pp. 106–

119. ISSN: 00219517. DOI: 10.1016/j.jcat.2009.05.020. URL: http://dx.doi.org/10.1016/j.jcat.2009.05.020.

[7] M. Rafigh, R. Dudgeon, et al. "Development of a Global Kinetic Model for a Commercial Lean NOx Trap Automotive Catalyst Based on Laboratory Measurements". In: *Emission Control Science and Technology* 3.1 (Mar. 2017), pp. 73–92. ISSN: 2199-3629. DOI: 10.1007/s40825-016-0049-8. URL: http://link.springer.com/10.1007/s40825-016-0049-8.

[8] G. C. Koltsakis, N. K. Margaritis, et al. "Development and Experimental Validation of a NOx Trap Model for Diesel Exhaust". In: vol. 2006. Apr. 2006. DOI: 10.4271/2006-01-0471. URL: https://www.sae.org/content/2006-01-0471/.

[9] J. Sjöblom. "Bridging the Gap Between Lab Scale and Full Scale Catalysis Experimentation". In: *Topics in Catalysis* 56.1-8 (May 2013), pp. 287–292. ISSN: 1022-5528. DOI: 10.1007/s11244-013-9968-6. URL: http://link.springer.com/10.1007/s11244-013-9968-6.

[10] J. Xu, M. P. Harold, and V. Balakotaiah. "Modeling the effects of Pt loading on NOx storage on Pt/BaO/Al2O3 catalysts". In: *Applied Catalysis B: Environmental* 104.3-4 (May 2011), pp. 305–315. ISSN: 09263373. DOI: 10.1016/j.apcatb.2011.03.014. URL: http://linkinghub.elsevier.com/retrieve/pii/S0926337311001275%20https://linkinghub.elsevier.com/retrieve/pii/S0926337311001275.

[11] W. S. Epling, J. E. Parks, et al. "Further evidence of multiple NOx sorption sites on NOx storage/reduction catalysts". In: *Catalysis Today* 96.1-2 (Oct. 2004), pp. 21–30. ISSN: 09205861. DOI: 10.1016/j.cattod.2004.05.004. URL: http://linkinghub.elsevier.com/retrieve/pii/S092058610400197X.

[12] J. Koop and O. Deutschmann. "Modeling and Simulation of NOx Abatement with Storage/Reduction Catalysts for Lean Burn and Diesel Engines". In: Apr. 2007. DOI: 10.4271/2007-01-1142. URL: https://www.sae.org/content/2007-01-1142/.

[13] I. Nova, L. Lietti, et al. "Experimental investigation of the reduction of NOx species by CO and H2 over Pt–Ba/Al2O3 lean NOx trap systems". In: *Catalysis Today* 151.3-4 (June 2010), pp. 330–337. ISSN: 09205861. DOI: 10.1016/j.cattod.2010.02.075. URL: https://linkinghub.elsevier.com/retrieve/pii/S0920586110002221.

[14] S. Morandi, G. Ghiotti, et al. "Reduction by CO of NOx species stored onto Pt–K/Al2O3 and Pt–Ba/Al2O3 lean NOx traps". In: *Catalysis Today* 176.1 (Oct. 2011), pp. 399–403. ISSN: 09205861. DOI: 10.1016/j.cattod.2010.11.024. URL: https://linkinghub.elsevier.com/retrieve/pii/S0920586110007650.

[15]   L. Masdrag, X. Courtois, et al. "Understanding the role of C3H6, CO and H2 on efficiency and selectivity of NOx storage reduction (NSR) process". In: *Catalysis Today* 189.1 (July 2012), pp. 70–76. ISSN: 09205861. DOI: 10.1016/j.cattod.2012.03.053. URL: http://linkinghub.elsevier.com/retrieve/pii/S0920586112002192%20https://linkinghub.elsevier.com/retrieve/pii/S0920586112002192.

[16]   F. Millo, M. Rafigh, et al. "Modeling NOx Storage and Reduction for a Diesel Automotive Catalyst Based on Synthetic Gas Bench Experiments". In: *Industrial & Engineering Chemistry Research* 57.37 (Sept. 2018), pp. 12335–12351. ISSN: 0888-5885. DOI: 10.1021/acs.iecr.8b01813. URL: http://pubs.acs.org/doi/10.1021/acs.iecr.8b01813%20https://pubs.acs.org/doi/10.1021/acs.iecr.8b01813.

[17]   K. Deb and H. Jain. "An Evolutionary Many-Objective Optimization Algorithm Using Reference-Point-Based Nondominated Sorting Approach, Part I: Solving Problems With Box Constraints". In: *IEEE Transactions on Evolutionary Computation* 18.4 (Sept. 2014), pp. 577–601. ISSN: 1089-778X. DOI: 10.1109/TEVC.2013.2281535. URL: http://ieeexplore.ieee.org/document/6600851/.

[18]   S. E. Voltz, C. R. Morgan, et al. "Kinetic Study of Carbon Monoxide and Propylene Oxidation on Platinum Catalysts". In: *Industrial & Engineering Chemistry Product Research and Development* 12.4 (Nov. 1973), pp. 294–301. ISSN: 0196-4321. DOI: 10.1021/i360048a006. URL: https://pubs.acs.org/doi/abs/10.1021/i360048a006.

[19]   V. Piacente, G. Bardi, et al. "Dissociation energy of CeO 2 and Ce 2 O 2 molecules". In: *The Journal of Chemical Physics* 59.1 (July 1973), pp. 31–36. ISSN: 0021-9606. DOI: 10.1063/1.1679807. URL: http://aip.scitation.org/doi/10.1063/1.1679807.

[20]   P. Kočí, F. Plát, et al. "Dynamics and selectivity of NOx reduction in NOx storage catalytic monolith". In: *Catalysis Today* 137.2-4 (Sept. 2008), pp. 253–260. ISSN: 09205861. DOI: 10.1016/j.cattod.2007.11.023. URL: http://linkinghub.elsevier.com/retrieve/pii/S0920586107007547%20https://linkinghub.elsevier.com/retrieve/pii/S0920586107007547.

[21]   A. Güthenke, D. Chatterjee, et al. "Development and application of a model for a NOx storage and reduction catalyst". In: *Chemical Engineering Science* 62.18-20 (Sept. 2007), pp. 5357–5363. ISSN: 00092509. DOI: 10.1016/j.ces.2007.01.049. URL: http://linkinghub.elsevier.com/retrieve/pii/S0009250907001121%20https://linkinghub.elsevier.com/retrieve/pii/S0009250907001121.

[22] T. Gu and V. Balakotaiah. "Impact of heat and mass dispersion and thermal effects on the scale-up of monolith reactors". In: *Chemical Engineering Journal* 284 (Jan. 2016), pp. 513–535. ISSN: 13858947. DOI: 10.1016/j.cej.2015.09.005. URL: http://linkinghub.elsevier.com/retrieve/pii/S1385894715012425%20https://linkinghub.elsevier.com/retrieve/pii/S1385894715012425.

[23] C. S. Sampara, E. J. Bissett, et al. "Global Kinetics for Platinum Diesel Oxidation Catalysts". In: *Industrial & Engineering Chemistry Research* 46.24 (Oct. 2007), pp. 7993–8003. ISSN: 0888-5885. DOI: 10.1021/ie070642w. URL: http://pubs.acs.org/doi/abs/10.1021/ie070642w%20https://pubs.acs.org/doi/10.1021/ie070642w.

[24] S. R. Katare and P. M. Laing. "Hydrogen in Diesel Exhaust: Effect on Diesel Oxidation Catalyst Flow Reactor Experiments and Model Predictions". In: *SAE International Journal of Fuels and Lubricants* 2.1 (Apr. 2009), pp. 2009–01–1268. ISSN: 1946-3960. DOI: 10.4271/2009-01-1268. URL: https://www.sae.org/content/2009-01-1268/.

[25] K. Ramanathan and C. S. Sharma. "Kinetic Parameters Estimation for Three Way Catalyst Modeling". In: *Industrial & Engineering Chemistry Research* 50.17 (Sept. 2011), pp. 9960–9979. ISSN: 0888-5885. DOI: 10.1021/ie200726j. URL: https://pubs.acs.org/doi/10.1021/ie200726j.

[26] F. Millo, M. Rafigh, et al. "Application of Genetic Algorithm for the Calibration of the Kinetic Scheme of a Diesel Oxidation Catalyst Model". In: *SAE Technical Papers*. Vol. 2018-Septe. Sept. 2018. DOI: 10.4271/2018-01-1762. URL: https://www.sae.org/content/2018-01-1762/.

[27] F. Birkhold, U. Meingast, et al. "Analysis of the Injection of Urea-Water-Solution for Automotive SCR DeNOx-Systems: Modeling of Two-Phase Flow and Spray/Wall-Interaction". In: *SAE International*. Vol. 2006-01-06. 724. Apr. 2006. DOI: 10.4271/2006-01-0643. URL: http://papers.sae.org/2006-01-0643/%20https://www.sae.org/content/2006-01-0643/.

[28] F. Birkhold, U. Meingast, et al. "Modeling and simulation of the injection of urea-water-solution for automotive SCR DeNOx-systems". In: *Applied Catalysis B: Environmental* 70.1-4 (Jan. 2007), pp. 119–127. ISSN: 09263373. DOI: 10.1016/j.apcatb.2005.12.035. URL: https://linkinghub.elsevier.com/retrieve/pii/S0926337306002402.

[29] H. Smith, T. Lauer, et al. "Optical and Numerical Investigations on the Mechanisms of Deposit Formation in SCR Systems". In: *SAE International Journal of Fuels and Lubricants* 7.2 (Apr. 2014), pp. 2014–01–1563. ISSN: 1946-3960. DOI: 10.4271/2014-01-1563. URL: https://www.sae.org/content/2014-01-1563/.

[30] S. Knirsch, U. Weiss, et al. "New Generation of the Audi V6 TDI Engine Part 2: Thermodynamics, Application and Exhaust Cleaning". In: *MTZ worldwide* 75.10 (Sept. 2014), pp. 22–27. ISSN: 2192-9114. DOI: 10.1007/s38313-014-0231-8. URL: http://link.springer.com/10.1007/s38313-014-0231-8.

[31] T. Eder, P. Lückert, et al. "OM 654 — Launch of a New Engine Family by Mercedes-Benz". In: *MTZ worldwide* 77.3 (Mar. 2016), pp. 60–67. ISSN: 2192-9114. DOI: 10.1007/s38313-015-0097-4. URL: http://link.springer.com/10.1007/s38313-015-0097-4.

[32] D. Naber, A. Kufferath, et al. "Measures to fulfill "real driving emission (RDE)" with Diesel passenger cars". In: 2017, pp. 423–446. DOI: 10.1007/978-3-658-16988-6_34. URL: http://link.springer.com/10.1007/978-3-658-16988-6%7B%5C_%7D34.

[33] D. Landsberg, U. Zink, et al. "Emission Control System for RDE -Catalyst Technology and Application Requirements". In: 2018.

[34] J. Seo. "Aftertreatment Package Design for SCR Performance Optimization". In: Apr. 2011. DOI: 10.4271/2011-01-1135. URL: http://papers.sae.org/2011-01-1135/%20https://www.sae.org/content/2011-01-1135/.

[35] P. Way, K. Viswanathan, et al. "SCR Performance Optimization Through Advancements in Aftertreatment Packaging". In: Apr. 2009. DOI: 10.4271/2009-01-0633. URL: https://www.sae.org/content/2009-01-0633/.

[36] F. Ekström and B. Andersson. "Pressure Drop of Monolithic Catalytic Converters Experiments and Modeling". In: Mar. 2002. DOI: 10.4271/2002-01-1010. URL: https://www.sae.org/content/2002-01-1010/.

[37] R. M. Heck and R. J. Farrauto. "Automobile exhaust catalysts". In: *Applied Catalysis A: General* 221.1-2 (Oct. 2001), pp. 443–457. ISSN: 0926860X. DOI: 10.1016/S0926-860X(01)00818-3. URL: https://linkinghub.elsevier.com/retrieve/pii/S0926860X01008183.

[38] C. H. Kim, M. Schmid, et al. "The Effect of Pt-Pd Ratio on Oxidation Catalysts Under Simulated Diesel Exhaust". In: *Sae.* Vol. 2011-01-11. 1. Apr. 2011, pp. 1–10. DOI: 10.4271/2011-01-1134. URL: https://www.sae.org/content/2011-01-1134/.

[39] W. S. Epling, L. E. Campbell, et al. "Overview of the Fundamental Reactions and Degradation Mechanisms of NOx Storage/Reduction Catalysts". In: *Catalysis Reviews* 46.2 (Nov. 2004), pp. 163–245. ISSN: 0161-4940. DOI: 10.1081/CR-200031932. URL: http://www.tandfonline.com/doi/abs/10.1081/CR-200031932.

[40] K. Aravelli and A. Heibel. "Improved Lifetime Pressure Drop Management for Robust Cordierite (RC) Filters with Asymmetric Cell Technology (ACT)". In: Apr. 2007. DOI: 10.4271/2007-01-0920. URL: http://papers.sae.org/2007-01-0920/%20https://www.sae.org/content/2007-01-0920/.

[41] P. S. Metkar, M. P. Harold, and V. Balakotaiah. "Experimental and kinetic modeling study of NH3-SCR of NOx on Fe-ZSM-5, Cu-chabazite and combined Fe- and Cu-zeolite monolithic catalysts". In: *Chemical Engineering Science* 87.x (Jan. 2013), pp. 51–66. ISSN: 00092509. DOI: 10.1016/j.ces.2012.09.008. URL: http://dx.doi.org/10.1016/j.ces.2012.09.008%20https://linkinghub.elsevier.com/retrieve/pii/S0009250912005751.

[42] G. W. Zack, W. E. Rogers, and S. A. Latt. "Automatic measurement of sister chromatid exchange frequency." In: *Journal of Histochemistry & Cytochemistry* 25.7 (July 1977), pp. 741–753. ISSN: 0022-1554. DOI: 10.1177/25.7.70454. URL: http://journals.sagepub.com/doi/10.1177/25.7.70454.

[43] L. Postrioti, G. Brizi, et al. "A methodology to investigate the behaviour of urea-water sprays in high temperature air flow for SCR de-NOx Applications". In: *Fuel* 150 (June 2015), pp. 548–557. ISSN: 00162361. DOI: 10.1016/j.fuel.2015.02.067. URL: https://linkinghub.elsevier.com/retrieve/pii/S0016236115002203.

[44] R. Finesso, D. Misul, and E. Spessa. "Estimation of the Engine-Out NO2/NOx Ratio in a EURO VI Diesel Engine". In: Apr. 2013. DOI: 10.4271/2013-01-0317. URL: https://www.sae.org/content/2013-01-0317/.

[45] P. K. Senecal, K. Richards, and E. Pomraning. *CONVERGE 2.4 Manual.* Madison, WI, 2019.

[46] V. Yakhot, S. A. Orszag, et al. "Development of turbulence models for shear flows by a double expansion technique". In: *Physics of Fluids A* (1992). ISSN: 08998213. DOI: 10.1063/1.858424.

[47] G. C. Papageorgakis and D. N. Assanis. "Comparison of linear and nonlinear rng-based k-epsilon models for incompressible turbulent flows". In: *Numerical Heat Transfer, Part B: Fundamentals* (1999). ISSN: 15210626. DOI: 10.1080/104077999275983.

[48] P. K. Senecal, E. Pomraning, et al. "Grid-Convergent Spray Models for Internal Combustion Engine CFD Simulations". In: *ASME 2012 Internal Combustion Engine Division Fall Technical Conference.* ASME, Sept. 2012, p. 697. ISBN: 978-0-7918-5509-6. DOI: 10.1115/ICEF2012-92043. URL: http://proceedings.asmedigitalcollection.asme.org/proceeding.aspx?doi=10.1115/ICEF2012-92043.

[49] N. M. Wruck and U. Renz. "Transient phase-change of droplets impacting on a hot wall". In: *Transient Phenomena in Multiphase and Multicomponent Systems*. 2007. ISBN: 9783527610785. DOI: 10.1002/9783527610785.ch14.

[50] V. Ebrahimian, A. Nicolle, and C. Habchi. "Detailed modeling of the evaporation and thermal decomposition of urea-water solution in SCR systems". In: *AIChE Journal* 58.7 (July 2012), pp. 1998–2009. ISSN: 00011541. DOI: 10.1002/aic.12736. URL: http://doi.wiley.com/10.1002/aic.12736.

[51] H. Ström, A. Lundström, and B. Andersson. "Choice of urea-spray models in CFD simulations of urea-SCR systems". In: *Chemical Engineering Journal* 150.1 (July 2009), pp. 69–82. ISSN: 13858947. DOI: 10.1016/j.cej.2008.12.003. URL: https://linkinghub.elsevier.com/retrieve/pii/S1385894708008140.

[52] S. D. Yim, S. J. Kim, et al. "Decomposition of Urea into NH3 for the SCR Process". In: *Industrial & Engineering Chemistry Research* 43.16 (Aug. 2004), pp. 4856–4863. ISSN: 0888-5885. DOI: 10.1021/ie034052j. URL: https://pubs.acs.org/doi/10.1021/ie034052j.

[53] A. Munnannur, C. M. Cremeens, and Z. G. Liu. "Development of Flow Uniformity Indices for Performance Evaluation of Aftertreatment Systems". In: *SAE International Journal of Engines* 4.1 (Apr. 2011), pp. 2011–01–1239. ISSN: 1946-3944. DOI: 10.4271/2011-01-1239. URL: https://www.sae.org/content/2011-01-1239/.

This Ph.D. thesis has been typeset by means of the TeX-system facilities. The typesetting engine was pdfLaTeX. The document class was `toptesi`, by Claudio Beccari, with option `tipotesi=scudo`. This class is available in every up-to-date and complete TeX-system installation.